NEW METHODS AND DEVELOPMENTS IN NANOPARTICLE MASS SPECTROMETRY AND MODE- AND BOND-SPECIFIC REACTIONS OF HOD+

by

David M. Bell

A dissertation submitted to the faculty of
The University of Utah
in partial fulfillment of the requirements for the degree of

Doctor of Philosophy

Department of Chemistry

The University of Utah

December 2014

Copyright © David M. Bell 2014

All Rights Reserved

The University of Utah Graduate School

STATEMENT OF DISSERTATION APPROVAL

The dissertation of **David M. Bell**

has been approved by the following supervisory committee members:

Scott L. Anderson	, Chair	**3/14/14** Date Approved
Peter B. Armentrout	, Member	**3/14/14** Date Approved
Michael D. Morse	, Member	**3/14/14** Date Approved
Jennifer S. Shumaker-Parry	, Member	**3/14/14** Date Approved
Jordan Gerton	, Member	Date Approved

and by **Cynthia J. Burrows**, Chair/Dean of

the Department/College/School of **Chemistry**

and by David B. Kieda, Dean of The Graduate School.

ABSTRACT

This dissertation focuses initially on development of a nanoparticle mass spectrometer (NPMS) for single particle analysis utilizing a split ring electrode trap (SRET). Electrospray ionization generates nanoparticle ions that are guided and trapped in the SRET. Detection of single particles occurs by observing light scattered or fluorescence emitted from the particle. Three methods are used to determine the secular frequency (ω_z) of a single trapped particle: Fourier transform analysis of scattered light intensity, frequency sweep of the laser force, or frequency sweep of a constant AC voltage. From ω_z, the mass-to-charge ratio may be ascertained. The AC frequency sweep method results in a peak width nearing 10 ppm. By averaging the peak position of multiple AC frequency sweep measurements, precision approaches 1 ppm. This method is then applied to single core-shell CdSe/ZnS quantum dots by activating their fluorescence with a CO_2 laser. The secular frequency, mass, charge, and fluorescence intensity are tracked for a single QD over multiple days. Heating the QD sublimates the particle and causes it to eventually go dark. Once dark, the QD remains in the trap and begins to fluoresce intermittently.

The focus of the later half is on reactions of vibrationally state-selected HOD^+. Each of the fundamental vibrational states of HOD^+ was investigated. Cross sections and product velocity distributions were obtained for every product for each reaction and each vibrational state investigated. Reactions of HOD^+ with CO, N_2O, CO_2, and N_2 were investigated. These reactions were chosen because proton transfer is endoergic for each reaction or thermoneutral. Mode- and bond-selective enhancement was observed for the cross sections of H^+ and D^+ transfer for the OH and OD stretch, respectively. The bend vibration also enhances reactivity; in some cases, the total

enhancement for the bend is greater than that of the OH or OD stretches. Velocity distributions indicated that the mechanism for H^+ and D^+ transfer near threshold might be complex mediated, but it is difficult to tell because there is little energy available to the system near threshold. However, with increasing collision energy (E_{col}), the reaction becomes increasingly direct and backward scattered.

TABLE OF CONTENTS

ACKNOWLEDGEMENTS

I would like to thank Scott L. Anderson for the many opportunities he has provided me in my time at the University of Utah. Scott gave me the opportunity to work with him during the summer of 2007 on an REU and from that time on, I knew I wanted to study physical chemistry and, specifically, develop new techniques in mass spectrometry. Scott has been very patient, kind, and encouraging in the development and construction of the nanoparticle mass spectrometer over the past two years. I am grateful for the opportunity to have built this instrument and learn from the frustrations and joys of developing an instrument from the ground up.

I would also like to thank the members of the Anderson group throughout my time in Utah for they have been instrumental in my development as a chemist. It has been a joy working with everyone in the group and it has been a truly wonderful place to study chemistry. The group has been a great place for intellectual discussions, experimental insights, enjoyment of the outdoors, and other fun activities. I would like to specifically thank Dr. Jason M. Boyle for his guidance and Collin R. Howder for his encouragement and his help in constructing the nanoparticle mass spectrometer. Dieter Gerlich has been a tremendous collaborator in encouraging the development of this project and being a source of many helpful and stimulating discussions. I would like to thank my friends for their support throughout the various seasons of my academic career. The encouragement and support of Shawn Soward, Matt Whitehead, Jonathan Hickerson, and Eric Brozek have been invaluable to me over the years.

Most of all, I would like to thank my parents for loving support, giving me the opportunity to study chemistry, and their encouragement to pursue a graduate degree.

CHAPTER 1

OVERVIEW

Brief Overview on Mass Spectrometry

The main challenges in the field of chemistry revolve around understanding the physical properties of molecules and how chemical reactions take place.[1] This pursuit necessitates having or developing the right tools or techniques to investigate molecules and how they react with one another. One of the oldest known tools is a balance, which present day has evolved greatly from its initial crude forms. With the advent of mass spectrometry, a type of balance for ions, it is possible to measure the mass-to-charge ratio of an ion to very high resolution, precision, and accuracy.[2] The first example of this was shown by W. Wien, who discovered the mass of the proton.[3] However, this result was not fully accepted until J. J. Thomson demonstrated the ability to obtain a mass spectrograph of two different isotopes of Neon (20 and 22).[4]

Mass spectrometry was furthered by the development of ion trapping techniques put forth by Paul[5] and by ion guiding techniques demonstrated by von Zahn.[6] The history of mass spectrometry and the physics surrounding it has been discussed at length in a variety of reviews.[7-11] Mass spectrometry has developed into a very important technique and has had far reaching applications in the realm of chemistry because knowing the mass of a molecule is an important part of assigning its structure.[12] This is especially true in organic chemistry; a mass spectrum is a routine part of determining the structure of a molecule based on its fragmentation pattern. Biological chemistry, specifically the omics community, routinely uses a mass spectrometer in combination with various separations techniques to analyze complicated biological assays and better understand what is present in these complex mixtures and the structures of these species.[13-15]

Physical chemists use a mass spectrometer in a slightly different way. A mass spectrometer can be used to prepare a well-defined system. By using a well-characterized ion source, it is possible to know the make-up of a mass-selected ion beam. The ion beam may then be manipulated in a variety of ways, such as: colliding it with an unreactive neutral species to determine bond energies of the precursor ion,[16-19] preparing a specific ion for spectroscopic

investigations,[20-23] using a specific ion in ion–molecule reactions to further understand reaction dynamics,[1, 24-26] and depositing an ion of interest on a surface.[27-30] Thus, the use of a mass spectrometer makes it possible to study a wide variety of problems.

Here, this dissertation will focus on two very different uses of mass spectrometry: one involves advances made in nanoparticle mass spectrometry (NPMS) and the other involves using a tandem mass spectrometer to investigate vibrationally state-selected HOD^+ to probe endoergic H^+/D^+ transfer. NPMS will be discussed in Chapters 2 through 6. Reaction dynamics of HOD^+ will be discussed in Chapters 7 through 11.

References

1. R. D. Levine, *Molecular Reaction Dynamics*. (Cambridge U. Pr., Cambridge, 2005).
2. H. E. Duckworth, R. C. Barber and V. S. Venkatasubramanian, *Mass Spectrometry*, 2nd ed. (Cambridge, Cambridge, 1986).
3. W. Wien, Annalen der Physik **5**, 421 (1901).
4. J. J. Thomson, Proceedings of the Royal Soceity A **89**, 1 (1913).
5. W. Paul and H. Steinwedel, Zeitschrift Naturforsh. **8A**, 448 (1953).
6. U. von Zahn and H. Tatarczyk, Phys. Lett. **12**, 190 (1964).
7. D. Gerlich, in *State-selected and state-to-state ion-molecule reaction dynamics, Part I. Experiment*, edited by C. Y. Ng and M. Baer (Wiley, New York, 1992), Vol. LXXXII, pp. 1-176.
8. D. Gerlich, Adv. Chem. Phys. **82**, 1 (1992).
9. P. H. Dawson, *Quadrupole Mass Spectrometry*. (Elsevier Scientific Pub., Amsterdam, 1976).
10. L. D. Landau and E. M. Lifshitz, *Mechanics*. (Pergamon Pr., Oxford, 1960).
11. D. Gerlich, in *Advances in Chemical Physics: State-Selected and State-To-State Ion-Molecule Reaction Dynamics, Part 1*, edited by C. Y. Ng and M. Baer (J. Wiley & Sons, 1992), Vol. 82, pp. 1-176.
12. T. N. Sorrell, *Organic Chemistry 2nd Edition*. (University Science Books, 2006).
13. R. Aebersold and M. Mann, Nature **422**, 198 (2003).

14. G. J. Patti, O. Yanes and G. Siuzdak, Nature Reviews: Molecular Cell Biology **13**, 263 (2012).

15. J. Zaia, OMICS **14**, 401 (2010).

16. P. B. Armentrout, in *The Encyclopedia of Mass Spectrometry. Volume 1: Theory and Ion Chemistry*, edited by P. B. Armentrout (Elsevier, Amsterdam, 2003), pp. 426-434.

17. R. G. Cooks, in *Collision Spectroscopy*, edited by R. G. Cooks (Plenum Press, New York, 1978).

18. F. Muntean and P. B. Armentrout, J. Chem. Phys **115** (3), 1213 (2001).

19. M. T. Rodgers and P. B. Armentrout, J. Chem. Phys. **109**, 1787 (1998).

20. H. Yao and R. Jockusch, J. Phys. Chem. A **117**, 1351 (2013).

21. Q. Bian, M. W. Forbes, F. O. Talbot and R. A. Jockusch, Physical Chemistry Chemical Physics **12**, 2590 (2010).

22. S. K. Sagoo and R. A. Jockusch, Journal of Photochemistry and Photobiology A: Chemistry **220**, 173 (2011).

23. A. Fujii, T. Ebata and M. Ito, Chem. Phys. Lett. **161**, 93 (1989).

24. S. L. Anderson, NATO ASI Ser., Ser. C **347**, 183 (1991).

25. J. M. Farrar, Annu. Rev. Phys. Chem **46**, 525 (1995).

26. J. Liu and S. L. Anderson, Int. J. Mass Spectrom. **241**, 173 (2005).

27. M. Aizawa, S. Lee and S. L. Anderson, Surf. Sci. **542**, 253 (2003).

28. M. Aizawa, S. Lee and S. L. Anderson, J. Chem. Phys. **117**, 5001 (2002).

29. W. E. Kaden, W. A. Kunkel, M. D. Kane, F. S. Roberts and S. L. Anderson, J. Am. Chem. Soc. **132,** 13097 (2010).

30. W. E. Kaden, T. Wu, W. A. Kunkel and S. L. Anderson, Science **326**, 826 (2009).

CHAPTER 2

INTRODUCTION TO NANOPARTICLE MASS SPECTROMETRY

Pioneering Work

Developments in the field of nanoparticle mass spectrometry (NPMS) have slowly progressed since the late 1950s,[1] but since 2000, renewed interest in the field spurred the development of a number of nanoparticle mass spectrometers.[2-14] NPMS was first demonstrated by Wuerker *et al.* in 1959 by trapping aluminum dust in a quadrupole ion trap.[1] Trapped particles, in this experiment, were so large they were visible to the eye. Pictures of the particles were taken by shining light on them. The pictures showed that a single particle had a lissajous orbit. When more than one particle was present in the trap, the ensemble formed a lattice structure at high pressures, also known as a Coulomb crystal.[15-17] Lattice formation was a result of the thermal energy of the trapped particles being significantly smaller than the Coulomb repulsion between the particles. Coulomb crystals have been studied in detail and are observed in sympathetically cooled atomic ions.[15-19] Wuercker *et al.* also demonstrated that by applying a sinusoidal AC voltage to the trap, it was possible to resonantly excite the motional (or secular) frequency (ω_z) of a single particle or a swarm of particles.[1] Resonantly exciting a single particle or a swarm causes them to disappear or appear as a smear in the trap. When performed on an ensemble of particles, the lattice structure melted and became a blur because the translational energy of the ions became greater than the Coulomb repulsion. The frequency at which the ions were excited relates to the mass-to-charge ratio of the micro- or nanoparticle.

NPMS relies on the special relationship between the mass-to-charge ratio of an ion in a quadrupole field and ω_z.[20] In a quadrupole field, the mass-to-charge ratio is defined as:

$$\frac{M}{Q} = \frac{\sqrt{2}V_0^2}{\omega_z \Omega z_0^2} \qquad (1)$$

where M is the mass of the ion, Q is the number of charges on the ion, V_0 is the radio frequency (RF) voltage amplitude, ω_z is the motional (secular) frequency of the ion, Ω is the RF frequency (in radians), and z_0 is a geometric parameter of the field. Since V_0, Ω, and z_0 are known because

they are not changed during an experiment, it is possible to determine the mass-to-charge ratio of an ion by measuring ω_z.

Resolution and Size Limit

Although first demonstrated in 1959, questions remained: what ω_z resolution could be obtained by optical detection of a single trapped nanoparticle? What is the size limit for detection? What is the usefulness of this technique? What types of systems would be useful to study in this way? Unfortunately, it would be decades until this research was expanded upon. In 1995 Hars and Tass[21] used a laser to scatter light off of a nanoparticle and observed that by making the ω_z an interger multiple of the RF frequency (Ω), the trajectory of an ion became a star-like lissajous orbit. This technique showed it was possible to determine ω_z with a precision of 1,000 ppm, by counting the points on the trajectory of the ion's motion. Later, Schlemmer *et al.* demonstrated that Fourier transforming the time record of the scattered light signal from a 500 nm SiO_2 particle determined ω_z to within 100 ppm for a single measurement. By creating a histogram of the peak positions over an hour, they achieved precision of 10 ppm.[2, 22]

A limitation of this method is that it requires light scattering to detect micro- and nano-particles. If a particle is too small (<25 nm), it becomes difficult to detect because it does not scatter light efficiently. The scattered light intensity from a small particle smaller than the wavelength of light used is governed by Rayleigh scattering and scales like d^6, where d is the diameter of the particle.[23] Chang *et al.* used small dye-doped polystyrene particles (~25 nm) to increase signal for smaller particle sizes, but this was a destructive technique.[4, 5] It may be possible to push this boundary further by investigating very small nanoparticles (<25 nm) if they are sufficiently fluorescent or photoluminescent.

Image charge detection is another way to detect large particles. Recently, Jarrold and co-workers demonstrated the ability to determine both the mass and charge from a virus capsid in a cone trap.[24] They determined the charge by the amplitude of the image charge signal, and the

mass-to-charge ratio by the frequency at which the ion passed through the image charge detector. Image charge detection is a robust technique used in a variety of methods[25, 26] and has the advantage that it is possible to track both bright and dark particles. Compared to an electrostatic trap, a Paul trap has the advantage that an ion can be trapped for more than a day, which is not true in an electrostatic trap. Image charge detection is difficult in a Paul trap because the large RF voltages present on the trap make it difficult to observe small fluctuations in voltage due to the trapped ion.

Using Quantum Dots

In order to decrease the size of particles detected by this method, they must be very bright despite being small in size. Core-shell CdSe/ZnS nanocrystal quantum dots (QDs) are an excellent candidate for such studies. QDs are generally between 2 nm – 10 nm in diameter, significantly smaller than previous particles used for these studies. CdSe/ZnS QDs can be very bright, having a quantum yield of 50 – 85%.[27] Unfortunately, little is known about how QDs will behave when charged with more than one charge or detached from a surface / out of solution. To date, there has only been one study analyzing QDs detached from a surface or not in solution.[28] This gas phase study examined the photoelectron spectra of neutral QDs and determined the fraction of the evanescent wavefunction that extends past the QD surface.

However, charging QDs should have a large effect on their optical properties (i.e., absorption and emission spectra, fluorescence intermittency (blinking), and fluorescence lifetime). A number of groups have shown that charging a QD on an electrode with one charge, positive or negative, can change its optical properties.[29-36] Guyot-Sionnest and co-workers showed that putting an electron on a QD by applying a negative voltage (-0.7 V) quenched the fluorescence of QDs. Conversely, applying a positive voltage (+0.3 V), removing the electron, immediately restored the fluorescence.[30] Galland *et al.* subsequently showed that there were two blinking mechanisms, both of which could be electrochemically controlled.[36] One type is due to

an excess electron causing Auger recombination, thus a positive voltage quenches blinking by removing the electron from the QD. The other type is due to interaction between the Fermi level of the substrate with dark trap states on the surface of the QD. It is hypothesized that applying a negative voltage quenches blinking because the surface states are filled, so there may only be radiative recombination. Since charging a QD positive or negative can both quench blinking or fluorescence, it is difficult to predict if a charged QD will fluoresce at all in an ion trap.

Potential Applications of Nanoparticle Mass Spectrometry

Schlemmer *et al.* also showed it was possible to determine the absolute mass and charge of a nanoparticle by observing discrete quantized steps in ω_z that were stimulated by an electron gun. The steps resulted from changes in the number charges present. After determining the absolute mass, it is possible to conduct chemistry on a nanoparticle and track how the mass, alone, changes as molecules adsorb to the surface. Schlemmer illustrated this by depositing C_{60} on a trapped nanoparticle and burning off the carbon layer with a CO_2 laser.

There have been limited applications of studying chemical systems with NPMS so far, but there are many potential uses of this technique. Further increases in precision and resolution would make it possible to observe smaller changes in mass and hypothetically individual molecules absorbing to and desorbing from the surface. Utilizing a CO_2 laser can make it possible to study high temperature surface chemistry and thermal emission from a variety of nanoparticles. NPMS could be a useful technique to investigate high temperature chemistry on nanoparticle surfaces. Another application of this method would be to use a bright particle to observe the mass-to-charge ratio of a dark particle, which would increase the potential uses of this technique dramatically. A prerequisite is that the motion of the two particles must not strongly couple (form a Coulomb crystal), or have secular frequencies that are close to one another. Specifically, viruses would be an interesting candidate to study with this dark particle detection scheme. A final potential use would be to build nanostructures in the trap by trapping a positively charged

nanoparticle and then introducing a more negatively charged nanoparticle. The Coulomb attraction between the particles would bring them together in the trap. This could be done repeatedly to build very specific nanostructures and to study the optical properties of these interesting species, such as energy transfer between two QDs.

Here, two methods were used to ascertain the mass-to-charge ratio of a >100 nm polystyrene nanoparticle with light scattering. One of the methods exhibited precision approaching 10 ppm for a single spectrum. Chapters 4 shows that fluorescence from QDs enhanced when exposed to a CO_2 laser (λ = 10.6 μm). Chapter 5 demonstrates that single QDs were trapped over the course of hours and days and charge steps revealed the absolute charge and mass. When heated, the QD sublimates until it goes dark, and once dark, the QD begins to fluoresce intermittently or blink.

References

1. R. F. Wuerker, H. H. Shelton and R. V. Langmuir, Journal of Applied Physics **30**, 342 (1959).
2. S. Schlemmer, J. Illemann, S. Wellert and D. Gerlich, AIP Conf. Proc. **457**, 80 (1999).
3. Y. Cai, W. P. Peng, S. J. Kuo, Y. T. Lee and H. C. Chang, Anal. Chem. **74**, 232 (2002).
4. Y. Cai, W. P. Peng and H. C. Chang, Anal. Chem. **75**, 1805 (2003).
5. W. P. Peng, Y. Cai, Y. T. Lee and H. C. Chang, Int. J. Mass Spectrom. **229**, 67 (2003).
6. M. Grimm, B. Langer, S. Schlemmer, T. Lischke, W. Widdra, D. Gerlich, U. Becker and E. Ruehl, AIP Conf. Proc. **705**, 1062 (2004).
7. W.-P. Peng, Y.-C. Yang, M.-W. Kang, Y. T. Lee and H.-C. Chang, J. Am. Chem. Soc. **126**, 11766 (2004).
8. W. Ping-Peng, Y.-C. Yang, C.-W. Ling and H.-C. Chang, Analytical Chemistry **77**, 7084 (2005).
9. M. Grimm, B. Langer, S. Schlemmer, T. Lischke, U. Becker, W. Widdra, D. Gerlich, R. Flesch and E. Ruehl, Phys. Rev. Lett. **96**, 066801 (2006).
10. C. Graf, B. Langer, M. Grimm, R. Lewinski, M. Grom and E. Ruehl, J. Electron Spectrosc. Relat. Phenom. **166-167**, 74 (2008).

11. A. J. Trevitt, P. J. Wearne, E. J. Bieske and M. D. Schuder, Opt. Lett. **31**, 2211 (2006).

12. A. J. Trevitt, P. J. Wearne and E. J. Bieske, International Journal of Mass Spectrometry **262**, 241 (2007).

13. T. A. Smith, A. J. Trevitt, P. J. Wearne, E. J. Bieske, L. J. McKimmie and D. K. Bird, Springer Ser. Fluoresc. **4**, 415 (2008).

14. A. J. Trevitt, P. J. Wearne and E. J. Bieske, J. Aerosol Sci. **40**, 431 (2009).

15. M. Drewsen, I. Jensen, J. Lindballe, N. Nissen, R. Martinussen, A. Mortensen, P. Staanum and D. Voigt, Int. J. Mass Spectrom. **229**, 83 (2003).

16. B. Roth, P. Blythe and S. Schiller, Phys. Rev. A: At., Mol., Opt. Phys. **75**, 023402 (2007).

17. B. Szymanski, R. Dubessy, B. Dubost, S. Guibal, J. P. Likforman and L. Guidoni, Applied Physics Letters **100**, 171110 (2012).

18. M. A. van Eijkelenborg, M. E. M. Storkey, D. M. Segal and R. C. Thompson, Phys. Rev. Lett. **60**, 3903 (1999).

19. S. Willitsch, M. T. Bell, A. D. Gingell and T. P. Softley, Phys. Chem. Chem. Phys. **10**, 7200 (2008).

20. P. H. Dawson, *Quadrupole Mass Spectrometry*. (Elsevier Scientific Pub., Amsterdam, 1976).

21. G. Hars and Z. Tass, J. Appl. Phys. **77**, 4245 (1995).

22. S. Schlemmer, J. Illemann, S. Wellert and D. Gerlich, Journal of Applied Physics **90**, 5410 (2001).

23. C. F. Bohren and D. R. Huffman, *Absorption and Scattering of Light by Small Particles*. (Wiley-VCH, 1983).

24. N. C. Contino, E. E. Pierson, D. Z. Keifer and M. F. Jarrold, J. Am. Soc. Mass Spectrom. **24**, 101 (2013).

25. R. H. Perry, R. G. Cooks and R. J. Noll, Mass Spectrom. Rev. **27**, 661 (2008).

26. E. R. Badman, G. E. Patterson, J. M. Wells, R. E. Santini and R. G. Cooks, J. Mass Spectrom. **34**, 889 (1999).

27. M. A. Hines and P. Guyot-Sionnest, J. Phys. Chem. **100**, 468 (1996).

28. W. Xiong, D. D. Hickstein, K. J. Schnitzenbaumer, J. L. Ellis, B. B. Palm, K. E. Keister, C. Ding, L. Miaja-Avila, G. Dukovic, J. L. Jimenez, M. M. Murnane and H. C. Kapteyn, Nano Lett. **13**, 2924 (2013).

29. P. Guyot-Sionnest, Microchim Acta **160**, 309 (2008).

30. P. P. Jha and P. Guyot-Sionnest, J. Phys. Chem. C **114**, 21138 (2010).

31. W. Qin, R. A. Shah and P. Guyot-Sionnest, ACS Nano **6**, 912 (2012).

32. M. Shim, C. Wang and P. G. Sionnest, J. Phys. Chem. B **105**, 2369 (2001).

33. C. Wang, B. L. Wehrenberg, C. Y. Woo and P. Guyot-Sionnest, J. Phys. Chem. B **108**, 9027 (2004).

34. Z. Ding, B. M. Quinn, S. K. Haram, L. E. Pell, B. A. Korgel and A. J. Bard, Science **296**, 1293 (2002).

35. N. Myung, Z. Ding and A. J. Bard, Nano Letters **2** , 1315 (2002).

36. C. Galland, T. Ghosh, A. Steinbruck, M. Sykora, J. A. Hollingsworth, V. I. Klimov and H. Htoon, Nature **479**, 203 (2011).

CHAPTER 3

NONDESTRUCTIVE, HIGH PRECISION MASS DETERMINATION FOR SINGLE, TRAPPED, GIGADALTON NANOPARTICLES

Overview

Several methods for nondestructive mass measurements on single, trapped nanoparticles in the gigadalton (GDa) mass range are demonstrated, and the trade-offs between speed, precision, and ease of use are discussed. Charged nanoparticles are introduced into vacuum by electrospray ionization, and trapped in a quadrupole ion (Paul) trap, with detection by light scattering. The mass/charge ratio of the particle was then probed by one or more of four methods, all based on detecting the secular frequency for motion of the particle in the trap, working in either the time or frequency domains. Use of selective ejection from coulomb crystals to trap single particles, the effects of pressure on coulomb crystals and secular resonance width, and the spectrum of simultaneously trapped particles are also discussed. Precision approaching 1 ppm for mass-to-charge ratio determination is demonstrated.

Introduction

Nanoparticle mass spectrometery (NPMS) provides a tool for precise mass measurements on single objects such as nanoparticles[1-8] and whole cells,[9] which are difficult to study in conventional mass spectrometers. Three-dimensional quadrupole (Paul) traps have been used by several groups for nondestructive, high precision mass measurements on single nano- and micro-particles.[3, 8, 10-13] These methods utilize light scattering or laser-induced fluorescence (LIF) by the trapped particle, to detect the particle and monitor its motions. Because detection is nondestructive, particles can be probed for long time periods, enabling studies of surface chemistry,[2, 3] optical properties,[13-16] and charging under photon flux,[5, 7, 17] in conjunction with mass measurements.

The usual problem in mass spectrometry is to resolve closely spaced peaks in a spectrum of intensity as a function of mass/charge ratio (M/Q). Common, IUPAC-defined figures of merit are "resolving power" (ΔM) and "resolution" ($M/\Delta M$), where ΔM is essentially a measure of the peak width in the spectrum.[18] For single particle mass spectrometry, a typical spectrum has, at

most, a few well-separated peaks, thus the critical figure of merit is the uncertainty with which peak position can be determined. Peak width is still important because it affects this positional uncertainty. Another important factor is that the detection method used here is nondestructive, allowing repeated measurements of M/Q for a single particle. In the following, we use the term "precision" to mean the uncertainty in M/Q, divided by M/Q, (i.e., $\Delta(M/Q)/(M/Q)$ determined over multiple measurements. As defined, the precision is the reciprocal of the more typically quoted "resolution". We will mainly use the figure of "width" or full width at half maximum, which refers to a single measurement of a peak, and is identical to "resolving power". Plotting the peak position over multiple measurements is the ideal way to obtain high precision, as demonstrated by Gerlich and co-workers, but requires that the mass does not change slightly over time.

Particles (or ions) are confined in a Paul trap by a combination of DC (U_0) and AC potentials (V_0 at angular frequency Ω). Under appropriate conditions discussed below, the trajectories are well described as rapid driven oscillations at frequency Ω, superimposed on slow, "secular" motion. For an ideal Paul trap, the secular motion is harmonic and, as a result, has well-defined secular frequencies ω_r and ω_z, for radial and axial motion, respectively, which depend on the particle's mass-to-charge ratio, M/Q, as well as the trap dimensions and applied potentials.[1, 3] The goal is, therefore, to measure one or both of the secular frequencies of the trapped particle, thereby obtaining M/Q. M is determined by extracting Q, as discussed below.

Several approaches have been demonstrated for secular frequency measurement. The secular frequency can be tuned (e.g., by adjusting V_0), such that the frequency of the rapid driven motion (at Ω) is an integer multiple of the secular frequency. When this occurs, the particle's motion can become a Lissajous orbit, which can be imaged in scattered light or LIF, appearing as a multilobed standing wave, the structure of which reveals the ratio ω/Ω.[3, 8, 19, 20] The secular frequency (thus, M/Q) can be measured with precision of between 1000 ppm and 100 ppm by this method.[19] Another approach, demonstrated by Gerlich and co-workers, is to measure scattered

light intensity as a function of time, I(t), as the trapped particle oscillates relative to a low powered laser focused through the trap center. I(t) can then be Fourier transformed to obtain the secular frequency spectrum. Working with 500 nm SiO_2 particles, Gerlich and co-workers demonstrated precision of ~100 ppm for a single ten second I(t) measurement. By analyzing the spread in ω from many such I(t)/FT experiments over the course of an hour, they showed that M/Q could be determined with precision of ~10 ppm.[3] A weakness of this method is that as particle size decreases, higher signal levels are needed to give time resolution high enough to resolve the higher secular frequency, which scales like M^{-1}; however, light scattering signal is a strong function of particle diameter ($I \propto d^6$), making measurements on small particles difficult.

Here, we compare results of four different approaches to secular frequency measurement – two in the time domain, and two in the frequency domain. The different methods involve different compromises between measurement speed and precision, and therefore can be chosen for the problem at hand.

Experimental Setup

Instrumentation

The experimental setup is described in detail elsewhere.[12] The instrumentation comprises a small vacuum system with two differentially pumped chambers, sitting on a pneumatically isolated laser table, which is surrounded by a light-tight enclosure, which also attenuates acoustic noise reaching the instrument. The turbomolecular and mechanical pumps are isolated by bellows to minimize vibration. The instrument includes an electrospray source used to get nanoparticles into the gas phase, several ion guides used for differential pumping and mass pre-filtering, the quadrupole trap, and optics and detectors for monitoring trapped nanoparticles by light scattering.

The Particle Trap

The heart of the experiment is the 3-dimensional quadrupole ion (Paul) trap based on a design by Gerlich *et al.*[21] with $r_0 = 4.2$ mm and $z_0 = 2.97$ mm, as shown in Fig. 3.1. The central ring electrode is split to allow optical access to the trap volume, while still preserving cylindrical symmetry. The end cap electrodes are truncated cones, with holes allowing optical access or passage of nanoparticles along the axis. The field near the electrodes clearly deviates from the ideal hyperbolic geometry; therefore, one requirement for high precision mass determination is that particles must remain near the trap center during analysis.

The physics of ions in quadrupolar AC fields has been discussed in detail, and the approach to mass determination by nonimaging optical detection of a particle's motional frequencies has been discussed by Schlemmer, Gerlich, and co-workers.[3, 22] Stable trapping in the axial (z) direction is defined using the two parameters:

$$a_z = \frac{-8QU_0}{Mz_0^2\Omega^2} \qquad (3.1)$$

$$q_z = \frac{-4QV_0}{Mz_0^2\Omega^2} \qquad (3.2)$$

Analogous equations govern trapping in the radial direction. For an ideal Paul trap with hyperbolic electrodes, z_0 is the axial distance from the trap center to one of the end cap electrodes. For a trap like ours, z_0 must be obtained by calibration, but this is true for any real trap due to construction nonidealities. For the experiments described below, no DC offset voltage (U_0) was used, thus a_z is zero. If the parameter q_z is small enough (a limit of $q_z < 0.3$ has been suggested by Gerlich),[23] then the motion of the particle in the trap is, to a good approximation, described by a combination of slow secular motion, with superimposed micromotion at frequency Ω, driven by V_0.[24] The secular motion can be described by motion in the time-independent effective potential:

$$V_{eff}(z) = \frac{(Q \cdot V_0)^2}{M \cdot \Omega^2 \cdot z_0^2}\left(\frac{z}{z_0}\right)^2 \qquad (3.3)$$

where $V_{eff}(z)$ is the effective potential for motion in the axial direction, and the other parameters are defined above. The analogous expression for the effective potential governing radial motion is:

$$V_{eff}(r) = \frac{(Q \cdot V_0)^2}{M \cdot \Omega^2 \cdot r_0^2} \left(\frac{r}{r_0}\right)^2. \qquad (3.4)$$

For the ideal Paul trap geometry, $V_{eff}(r)$ grows more slowly with distance from the trap center than $V_{eff}(z)$, thus for a given amount of energy, the amplitude of motion in the radial direction is larger. The relationship between the secular frequency for axial motion (ω_z) and the mass-to-charge ratio (M/Q) is:

$$\frac{M}{Q} = \frac{\sqrt{2} \cdot V_0}{\omega_z \cdot \Omega \cdot z_0^2}. \qquad (3.5)$$

Because of the form of the radial and axial effective potentials, the axial and radial secular frequencies are simply related:

$$\omega_z = 2\omega_r. \qquad (3.6)$$

In reality, the cylindrical symmetry of the trap is broken by construction nonidealities, gravity (the trap axis is horizontal), and by the light pressure on the particle from the detection laser, which passes through the trap radially. As a result, ω_r is split into x and y components, $\omega_{r,x}$ and $\omega_{r,y}$. In the discussion below, we report frequencies in Hertz ($F = \Omega/2\pi$, $f_z = \omega_z/2\pi$, $f_r = \omega_r/2\pi$).

The trapping voltage, V_0, was generated by two different home-built sources. The first is similar to a radio-frequency source described elsewhere,[25] modified to allow operation at V_0 up to 1 kV, by replacing the tetrodes used in the original design, with a pair of high voltage triode tubes (811A). The RF frequency, F, can be varied over a wide range (100 kHz – 1 MHz), but for the measurements discussed below, it was fixed at F = 145 kHz. In this RF generator design, V_0 is controlled by the DC voltage applied to the anodes of tubes, supplied by an HP6448B power supply. This RF-source design becomes increasingly inefficient at lower frequencies, and to allow operation in the 5 kHz – 70 kHz range, we constructed an amplifier system that is driven by

the sine wave output of an Agilent 33220A function generator. For the present work, the frequency was fixed at 15 kHz.

To obtain accurate M/Q values, all parameters in Equation 3.5 must be known accurately. Frequencies are easily measured to better than ppm accuracy, thus the limiting factors are the geometrical parameter z_0, and measurement of the trapping amplitude, V_0. We have implemented a design by Peng *et al.* for a ppm-accuracy AC voltmeter designed to measure V_0[26]; however, V_0 will ultimately need to be determined by mass-based calibration. Calibration is also clearly required to obtain the z_0 parameter, which depends on the construction accuracy of the trap, estimated to be ~10 μm, corresponding to uncertainty in z_0 of 0.3 %. A proposed approach for high accuracy mass calibration is discussed below. The focus of this report, however, is on comparing methods for high precision (as opposed to absolute) M/Q measurements, and for this purpose, it suffices that the trapping parameters be stable to ppm levels over several hours.

Ion Formation and Trapping

Charged nanoparticles were generated by electrospraying Nile red-doped polystyrene particles (Invitrogen) using a capillary voltage of 3.5kV and a cone voltage of 210V, spraying a solution obtained by diluting the 2 wt% stock solution 1:20 in methanol. The particles are non-toxic, but it is recommended to wear gloves when handling the solution. Dynamic light scattering indicated that the average particle size in solution is 24 nm, but the solution also contained a small fraction of aggregates in the 200nm – 400nm size range. Positively charged nanoparticles were formed by electrospray, presumably due to excess Na^+ originating from NaN_3 present in the stock solution. Particles were collected by a hexapole ion guide, operating at 24mTorr background pressure to collisionally focus the particle beam, as demonstrated for whole virus particles.[27] The particles then passed through a linear radio-frequency quadrupole guide operated with the same V_0 and Ω as the trap, thereby selectively transmitting only particles in the M/Q range of interest for trapping. To aid trapping, 20 – 30 mTorr of argon was leaked into the

chamber containing the trap. Under these conditions, the trap is filled with a small swarm of nanoparticles in ~3 seconds. After filling, an isolation valve built into an ion lens that separates the hexapole and linear quadrupole is closed, allowing the pressure in the trapping section of the instrument to reach 10^{-8} Torr. Alternatively, single particles can be gated into the trap using either the isolation valve or one of the "Lens" electrodes (Figure 3.1).

Optical Detection

In the experiments described here, the nanoparticle ion beam was injected along the axis of the trap, leaving the azimuthal gap in the split ring electrode available for laser passage and light collection. The light scattering laser was a cw diode-pumped solid state laser operating at 532 nm (UltraLasers), loosely focused through the trap center along what is denoted the x-axis in Figure 3.1. The intensity was adjusted to ~500 W/cm^2 at the focus. The beam waist diameter was measured by observing light scattering from a single particle in the trap, as the laser focal spot was translated along the y axis. The effective "size" of the particle for this measurement is determined by the time-averaged thermal motion of the particle in the trap, because secular motion is much faster than the measurement time. Decker *et al.*[28] have shown that the mean square thermal motion amplitudes are:

$$r_m^2 = 8k_BT\frac{Mz_0^4\Omega^2}{Q^2V_{RF}^2}\ , \text{ and } \quad z_m^2 = 2k_BT\frac{Mz_0^4\Omega^2}{Q^2V_{RF}^2}, \qquad (7)$$

For particles in the M and Q range examined here and for V_0 = 500 V and F = 145 kHz, the full widths of the radial and axial distributions ($2\cdot r_m$ and $2\cdot z_m$) are ~7.2 μm and ~3.6μm, respectively. After correcting for the thermal motion, the laser beam waist is estimated to be ~260 μm. The loose focus allows experiments combining imaging and frequency detection.

Light scattered by trapped particles was collected and collimated by an aspheric lens located along the y-axis, 25 mm from the trap center, passed through a beam expander, and then either imaged onto the focal plane of a CCD camera, or focused onto the 100 μm x 100 μm active

area of an avalanche photodiode (APD) with a magnification of ~2 (i.e, the APD detected light from a 50 μm x 50 μm area in the horizontal plane of the trap). The TTL pulses from the APD were counted by a ComTec multichannel scalar with up to 2^{19} bins, the width of which could be varied down to 200ns.

Single dye-doped nanospheres (24 nm) can easily be detected by LIF; however, our CCD camera is not sensitive enough to image a single nanosphere by LIF. For the purposes of demonstrating the various M/Q measurement modes, we, therefore, used particles which were aggregates of the nanospheres, large enough to be detected and photographed by light scattering. For particles smaller than the 532 nm detection wavelength, the scattered light intensity (I) can be described by Rayleigh scattering,[29] in terms of the intensity of the laser, I_0:

$$I = I_0 \frac{1+\cos^2\theta}{2R^2}\left(\frac{2\pi}{\lambda}\right)^4\left(\frac{n^2-1}{n^2+2}\right)^2\left(\frac{d}{2}\right)^6 \qquad (8)$$

where θ is the scattering angle (±11° by ± 27° collection angle range centered around 90°), R is the distance from the particle to the collimating lens (25 mm), n is the refractive index of the particle (1.55 for polystyrene), λ is the wavelength of the light source (532 nm), and d is the particle diameter. Note that intensity varies like d^6, making LIF the preferred detection method for particles smaller than ~50 nm.[30]

Exciting Motion of Trapped Particles

It is necessary to drive motion of trapped particles, both to measure secular frequencies, and to selectively eject particles from the initially trapped swarm. Four methods were used here. In the first, the motion is driven by random mechanical vibration of the trap, from sources such as pumps or acoustic coupling to the vacuum system. In this case, the secular frequency is determined by Fourier transforming a record of light scattering intensity vs. time, as demonstrated by Schlemmer *et al.*[3]

For most measurements, however, we applied a time-varying driving force to excite

secular motion. In most experiments, the driving force comes from a weak sinusoidal electrical potential, and for this purpose, an AC signal was generated by an Agilent 33220A function generator, applied either to one of the trap end cap electrodes (for particle ejection) or to one of the "lens" electrodes just outside the trap, relying on field penetration to provide a weak driving force for precision measurements. Another approach was to use modulated light pressure from the light scattering laser to drive the particle motion. Analogous approaches have been applied to the study of trapped laser-cooled atomic ions, (e.g. Be^+, Ca^+, Ba^+ …) which condense into a lattice structure (coulomb crystal), in either a Paul trap or a linear ion trap, where they are detected by LIF.[31-33]

The different methods are useful in different contexts. For example, in the highest precision method, it is only practical to probe a narrow range of secular frequency, thus it is essential to first determine a rough (100 ppm) value of the secular frequency using some fast method. Fast methods are also critical in experiments where either the particle or charge change on a fast timescale, as in particle surface chemistry or collision experiments.

Results and Discussion

Preparing a Single Trapped Particle from a Trapped Ensemble

Figure 3.2(a) shows an image of scattered light from an ensemble of trapped particles immediately after filling. The scattered light forms an image with its long axis (~1 mm) along the laser propagation direction, and short axis (~0.3 mm) collinear with the trap axis, perpendicular to the laser direction. The visible image is determined by overlap of the focused laser beam (beam waist diameter ~260 μm) and the ion cloud, which is cylindrically symmetric about the trap axis, i.e., the short axis of the image. The ~0.3 mm extent along the short axis is, therefore, consistent with the estimated laser beam waist. The fact that the image tapers near the long ends reflects the lenticular shape of the ion cloud.

The trapped ions have obviously condensed into a lattice structure, with each particle in a well-defined spatial position, i.e., a coulomb crystal. Coulomb crystals of trapped particles were first observed in 1959 by Wuerker *et al.* for trapped aluminum dust,[20] and the phenomenon has been discussed in depth by others.[34, 35] In essence, confined, charged particles crystalize into a lattice when the coulomb repulsion between the particles is much greater than the thermal kinetic energy. Each point represents the region an individual charged particle explores due to thermal motion, and in these pictures, each point is ~10 - 30 μm. One interesting point is that in order to see discrete lattice spots, the ion cloud must be stationary, even though the cylindrical symmetry of the trap might be expected to result in free rotation of the ion cloud. In this case, asymmetry resulting from construction nonidealities, gravity, and light pressure from the laser was evidently large enough to prevent rotation of the crystal.

Panels (b) - (d) show changes in the image as particles of lower M/Q are resonantly ejected from the trap in successive steps to prepare the trap with only a single particle. The argon pressure during particle ejection was increased to 10^{-3} Torr to broaden the frequency response so that fast, high amplitude frequency sweeps could be used. To reduce the cloud to the size shown in panel (b), a 2 V sine wave was applied (in addition to the 145 kHz trapping voltage) to one of the end cap electrodes of the trap, and swept in 15 seconds from 30kHz to 3kHz, thereby resonantly ejecting particles with secular frequencies in that range. As the AC frequency approaches resonance with the lower M/Q particles in the cloud, the excitation leads to "melting" of the lattice and ejection of the low M/Q particles. As soon as the excitation stops, the remaining cloud immediately crystallizes again, as collisions with Ar damp the kinetic energy. To obtain the image in panel (c), the sweep was continued to 2.5 kHz, ejecting most of the remaining particles. Finally, after a sweep to 2.35 kHz, only a single particle, corresponding to the one with the highest M/Q ratio, remains. By varying the range of a frequency sweep, it is possible to pick a single particle out of any part of the initial M/Q distribution.

I(t)/FT Method

If the signal levels are high enough, it is possible to observe the secular frequency directly in the time domain, as fluctuations in light scattering signal due to motion of the particle relative to the detection volume defined by the overlap of the light scattering laser focus and the APD imaging system. The record of intensity vs. time (I(t)) can then be Fourier transformed to give the frequency spectrum, as demonstrated by Gerlich and co-workers,[3] and illustrated in Figure 3.3. Both here and in the original experiments by Gerlich and co-workers,[3] the secular motion was driven by instrument vibration; however, we have tried to minimize the vibration in order to minimize precision degradation from large amplitude motion. Nonetheless, there is still enough instrument vibration to drive secular oscillation leading to scattered light modulation of 10 - 20% as the particle moves relative to the detection volume. The top frame of Figure 3.3 shows a typical FT spectrum of an I(t) record with 524,288 bins and a bin size of 300 μsec, for trapping conditions of V_0 = 78 V and F = 15 kHz. The two main frequency components over this range are f_r and f_z (at 2 f_r) and the insets show these peaks in detail. The frequencies are f_r = 629.276 Hz and f_z = 1258.56 Hz, and correspond to M/Q = 1.59805 MDa (uncalibrated). The precision of these measurements is ~10 ppm, which is a roughly 5-fold improvement over the best previous measurements by this method. In addition to the two main peaks, there is additional weak structure. The f_r and f_z peaks show roughly symmetric side-bands at f_r (or f_z) ± 13.6 Hz, and the 13.6 Hz frequency is also seen in the FT spectrum. There presumably is a mechanical resonance of the instrument at this frequency leading to coupling to the particle motion.

If the bin size of the I(t) measurement is decreased to 20 μsec to allow higher frequencies to been seen in the FT, then the influence of the AC trapping potential (V_0) can be observed. The bottom frame of Figure 3.3 shows the frequency range from 13kHz to 17 kHz, centered about the frequency of the trapping potential (F = 15 kHz). As shown, in addition to the peak from the trapping potential, there are symmetric side bands corresponding to F ± f_r and F ± (f_r + f_z). A small peak was also observed for F – f_z (~13,751 Hz), but the corresponding F + f_z peak does not

rise above baseline. As discussed above, the motion of particles can be described as slow motion at f_z and f_r, with small amplitude motion at F superimposed, and the peaks observed in this frequency range are the result of modulation of the light scattering signal by the coupled motion at F, f_z, and f_r. Modulation occurs only if the particle motion carries it out of the ~50 μm x 50 μm viewing area of the APD detector, and the weakness of the $F \pm f_z$ side bands (and the f_z peak in the top frame of Figure 3.3) is attributable to the fact that $V_{eff}(z) > V_{eff}(r)$. As a result, the motion has smaller amplitude in the axial direction, and therefore, there is less signal modulation associated with f_z.

The insets show the peak shapes for the both the central peak and one of the side bands. From the side band positions, f_r and f_z can be determined. For example, from the radial side bands at 14369.51 Hz and 15628.07 Hz and the value of F (14998.79 Hz), f_r is found to be 629.28 Hz – nearly identical to the 629.276 value obtained from the direct measurement in the top frame of Figure 3.3. Similarly, from the $F \pm (f_r + f_z)$ side bands at 16886.63 Hz and 13110.95 Hz, the value of f_z = 1258.56 Hz, again identical to directly measured value. The disadvantage to extracting the secular frequencies from F ± f sidebands is that the frequencies that must be measured are high, requiring short time bins for the I(t) measurement, increasing the effects of noise. In this example, the secular frequency precision obtained from the side bands was ~60 ppm – ten times worse than from the direct measurement.

Beat Frequency Measurements

Ultimately, the limiting factor of the I(t)/FT method is that the signal levels need to be high enough to give good statistics in the time bins of the I(t) record. This is not a problem for the large particles used here for demonstration purposes, where the light scattering signal is ~10^6 counts/second. As particle diameter (d) decreases, however, two factors rapidly degrade the I(t) statistics. Light scattering intensity ($I \propto d^6$) drops rapidly, and at the same time, shorter time bins must be used to record the I(t) record because less massive particles ($M \propto d^3$) tend to have

higher secular frequencies. We have used LIF to detect small particles, such as quantum dots[13]; however, for laser intensities low enough to avoid excessive particle heating, the signal levels are far too low for I(t)/FT measurements. It is possible, however, to extend the usability range of the I(t)/FT approach by measuring the beat frequency between the particle secular motion, and a fixed frequency drive signal. Because the beat frequency is much lower than the secular frequency, longer time bins can be used, with concomitant increase in I(t) statistics.

Figure 3.4 shows an example of raw I(t) signals, for the same particle that was probed in Figure 3.3. A 400 mV sine wave was applied to one of the "Lens" electrodes outside the trap, creating a weak drive signal at f_{Drive} = 1258.46 Hz. The I(t) record for the particle excited only by random mechanical vibration is shown in the top trace, while the bottom trace shows the signal for the particle driven at $f_{Drive.}$ The signal from this large particle was adequate to allow the I(t) records to be recorded with short enough bin sizes (300 μsec) for direct secular frequency measurement, but in the figure, the I(t) data are rebinned with 50 msec bins to allow the low frequency components of interest to be seen clearly. In the top trace, the fastest oscillations in this frequency range correspond to the aforementioned 13.6 Hz mechanical resonance. When f_{Drive} is present (lower trace), the average signal decreases because the driven particle spends less time in the detection volume, and strong oscillations are observed at the ~2 Hz beat frequency between f_{Drive} and f_z. Figure 3.5 shows FTs of the two I(t) time traces. The main frame of the figure shows the FT (of the raw signal with 300 μsec bins) in the range near f_{Drive} and f_z (1256.53 Hz). The inset shows the frequency range centered on the beat frequency, $f_{Drive} - f_z$, showing a prominent peak at 1.931 Hz. As expected, the value of f_z given by $f_{Drive} - f_{Beat}$ is in excellent agreement with the value measured directly.

There are two issues that affect the beat frequency measurement. It is possible that there may be instrument mechanical resonances that interfere with measurement of beat frequency, which tends to be in the same low frequency range. Indeed, it can be seen that a weak resonance at ~2 Hz is present in the FT even when the drive signal is not present. The beat frequency signal

when the drive is present is much stronger; nonetheless, coupling to the mechanical resonance may be responsible for broadening the beat frequency peak, resulting in precision of only ~35 ppm for f_z extracted by this method. By making measurements with at several different drive frequencies, it should be possible to shift f_{Beat} into "quiet" ranges of the vibrational spectrum. The beat frequency method, therefore, appears promising as a relatively fast method that can be applied to smaller particles than direct secular frequency measurement.

Particle Oscillation Driven by Laser Modulation

The time-domain/FT approach to frequency determination is fast, but it has several drawbacks. If mechanical vibration or some other broad-band stimulus (e.g., a voltage pulse) is used to drive secular motion, it needs to be strong enough to stimulate motion over a wide range of secular frequencies. Such excitations tend to result in large amplitude motions, exploring regions where the trap potential has significant nonidealities, and causing broadening of the FT frequency spectrum. The other issue, discussed above, is that signal levels for small particles may be too small to allow time domain measurements. The alternative is to use frequency-domain approaches, where a narrow-band excitation source is scanned, looking for signal changes when the excitation is in resonance with the secular frequency.

One approach is to take advantage of the force exerted on the particle by the light scattering laser, by modulating the laser power to provide a weak, variable frequency excitation source. An example of this approach is shown in Figure 3.6, again probing the same particle that was examined in Figures 3.3 – 3.5. This spectrum was taken by square-wave modulating the 532 nm light scattering laser by ~70%, and sweeping the modulation frequency (f_{Drive}) over the secular frequency of the particle, at a rate of 1.5 Hz/minute. A 10^{-8} Torr background pressure of Ar was used to provide a moderate level of motional damping. For a particle in this size range, the damping time constant is on the order of hundreds seconds. Before the scan, the light scattering signal was optimized, i.e., the laser focus and light detection volume were overlapped

with the equilibrium particle position. Therefore, when the modulation frequency was resonant with the secular frequency (f_r for this excitation geometry), the motion of the particle caused a drop in light scattering signal. Because the driven motion is along the axis of the laser beam, the main loss of signal results from the particle moving out of the volume visible to the APD detector (> ±25 μm motion). The oscillations observed as f_{Drive} is scanned through the secular frequency resonance are the result of beating of the secular motion with f_{Drive}.

To extract the secular frequency from the signal, we fit the spectrum with a Gaussian-convoluted step function, obtaining a convoluted with a step function. The transition frequency (i.e., f_r) obtained from the sweep was 626.733 Hz with a fwhm of 0.04 Hz, corresponding to width of 60 ppm. The M/Q value extracted from f_r is 1.604 MDa/e, given the operating parameters if F = 15 kHz and V_0 = 77 V.

Note that f_r measured by this method is ~0.4% lower than that measured by the I(t)/FT method, continuing the small decrease (~0.15 % f_z) observed between the I(t)/FT and beat frequency measurements. The I(t)/FT, beat frequency, and laser modulation experiments were made on the same particle, but over a ~ 24 hour period. While we cannot exclude some drift in the trapping potential (V_0), such changes are not unexpected because trapped particles undergo collisions with both charged and neutral species in the chamber background, which can change both M and Q (see below).

AC Voltage Sweeps

For our configuration, the highest precision measurements are obtained by measuring f_z using a weak AC potential to drive axial oscillation of the particle. As noted above, this small voltage is applied to the second electrode ("Lens", Figure 3.1) outside the trap, because the minimum AC amplitude (10 mV) from our function generator is too large for optimal precision if applied directly to a trap electrode. When the AC potential is resonant with the secular frequency (f_z for axisymmetric excitation) the particle oscillation amplitude increases, so that it spends less

time in detection volume, resulting in a decrease in the scattered light signal similar to that for the laser frequency sweep. At high pressures of Argon (10^{-3} Torr), scans over the secular frequency cause excitation that is quickly damped by collisions after the resonance is passed. For a single particle, the result is a dip in light scattering intensity on resonance, with width that depends on both pressure and AC drive amplitude. Such conditions are useful in experiments (e.g., monitoring particle M/Q changes at high temperatures)[13] where repeated fast M/Q determinations are required.

For low pressures (10^{-8} Torr), the f_z resonance is sharp but the signal takes hundreds of seconds to be restored by collisions with background gas. As a result, the "spectrum" takes the appearance of a step function, as shown in Figure 3.7. Note that this and other measurements discussed below were done on a different particle than that probed in Figures 3.3 – 3.6. The particle was trapped using F = 145 kHz and V_0 = 500 V. A signal of 125 mV amplitude was swept from 2336.5 to 2337 Hz over 90 seconds (~5.5 mHz/second), while the scattered light signal was collected in 250 millisecond wide bins (~0.1mHz/bin). Between 2336.5 – 2336.6 Hz signal oscillations were observed (similar to Figure 3.6) due to beating of the drive and secular frequencies. The large drop in intensity when the frequency was scanned through f_z was fit to a Gaussian-convoluted step function, giving a center frequency of 2336.8342 Hz, and a full-width at half max of 0.0343 Hz, corresponding to 14.7 ppm. Taking the trapping parameters into account, the corresponding M/Q is 582062.44 ± 8.7 Da/e. Note: operation at higher F tends to result in trapping of particles with lower M/Q – here about three times lower than the particle probed in Figures 3.3 – 3.6. If we assume that the center frequency can be determined to ~10% of the width, the "single measurement precision" would correspond to ~1.5 ppm. The entire procedure consistent of trapping a swarm of particles, selectively ejecting all but one, using a fast AC sweep at high pressure determine f_z approximately, and finally measuring f_z in with high precision, took about 10 minutes.

Figure 3.8 compares the effects of sweeping the AC voltage toward lower frequency and toward higher frequency, for the same particle. Both sweeps were carried out at the same rate (1Hz/180sec), but with somewhat different AC driving amplitudes. The fits are quite similar, indicating the direction of the sweep is not important. The center frequency of the two fits agrees within ±0.002 Hz, corresponding to agreement within about ~1 ppm. Comparison of the two sweeps clearly shows the effects of the AC driving amplitude: the low-to-high frequency sweep (blue) was done with AC amplitude of 72.5 mV, while the high-to-low (red) sweep used 87.5 mV amplitude. As expected, the larger AC amplitude leads to a larger decrease in signal at resonance, but also clearly broadens the transition (red, fwhm = 0.081Hz) compared to the lower voltage sweep (blue, fwhm = 0.032Hz). This difference suggests that driving smaller amplitude motion should lead to further increase in measurement precision; however, significant improvement will probably also require further reduction in instrument vibration, cooling of the trap to reduce the thermal motion amplitude, and shrinking the detection spatial resolution by improvements to both the laser mode quality and light collection optics.

Charge and Mass Determination

The final step in the mass measurement process is to determine the absolute charge, and therefore the absolute mass. The approach is to make repeated measurements of the secular frequency, and therefore M/Q, as the particle gains and loses charges, looking for the step size associated with a single elementary unit of charge. Various approaches to changing the charge state have been used,[3, 5, 6, 8] but for our purposes, it suffices to turn on a cold-cathode ionization gauge located on a side port of the trap vacuum chamber, resulting in occasional collisions of the particle with electrons, ions, and/or metastables (e.g., Ar^*) that penetrate into the trap.

Figure 3.9 shows the secular frequencies (left-hand scale) measured periodically over the course of 2 hours, using AC sweeps like those in Figure 3.7 to measure the center frequency of the resonance. Obtaining such a data series is complicated by the fact that when a charge step

occurs, the secular frequency can move outside the narrow sweep range used in the high precision measurements. When this occurred, a fast, low-precision sweep was used (~0.3 Hz/sec with 200 mV AC amplitude) to determine the approximate new secular frequency, and then slow, low amplitude sweeps were used to obtain the new frequency with precision of at least 10 ppm. The charge of the particle can be obtained from the relation: $Q = f_z \cdot \Delta Q / \Delta f_z$, where Δf_z is the observed step size and ΔQ is the change in charge associated with each frequency step. Both single and multiple quantum charge changes were observed, probably because the period between measurements was long enough to allow multiple collisions. The frequency step associated with $\Delta Q = \pm e$ is 0.380 ± 0.005 Hz/e, determined by fitting the entire series of charge steps.

In this case, because the individual frequency measurements were only done with ~10 ppm precision, the uncertainty in the charge step magnitude corresponds to ±1.3 % uncertainty in the absolute charge. For the large particle probed in Figures 3.7 – 3.9, $Q = 6146 \pm 80$ charges, leading to $M = 5.94 \pm 0.08$ fg or 3.58 ± 0.05 GDa using Eq. 3.5. The absolute mass and charge was obtained by a similar algorithm that was developed by Peng *et al.* and used by others for absolute charge determination.[8, 36] If the particle were a sphere with the density of bulk polystyrene (1.06 g/cm^3), the diameter would be ~220 nm; however, the structure of such an aggregate of 24 nm nanospheres (each with a mass ~4.62 MDa) is most probably less compact, and therefore larger. The stability parameter (q_z) for such a particle under the trapping conditions used ($V_0 = 500$V, F = 145 kHz, $z_0 = 2.96$ mm) is $q_z = 0.045$, i.e., well within the validity range of the effective potential approximation. As indicated, absolute charge determination is nontrivial for such highly charged nanoparticles, and Peng *et al.* developed an algorithm to determine the charge accurately without manual assignment of charge state.[36] For particles with only a few tens or hundreds of charges, the exact charge is easily determined even with modest M/Q precision.[1, 3, 8, 10, 12, 13, 36]

Approaches for Absolute Mass Calibration

These experiments have focused on demonstrating optical techniques for particle detection and high precision mass-to-charge determination. We have, therefore, not attempted to calibrate the *absolute* M/Q scale, which could be in error by up to 0.5%, due to systematic uncertainties in the z_0 geometric parameter and V_0 trapping amplitude. For many applications, it will be important to determine the absolute mass, thus it is useful to discuss possible calibration schemes and their limitations.

The V_0 and z_0 parameters could, in principle, be measured by using mass-selective ejection to record spectra for some molecular ion; however, such ions, in the process of being ejected, make much larger radial and axial excursions, and therefore respond very differently to nonidealities in the trap construction, compared to particles detected on the basis of small amplitude oscillations.

A more promising approach to absolute mass calibration is suggested by analogy to the method used for charge determination. There, Q is changed by known amounts (i.e., $\pm n \cdot e$) resulting in quantized steps in the secular frequency, Δf, which can be analyzed to determine Q. By analogy, the absolute mass can be determined by observing steps in f when the particle mass is changed by a known amount. The particle might be exposed to a beam of neutral molecules, such as C_{60}, measuring Δf associated with adsorption on the particle. Alternatively, an ion source could be used to inject ions with known M/Q and polarity opposite to that of the particle. Because the particle would serve as a heat sink with many degrees of freedom, intact adsorption would be expected in either case, leading to a calibrated change in M/Q. An example that appears particularly attractive would be to use electrospray of dilute H_3PO_4 to generate sparse spectra of cluster ions with $(H_3PO_4)_n+H^+$ or $(H_3PO_4)_n-H^+$ stoichiometries, in positive or negative ion modes, respectively. In our instrument, the linear quadrupole would then be used as a medium resolution mass filter to select a particular cluster size, for injection into the trap. Unlike

carbon-containing calibrant species, M/Q would be well defined because a single natural isotope dominates for H, P, and O.

Conclusion

We have compared several different time and frequency domain approaches to determining M/Q for single trapped nanoparticles. Precision approaching 10 ppm in single measurements is enabled by vibrationally isolating the trap from its surroundings. Using frequency sweep methods, transitions as narrow as ~15 ppm are obtained, with center frequency repeatability approaching 1 ppm. The precision and speed of the methods described here should enable measurements, for example, of surface adsorption/desorption/reaction kinetics with sensitivity well below one monolayer.

Acknowledgements

We would like to thank Stephan Schlemmer for helpful discussions. The work was supported by the Chemistry Division of the U.S. National Science Foundation, under grant CHE-1111935.

References

1. S. Schlemmer, J. Illemann, S. Wellert and D. Gerlich, AIP Conf. Proc. **457**, 80 (1999).

2. S. Schlemmer, J. Illemann, S. Wellert and D. Gerlich, in *The Physics and Chemistry of the Interstellar Medium, Proceedings of the 3rd Cologne-Zermatt Symposium*, edited by V. Ossenkopf, J. Stutzki and G. Winnewisser (GCA-Verlag Herdecke, Aachen, 1999), pp. 391-394.

3. S. Schlemmer, J. Illemann, S. Wellert and D. Gerlich, Journal of Applied Physics **90**, 5410 (2001).

4. T. Henning, H. Mutschke, S. Schlemmer and D. Gerlich, NASA Conf. Publ. **2002-211863**, 175 (2002).

5. M. Grimm, B. Langer, S. Schlemmer, T. Lischke, W. Widdra, D. Gerlich, U. Becker and E. Ruehl, AIP Conf. Proc. **705**, 1062 (2004).

6. S. Schlemmer, S. Wellert, F. Windisch, M. Grimm, S. Barth and D. Gerlich, Appl. Phys. A: Mater. Sci. Process. **78**, 629 (2004).

7. M. Grimm, B. Langer, S. Schlemmer, T. Lischke, U. Becker, W. Widdra, D. Gerlich, R. Flesch and E. Ruehl, Phys. Rev. Lett. **96**, 066801 (2006).

8. A. J. Trevitt, P. J. Wearne and E. J. Bieske, International Journal of Mass Spectrometry **262**, 241 (2007).

9. W.-P. Peng, Y.-C. Yang, M.-W. Kang, Y. T. Lee and H.-C. Chang, J. Am. Chem. Soc. **126**, 11766 (2004).

10. Y. Cai, W. P. Peng, S. J. Kuo, Y. T. Lee and H. C. Chang, Anal. Chem. **74**, 232 (2002).

11. Y. Cai, W. P. Peng, S. J. Kuo, S. Sabu, C. C. Han and H. C. Chang, Anal. Chem. **74**, 4434 (2002).

12. C. R. Howder, D. M. Bell and S. L. Anderson, Rev. Sci. Instrum. **85**, 014104 (2014).

13. D. M. Bell, C. R. Howder, R. C. Johnson and S. L. Anderson, ACS Nano *in press* (2014).

14. A. J. Trevitt, P. J. Wearne, E. J. Bieske and M. D. Schuder, Opt. Lett. **31**, 2211 (2006).

15. T. A. Smith, A. J. Trevitt, P. J. Wearne, E. J. Bieske, L. J. McKimmie and D. K. Bird, Springer Ser. Fluoresc. **4**, 415 (2008).

16. A. J. Trevitt, P. J. Wearne and E. J. Bieske, J. Aerosol Sci. **40**, 431 (2009).

17. C. Graf, B. Langer, M. Grimm, R. Lewinski, M. Grom and E. Ruehl, J. Electron Spectrosc. Relat. Phenom. **166-167**, 74 (2008).

18. *IUPAC. Compendium of Chemical Terminology, 2nd ed. (the "Gold Book"), compiled by A. D. McNaught and A. Wilkinson*, 2nd ed. (Blackwell Scientific Publications, Oxford, 1997).

19. G. Hars and Z. Tass, J. Appl. Phys. **77**, 4245 (1995).

20. R. F. Wuerker, H. H. Shelton and R. V. Langmuir, Journal of Applied Physics **30**, 342 (1959).

21. D. Gerlich and S. Decker, Applied Physics B: Lasers and Optics **114**, 257 (2014).

22. D. Gerlich, Hyperfine Interact. **146/147**, 293 (2003).

23. D. Gerlich, in *Advances in Chemical Physics: State-Selected and State-To-State Ion-Molecule Reaction Dynamics, Part 1*, edited by C. Y. Ng and M. Baer (J. Wiley & Sons, 1992), Vol. 82, pp. 1-176.

24. L. D. Landau and E. M. Lifshitz, *Mechanics*. (Pergamon Pr., Oxford, 1960).

25. R. M. Jones and S. L. Anderson, Review of Scientific Instruments **71**, 4335 (2000).

26. W.-P. Peng, Y. T. Lee, J. W. Ting and H.-C. Chang, Rev. Sci. Instrum. **76**, 023108 (2005).

27. G. K. Shoemaker, E. van Duijn, S. E. Crawford, C. Uetrecht, M. Baclayon, W. H. Roos, G. J. L. Wuite, M. K. Estes, B. V. V. Prasad and A. J. R. Heck, Molecular and Cellular Proteomics **9**, 1742 (2010).

28. S. Decker, TU Chemnitz, 2009.

29. C. F. Bohren and D. R. Huffman, *Absorption and Scattering of Light by Small Particles*. (Wiley, New York, 1983).

30. W. P. Peng, Y. Cai, Y. T. Lee and H. C. Chang, Int. J. Mass Spectrom. **229**, 67 (2003).

31. B. Szymanski, R. Dubessy, B. Dubost, S. Guibal, J. P. Likforman and L. Guidoni, Applied Physics Letters **100**, 171110 (2012).

32. M. Drewsen, I. Jensen, J. Lindballe, N. Nissen, R. Martinussen, A. Mortensen, P. Staanum and D. Voigt, Int. J. Mass Spectrom. **229**, 83 (2003).

33. M. Drewsen, A. Mortensen, R. Martinussen, P. Staanum and S. J. L., Physical Review Letters **93**, 243201 (2004).

34. S. Ichimaru, Review of Modern Physics **54**, 1017 (1982).

35. J. H. Chu and L. I., Physical Review Letters **72**, 4009 (1994).

36. W. P. Peng, Y. C. Yang, C. W. Lin and H. C. Chang, Anal Chem. **77**, 7084 (2005).

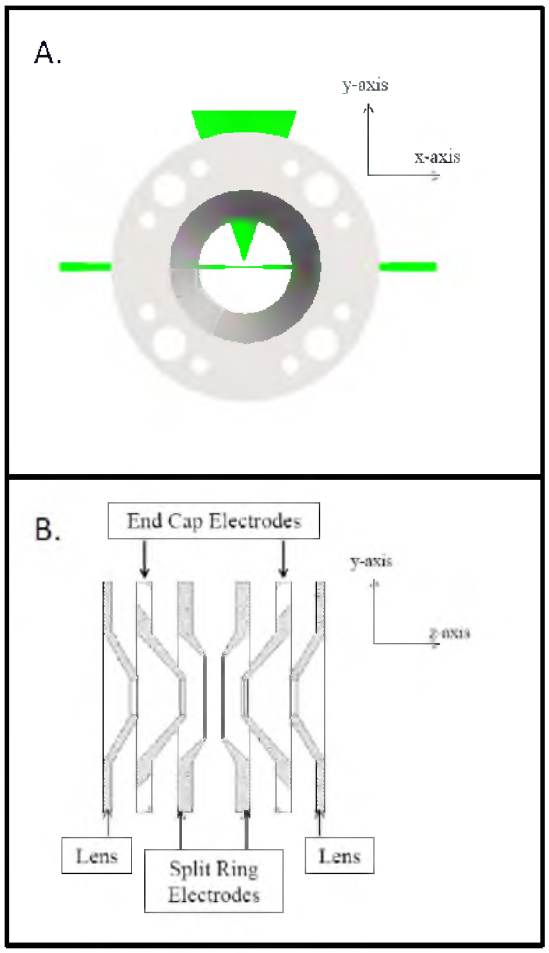

Figure 3.1: A general schmatic of the ion trap used. (A) End view of the trap looking down the z-axis, showing the axes for the laser (x) and light collection (y). (B) Cross-sectional view of the trap along the x-axis.

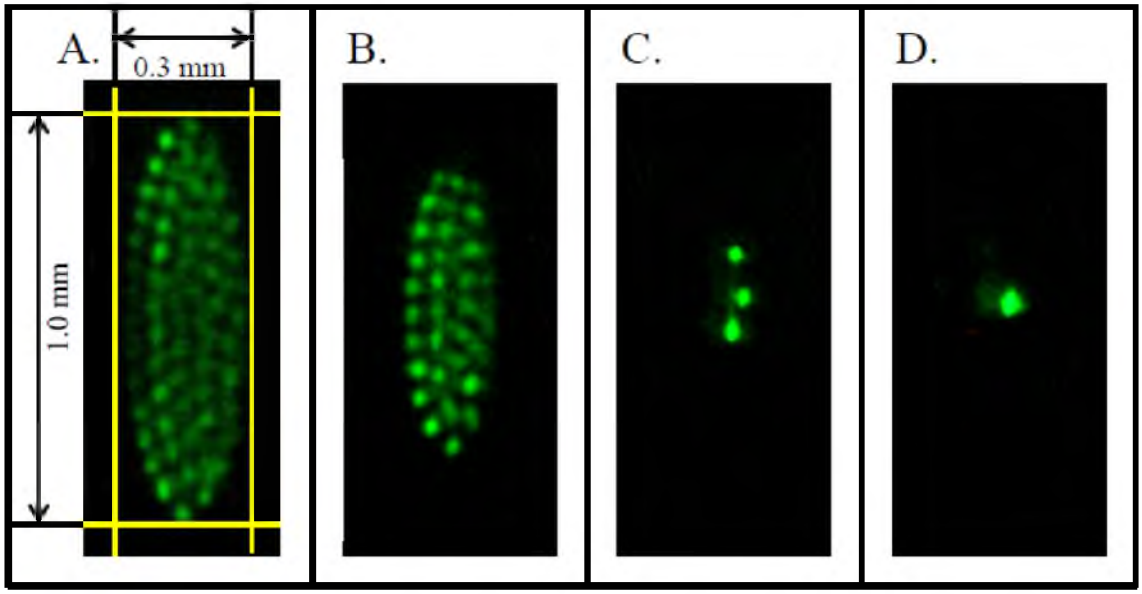

Figure 3.2: Images of charged nanoparticles in our ion trap. (a) An image of the trap when filled. (b) The contents of the trap after some ions have been swept out of the trap by an AC frequency sweep from 30 kHz – 3 kHz. (c) The contents of the trap after a sweep of 30 kHz – 2.5 kHz, leaving 3 particles in the trap. (d) The contents of the trap after a sweep of 30 kHz – 2.35 kHz, leaving a single particle in the trap.

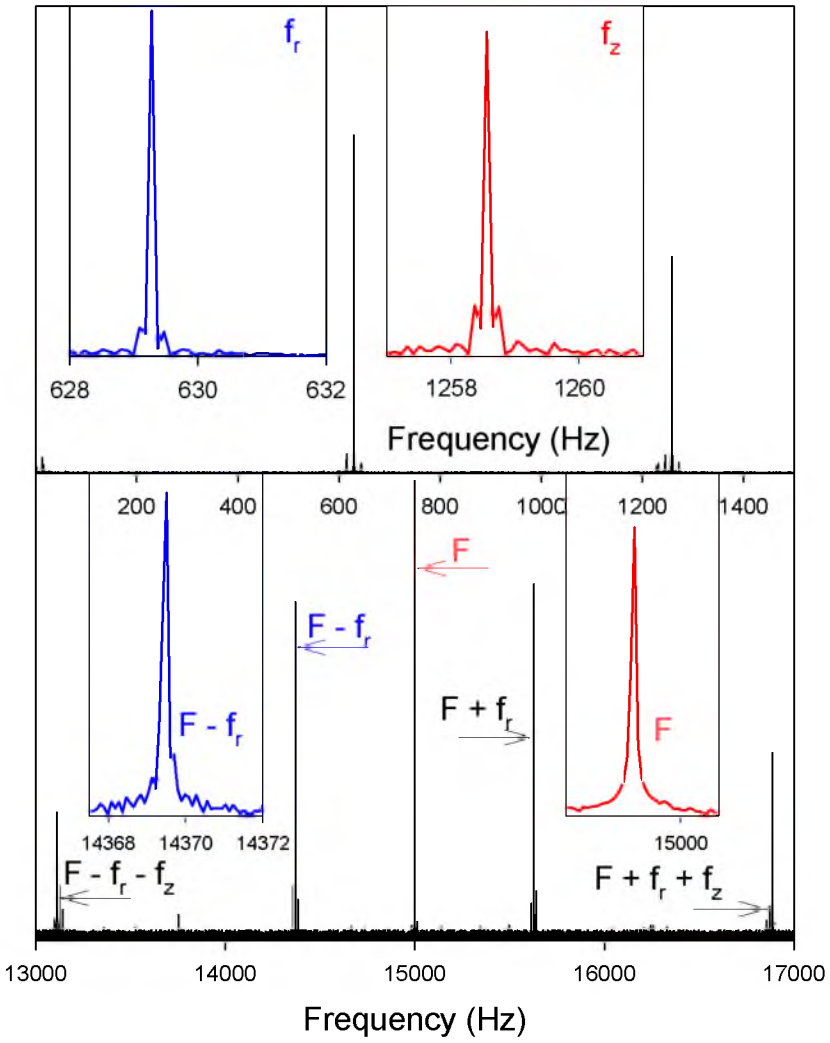

Figure 3.3: Typical FFT spectrum for a single trapped particle. (Top) Frequency range between 1 – 1400 Hz showing both f_r and f_z. (Bottom) Frequency range between 13 – 17 kHz containing the difference frequencies with respect to F.

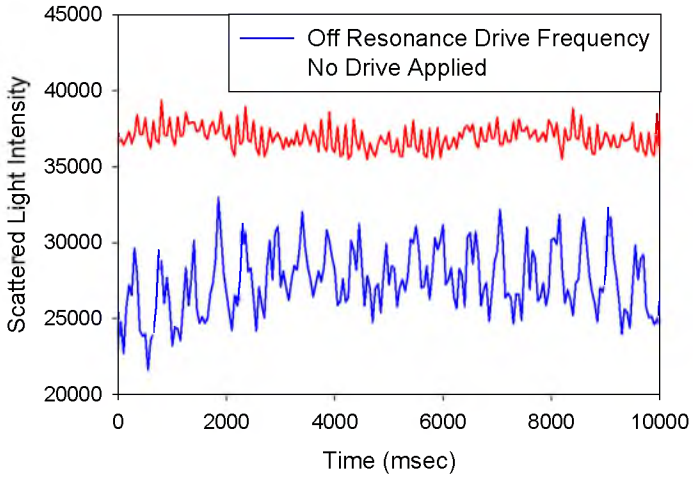

Figure 3.4: The scattered light intensity from a particle with an off resonance drive applied to the trap at f_{Drive} = 1258.43 Hz (blue) and without the drive (red). The scattered light intensity is photons per 50 ms.

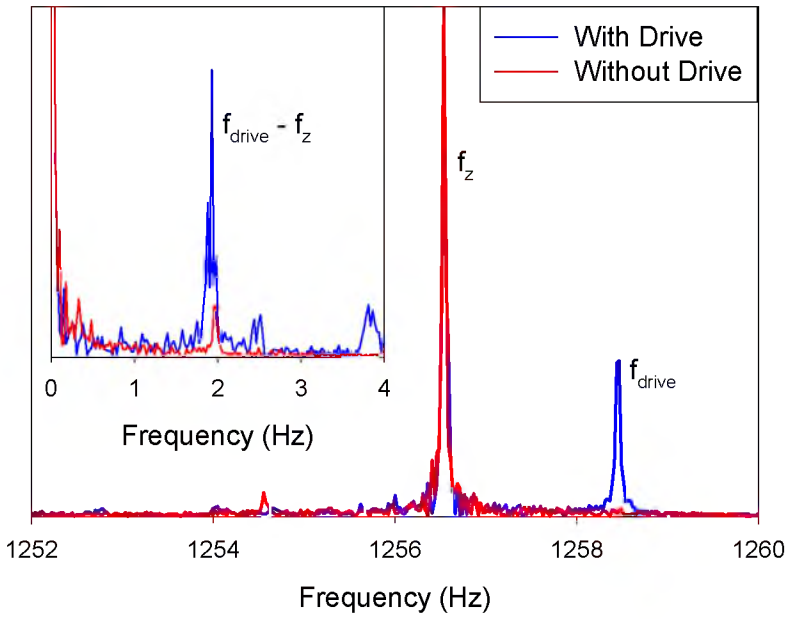

Figure 3.5: I(t)/FT analysis of a single particle with (blue) and without (red) an off-resonance drive frequency (f_{Drive}) applied to an electrode outside of the trap. (Inset) The low frequency region of the FT spectrum and the presence of $f_{Drive} - f_z$ when f_{Drive} is present.

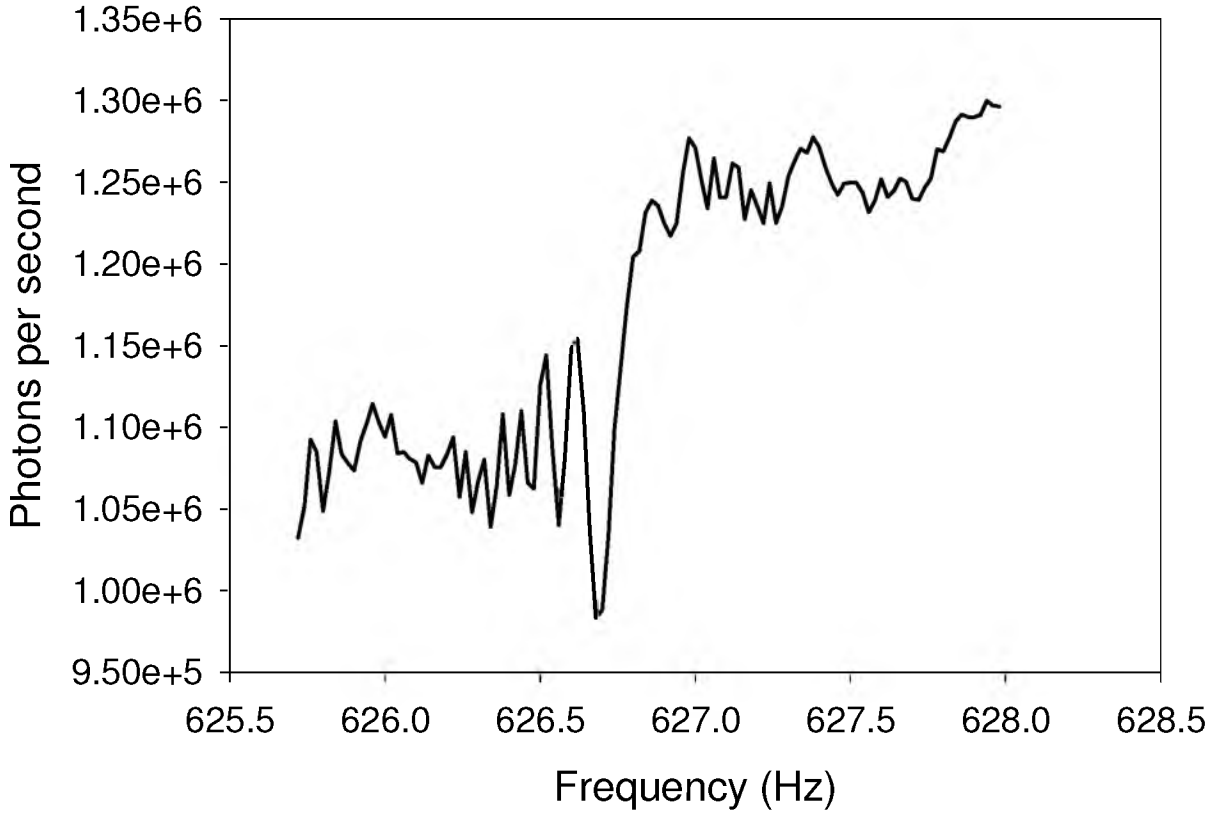

Figure 3.6: Laser modulation sweep of a single particle, resulting in a dip in scattered light intensity when the particle is resonantly excited.

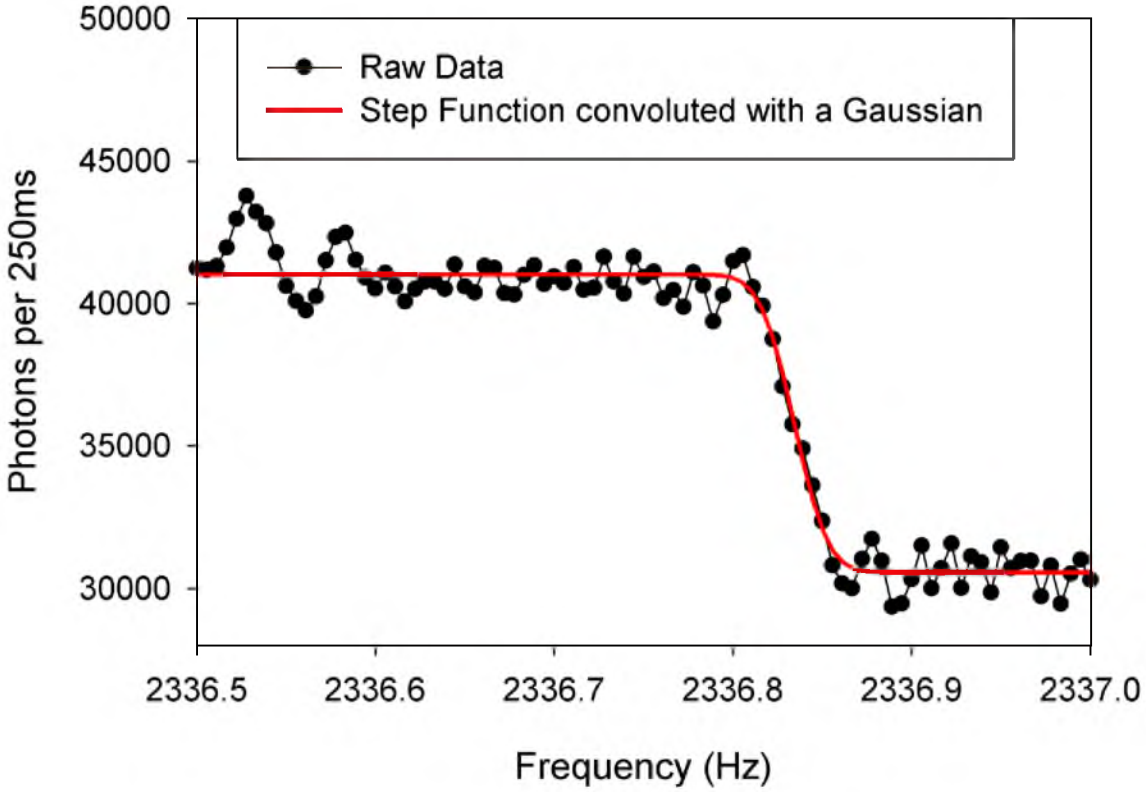

Figure 3.7: The scattered light intensity per 250ms during an AC frequency sweep of a single particle at 10^{-8} Torr. The drop corresponds to resonant excitation of the axial secular frequency of the particle. The raw data are fit with a step function convoluted with a Gaussian with parameters listed on the figure in red.

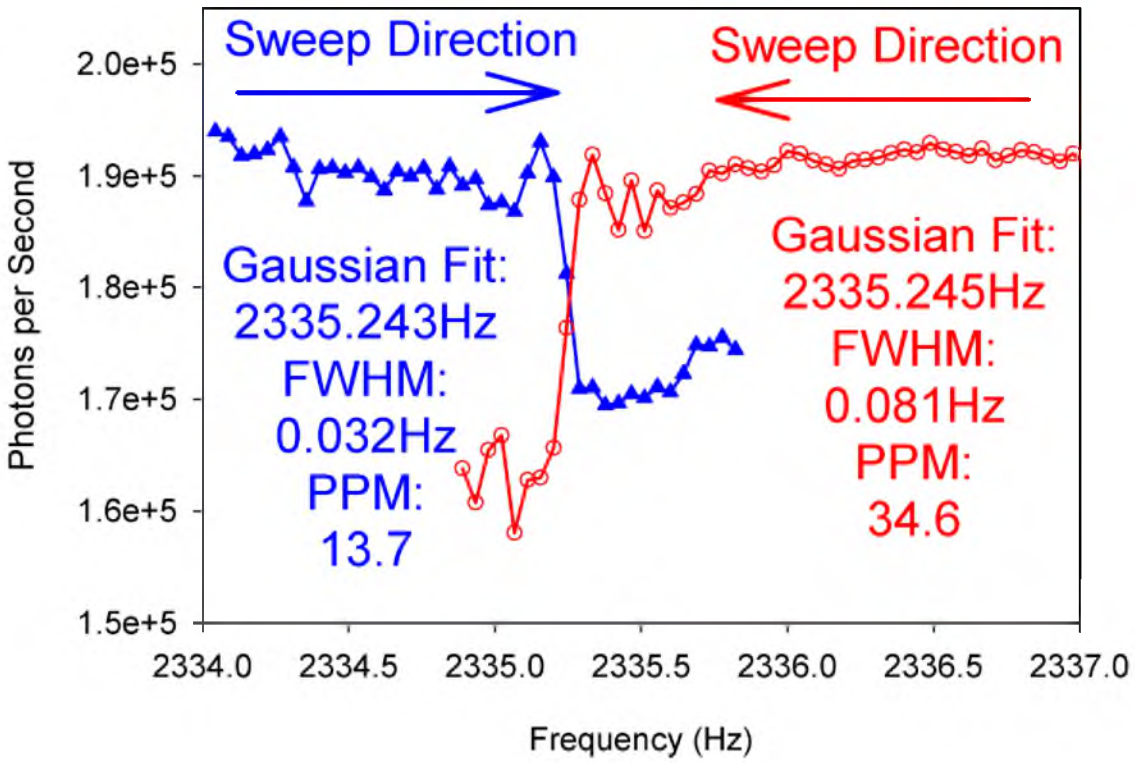

Figure 3.8: The scattered light intensity per second during an AC frequency sweep from low to high frequency ( ) and high to low frequency ( ). The blue plot was carried out the AC peak-to-peak voltage of 125mV and the red plot with AC peak-to-peak voltage of 175mV. These plots are fit with a step function convoluted with a Gaussian to obtain the fit parameters listed in the figure.

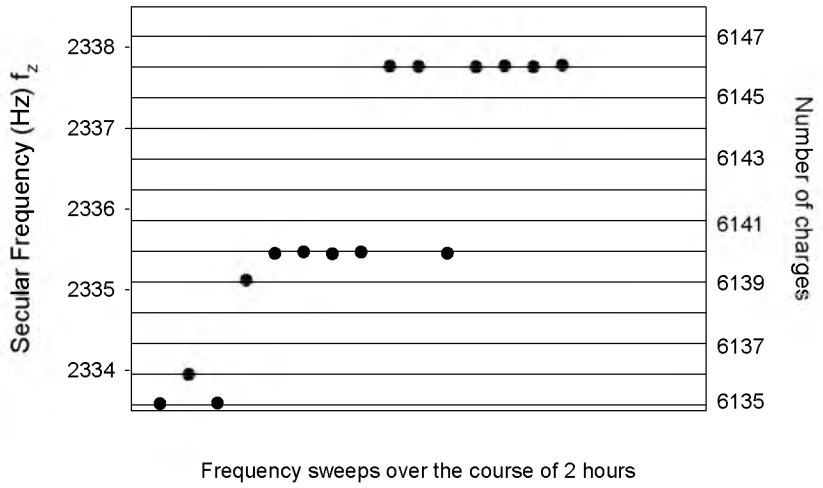

Figure 3.9: Variation in axial secular frequency over time due to the particle gaining and losing charge. The steps on the plot correspond to individual charge steps (0.380 Hz). From these steps, the total charge on the particle may be determined.

CHAPTER 4

USING A CO_2 LASER TO ACTIVATE FLUORESCENCE FROM CORE-SHELL CdSe/ ZnS NANOCRYSTAL QUANTUM DOTS

Introduction

Over the past two decades, core-shell CdSe/ZnS nanocrystals quantum dots (QDs) have received much interest because of their tunable size-dependent optical properties.[1-3] The quantum efficiency of these nanocrystals approaches ~85%,[4] making them suitable for many applications such as lasers,[5-8] sensors,[9] solar cells,[2, 10-13] and biological labels.[14, 15] The absorption and emission spectrum of a QD is dominated by formation of an exciton. An exciton is formed when an QD absorbs a photon creating an electron–hole pair, a photon is emitted when the electron – hole pair radiatively recombine. However, most QDs exhibit fluorescence intermittency, also known as blinking.[16, 17] Understanding what causes blinking is necessary to synthesize and properly use QDs that either do not blink or are predominately "on". In order to study QDs in an ion trap using the methods demonstrated in Chapter 3, the QDs must be fluorescent for our experimental setup to work. This chapter is devoted to a peculiar way to activate fluorescence from QDs in an ion trap.

Changes in the Experimental Setup

A few changes were made to the experimental setup from Chapter 3. In the work presented here, green water-soluble core-shell CdSe/ZnS QDs obtained from nn-labs were electrosprayed, guided by a series of ion guides, and subsequently confined in an ion trap in the presence of Argon (15 mTorr). The QD solution was diluted ~200:1 with methanol. Methanol was used in these cases because it was relatively easy to electrospray. Na^+ or H^+ present in solution presumably ionized the QDs. The trap parameters were $V_0 = 500$ V, $\Omega/2\pi = 143.3$ kHz and $z_0 = 2.97$ mm. A cw 532 nm laser excited fluorescence from the QDs and a CCD camera collected light emitted from the QDs. A shorter focal length lens (4') decreased the spot size of the 532 nm laser to about 100 μm. A notch filter installed in the light collection pathway blocked any scattered light, which should be negligible from particles of this size (4 – 6 nm), but is an

issue from the trap itself. A pair of paraboloidal mirros focused a Synrad CO_2 laser diagonally through the trap.

QD Fluorescence Activated by the CO_2 Laser

Figure 4.1(a) shows fluorescence from core-shell QDs trapped with only the 532 nm laser present (100 W/cm^2) during a 2-second exposure. Figure 4.1(b) is a picture of the fluorescence from the same swarm of QDs with only the 532 nm laser present (100 W/cm^2) after they were exposed to the CO_2 laser for 2 seconds, at half duty cycle (~2 Watts in the trap). There is some fluorescence in Figure 4.1(a) coming from the swarm, but it is very limited. However, after the swarm was exposed to the CO_2 laser for 2 seconds, the fluorescence signal increases dramatically.

The role of the CO_2 laser is interesting and not well understood. The core and shell of the QDs should not efficiently absorb this wavelength of light because there are no vibrational modes present in this region for CdSe or ZnS bulk material. For this reason, CdSe and ZnS are commonly used for CO_2 laser windows. In addition, for sufficiently small particles like the ones used here, the efficiency of absorption (Q_{abs}) is inversely proportional to the wavelength of light used.[18]

On the other hand, mercaptoundecanoic acid does have a vibrational band that overlaps with the CO_2 laser wavelength. These species likely absorb the CO_2 laser, heating the particle and subsequently driving off excess solvent and ligands present on the surface of the QDs. If the ligand layer evaporates in this process, the surface will undergo significant reorganization, possibly creating significant defects and vacancies. This result significantly changes in the emission features of these QDs going from being dominated by exciton emission to being dominated by deep and shallow level emission, red shifting the spectra. It has been shown by Biju *et al.* that heating has a propensity to activate surface trap states for nonradiative decay, but not for deep level emission.[19] These states are thought to arise during heating due to expansion of the QDs creating defects and vacancies on the surface. The study by Biju *et al.* showed it was

possible to reversibly form and heal these defects by repeated heating and cooling the sample.[19] If the QDs are being heated hot enough to evaporate the ligands attached to the surface, the QD must be getting very hot and the sudden expansion of the surface could significantly change the absorption and emission characteristics of the QDs.

Conclusions

The CO_2 laser stimulates fluorescence from the QDs, but little is known about the process by which it takes place. Presumably, the ligand layer absorbs the CO_2 laser wavelength and causes the ligand layer to evaporate in the process. Ligand evaporation then could cause significant changes to the surface of the QD, changing the emission characteristics of the QD and where the charges are located. This is an interesting result and it should be possible to determine the source of this brightening with this experimental setup, but more studies are needed.

References

1. J. Y. Kim, O. Voznyy, D. Zhitomirsky and E. H. Sargent, Advanced Materials **25**, 4986 (2013).

2. E. H. Sargent, Nature Photonics **6**, 133 (2012).

3. R. Debnath, O. Bakr and E. H. Sargent, Energy and Environmental Science **4**, 4870 (2011).

4. M. A. Hines and P. Guyot-Sionnest, J. Phys. Chem. **100**, 468 (1996).

5. S. G. Li, Q. Gong, C. F. Cao, J. Y. Yan, Y. Wang and H. L. Wang, Infrared Physics and Technology **60**, 216 (2013).

6. A. E. Zhukov, M. V. Maksimov and A. R. Kovsh, Semiconductors **46** (10), 1225 (2012).

7. L. V. Asryan, Journal of Nanophotonics **3**, 31601 (2009).

8. J. Schafer, J. P. Mondia, R. Sharma, Z. H. Lu, A. S. Susha, A. L. Rogach and L. J. Wang, Nano Letters **8**, 1709 (2008).

9. L. Zhang, R. Zhang, P. Cui, W. Cao and F. Gao, Chemical Communications **49**, 8102 (2013).

10. P. K. Santra and P. V. Kamat, Journal of the American Chemical Society **135**, 877 (2013).

11. E. Strein, A. Colbert, S. Subramaniyan, H. Nagaoka, C. W. Schlenker, E. Janke, S. A. Jenekhe and D. S. Gingera, Energy and Environmental Science **6**, 769 (2013).

12. J. Wu, S. C. Mangham, V. R. Reddy, M. O. Manasreh and B. D. Weaver, Solar Energy Materials &Solar Cells **102**, 44 (2012).

13. A. Kongkanand, K. Tvrdy, K. Takechi, M. Kuno and P. V. Kamat, Journal of the American Chemical Society **130**, 4007 (2008).

14. Q. Huo, Colloids and Surfaces B: Biointerfaces **59**, 1 (2007).

15. A. C. S. Samia, S. Dayal and C. Burda, Photochemistry and Photobiology **82**, 617 (2006).

16. C. Galland, T. Ghosh, A. Steinbruck, M. Sykora, J. A. Hollingsworth, V. I. Klimov and H. Htoon, Nature **479**, 203 (2011).

17. K. L. Knappenberger, Jr., D. B. Wong, Y. E. Romanyuk and S. R. Leone, Nano Letters **7**, 3869 (2007).

18. C. F. Bohren and D. R. Huffman, *Absorption and Scattering of Light by Small Particles*. (Wiley-VCH, 1983).

19. V. Biju, Y. Makita, A. Sonoda, H. Yokoyama, Y. Baba and M. Ishikawa, J. Phys. Chem. B **109**, 13899 (2005).

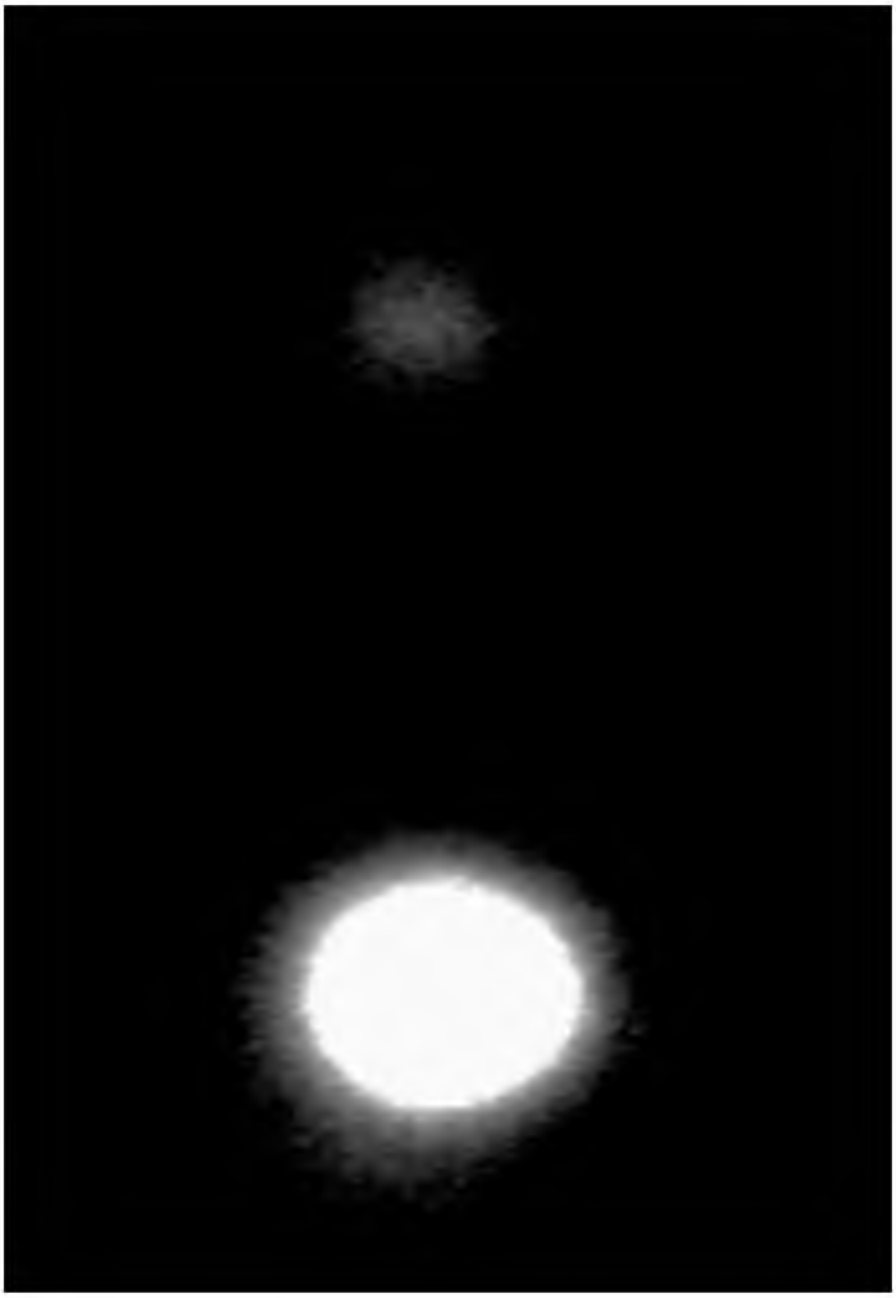

Figure 4.1: Images for a swarm of particles in the ion trap. (A) An image of the fluorescence observed from a swarm of QDs trapped taken with our CCD camera with a 2 second exposure while only exposed to the 532 nm laser (100 W/cm^2). (B) An image of the same swarm after it had been exposed to the CO_2 laser for 2-seconds. During the picture, only the 532 nm laser (100 W/cm^2) was present; the exposure time is also 2 seconds.

CHAPTER 5

SINGLE CdSe/ZnS NANOCRYSTALS IN AN ION TRAP: CHARGE AND MASS DETERMINATION, AND PHOTOPHYSICS EVOLUTION WITH CHANGING MASS, CHARGE, AND TEMPERATURE

Reprinted with permission from David M. Bell, Collin R. Howder, Ryan C. Johnson, Scott L. Anderson, and ACS Nano DOI: 10.1021/nn405920k Copyright 2014, American Chemical Society

Overview

We report the first measurements of fluorescence intermittency (blinking) and spectral behaviors for a single semiconductor nanocrystal quantum dot (QD) isolated in the gas phase, and discuss the effects on fluorescence of the QD charge state and heating to the point of sublimation. Core-shell CdSe/ZnS QDs were trapped in a quadrupole ion trap, and detected by laser-induced fluorescence (LIF). The mass (M) and charge (Q) were determined nondestructively; both were followed continuously over the course of hours or days. Emission spectra of the trapped QDs are significantly red-shifted relative to the solution-phase emission from the same particles. The temperature of the trapped QDs is determined by the balance between laser heating and collisional cooling and thermal emission, and it is possible to heat the particles to remove ligands or to the point of sublimation. QDs are observed to be emissive during sublimation, up to 85% mass loss. Eventually, the fluorescence quantum yield drops suddenly, and the QDs begin to blink. The method used is versatile, and will allow studies of quantum dot optical properties as a function of size, ligand removal, heating, surface oxidation, and other manipulations, where these properties are continuously correlated with the mass and charge.

Introduction

Nanoparticle mass spectrometry (NPMS) allows for repeated, nondestructive measurements of the mass, M, and charge, Q, of single trapped nanoparticles, making it possible to study correlations between M, Q, surface chemistry, and optical properties, as particles are manipulated by heating, exposed to reactants, etc.[1-9] As discussed below, the mass and charge are obtained by observing the particle's motion in a quadrupole trap, using either light scattering or fluorescence to track its the motion. In addition to obtaining M and Q, it is possible to measure optical properties, such as the emission spectrum, temporal behavior such as blinking (intermittent fluorescence) or bleaching, and to correlate the appearance of these optical effects with changes in particle mass, charge, or surface chemical state. Here, we report the first

measurements of blinking and spectral behaviors for a single charged semiconductor nanocrystal quantum dot (QD) isolated in the gas phase, and discuss the effects on fluorescence of charge state, heating, and mass loss by sublimation.

The basis of the NPMS method is to trap a single, charged nanoparticle in a quadrupole ion trap, using light scattering or laser-induced fluorescence (LIF) to detect and track the motion of the particle. The motional secular frequency (ω_z) of a charged particle in such a trap is inversely proportional to the mass/charge ratio, M/Q.[10] By making repeated measurements over the course of hours or days, it is possible to track the emission properties, and to observe how they respond to changes in M/Q as the particle is heated, exposed to reactants, or otherwise manipulated. By allowing occasional collisions with ions, electrons, or metastables created in a discharge, the charge, Q, can be changed. By measuring the change in secular frequency accompanying Q changing by one elementary charge ($\Delta\omega_z/e$), the exact value of Q is determined.[1, 3, 5] With Q, we obtain M, limited only by the precision of the ω_z measurement, which can be as high as 1 ppm.[1]

CdSe nanocrystals, also known as quantum dots (QDs), are too small to efficiently scatter light, but are efficient emitters (quantum yield 50 - 85%)[11, 12] with interesting photophysics, making them good candidates for NPMS. For NPMS, the QDs must be charged, so one important issue is the effect of charging on fluorescence intensity. A number of groups have examined the effects of charging QDs on various electrodes or in solution.[13-20] Guyot-Sionnest and co-workers attached QDs to an electrode and by applying a negative voltage (-1 V) were able to turn a QD off. This change was reversible by then applying a slight positive (+0.3 V) to turn the QD back on.[16] Galland *et al.* recently used a similar approach to gather fluorescence information while simultaneously collecting lifetimes.[18] In this study, there were two types of blinking (different lifetimes and blinking on and off statistics) that could both be controlled electrochemically: one type due to Auger recombination and another due to interactions between the Fermi level of the electrode and the trap states present on the QDs. Interestingly, a QD could

exhibit both types of blinking mechanisms at different times, meaning this is not due to the chemical makeup of an individual QD, but rather is inherent to QDs.[18]

QDs have been studied extensively in solution[21-23] or on a surface,[16, 24-26] but little is known about their optical properties when they are charged and detached from a surface.[27] In summary, it is not obvious what might be expected for fluorescence of QDs in the gas phase with up to 20 charges, in the form of Na^+ adsorbed on the surface. In this paper, we present the first observation of fluorescence from single, trapped QDs in the gas phase, and demonstrate determination of the absolute mass and charge for both individual QDs and QD aggregates, the first such measurements for particles smaller than ~20 nm. In addition, we examine emission intensities and spectral properties over time as the QDs are heated and undergo charge changes.

Methods

Ion Trap and Optical Detection

To investigate charged QDs, we used a split ring electrode trap (SRET) based on the design by Gerlich and co-workers,[28] and is shown in Figure 5.1. The SRET is a type of Paul trap, with the center ring electrode split to allow optical access through the trap. In addition, the end cap electrodes are truncated cones with holes to allow a particle beam to pass through along the trap axis. We added a pair of diagonal channels that allow lasers to be focused through the trap center, and for the work presented here, one pair was used, together with a pair of confocal off-axis paraboloidal mirrors, to focus a CO_2 laser (Synrad, 10 W, duty cycle modulated) through the trap for particle heating. Near the electrodes, the fields are far from the fields in an ideal hyperbolic Paul trap; however, for sufficiently small excursions from the trap center, the non-idealities are small. Under appropriate operating conditions,[2, 10, 29] the motion in such a trap is harmonic, with well-defined frequencies associated with radial and axial motion, ω_r and ω_z, respectively. Either of the frequencies can be used to calculate the M/Q ratio for the trapped particle, but in our geometry, ω_z is more easily and precisely measured, and in this case:

$$\frac{M}{Q} = \frac{\sqrt{2}V_0}{\omega_z \Omega z_0^2},$$

where V_0 and Ω are the amplitude and frequency of the radio-frequency voltage applied to the trap (V_0 = 500V, $\Omega/2\pi$ = 143.3 kHz), and z_0 (2.96mm) is a parameter describing the field geometry.

Particles were detected by focusing a cw 532 nm laser (Ultra Lasers) through the trap (into the page on Figure 5.1) with a beam waist diameter of ~100 μm, to excite fluorescence of the trapped QD. The effects of varying the laser intensity between roughly 100 W/cm^2 and 220 W/cm^2 are also examined. The laser spot size is an improvement on previous studies, which was accomplished by moving the focus closer to the trap. Fluorescence emitted from the QDs in the trap was collimated by an aspheric lens with a 25 mm focal length, passed through a 532 nm notch filter to block scattered light, and focused onto an avalanche photodiode module (Laser Components: Count™). To obtain emission spectral information, long-pass filters with cut-off wavelengths of 590 nm, 645 nm, 695 nm, 780 nm, and 850 nm (Thorlabs) were installed in line with the APD.

We operated a CO_2 laser at a 50% duty cycle (5 W average power) during particle injection because we find that this leads to substantial increase in fluorescence quantum yield, making the particles much easier to detect. The mechanism of this "brightening" process is not completely understood; however, the mercaptoundecenoic acid ligand layer has an absorption band at 10.6 μm, and therefore should be heated by the CO_2 laser, while neither CdSe and ZnS absorb strongly at 10.6 μm (absorption coefficient 0.016 cm^{-1},[30] and 0.2 cm^{-1}, respectively). Therefore, it appears that the brightening process involves heating the ligand layer, possibly driving additional loss of solvent molecules or some ligand desorption. Additional studies of this phenomenon are planned.

Method

The instrument, described in Chapter 3, consists of an electrospray source used to get nanoparticles into the gas phase, a hexapole guide for differential pumping and desolvation, a quadrupole ion guide used to prefilter the M/Q distribution fed to the trap, and finally the trap.

Water-soluble core-shell CdSe/ZnS (with mercaptoundecanoic acid as a ligand) QDs were obtained from nn-labs. The QDs used in these studies have a solution-phase emission maximum near 550nm, although it is not obvious what to expect for charged QDs in the gas phase. The QD stock solution was diluted in methanol (1:100) and electrosprayed in a Micromass (now Waters) z-spray source with a capillary voltage of 3.5kV and a cone voltage of 210V. Positive ions formed by the electrospray source were guided through the hexapole ion guide at a pressure of ~20mTorr to collisionally cool and focus the particle beam. We presume that the presence of positive ions in the solution (mostly Na^+) was responsible for charging the QDs. The QDs passed from the hexapole, through a pneumatically operated isolation valve, and into a linear quadrupole guide, which has similar trapping properties to those of the SRET, and therefore functions as a prefilter to reject ions and particles outside the M/Q range of interest. From the linear quadrupole guide, the QDs are injected into the trap, using 15 mTorr of argon buffer gas to aid trapping, and damp the initial kinetic energy of the trapped QD. With the isolation valve closed, the base pressure in the trap chamber is ~2 x 10^{-8} Torr. While trapping, both the 532nm laser (100 W/cm^2) and the CO_2 laser (1000 W/cm^2) was focused through the trap to enable immediate detection of the trapped QD. To inject a QD, the isolation valve was repeated pulsed open (open time ~1 second), while monitoring LIF signal, looking for the signature of a trapped QD (~300 – 500 counts per second). TTL pulses from the APD were counted by a ComTec multichannel scalar (P7882). As soon as signal was observed, the CO_2 laser was turned off, and the pressure was dropped to between 0.1 – 1 mTorr, and a scan of ω_z was made to verify that only a single particle was trapped (80% of the time). In the event that more than one secular frequency resonance was observed, the trap was simply dumped and the fill process was restarted.

Safety

Since cadmium is toxic, precautions were taken to avoid contact with the particles. The electrospray source is contained within a glass cylinder to ensure that CdSe/ZnS particles do not spray into the atmosphere. The glass cylinder and other electrospray components were periodically cleaned in methanol. Whenever handling particles or contaminated parts, it is important to wear necessary attire (gloves, eye protection). Syringes and used solvent are hazardous waste and must be disposed of appropriately.

Measuring the Secular Frequency

The approach we have found best for secular frequency measurement is to apply a sinusoidal "drive" signal to one of the lens electrodes just outside the trap, creating a sinusoidal field that penetrates to the trap center. The field is too weak to have significant effect on the trapped QD motion, except when the drive frequency is resonant with the QD axial secular frequency, ω_z. On resonance, the amplitude of the ω_z oscillations becomes large enough to reduce the fraction of time that the QD spends in the detection volume, resulting in a drop in LIF signal. The detection volume is determined by the overlap of the LIF laser focus and APD imaging lens focus, and has characteristic dimensions of roughly 50 – 100 μm. It is possible to obtain ppm mass precision in slow scans with low drive amplitudes and low pressure,[1] but here the goal was to follow changes in QD properties over time; therefore, the sweeps were fast (>1 kHz/sec) and a high (2 V) drive amplitude was used to ensure measurable response during the short time on resonance. To measure the fast sweeps, short dwell times were also needed, resulting in poor signal/noise. Figure 5.2 shows an example of a single sweep (data points) as well as the average of five sweeps scanned both to higher (20 kHz to 60 kHz) and to lower (60 kHz to 20 kHz) frequency. Note that the sweeps to higher and lower frequencies both show a sharp resonance at 32.67 kHz, and even in the single scan, the signal dip is well outside the scatter in the data points. The ω_z resonance appears as a peak in these data because the

experiments were done with the trap filled to 1 mTorr with argon (P_{trap} = 1 mTorr). As a result, the driven motion excited at resonance is quickly damped by Ar collisions, resulting in quick signal recovering. This damping also, in principle, broadens the resonance, degrading precision; however, in this case, the factor limiting precision is the scan rate. By performing repeated frequency sweeps, the secular frequency (i.e., M/Q) for a single QD can be tracked for many hours. To extract the ω_z values for each sweep, the negative peak, as seen in Figure 5.2, is fit with a Gaussian, the center of which is reported as ω_z.

Note that the scatter in the single scan data points is substantially greater than would be expected for statistical noise. The scatter partly reflects oscillations (at ω_r and ω_z) due to thermal (Brownian) motion of the QD. Decker has discussed the expected amplitude of thermal motion, which scales like $\sqrt{TM/Q^2}$, and for QDs with T=300 K, the root mean square excursions are on the order of 30 μm and 60 μm, respectively, in the axial and radial directions.[31] These are comparable to the dimensions of our detection volume, thus thermal motion leads real fluctuations in LIF intensity.

The fact that a single peak is observed in the frequency spectrum indicates that there is only one particle in the trap. The charge on these small QDs is low enough that coupling between the particles is weak compared to thermal energy, i.e., each particle behaves quasi-independently with its own ω_z resonance. In principle, it is possible that a single peak could result from two or more particles which coincidently happen to have nearly identical ω_z's; however, this unlikely situation would be revealed as soon as one of the particles changed charge.

Results

Tracking M/Q and Determination of Q and M

Figure 5.3 shows an example time record for a single QD observed for 12.5 hours at low enough LIF laser intensity (100 W/cm^2) to minimize mass or other changes due to heating. The

secular frequency (ω_z) shows discrete steps corresponding to events where QD charge changed by one elementary charge ($\Delta Q = \pm e$). Charge changes occur due to occasional (~1/hour) collisions of the QD with electrons, ions, or metastables in the chamber background, and because we need such events to determine Q and M,[5] a cold cathode gauge is left on to create electrons, Ar^+ and Ar^* from the 1 mTorr argon buffer gas. In this case, $\Delta\omega_z/e = 2682 \pm 44$ Hz, as determined by fitting the 16 steps observed. From $\omega_z/\Delta\omega_z$, we can determine Q at each step (values indicated on the figure), and once we know Q, we can convert M/Q to M, which is also plotted on the figure. In this case, the mass record is deliberately boring – just a gradual loss (0.5% per hour) of mass, presumably from the ligand layer, due to mild heating from the LIF laser.

The diameter of these (nn-labs) QDs is reported to be 6 ± 0.6 nm, which corresponds to roughly a factor of two variation in mass, with estimated masses ranging from ~480 kDa to ~1.1 MDa, not including the ligand layer. (The masses are estimated assuming a nominal ZnS shell thickness of 1 nm, and using bulk densities for CdSe and ZnS. For the nominal 6 nm QD, the core and shell masses are nearly equal). For core-shell CdSe/ZnS, it has been shown between 800 – 1,000 dithiocarbamate ligands are present.[32] If we presume the same coverage (~18 $Å^2$/molecule) on a 6nm QD, there should be ~630 ligands present with a mass of ~137 kDa, for the nascent QD. However, we believe that there is significant ligand desorption/decomposition during the CO_2 brightening process. In this example, the mass is near the low end of the expected mass range, and therefore, we can safely conclude that the particle was a single QD, presumably having lost most of the ligand mass.

Figure 5.3 also shows the LIF intensity as a function of time, and it can be seen that there are steps in LIF intensity that track the charge steps in ω_z. These do not represent real changes in the fluorescence quantum yield with charge. Instead, they result from the effects of charge on photon collection efficiency. Recall that the root mean square amplitude of thermal motion of the QD scales like $\sqrt{TM/Q^2}$, and that the amplitudes are comparable to the detection volume defined

by the laser and APD foci. Therefore, when Q increases (decreases) by e, the rms thermal amplitude decreases (increases) by 8 to 10%, resulting in a small increase (decrease) in collection efficiency. The detection volume can be increased to avoid this effect, but decreases the sensitivity for measuring ω_z, requiring higher drive amplitudes. In the following figures, small fluctuations in LIF, correlated with charge steps, should be ignored.

Effects of Heating and Particle Sublimation

Figure 5.4 shows the first ~83 hours of the time record for a single particle tracked for more than 4 days, during which time we substantially changed the particle properties by driving large mass losses. Emission spectra were acquired during several intervals, by swapping filters on the APD, turning the laser intensity back to the initial low level as needed. These intervals are delineated by pairs of vertical lines. To allow the changes in particle properties to be seen more clearly, Figure 5.5 shows the data with magnified vertical scales for the following time intervals: 0 to 2000 minutes, 2000 to 2500 minutes, and 4000 to 5000 seconds.

Consider the first 0 to 2000 minute period, where the LIF laser was left at low intensity (100 W/cm^2) to minimize QD heating. As in Figure 5.3, the secular frequency undergoes a series of steps, with $\Delta\omega_z/e = 733.6 \pm 5$ Hz, averaged over the steps observed between 0 and 2000 minutes. Q was 17e at the onset, and varied between 20 and 17 during this time period. The LIF intensity fluctuated in concert with the charge steps, due to the collection efficiency artifact discussed above. Just before 2000 minutes, the mass and LIF intensity measurements were interrupted to obtain spectral information by sequentially measuring LIF through a series of long pass filters. During this interval, the mass and frequency series are not plotted, and the LIF intensity is also perturbed by the filters. As in Figure 5.3, the mass simply dropped slowly (1.07 %/hour), and similar steps in LIF intensity are seen, attributed to Q-dependent collection efficienty. The initial mass of this particle is 1877.8 ± 25.6 kDa, i.e., it is almost certainly an aggregate of either two or three QDs. These aggregates are probably present to some extent in

the methanol-diluted electrospray solution and additional aggregates may also form during electrospray. Such aggregate particles tend to have M/Q ratios greater than single QDs, and if desired, they can largely be filtered out by operating the linear quadrupole and trap at 280 kHz.[33]

At 2140 minutes, the LIF laser intensity was increased to ~216 W/cm^2 in order to heat the particle, and then reduced back to 100 W/cm^2 (the original intensity) at 2380 minutes. As shown in Figures 5.4 and 5.5b, the increase in laser power is accompanied by a sharp increase in emitted photon intensity, and the beginning of a rapid decrease in the particle mass. The total mass loss during this first heating period was a factor of roughly two – too large to be explained entirely by ligand loss. In addition, a series of rapid charge steps, monotonically increasing the positive charge by 5e, was observed at the beginning of the heating period. Since the rate of collisions with electrons, Ar^+, and Ar^* should not have increased dramatically (P_{trap} was not changed during the heating period), these rapid charge steps appear to indicate charging by thermionic electron emission. The fact that the rate of charging decreased with increasing particle charge is also consistent with this mechanism, because electron binding energy should increase as the positive charge left behind increases, thus reducing the emission rate. Both the rapid mass loss and thermionic emission indicate that the temperature reached during this heating period was quite high, as discussed below. It is also likely that a substantial fraction of the increased photon emission at high laser intensity is thermal emission. To allow comparison with the emission spectrum measured during the initial low temperature period, the laser intensity was briefly reduced to the initial intensity (100 W/cm^2) during the period between 2296 and 2325 minutes. In Figure 5.5b, the effect of this interruption of the heating period is obvious. The mass and charge state both immediately stopped changing, and then mass loss resumed as soon as the laser intensity was increased back to 216 W/cm^2. Finally, at 2380 minutes, the heating period was terminated by reducing the laser intensity back to the original 100 W/cm^2 level, and the particle was monitored for 2000 minutes (~33 hours). During this "rest" period, the particle mass was nearly constant, initially *increasing* by 3.3 % during the first few hours, presumably due to

adsorption of adventitious gasses. For example, the vacuum chamber undoubtedly has species such as O_2, CO, CO_2, H_2O, and hydrocarbons at partial pressures in the 10^{-9}-10^{-8} Torr range, which certainly might react and bind to the naked surface of the partially sublimated particle. The charge state also showed signs of "recovering" from the high positive charge attained at high temperature. A series of charge steps monotonically decreased the positive charge during the first few hours, as the highly positively charged particle preferentially combined with electrons. Only after the charge state had declined to Q = 12 – 14 did the charge begin to step bidirectionally, indicating that steady state had been reached. To probe the effects of these charge steps and surface reactions on the emission, spectra were acquired in two intervals, near the beginning and near the end of this "rest" period. Note that during the rest period, the LIF intensity was only ~half that during the first 2000 minutes, roughly mirroring the reduction in particle mass. Nonetheless, it is interesting that the particle continued to be emissive even though it had lost such a large fraction of its mass during the heating period.

Finally, at t = 4400 minutes, the LIF laser intensity was again increased to 216 W/cm^2 and left high, allowing us to observe changes in mass, charge, and emission intensity as the particle sublimated. Note the rapid mass loss, and the rapid charge stepping, interrupted by two brief periods where the laser intensity was reduced back to 100 W/cm^2 to allow spectral measurements. Emission was observed until at 4836 minutes, the particle abruptly went completely dark. At that point, the mass was only 290 kDa, corresponding to loss of 84.7 % of the initial particle mass and the charge was 13e. The simplest explanation for the final abrupt loss of emission would be ejection of the particle from trap, and indeed, the final M/Q is outside the range recommended by Gerlich[3, 34] for safely adiabatic trapping. As discussed below, however, there is actually still barely detectable emission after the "darkening" transition, leading us to conclude that the particle was still present.

Emission Spectrum

As noted, during several intervals over the course of the 83-hour particle time record, emission spectral information was acquired using long-pass color filters on the APD detector. To avoid contributions to the signal from thermal ("blackbody") emission, the LIF laser intensity was reduced to 100 W/cm^2 for each of these spectral measurement intervals (see below). The data were converted to emission spectra by taking differences between intensities measured with successive filters, and the results are shown in Figure 5.6. Spectra are shown for each measurement interval indicated on Figure 5.4, along with an average over all the spectra. Because the total LIF intensity decreased as the particle sublimated, the spectra are normalized to allow easier comparison. In addition, the spectra are corrected for the APD sensitivity variations over the spectral range of interest, using quantum efficiency values provided for our APD module by the manufacturer. To test the filter/APD approach to spectral measurement, the spectrum for a solution of the QDs was measured using the same APD, color filters, and laser intensity, and this control spectrum is also shown. As expected from the manufacturer's data, the stock QD solution has an emission maximum at 550 nm, although we also see a small peak near 750 nm.

The emission spectra for the trapped gas-phase particle are significantly red-shifted with little intensity at 550 nm, and most of the intensity in a broad peak 590 nm and 695 nm. The emission also rises again toward 850 nm, suggesting that there may be a substantial peak in the near-IR. The possible origin of these spectral features is discussed below.

We have demonstrated that single QDs, and small aggregates of QDs, isolated in the gas phase, have substantial LIF quantum yields, and that the emission intensity is not strongly affected by changes in the charge. Furthermore the QDs can be heated to temperatures where sublimation and thermal emission of electrons and photons is efficient, yet still retain significant LIF quantum yield when the particles are allowed to cool again, to temperature well below those required for significant thermal emission. Several points merit additional discussion.

Discussion

Temperature Estimates for "Heating" and "Rest" Periods

As noted above, Figure 5.5b and 5.5c show evidence that the QD aggregate reached temperatures during the "heating" periods high enough to drive sublimation and thermal emission. For reference, bulk ZnS is observed to sublime at about 1450 K, although the temperature should be lower for small particles in vacuum. Bulk CdSe sublimes at about 1420 K; however, sublimation of CdSe nanostructures has been reported at temperatures as low as 773K.[35]

Particle heating is via absorption of energy from the LIF laser, only part of which is radiated as fluorescence. A rough estimate of the heat deposition rate can be made using the LIF intensity to estimate the excitation rate. In Figure 5.3, and in the "rest" periods in Figure 5.4, where the particles show no signs of being hot enough for thermal emission or sublimation, it is reasonable to assume that the only significant emission process is LIF. Under these conditions, the LIF count rate was 500/second, and if we correct for APD quantum efficiency, reflection losses in the optics, and the collection solid angle, we can estimate that the particles were emitting on the order of 30,000 photons/second. A lower limit on the heating rate can be obtained by assuming that the LIF quantum yield is unity, so that the heating comes only from the Stokes shift between the 532 nm pump and the emission spectrum (Figure 5.6). Since we have no information on the spectral dependence of the emission at $\lambda \geq 850$ nm, we assume that this near-IR emission is all at 900 nm, for this estimation. With these assumptions, we reach a not unreasonable estimate for the heat deposition rate of ~16,000 eV/second $\approx$ 2.6 fW. If we assume that the heating rate for the higher laser power used in the heating periods in Figure 5.4 (for LIF count rate of 3300/second) is simply proportional to the increased laser power, the heat deposition rate would be ~105,000 eV/second $\approx$ 18 fW.

The particle temperature is set by the balance between these heating deposition rates and all cooling mechanisms. Since there is no evidence for thermal emission or rapid sublimation at the lower LIF laser intensity, the only significant cooling mechanism is via collisions with the 1

mTorr of Ar buffer gas. The mean free path of the argon is much larger than the trap dimensions, and the velocities of the massive particles are negligible compared to the argon velocity. Therefore, the collisions are essentially of argon at the trap temperature (near 300 K) with the hot particle surface. The flux-weighted collisional cooling power can be estimated as:

$$P = 2kAZ\left(T_{QD} - T_{Trap}\right) * Accom$$

where k is Boltzmann's constant, A is the surface area of the QD, Z is the collision rate per unit surface area, T_{QD} is the temperature of the QD, and Accom is an accommodation coefficient.[36] The accommodation coefficient accounts for the inelasticity of the Ar-surface collisions, where Accom=1 corresponds to collisions where the scattered argon is thermal at T_{QD}, and Accom=0 means no cooling. For a noble gas, Ar is a reasonably efficient collider, with, for example, Accom = 0.24 in collisions with a tungsten filament between 1073 – 1785 K.[37] For 1mTorr of Ar at 300 K, there would be ~450,000 collisions per second with a single QD, and roughly double that for a QD dimer, assuming that the QDs in the dimer remain unfused, which is probably a reasonable assumption for low temperatures. If we assume Accom = 0.24, then the collisional cooling power equals the laser heat deposition rate at T_{QD} = ~630 K. This is certainly (see below) well below the temperature where thermal electron or photon emission would be expected, and thus seems reasonable. The slow mass losses seen Figure 5.3 and the initial period in Figure 5.4 may indicate that sublimation is occurring, albeit very slowly, again, consistent with T_{QD} being below $T_{sublimation}$. Note that the measured mass losses of 1.0 – 1.1 % /hour correspond to a desorption rate of less than 5.8 Da/second.

If the higher heat load at high laser intensity were balanced only by collisional cooling, then the particle temperature would be ~2800K; however, well below this temperature, additional cooling by sublimation and thermal emission of photons and electrons becomes significant. If the particles behaved like black bodies, the thermal photon emission would be governed by the Stefan-Boltzmann law:

$$P = A\epsilon\sigma T^4$$

where P is the radiated power, A is the surface area of the QD, ε is the emissivity constant, σ Stefan's constant, and T is the temperature.[38] Subwavelength diameter particles do not behave as black bodies, however, and have emissivities well below unity and with substantial wavelength dependence.[39-41] A number of studies suggest that $\epsilon = 0.04$ for refractory nanoparticles (W, Fe, and C).[42] For CdSe, $\epsilon = 0.001$ might be a reasonable value since it is not a refractory material and thus provides a lower bound on the radiative cooling. Without collisional cooling, the thermal emission would balance the heating power at ~1300 K.

Thermionic emission of electrons is governed by the Richardson-Dushman equation: $I(\text{amps}) = AT^2 \exp(-\Phi/kT)$, where Φ is the material work function, and $A=4\pi m_e e k^2/h^3$, where m_e and -e are the electron mass and charge, k is the Boltzmann constant, and h is Planck's constant. The minimum energy carried away by each electron is Φ, however, because the electrons leave behind an increasingly positively charged particle, the actual energy loss per electron is significantly higher. Nonetheless, the frequency of electron emission is small – there are only 5 emission events between 2140 and 2210 minutes. Even taking the high positive charge (starting at 19 e, rising to 24 e) into account, the time averaged cooling power from electron emission is only ~0.1 eV/second – negligible compare to the heating power.

Similarly, there is also contribution to cooling from subliblimation. During each high laser power heating period in Figure 5.4, the mass loss corresponds to ~40% of the initial particle mass; however, this corresponds to loss of only ~ 0.8 ZnS units/second or ~0.4 CdSe units/second. The bulk heat of sublimation of CdSe and ZnS are, respectively, 405 kJ/mol (4.198 eV) and 468 kJ/mol (4.68 eV).[43] If we take the average of the two values, the sublimation cooling power is ~10 eV/second – large compared to that from thermionic emission, but still negligible compared to the laser heating power.

The particle temperature is set by the balance between laser heating power and the total cooling by collisions, sublimation, and thermal emission of electrons and photons; however, only

collisions and thermal photon emission are significant. Taking both into account, the particle temperature is estimated to be ~1200 K; however, this estimate is certainly too high, because in estimating the laser heating rate, we assumed that all detected photons were LIF, whereas a significant fraction actually results from thermal emission. Correcting for this factor lowers the estimated temperature to ~1150 K. This should still be regarded as a crude estimate, due to uncertainties in the emissivity vs. wavelength, and other factors relating both to the laser heating and thermal emission cooling rates. Nonetheless, the estimated temperature is not unreasonable, in the sense that it is in the range where both sublimation and thermionic emission should be slow but observable. Because the rates for these processes are so strongly temperature dependent, the temperature estimate is unlikely to be in error by more than ~100 K.

One other question is the extent to which thermal ("blackbody") photon emission contributes to the LIF signal seen under low power laser irradiation ($T_{QD} \approx 630$ K). Figure 5.7 shows blackbody emission curves for 630 K and 1150 K. It can be seen that the thermal contribution to the APD-sensitive wavelength range below 1000 nm is negligible at 630 K. The absence of thermal emission at the lower laser power was confirmed by measuring the effect of argon buffer gas pressure on the emission intensity, in the range from 1 mTorr to 30 mTorr. If thermal emission were significant, it would have been quenched at higher buffer gas pressure, because T_{QD} is considerably lower (315 K from collisional cooling). No change in intensity was observed, ruling out a contribution from significant thermal emission at low laser power.

The Nature of the Emission Process

The absorption and emission spectra for QDs in solution is dominated by exciton formation, as shown in Figure 5.6. This results in an emission band around 550nm for the QDs used. However, the emission spectra acquired at various times for the trapped QD aggregate are significantly red-shifted with two peaks: one between 590 nm and 780 nm, and the other above 850 nm. The differences between the gas phase and solution phase spectra cannot be attributed

only to some effect of electrospray ionization, because it has been shown electrosprayed QDs deposited on surfaces have optical properties similar to those of the starting material. [44] Generally, red-shifted spectra, as seen in Figure 5.6, are a result of deep level emission from surface states, most commonly seen for small QDs where a majority of atoms are found on the surface. In our case, the particle is likely an aggregate of 2 or 3 QDs, which possibly could coalesce into a single sphere when heated at high laser power. Coalescence would dramatically change the emission spectra in unknown ways because the core and the shell would mix creating an ill-characterized nanoparticle. In this context, it is interesting that the emission spectra taken before and after periods of high power laser heating are not very different, even though there was mass loss and changes in charge. This insensitivity to the details of the particle structure is consistent with emission from surface states, rather than core excitonic emission. A factor to consider is that there is a ~12% lattice mismatch between CdSe and ZnS in the bulk.[45, 46] Thus interdiffusion/mixing of the core and shell upon heating would tend to create additional defects at the core-shell interface.

Heating to "Darkness"

Figure 5.5d shows the final time period, where the particle is heated until it finally goes almost "dark". The total mass at that point is about what we would expect for a single CdSe core (290 kDa). Emission spectra were acquired in several intervals during the final heating period, and for these, the laser intensity was returned to the same low (100 W/cm^2) level used for all the other emission spectra, where thermal emission makes a negligible contribution (see above). As shown in Figure 5.6, the emission spectra taken late in the sublimation process are not radically different from those taken before significant mass loss occurred, although the intensity is significantly lower, even before the final abrupt "darkening" transition at 4836 minutes. This slow decrease in emission intensity may simply reflect a decrease in surface area of the particle, particularly if surface states are involved in the observed red-shifted emission. Note that there is

also a slow decrease in fluorescence intensity at high laser intensity, where thermal emission is expected to make a significant contribution, and surface area certainly plays a role in this case.

One question is whether the final abrupt near-total loss of emission at 4836 minutes results from the particle no longer absorbing the 532 nm laser, or if the particle continues to absorb, but with near-zero fluorescence quantum yield. If the latter explanation were true, we would still expect to see thermal emission from the hot particle -- indeed, the temperature should increase if the absorbed laser energy is no longer partly radiated as fluorescence. Therefore, we tentatively conclude that the loss of emission reflects a sudden loss of absorption, which is not unexpected. The band gap for the QD should increase with decreasing size, and at some point, the 532 nm laser would simply no longer be able to excite the particle. Because we are not averaging over a distribution of QDs, the drop in excitation rate could be abrupt. Note that as soon as the particle stops absorbing, its temperature would rapidly drop to ~300 K.

Blinking after Darkening of the Particle

During the ~80 hours preceding the final darkening transition at 4836 minutes, the particle in Figures 5.4 and 5.5 was never observed to blink, i.e., show intermittent fluorescence. However, after the final darkening transition, the small remaining signal shows significant intermittency, if it is binned in 1 or 10 second time intervals. Figure 5.8 shows a 14 hour continuation of the signal record, starting just after the abrupt darkening transition, binned in 1 second intervals. Figure 5.9 shows a histogram of the intensity levels observed, and the distributions of bright ("on") and dark ("off") time intervals. The intensity histogram is clearly bi-modal, with the major peak simply reflecting the APD dark count rate, but with a small peak at about twice the dark count level. The "On"/"Off" distributions show that there are reasonably frequent "On" intervals lasting between 1 and 20 seconds, but that the "Off" intervals are much longer, consistent with the histogram showing that the particle is dark most of the time.

It is not clear why this particle, having lost ~85% of its initial mass, and having apparently ceased to absorb the 532 nm pump laser, should show intermittent emission. One possibility is that in the nonabsorbing state, with T_{QD} = 300 K, the particle slowly absorbs or reacts with background gases, modifying the surface such that the band gap becomes small enough to allow 532 nm absorption again. At that point, the particle would heat rapidly, presumably because driving off the adsorbed surface species within seconds, increasing the band gap, causing the particle to stop absorbing again. In this scenario, the "on" times should be short, because surface species should desorb rapidly from the particle once it begins to absorb again. The "off" times should be much longer, determined by time it takes for adsorption of appropriate adventitious species from the rather clean (base pressure 10^{-8} Torr) chamber background. Such a scenario could go on indefinitely, and as shown in Figure 5.8, rather stable blinking behavior was still occurring after almost 14 hours of monitoring.

Conclusion

In conclusions, we have demonstrated that it is possible to trap single QDs and small QD aggregates in a split-ring quadrupole trap, and report the first measurements of fluorescence and thermal emission behavior of QDs in the gas phase. It is possible to detect strong fluorescence from a single QD, after brightening the QD by brief CO_2 laser heating of the ligand layer. The mass and charge of trapped particles are easily determined by secular frequency measurements, and can be tracked for long times as the particles are manipulated by heating, exposure to charge changing collisions. Obviously, other manipulations, such as exposure to reactive gases to carry out surface chemical modification, are possible. The emission spectra of a single QD aggregate showed a significant red shift from would be expected from solution phase measurements. More studies are needed to understand the mechanism of fluorescence, the QD going dark, and blinking. We are confident that NPMS is a suitable and powerful tool to uncover these mechanisms.

Acknowledgements

We would like to thank D. Gerlich of TU Chemnitz, M. Bartl and J. Gerton from the University of Utah, and J. Hollingsworth of Los Alamos National Labs for helpful discussions. The work was supported by the Chemistry Division of the U.S. National Science Foundation, under grant CHE- 1111935.

References

1. D. M. Bell, C. R. Howder, D. Gerlich, D. K. Lewis and S. L. Anderson, Analytical Chemistry **(submitted)** (2013).

2. S. Schlemmer, J. Illemann, S. Wellert and D. Gerlich, AIP Conf. Proc. **457**, 80 (1999).

3. S. Schlemmer, J. Illemann, S. Wellert and D. Gerlich, Journal of Applied Physics **90**, 5410 (2001).

4. M. Grimm, B. Langer, S. Schlemmer, T. Lischke, U. Becker, W. Widdra, D. Gerlich, R. Flesch and E. Ruehl, Phys. Rev. Lett. **96**, 066801 (2006).

5. A. J. Trevitt, P. J. Wearne and E. J. Bieske, International Journal of Mass Spectrometry **262**, 241 (2007).

6. Y. Cai, W. P. Peng, S. J. Kuo, Y. T. Lee and H. C. Chang, Anal. Chem. **74**, 232 (2002).

7. Y. Cai, W. P. Peng, S. J. Kuo, S. Sabu, C. C. Han and H. C. Chang, Anal. Chem. **74**, 4434 (2002).

8. W. P. Peng, Y. Cai, Y. T. Lee and H. C. Chang, Int. J. Mass Spectrom. **229**, 67 (2003).

9. W.-P. Peng, Y.-C. Yang, M.-W. Kang, Y. T. Lee and H.-C. Chang, J. Am. Chem. Soc. **126**, 11766 (2004).

10. P. H. Dawson, *Quadrupole Mass Spectrometry*. (Elsevier Scientific Pub., Amsterdam, 1976).

11. S. F. Wuister, I. Swart, F. van Driel, S. G. Hickey and C. d. M. Donega, Nano Lett. **3**, 503 (2003).

12. C. D. M. Donegá, S. G. Hickey, S. F. Wuister, D. Vanmaeckelbergh and A. Meijerink, J. Phys. Chem. B **107**, 489 (2003).

13. M. Shim, C. Wang and P. G. Sionnest, J. Phys. Chem. B **105**, 2369 (2001).

14. C. Wang, B. L. Wehrenberg, C. Y. Woo and P. Guyot-Sionnest, J. Phys. Chem. B **108**, 9027 (2004).

15. P. Guyot-Sionnest, Microchim Acta **160**, 309 (2008).

16. P. P. Jha and P. Guyot-Sionnest, J. Phys. Chem. C **114**, 21138 (2010).

17. W. Qin, R. A. Shah and P. Guyot-Sionnest, ACS Nano **6**, 912 (2012).

18. C. Galland, T. Ghosh, A. Steinbruck, M. Sykora, J. A. Hollingsworth, V. I. Klimov and H. Htoon, Nature **479**, 203 (2011).

19. Z. Ding, B. M. Quinn, S. K. Haram, L. E. Pell, B. A. Korgel and A. J. Bard, Science **296**, 1293 (2002).

20. N. Myung, Z. Ding and A. J. Bard, Nano Letters **2**, 1315 (2002).

21. V. Lesnyak, N. Gaponik and A. Eychmuller, Chem. Soc. Rev. **42**, 2905 (2013).

22. J. Y. Kim, O. Voznyy, D. Zhitomirsky and E. H. Sargent, Advanced Materials **25**, 4986 (2013).

23. S. B. Brichkin and E. V. Chernykh, High Energy Chemistry **45**, 1 (2011).

24. A. Kongkanand, K. Tvrdy, K. Takechi, M. Kuno and P. V. Kamat, Journal of the American Chemical Society **130**, 4007 (2008).

25. K. Turdy, P. A. Frantsuzov and P. V. Kamat, Proceedings of the National Academy of Sciences **108**, 29 (2011).

26. E. H. Sargent, Nature Photonics **6**, 133 (2012).

27. W. Xiong, D. D. Hickstein, K. J. Schnitzenbaumer, J. L. Ellis, B. B. Palm, K. E. Keister, C. Ding, L. Miaja-Avila, G. Dukovic, J. L. Jimenez, M. M. Murnane and H. C. Kapteyn, Nano Lett. **13**, 2924 (2013).

28. D. Gerlich and S. Decker, Applied Physics B: Lasers and Optics **Published online Oct 24** (2013).

29. D. Gerlich, in *Advances in Chemical Physics: State-Selected and State-To-State Ion-Molecule Reaction Dynamics, Part 1*, edited by C. Y. Ng and M. Baer (J. Wiley & Sons, 1992), Vol. 82, pp. 1-176.

30. in *II-VI and I-VII Compounds; Semimagnetic Compounds*, edited by O. Madelung, U. Rössler and M. Schulz (Springer Berlin Heidelberg, 1999), Vol. 41B, pp. 1-7.

31. S. Decker, Tech. Univ. Chemnitz, 2010.

32. Y. Zhang, A. M. Schnoes and A. R. Clapp, Appl. Mater. Interfaces **2**, 3384 (2010).

33. C. R. Howder, D. M. Bell and S. L. Anderson, Rev. Sci. Instrum. **(Submitted)** (2013).

34. D. Gerlich, Hyperfine Interact. **146/147**, 293 (2003).

35. B. Goris, M. A. Van Huis, S. Bals, H. W. Zandbergen, L. Manna and G. Van Tendeloo, Small **8**, 937 (2012).

36. K. Hansen, *Statistical Physics of Nanoparticles in the Gas Phase*. (Spring Science+Buisness Media, Dordrecht, 2013).

37. W. Watt, R. Moreton and L. G. Carpenter, Surf. Sci. **45**, 238 (1974).

38. P. Roura and J. Costa, Eur. J. Phys. **23**, 191 (2002).

39. L. Landstrom, K. Elihn, M. Boman, C. G. Granqvist and P. Heszler, Appl. Phys. A **81**, 827 (2005).

40. S.-J. Yu, S. J. Youn and H. Kim, Physica B **405**, 638 (2010).

41. H. Odashima, M. Tachikawa and K. Takehiro, Phys. Rev. A **80**, 41806 (2009).

42. *Gas Phase Nanoparticle Synthesis*. (Kluwer Academic Publishers, Dordrecht, 2004).

43. L. v. Szentpaly, J. Phys. Chem. A **112**, 12695 (2008).

44. L. F. Pease, III, J. I. Feldblyum, S. H. D. Lacaerda, Y. Liu, A. R. H. Walker, R. Anumolu, P. B. Yim, M. L. Clarke, H. G. Kang and J. Hwang, ACS Nano **4**, 6982 (2010).

45. B. O. Dabbousi, J. Rodriguez-Viejo, F. V. Mikulec, J. R. Heine, H. Mattoussi, R. Ober, K. F. Jensen and M. G. Bawendi, J. Phys. Chem. B **101**, 9463 (1997).

46. A. M. Smith and S. Nie, Acc. Chem. Res. **43**, 190 (2010).

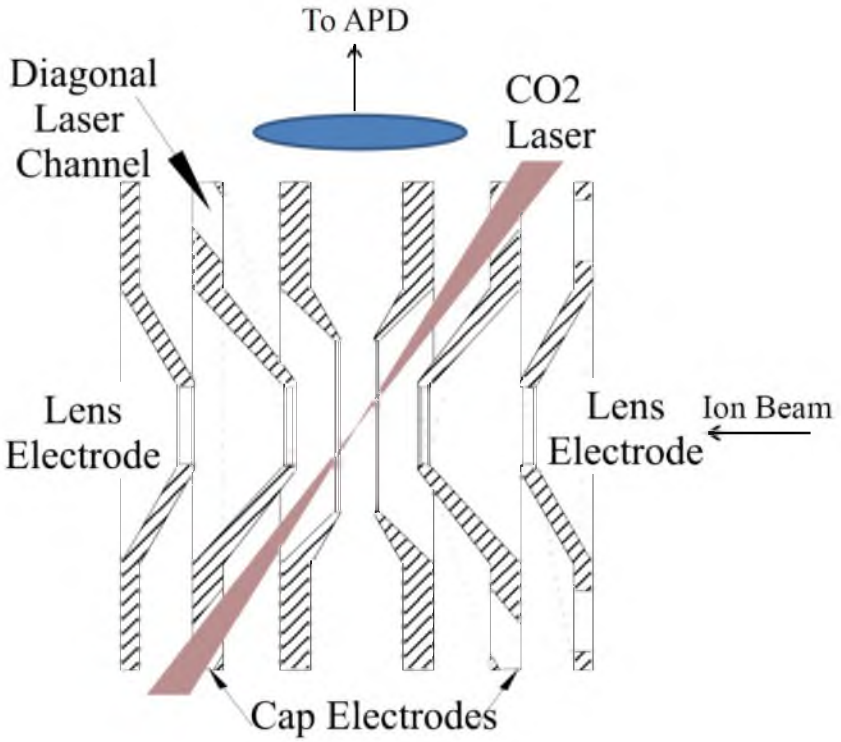

Figure 5.1: A cross-sectional view of the trap along the x-axis. Light is collected on the vertical axis and the 532 nm laser is introduced into the plane of the image in the center of the trap. Diagonal channels are used to introduce the CO_2 laser. The horizontal axis is used to introduce the ions to the trap.

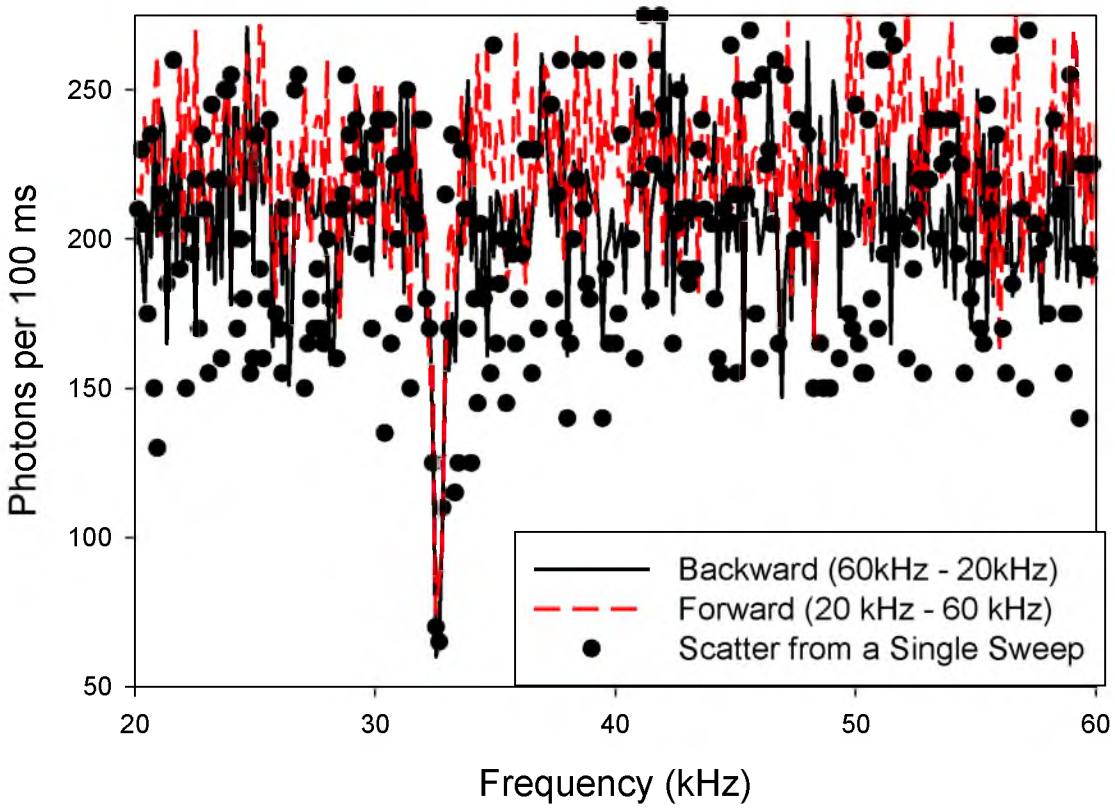

Figure 5.2: Sweeps across the secular frequency resonance for a single particle in the trap. The solid black line corresponds to an average of 5 sweeps from 60 kHz to 20 kHz. The dashed red line corresponds to an average of 5 sweeps from 20 kHz to 60 kHz. The scatter plot shows a noise in a single sweep.

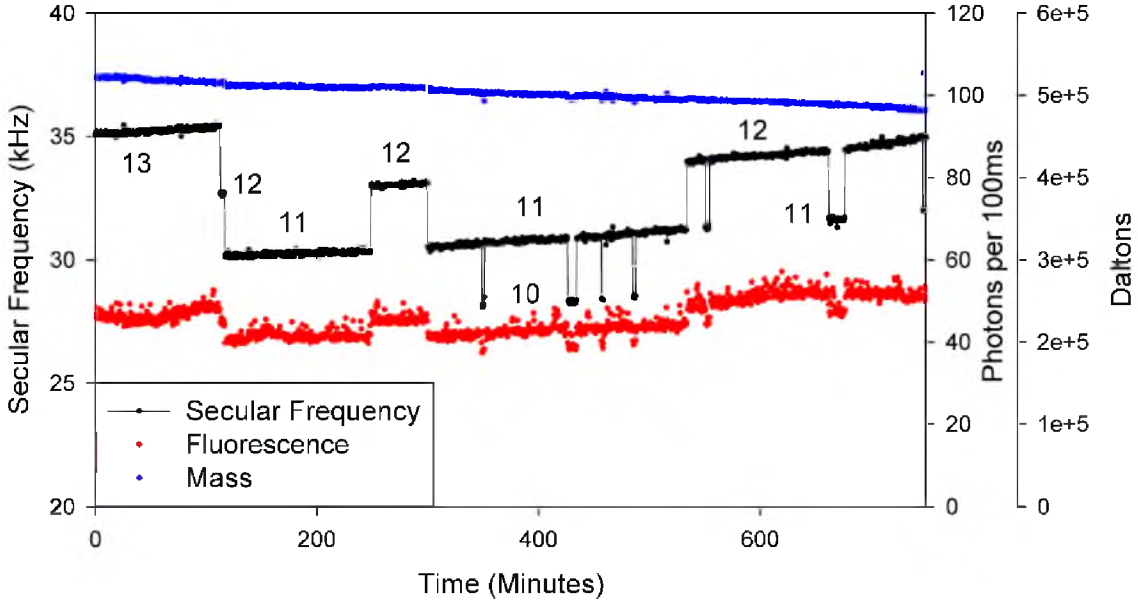

Figure 5.3: 12.5 hour time record for a single trapped quantum dot, showing variations in secular frequency (kHz - black), mass (Da - blue), and fluorescence intensity (photons per 100ms - red). The number of charges present are shown.

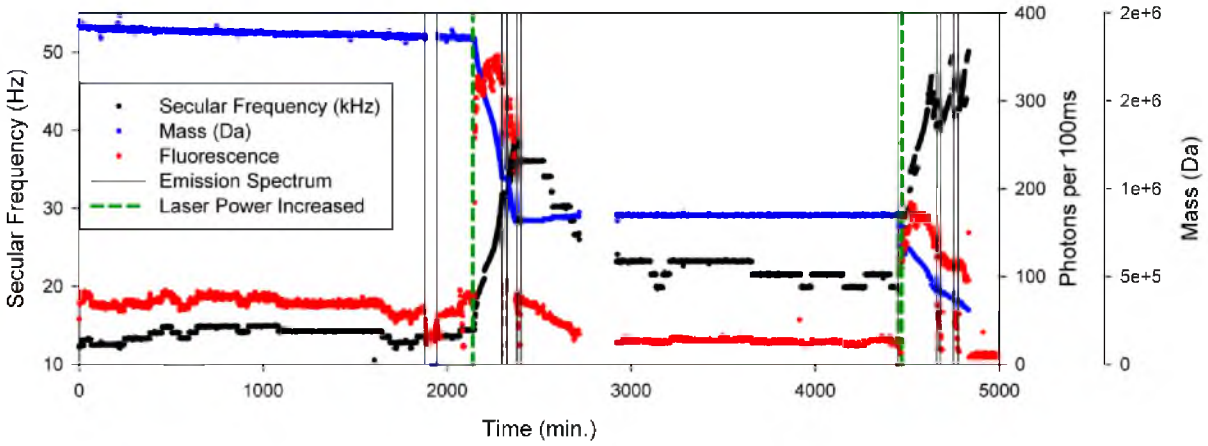

Figure 5.4: Time record of secular frequency (kHz - black), mass (Da - blue) and fluorescence intensity (photons per 100 ms - red) for a single small quantum dot aggregate, observed for four days. Pairs of vertical black lines indicate intervals when emission spectra were taken. The laser power density was 100 W/cm^2 except between 2100 and 2370 minutes and 4470 and 5000 minutes, when it was increased to 216 W/cm^2 to increase the particle temperature. The laser power density was turned down to 100 W/cm^2 when an emission spectrum was taken.

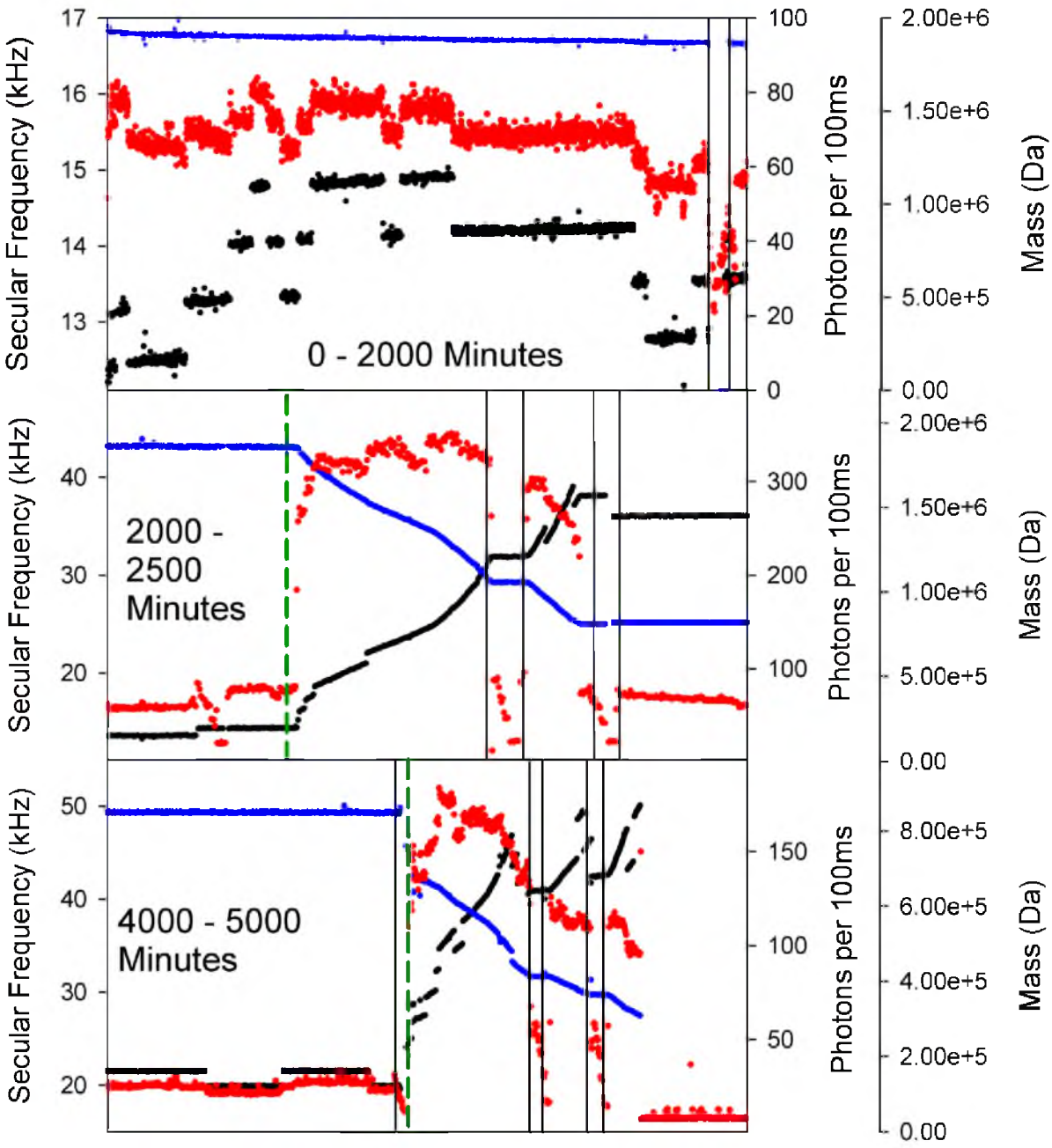

Figure 5.5: Detailed time records with expanded vertical scales, for the particle in Figure 5.4, in the indicated time ranges

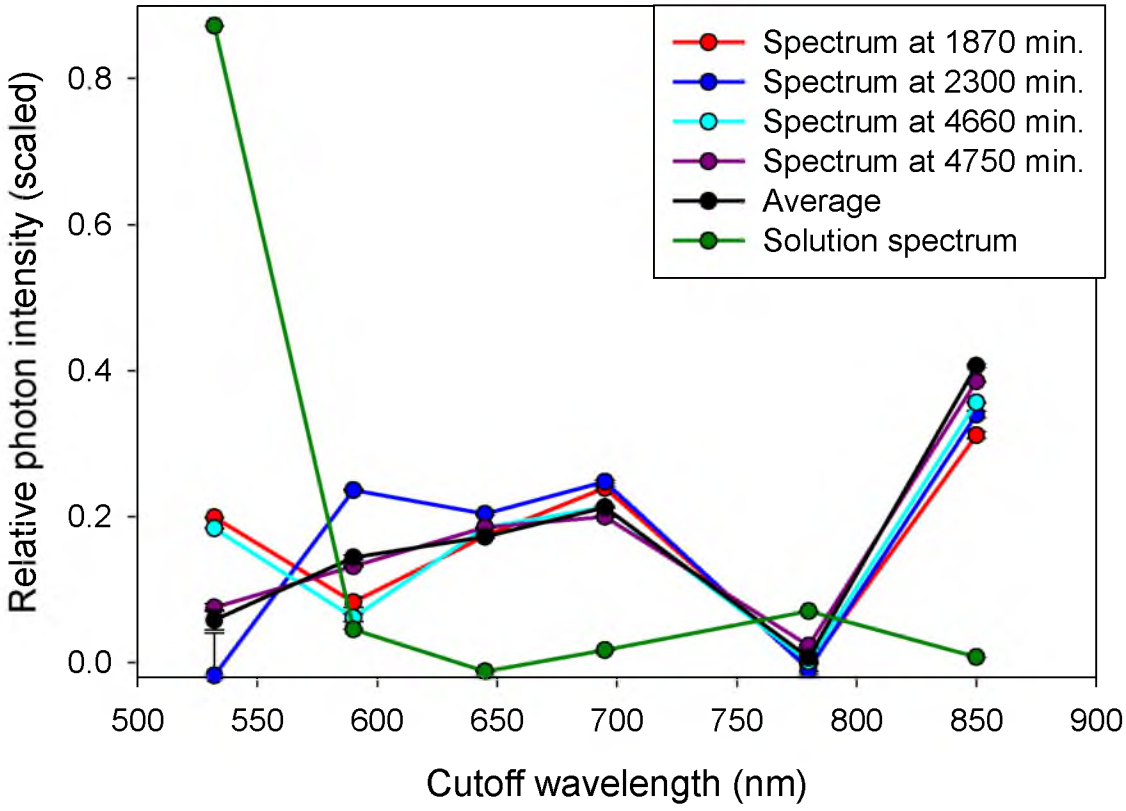

Figure 5.6: Emission spectra taken at the indicated times in Figures 5.4 and 5.5. An average of the spectra is shown with error bars denoting the standard deviation of the 4 measurements. A solution phase emission spectra was also obtained using the same optical arrangement, for comparison (dashed line).

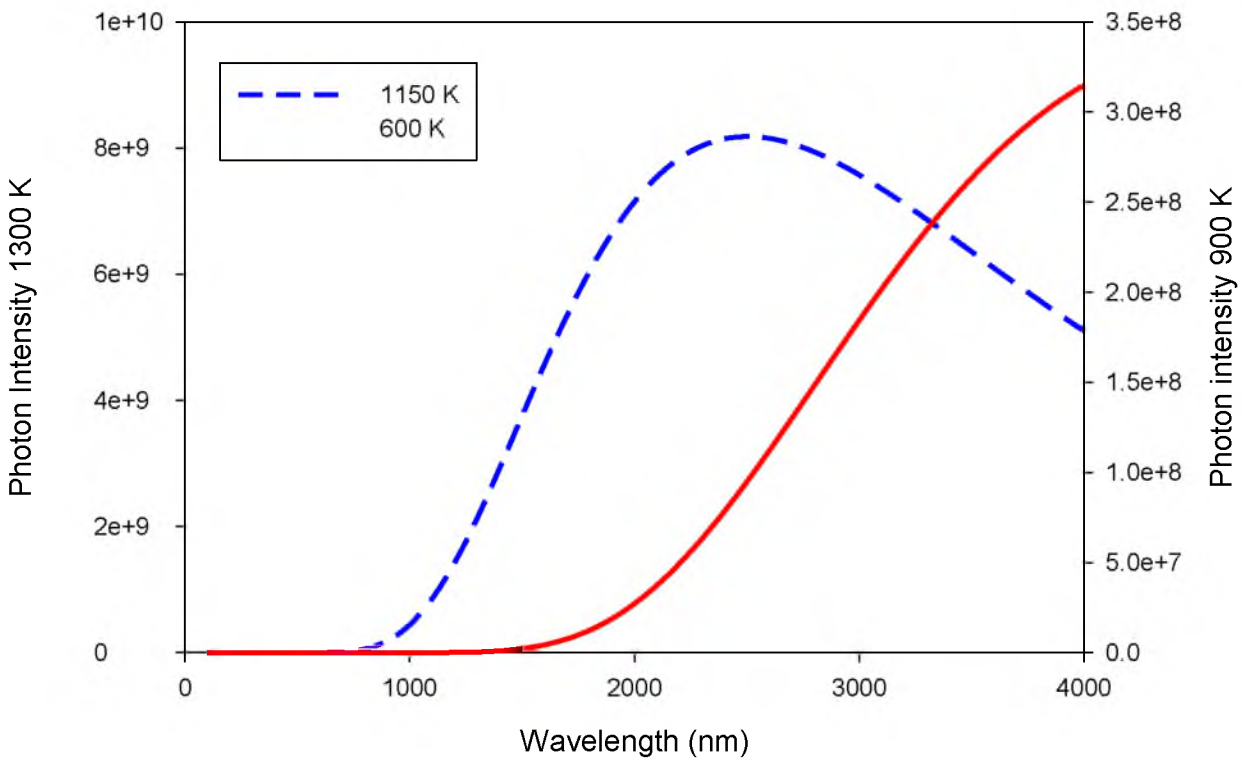

Figure 5.7: Black body emission curves for 1300 K (dashed blue line) and 600 K (solid red line).

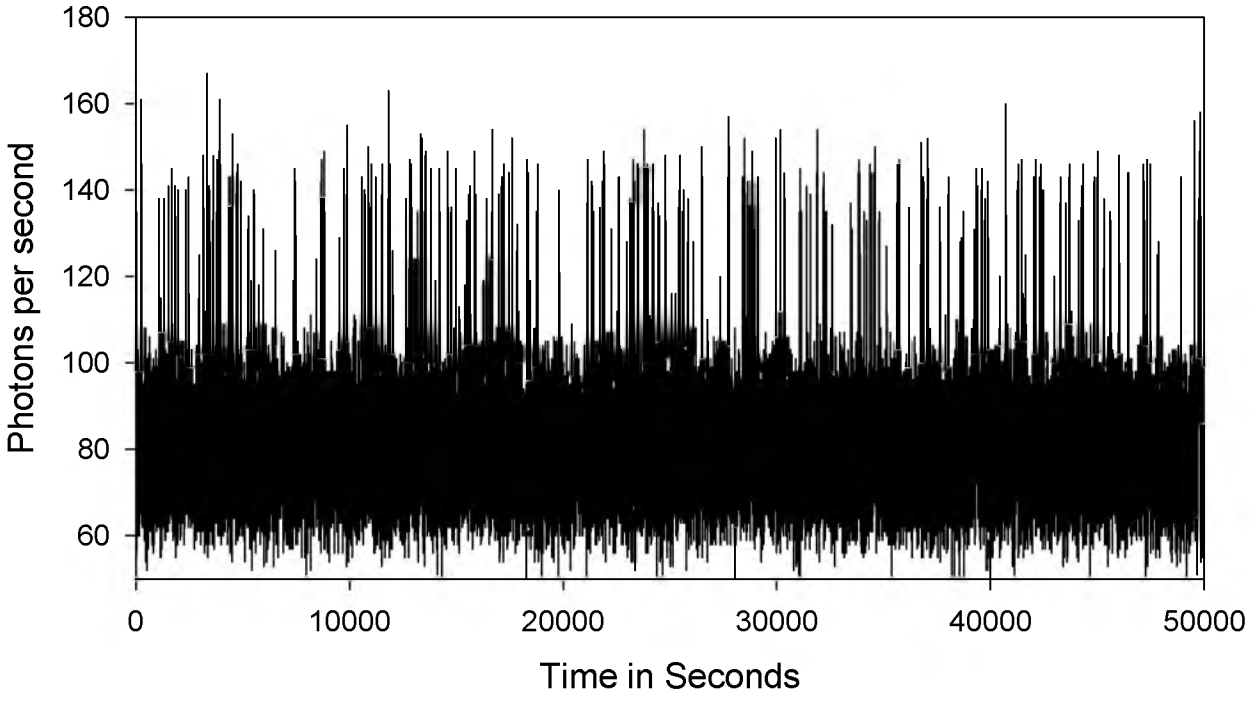

Figure 5.8: The time record for the first 50000 seconds after the QD from Figure 5.4 and 5.5 went "dark".

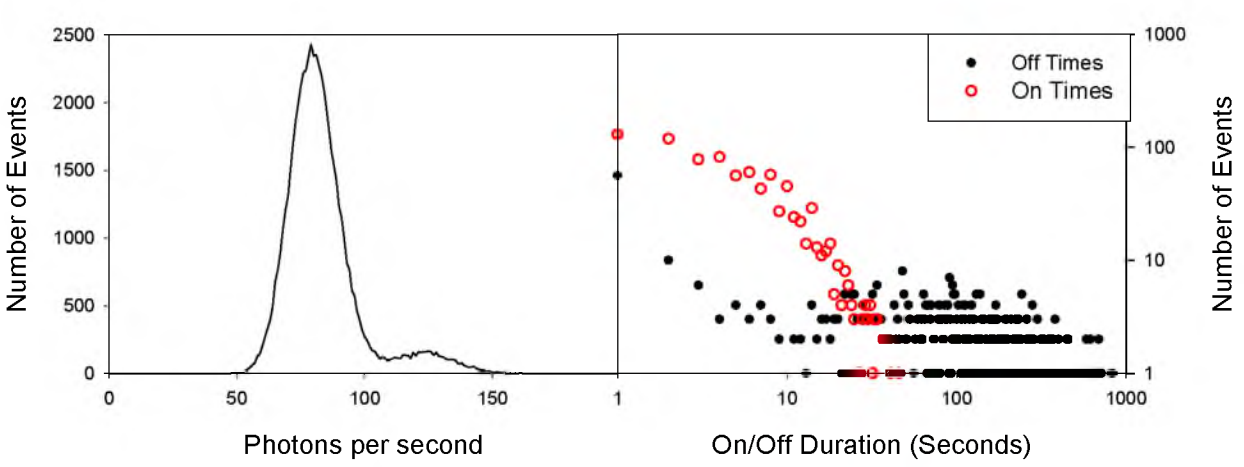

Figure 5.9: A statistical view on the blinking exhibited by a single QD. Left: A histogram of brightness levels observed in Figure 5.8. Right: The duration distributions of "On" (open red circles) and "Off" times (black filled circles) in the time record in Figure 5.8. The On/Off cutoff was chosen as 107 photons per second.

CHAPTER 6

CONCLUSION: THE FUTURE OF NANOPARTICLE MASS SPECTROMETRY

Development of a nanoparticle mass spectrometer (NPMS) has been shown for systems of large polystyrene particles and core-shell CdSe/ZnS quantum dots (QDs). Precision in the measurement of ω_z approached 1 ppm for a large polystyrene particle, which is an order of magnitude better than previous measurements. Fluorescence from QDs was activated by the presence of a CO_2 laser. The ability to trap a single QD was demonstrated. For a single QD the number of charges, mass, and fluorescence intensity was tracked as a function of time. Heating a single aggregate QD resulted in over 85% mass loss, after which the fluorescence dropped significantly and the QD began to blink.

The activation of QDs with the CO_2 laser needs to be studied further to have a better understanding of what is occurring. It would be ideal to study this process by trapping a pre-activated QD with a QD that is already bright. By this process, it could be possible to track how the ω_z of the dark particle changes when exposed to the CO_2 laser. The ideal situation would be to observe charge steps before activation to obtain the absolute mass and charge of the pre-brightened QD, and perform the same measurements after the QD is activated. This could show if evaporation of the ligand layer is occurring. We have begun preliminary studies to trap a dark particle with a bright particle and have demonstrated it is possible to trap a dark QD with a bright one and obtained the ω_z of both particles. It is exciting that this is a possible use of NPMS and more studies are needed to determine the resolution and usefulness of this method.

Another option that would be interesting to investigate, as mentioned in Chapter 2, would be to build nanostructures in the trap to investigate energy transfer between different types of QDs. This could be achieved by trapping a positively charged QD and then introducing a negatively charged QD. The two particles will be attracted to each other and form a dimer. In principle, any number of particles could be built in such a fashion. Overall, the future is very bright for NPMS and there are many interesting experiments that need to be completed to further understand QDs in the gas phase.

CHAPTER 7

INTRODUCTION TO VIBRATIONALLY STATE-SELECTED ION-MOLECULE REACTIONS WITH HOD^+

Introduction

Reaction dynamics studies how reactions take place and what controls reactivity on a very basic and fundamental level.[1] It is a daunting task to understand how a chemical reaction takes place as there are many variables and steps involved in a single reaction. Understanding a chemical reaction encompasses initial approach of the reactants, the reaction coordinate, scattering dynamics, and the deposition of energy in the products. Increasing the number of atoms present in a reaction also in turn increases the complexity in modeling a reaction and understanding the flow of energy. By using small model systems, it is possible to control more variables and model what is occurring in a timely manner. For this reason, HOD^+ provides an ideal ion with which to investigate simple H^+ and D^+ transfer reactions.

Although it is impossible to observe a single gas phase collision, it is possible, by using a large sample size, to build a statistically meaningful sample to understand how a reaction proceeds. Building a statistical sample requires an instrument with a high throughput and reproducibility. Ion guiding makes it possible to guide ions with high efficiency and very easily control their translational energy. Use of a tandem mass spectrometer accomplishes these ideals and couples ion guiding with mass selection of both the reactant and product ions. Laser ionization affords vibrational state-selection of the reactant ion by utilizing resonance enhanced multi-photon ionization (REMPI).[2-4] Thus, it is possible to create an energy-, mass-, vibrational state-selected reactant ion beam with which to study ion – molecule reactions.

In the work presented here, energy-, mass-, vibrational state-selected ions are guided to a scattering cell where the neutral reactant resides. The product and remaining reactant ions are guided through a time-of-flight region to allow separation and obtain product recoil velocity distribution. The final mass spectrometer cycles through the reactant beam and the product ions to determine the reactivity. Our detector collects the arrival times of the product ions to obtain product velocity distributions of each species separately. Coupling this method as a function of the reactant vibrational state allows for a fascinating view of a chemical reaction.

The purpose of using vibrationally state-selected ions is to investigate whether or not a reaction is under dynamical or statistical control.[5] Dynamical control relates to the dynamics of how the reactants are prepared with respect to one another, while reactions that are under statistical control are controlled by the amount of energy and angular momentum present in the collision environment. Vibrational state-selection of the reactant ion probes the initial interaction of the reactants. Once a bond is formed between the reactants, the vibrational energy becomes randomized throughout the system. As a result, the only impact the vibrational state should have as the products separate is in the additional energy present in the system.

Coupling the experimental results with ab initio calculations provides even further depth into what is occurring on the single collision level. Ab initio calculations make it possible to calculate the lowest energy pathway from the reactants to the products, known as the reaction coordinate. The use of a reaction coordinate lies in its ability to explain the processes necessary for a reaction to take place and a way to visualize how a reaction occurs. Typically, an ion – molecule reaction coordinate has an attractive potential on the initial approach due to the ion – induced dipole and in some cases, ion – dipole forces. The reaction coordinate consists of reactant-like and product-like complexes and transition states coupling the change from a reactant-like species to a product-like one. The practical use of the reaction coordinate is to determine if the reaction is governed by a statistical mechanism or if any bottlenecks exist along the reaction coordinate.

The recoil velocity distributions of the products give similar insight to the reaction by probing the lifetime of the collision complex. A long-lived lifetime, longer than the rotational period of the complex, is indicative of reaction that is complex mediated and could be complex mediated. While a collision with a short lifetime, shorter than the rotational period of the complex, is evidence that the reaction is direct. A direct reaction indicates there is not sufficient time for energy to be randomized throughout the collision environment nor for the products to fall apart in a statistical manner.

Here, HOD^+ is used to investigate a number of reactions where endoergic H^+ and D^+ transfer occurs. HOD^+ is an interesting molecule to use because of the wealth of information available in reactions of vibrationally excited neutral HOD. Neutral vibrationally excited HOD has been used to study reactions by a Zare and Crimm, most notably with H atoms.[6-15] The reaction of HOD + H → OH + HD or OD + H_2 has a barrier of 0.93eV and is endoergic by 0.65eV. To overcome the barrier to reactivity, two methods were employed by the Zare group and the Crim group to investigate this reaction. The Zare group utilized translationally hot H atoms, generated by photolysis of HI, with an energy of 1.6 eV.[13] By exciting HOD with 1 quanta of the OH stretch, the reaction favored H_2 formation (H transfer) over HD formation (D transfer) 25:1.[13] Conversely, exciting 1 quanta of the OD stretch of HOD, the reaction preferred HD formation (D transfer) over H_2 formation 5.8:1. Crim, on the other hand, utilized highly excited HOD to investigate this reaction, with either 5 quanta of the OD stretch or 4 quanta of the OH stretch.[6] These vibrational states are energetically similar and both in excess of the endoergicity of the reaction. In this case, the selectivity is magnified and the reaction nearly exclusively occurs by breaking the excited OH or OD bond. The bend vibration, on the other hand, was never investigated with the fundamental mode, but rather only through combination bands, and no enhancement was observed because of the bend vibration.[15]

There is a major difference between the aforementioned reaction and endoergic H^+ or D^+ transfer in an ion molecule reaction. That difference is the shape of the reaction coordinate. In the neutral-neutral reaction, there is a barrier between the reactants and products, while in an ion-molecule reaction the reactants are stabilized by ion-induced dipole interactions, creating a potential well between the reactants and products. The difference in the shape of the potentials could impact the magnitude of the enhancement due to reactant vibration. Also, the reactions presented herein investigate the true impact of the bend vibration without combination of either stretch, with unexpected results.

Here, reactions of HOD^+ with CO_2 (Chapter 8), N_2 (Chapter 9), CO (Chapter 10), and N_2O (Chapter 11) are presented. Each reaction exhibits endoergic H^+ and D^+ transfer, which are the dominant processes for most of these reactions, with exception of N_2O at high energies.

References

1. R. D. Levine, *Molecular Reaction Dynamics*. (Cambridge U. Pr., Cambridge, 2005).
2. S. Mark, T. Glenewinkel-Meyer and D. Gerlich, Int. Rev. Phys. Chem. **15**, 283 (1996).
3. S. L. Anderson, D. M. Rider and R. N. Zare, Chem. Phys. Lett. **93**, 11 (1982).
4. R. N. Zare, Science **279**, 1875 (1998).
5. J. Liu, K. Song, W. L. Hase and S. L. Anderson, J. Am. Chem. Soc. **126**, 8602 (2004).
6. A. Sinha, M. C. Hsiao and F. F. Crim, J. Chem. Phys. **92**, 6333 (1990).
7. M. C. Hsiao, A. Sinha and F. F. Crim, J. Phys. Chem. **95**, 8263 (1991).
8. A. Sinha, M. C. Hsiao and F. F. Crim, J. Chem. Phys. **94**, 4928 (1991).
9. F. F. Crim, A. Sinha, M. C. Hsiao and J. D. Thoemke, Jerusalem Symp. Quantum Chem. **25**, 217 (1991).
10. A. Sinha, J. D. Thoemke and F. F. Crim, J. Chem. Phys. **96**, 372 (1992).
11. R. B. Metz, J. D. Thoemke, J. M. Pfeiffer and F. F. Crim, J. Chem. Phys. **99**, 1744 (1993).
12. J. D. Thoemke, J. M. Pfeiffer, R. B. Metz and F. F. Crim, J. Phys. Chem. **99**, 13748 (1995).
13. M. J. Bronikowski, W. R. Simpson, B. Girard and R. N. Zare, J. Chem. Phys. **95**, 8647 (1991).
14. D. E. Adelman, S. V. Filseth and R. N. Zare, J. Chem. Phys. **98** (6), 4636 (1993).
15. M. J. Bronikowski, W. R. Simpson and R. N. Zare, J. Phys. Chem. **97**, 2204 (1993).

CHAPTER 8

H^+ VS. D^+ TRANSFER FROM HOD^+ TO CO_2: BOND-SELECTIVE CHEMISTRY AND THE ANOMALOUS EFFECT OF BENDING EXCITATION

Reprinted with permission from David M. Bell, Jason M. Boyle, Scott L. Anderson, and Journal of Chemical Physics **134,** 064312. Copyright 2011, American Institute of Physics

Overview

Reactions of HOD^+ with CO_2 have been studied for HOD^+ in its ground state, and with one quantum of excitation in each of its vibrational modes: (001) - predominately OH stretch, 0.396 eV, (010) - bend, 0.153 eV, and (100) - predominately OD stretch, 0.293eV. Integral cross sections and product recoil velocities were recorded for collision energies from threshold to 3 eV. The cross sections for both H^+ and D^+ transfer rise with increasing collision energy from threshold to ~1 eV, then become weakly dependent of collision energy. All three vibrational modes enhance the total reactivity, but quite mode-specifically. The H^+ transfer reaction is enhanced by OH stretch excitation, whereas OD stretch excitation has little effect. Conversely, the D^+ transfer reaction is enhanced by OD stretch excitation, while the OH stretch has little effect. Excitation of the bend strongly enhances both channels.

The effects of the stretch excitations are consistent with previous studies of neutral HOD mode-selective chemistry, and can be at least qualitatively understood in terms of a late barrier to product formation. The fact that bend excitation produces the largest overall enhancement is surprising, because this is the lowest energy excitation, and is not obviously connected with the reaction coordinates for either H^+ or D^+ transfer. A rationalization in terms of the effects of water distortion on the potential surface is proposed.

Introduction

The water cation is important in chemistry of the upper atmosphere[1-3] and in comet tails.[4-7] Previous studies of reactions of HOD, H_2O, or D_2O with H or Cl atoms have also shown that this is an interesting reactant molecule to test ideas about mode/bond-selective chemistry.[8-15] For example, Zare and co-workers studied reaction of fast H atoms with HOD, which is endoergic by ~0.65 eV, with a 0.93 eV barrier. In this case, the H atom translational energy was well in excess of the barrier height; nonetheless, it was found that excitation of the (001) state (predominantly OH stretch) led to a 25 : 1 ratio of H vs. D transfer, while excitation of the (100) state

(predominately OD stretch) resulted in a 1 : 5.8 ratio favoring D transfer.[8] Crim and co-workers examined the same reaction at thermal collision energies, with the energy needed to drive reaction coming mostly from excitation of HOD into either the OH stretch (004) or OD stretch (500) overtones, which are similar in energy. Reaction occurred almost entirely by transferring the H or D atom involved in the excited bond.[11-13]

In the neutral water experiments, it was not possible to excite pure bending vibrations, but bend effects were investigated through stretch-bend combination excitations. For example, Zare and co-workers examined the effect of bend excitation in the reaction of D_2O + H, by comparing the effects of exciting the (011) state (bend in combination with asymmetric stretch) with those from asymmetric stretch excitation alone (001). They found that the additional energy from the bend excitation had no effect,[9] presumably because the bend motion is uncoupled to the H transfer reaction coordinate. Similarly, Crim and co-workers studied the effects of overtone combination excitations on the reaction of H_2O with H and Cl.[13, 15] The (003) (asym. str.) and (022) (bend and asym. str.) overtone states are similar in energy. For reaction with both H and Cl, the (003) excitation results in 3 - 4 times greater reactivity than the (022) excitation, suggesting that bend excitation is significantly less effective than asymmetric stretch excitation. On the other hand, in reaction with Cl, the (004) and (023) states, which are also nearly isoenergetic, have similar reactivity, suggesting a comparable effect of bend and asymmetric stretch excitation, at least for these very high levels of water vibrational excitation.

Using REMPI, it is possible to selectively, and independently, populate the fundamental level of any of the three vibrational modes of HOD^+,[16] allowing us to examine the effects of mode- and bond-specific excitation on ion-molecule reactions of water over a wide range of collision energy. A major difference between neutral and ion reactions is that for ions, charge delocalization leads to considerable stabilization of the region of the potential energy surface where the reactants are close together. As a consequence, ion reactions tend not to have barriers in excess of the endoergicity. In this paper, we report a guided ion beam study of the reaction of

mode-selectively excited HOD^+ with CO_2. The endoergic H^+ and D^+ transfer reactions are analogous to the H/D transfer reactions observed in the neutral studies mentioned above, and because the energy rises only as the products begin to separate, it is similar to a neutral reaction with a late barrier, like HOD + H. A major difference is that there is also a potential energy well corresponding to hydrogen-bonded reactants, which may have a significant effect on the dynamics.

This reaction has been studied in Selected Ion Flow Tubes (SIFT) under thermal conditions by Karpas *et al.*[17] and Shul *et al.*[18]. Karpas *et al.* observed no reaction, which is reasonable given that both H^+ and D^+ transfer are endoergic. Shul *et al.* observed association to form $CO_2(H_2O)^+$, which is also reasonable, given the collisional stabilization possible in the SIFT. H^+ transfer is observed at thermal energies in ICR, due to the presence of vibrationally hot H_2O^+, and this reaction used to monitor radiative decay.[19] We are unaware of any previous beam studies.

Experimental and Computational Methods

The guided ion beam tandem mass spectrometer used in this study has been described previously, along with experimental and analysis protocols.[20, 21] Helium is bubbled through a 50/50 mixture of H_2O and D_2O to generate 96% He with 4% water, half of which is HOD. HOD^+ can be generated in selected vibrational states by REMPI through the **C** ($^1B_1$) state.[16]. In this study, HOD^+ was generated in the following states: (000), (001) - predominately OH stretch, 0.396 eV, (010) - bend, 0.153 eV, and (100) - predominately OD stretch, 0.293eV. The state selection purity is near 100% for the OH and OD stretch modes, but only ~56% for the bend, with the remaining 44% in produced in the ground state, as determined by photoelectron spectroscopy.[16] Because we also measure cross sections for the ground state reaction, the bend cross sections can be corrected, and this has been done for all the results reported below.

Ionization occurred between a pair of planar electrodes, and the resulting ions were injected into a quadrupole ion guide, which focused them into a quadrupole mass filter to remove any fragment ions or H_2O^+/D_2O^+ ions produced in the REMPI process. A time-of-flight (TOF) gating electrode pair at the end of this quadrupole mass filter was used to narrow the ion beam kinetic energy spread, which was ~0.2 eV. The mass-, state-, and kinetic energy-selected primary ions were injected into a system of 8-pole ion guides,[22] the first of which guided the ions through a 10 cm long scattering cell containing CO_2 (Matheson, 99%) at 1 x 10^{-4} Torr. Unreacted HOD^+ ions, together with product ions, were collected by the guide and passed into the second, longer guide section for TOF velocity analysis, before being mass analyzed and detected. Products that were backward-scattered in the laboratory frame were reflected at the entrance of the guide system, and detected at long times, corresponding to apparent low velocities. Ions were counted using a P7882 FAST ComTec multichannel scalar, controlled by a LabView program that cycled through collision energies and masses of interest, and switched the target gas flow between the scattering cell and chamber background. Integral cross sections were calculated from the ratio of reactant and product ion intensities, corrected for ions formed outside the scattering cell, using the calibrated effective length of the scattering cell and the pressure was measured with a capacitance manometer.

TOF was used both to measure the energy of the reactant ion beam, as well as the axial projection of the recoil velocity distribution of the products (v_{axial}). Several complete sets of cross sections for both product channels were measured for all reactant states of HOD^+ as a function of collision energy, taking several days each. To avoid systematic errors comparing reactions of different vibrational states, the ground state cross sections were collected every day as a check on possible changes in instrument conditions. All measurements of the ground state cross sections were within 10% of the average of the set, and therefore, all data sets were retained and averaged to generate the data presented below. The standard deviation of cross section values over the set of runs is ~20%, and is indicated by error bars in the figures. Note, however, that the run-to-run

variations include effects of systematic errors, such as changes in relative detection efficiency for CO_2H^+ and CO_2D^+ relative to HOD^+, or pressure measurement errors. This type of error affects both CO_2H^+ and CO_2D^+ identically, and thus does not influence the relative cross sections for the two channels, thus we estimate that the relative error is about half what is indicated by the error bars. To some extent, the same is true in comparing cross sections for different reactant states, although in some cases, these were split across multiday data sets, and thus subject to the systematic issues mentioned above. Therefore, we conservatively give the uncertainty in comparing results for different vibrational states as 20%. This is also our best estimate for the uncertainty in the absolute magnitude of the cross sections.

To map out the reaction coordinate, electronic structure calculations were performed at several levels of theory using GAUSSIAN03.[23] Geometries were optimized by calculating force constants at every step. For the reactants, complexes, and product species, we also calculated the structure and energies at the G3 level of theory. Because the PBE1PBE/6-311++G** level of theory was found to be in reasonable agreement with experiment and with the G3 calculations, we used this method in mapping out regions of the potential surface of interest for interpreting the dynamics.

Results

Computational Results

The reaction coordinate in this system is shown in the inset to Figure 8.1, and the computed energetics are summarized in Table 8.1. The energies shown in the figure are experimental for the reactants and products,[24] and the energy of the complex is from a G3 calculation, referenced to G3 calculations for the reactants. The complex has H_2O^+ hydrogen bonded to O of CO_2, with an OCO-H bond distance of 1.37 Å and COH bond angle of 149.5°. Note that the water moiety in the complex has HOH bond angle of 110.7°, and the length of the OH bond involved in the hydrogen bond is 1.08 Å. These values can be compared to the bond

angle (109.9°) and OH bond length (1.00 Å) in free H_2O^+, calculated at the same level of theory. In the CO_2H^+ product, the OCO-H distance is 0.98 Å, and the COH angle is 120.4°. Because no significant rearrangement is needed to form this complex from reactants, a barrier to complex formation is not expected. Similarly, we would not expect a barrier separating the complex from products, in excess of the endoergicity. These expectations are confirmed by potential energy scans discussed below.

Integral Cross Sections

Product ions were observed at masses 47 and 48, corresponding to CO_2H^+ and CO_2D^+, and the integral cross sections for both channels from reaction of ground state HOD^+ are given in Figure 8.1 over a center-of-mass (CM) collision energy (E_{col}) range from 0.25 to 2.87 eV. The reactions are:

$HOD^+ + CO_2$	$\rightarrow OCOH^+ + OD$	(H^+ transfer)	$\Delta_rH = 0.548$ eV
	$\rightarrow OCOD^+ + OH$	(D^+ transfer)	$\Delta_rH = 0.561$ eV

where the energetics for H^+ transfer are experimental[24] corrected to 0 K, and the D^+ transfer value is derived from the 0 K H^+ transfer enthalpy using zero point energies calculated at the B3LYP/6-311G(df,p) level, scaled by 1.0167.[25]

Given the E_{col} distribution resulting from the energy spread of the ion beam (~0.2 eV), and the thermal kinetic and rotational energy of the CO_2 target, the threshold behavior of the cross sections is consistent with the endoergicity of the reactions, indicating that there are no barriers in excess of the product channel energy, as expected. The H^+ and D^+ transfer cross sections both rise rapidly from threshold with nearly identical cross sections, but then plateau above ~1 eV. In this high energy region, the CO_2H^+ signal is significantly higher than the CO_2D^+ signal, and the sum of the two cross sections, σ_{total}, ranges from 15% to 23% of the collision cross

section, σ_{col}. σ_{col} was taken as the greater of either the ion-induced dipole capture cross section, or the hard sphere cross section, and $\sigma_{Hardsphere}$ was estimated using the angle-averaged contact distance and covalent radii. Over the plateau energy range from 1 eV to 3 eV, σ_{col} ranges from 27 to 19 Å.[26]

One interesting observation is that while the cross sections for CO_2H^+ and CO_2D^+ are essentially superimposable in threshold region, the CO_2H^+ cross section is >30% larger than the CO_2D^+ cross section at high E_{col}. At high energies, effects from zero point energy differences should be negligible, thus the difference must result from some kinematic/dynamic effect. One such effect is common if the primary product is weakly bound, such that its survival depends on its internal energy. In that case, there can be substantial isotope effects on the survival probability, a good example of which is the branching between VH^+ and VD^+ channels in reaction of V^+ with HD at high E_{col}.[27] In the $HOD^+ + CO_2$ reaction, however, this effect is irrelevant because there are no energetically accessible decomposition pathways for CO_2H^+ and CO_2D^+. A related effect also seen in systems such as M + HD, is that angular momentum conservation imposes greater restrictions on the MD + H channel, because the reduced mass of those products is much lower than that for MH + D products. For the $HOD^+ + CO_2$ system, the difference in reduced mass between the H^+ and D^+ transfer channels is only ~5% -- unlikely to result in a 30% difference in cross section.

In a statistical mechanism, product branching tends to favor product channels with higher densities-of-state (DOS), all else being equal. Such DOS effects are unlikely to be important at high energies, where the mechanism is clearly direct. Nonetheless, we used the direct state count algorithm in the Rice-Ramsperget-Kassel-Marcus (RRKM) program of Zhu and Hase[28] to calculate the DOS for the $CO_2D^+ + OH$ and $CO_2H^+ + OD$ channels at 2 eV. Both sets of products have both OH and OD stretch modes. However, the $CO_2D^+ + OH$ products also have OD bend modes with lower frequencies than the analogous OH bend modes in $CO_2H^+ + OD$. As a result,

the DOS for the CO_2D^+ + OH channel is ~7% higher than that for CO_2H^+ + OH channel, contrary to observation.

Note that the two channels have essentially identical rapidly rising cross sections below ~1 eV, at which point the CO_2D^+ channel abruptly stops rising, becoming nearly E_{col} independent. The CO_2H^+ cross section continues to rise to ~1.5 eV, at which point it also plateaus. This E_{col} dependence suggests that the H^+ and D^+ transfer reach some kind of high energy limiting behavior, and that the limit is reached sooner for CO_2D^+ , compared to CO_2H^+. In the limit of spectator stripping dynamics (see Levine[29]), the relevant interaction is between OCO and either an H or D atom on HOD^+. In this limit, the effective collision energy of OCO-D is nearly twice as great as for OCO-H. Thus, one might expect the CO_2D^+ channel to reach its high energy limit at lower E_{col} than the CO_2H^+ channel. On the other hand, the recoil dynamics, see below, while direct, are nowhere near the spectator stripping limit at E_{col} = 1 – 1.5 eV. Most likely, the unequal CO_2H^+/CO_2D^+ branching is related to the details of how the system gets through the critical part of the potential energy surface, and mass effects on this kind of dynamics are not unexpected. For example, the skew angle of the mass-weighted potential surface[29] is somewhat smaller for CO_2H^+ (15.8°) than for CO_2D^+ (22.3°). This issue will be one target of detailed quasiclassical trajectory study that we are beginning.

Recoil Velocity Distributions

The lab frame v_{axial} distributions for the CO_2H^+ and CO_2D^+ product ions from reaction of ground state HOD^+ are given in Figures 8.2 and 8.3, respectively. The solid vertical line in each figure shows the velocity of the CM frame with respect to the lab, $\langle V_{CM} \rangle$, averaged over the distributions of reactant velocities. v_{axial} distributions are simply projections of the full recoil velocity distributions on the ion guide axis. Because our experiment is axially symmetric, the lab frame v_{axial} distributions are related to the CM frame distributions by simple subtraction of $\langle V_{CM} \rangle$, i.e., v_{axial} greater than $\langle V_{CM} \rangle$ corresponds to forward scattering and v_{axial} less than $\langle V_{CM} \rangle$

corresponds to backward scattering. Note, however, that because the charge transfers in the course of both H^+ and D^+ transfer, the meaning of "forward" and "backward" is reversed from the more typical definition. Small angle stripping dynamics results in product *ions* that are backward-scattered relative to V_{CM}, while rebounding would lead to product *ions* in the forward direction.

The cylindrically symmetric lab ↔ CM frame transformation allows the qualitative dynamics to be inferred directly from the raw distributions. For example, if reaction is mediated by a complex with lifetime ($\tau_{collision}$) greater than its rotational period ($\tau_{rotation}$), the resulting v_{axial} distribution must be forward-backward symmetric about $<V_{CM}>$. An asymmetric v_{axial} distribution is proof that the mechanism is direct (i.e., not complex-mediated), and also reveals the dominant scattering mechanism. Finally, some insight into the partitioning of available energy, E_{avail}, into product recoil can be inferred from the shape of the v_{axial} distributions. In a system like $HOD^+ + CO_2$, where V_{CM} is slow, a significant fraction of the v_{axial} distribution may be scattered to negative lab velocities. To collect such ions, the ion lens at the guide entrance is biased to reflect these ions back toward the detector, where they appear at long TOF, corresponding to a pile up of apparent signal for v_{axial} near zero. Furthermore, slow ions are most likely to have their velocities distorted by small inhomogeneities in the surface potentials on the ion guides or by secondary collisions, and for all these reasons, we do not attempt to interpret the v_{axial} distributions below ~300 m/sec.

Because the CO_2H^+ and CO_2D^+ distributions are very similar, we will discuss only the CO_2H^+ results, and simply summarize the fitting results for both in Table 8.2. At high E_{col}, the distributions for CO_2H^+ (Figure 8.2) are strongly asymmetric with respect to $<V_{CM}>$, indicating a direct mechanism with $\tau_{collision} < \tau_{rotation}$. $\tau_{rotation}$ can be estimated at ~ 1 psec, from the moment of inertia and angular momentum of the collision complex, the latter estimated from the magnitude of the cross section and E_{col}, via $L_{max} = \mu \cdot v \cdot b_{max}$, where μ is the reduced mass, v is the collision relative velocity, and $b_{max} = sqrt(\sigma_{collision}/\pi)$. Because the charge transfers in the reaction, backward peaking of the v_{axial} distributions corresponds to small angle scattering, i.e., where

HOD^+ and transfers a proton, without transferring much momentum. Such collisions are most likely at large impact parameters and the tail of v_{axial} extending into the forward direction would then be attributed to small impact parameter collisions where the ion product rebounds from the collision. As E_{col} is reduced, the peaks of the v_{axial} distributions shift toward $<V_{CM}>$, but the distributions remain asymmetric. Results for lower E_{col} are not plotted because the energy available to drive recoil is so small that the recoil velocities are not resolvable due to broadening from the distributions of reactant velocities. The effects of HOD^+ vibrational excitation on the v_{axial} distributions are discussed below.

The data points connected by straight lines in Figures 8.2 and 8.3 represent our experimental data, and the solid curves were generated from a model of the recoil dynamics, which was then convoluted with the velocity distributions of the ion and neutral reactants, and finally projected on the relative velocity axis for comparison with the experimental v_{axial} distributions.[30] These simulations are somewhat noisy because the convolution process is Monte-Carlo based, and thus subject to sampling noise. The model used here[20] has an angular distribution based on the osculating complex model,[31] where a short-lived collision complex is assumed to form, with a rotational period of $\tau_{rotation}$, decaying to products with a lifetime $\tau_{collision}$. The actual fitting parameter is $\tau_{ratio} = \tau_{rotation}/\tau_{collision}$. If $\tau_{ratio} < 1$, then the angular distribution is isotropic, and if $\tau_{ratio} \gg 1$, corresponding to direct impulsive scattering, the angular distribution peaks sharply in a direction determined by the dominant reaction mechanism (here assumed to be 180°, corresponding to stripping dynamics). In this system, where reaction appears to be direct at all energies (see below), the τ_{ratio} parameter is best thought of as simply a parameter that describes how sharply backward-peaked the recoil distributions are. The recoil velocity is modeled by assuming a Gaussian recoil energy distribution, $P(E_{recoil})$, which is controlled by width and peak parameters, both defined in terms of E_{avail}.

The parameters extracted from the simulations are shown in Table 8.2. Values are given for τ_{ratio}, which simply reflects the degree of asymmetry, and $E_{ratio} = E_{recoil}/E_{avail}$, averaged over all

simulated collisions. For production of CO_2H^+ from reaction of ground state HOD^+, the fraction of energy going into recoil is nearly constant, varying from ~60% to 67% with increasing energy. τ_{ratio} increases as well, reflecting the fact that the forward-backward asymmetry of the angular distributions increases with energy. Such an increase in asymmetry is expected for two reasons. Increasing energy should decrease $\tau_{collision}$, thus decreasing angular broadening from rotation of the collision complex. Furthermore, in a hard sphere line-of-centers collision picture, increasing the collision energy also increases the maximum impact parameter that can lead to reaction.[32] In a reaction where a light atom is transferred, collisions at increasing impact parameter should result in increasingly backward-peaked recoil velocities. The fact that there are only modest changes in the fitting parameters between CO_2H^+ and CO_2D^+ over the entire range of E_{col} and HOD^+ reactant state indicates that the reaction mechanism is not changing significantly, at least in the high E_{col} range where the v_{axial} distributions are interpretable.

Discussion

Ground State Reaction Mechanism

Given the presence of a hydrogen-bonded complex on the reaction coordinate, one obvious question is whether the mechanism might be complex-mediated at low E_{col}, where we cannot resolve the v_{axial} distributions. To test the possible significance of the complex, we carried out Rice-Ramsperger-Kassel-Marcus[33] calculations of the complex lifetime and decay branching, using the RRKM program of Zhu and Hase,[28] with energetics and vibrational frequencies from the *ab initio* calculations, and assuming orbiting transition states for all decay channels. Even for E_{col} corresponding to the thermodynamic threshold, the rate of decay back to the reactants is in the 10^{14} sec^{-1} range (i.e., negligible lifetime). Furthermore, this calculation predicts that because of competition with decay back to reactants, branching to CO_2H^+ and CO_2D^+ products should be negligible for E_{col} < 1eV, whereas the experimental cross sections rise rapidly from threshold and have reached a plateau by 1 eV. Clearly, while forces associated with the hydrogen-bonded

potential well may affect the scattering dynamics, the complex itself is insignificant from a mechanistic perspective. Reaction is direct at all energies.

Vibrational Mode Effects

The cross sections for CO_2H^+ and CO_2D^+ production for the four different HOD^+ reactant states are plotted as a function of E_{col} in Figure 8.4, and as a function of total energy ($E_{total} \approx E_{col} + E_{vibration}$) in Figure 8.5. We omit rotational energy from E_{total}, because the HOD^+ has negligible rotational energy (low J selected by REMPI), and the contribution from CO_2 thermal rotational energy is small (~25 meV) and independent of HOD^+ state.

First, consider the plots vs. E_{col} in Figure 8.4. Here, exciting HOD^+ vibration increases the total energy available to reactants, thus it is not surprising that all modes of HOD^+ excitation enhance both reactions at low E_{col}, where much of the available energy is needed to overcome the endoergicity. It is clear, however, that the enhancement is mode-specific. As shown in the top frame of the figure, bend excitation (E_{vib}=153 meV) results in an enhancement for the CO_2H^+ channel greater than that from the OD stretch (293 meV), and nearly as large as that from the OH stretch (396 meV). The vibrational effects are biggest in the threshold energy range, peaking around E_{col} =1 eV. At higher energies, where E_{col} effects are small, the OH stretch and bend, but not the OD stretch, continue to have substantial effects, even though the vibrational contribution to the total energy becomes negligible. The CO_2D^+ cross sections, shown in the bottom frame, are qualitatively similar to those for CO_2H^+ with two exceptions. For CO_2D^+, it is the OD stretch that gives the largest enhancement, and the OH stretch is now the least effective. The bend still has a large enhancing effect, almost as big as that of the OD stretch.

The plots as a function of E_{total} in Figure 8.5 allow direct comparison of the effects of partitioning the available energy into E_{col} and different modes of HOD^+ vibration. Note that for both CO_2H^+ and CO_2D^+, the four reactant states have similar cross sections in the energy range close to the threshold energy. This indicates, not surprisingly, that all forms of energy are at least

approximately equivalent when essentially all available energy is needed to drive reaction. What is surprising is how quickly mode-specific behavior develops. Consider, first, the CO_2H^+ channel. By $E_{total} \approx 0.75$ eV, the reactant states have divided into two classes. OD stretch-excited and ground state HOD^+ have essentially identical cross sections, increasing with E_{total} to ~1.3 eV, then becoming nearly energy independent. The cross sections for bend and OH stretch-excited HOD^+ are similar to each other, but substantially (~70%) greater than those for ground state or OD stretch-excited HOD^+. They also both peak around 1.3 eV, and drop significantly at higher energies. The implication is that partitioning energy from E_{col} into the OD stretch, i.e., the stretch of the "spectator" bond, has essentially no effect on H^+ transfer. Shifting energy into either the OH stretch (i.e., the broken bond stretch) or the bend, results in similar, substantial increases in H^+ transfer cross section.

For the CO_2D^+ cross sections in the bottom frame of Figure 8.4, the results are a bit different, probably because in addition to switching the identity of the spectator and broken bonds, the relative energies of the spectator and broken bond stretches are reversed. Nonetheless, it is still the case that the ground state and spectator (OH) stretch-excited reactions have similar cross sections and E_{total} dependence, while excitation of the bend and broken bond (OD) stretch also produces similar, enhanced cross sections, with similar E_{total} dependence, falling significantly at high E_{total}. The fact that at low E_{total}, the OH stretch appears to actually inhibit the cross section simply means that while both E_{col} and OH stretch excitation enhance D^+ transfer, energy in the OH stretch is less effective than the same amount of E_{col}, at low E_{total}. This effect is not seen for the CO_2H^+ channel, but that may simply reflect the lower energy of the OD stretch, which is the spectator for that channel.

The fact that excitation of the bend and of the broken bond stretch both substantially enhance the cross sections for CO_2H^+ and CO_2D^+ suggests that they might alter the reaction mechanism enough to produce an effect on the recoil dynamics. As shown by the best-fit simulation parameters given in Table 8.2, however, this is not the case. There are small increases

in the amount of recoil energy, but the fraction E_{avail} going into recoil (E_{ratio}) is independent of HOD^+ state within the experimental uncertainty, as is the degree of forward-backward asymmetry (τ_{ratio}).

It is not surprising that OD stretch excitation enhances CO_2D^+ production, and OH stretch excitation enhances CO_2H^+ production, because these vibrations stretch the bond that must break. Polanyi and co-workers investigated the effects of barrier position on the relative effects from E_{col} and stretching vibration in model A + BC systems, and predicted that for late barriers, energy in the BC stretch should be more effective than E_{col}, because the momentum associated with the bend was along the right coordinate to drive the system over the barrier.[34, 35] An endoergic reaction, like $HOD^+ + CO_2$, has a late barrier in the sense that energy rises only as the system moves into the product channel. Because the barrier is related to breaking an OH or OD bond, stretch excitation of that bond clearly corresponds to momentum in the right coordinate to help drive the system up the potential slope leading to products, and thus is consistent with the "Polanyi rule". The observation that excitation of the spectator bond has little effect on reactivity is also consistent with this argument, because the spectator stretch is essentially orthogonal to the coordinate required to drive the reaction. Similar arguments can be made for the H/D transfer reaction studies from neutral HOD by the Zare and Crim groups.[10, 15]

In this context, the large effect of the bend is quite surprising. As shown in the bottom frame of Figure 8.5, which plots σ_{total} vs. E_{total} for the four reactant states, the effect of the bend is larger than those from either of the stretch modes, because it enhances both H^+ and D^+ transfer. As discussed in the Introduction, experiments on neutral water found no effect of bend excitation for some combination states, but at very high levels of water vibrational excitation, the effects of energy in the bend and asymmetric stretch overtones was comparable.[9, 15]

The "Polanyi rule" predicting vibrational enhancement in late barrier A + BC reactions is, essentially, based on considering the momentum associated with the stretching vibration, which is in the correct coordinate to help surmount the barrier. In polyatomic reactions, modes that might

at first appear to be unrelated to the reaction coordinate may actually be strongly coupled if they distort one of the reactants toward a more product-like geometry. For example, the reactions $H_2CO^+ + CH_4 \rightarrow H_2COH^+ + CH_3$,[36] and $C_2H_2^+ + CH_4 \rightarrow C_2H_3^+ + CH_3$,[20] are strong enhanced by excitation of bending modes that might seem irrelevant to breaking methane CH bonds. In the first case, it is the low frequency methane bending modes that have a large effect, and the coupling results from the fact that the CH_3 product is planar, and thus distortion of the CH_4 is a necessary part of the reaction coordinate. In the second case, it is the cis-bend of $C_2H_2^+$ that greatly enhances H transfer, but again, because the product ($C_2H_3^+$) requires bending and rehybridization at the carbon center(s) where the H attaches, the cis-bend is clearly coupled to the H-transfer reaction coordinate. In both systems, we were able to use detailed analysis of quasi-classical trajectories to identify and project out the important coordinates on the 21 dimensional potential surfaces, constructing reduced surfaces where the bending dynamics are seen to drive transition to products.[37, 38] When trajectories are projected onto these reduced surfaces, they are quite reminiscent of late barrier "Polanyi rule" behavior.

For $H_2O^+ + CO_2 \rightarrow CO_2H^+ + OH$, this approach seems inapplicable, because the reaction eliminates the bend coordinate. One might expect that H_2O^+ bending excitation would simply carry over into rotation of the products, and there is no reason to expect this effect to enhance reactivity. We intend to carry out a detailed trajectory analysis of this system, but for the present, we offer the following speculation about the bend enhancement.

"Polanyi rules" are based on an essentially kinematic approach to thinking about the problem, where vibration puts momentum into the correct coordinate to carry the system over a barrier, or through some bottleneck on the potential energy surface. Another approach is to consider the effects of the vibrationally-induced molecular distortions on the shape of the potential energy surface. This approach is applicable to fast (i.e., high energy) collisions, where the collision time is short compared to the vibrational period (~53 fsec for the HOD^+ bend). For comparison, the final column in Table 8.2 gives τ_{flyby}, which is intended as an estimate of the total

time over which the intermolecular forces are significant in a direct collision (estimated as the time it would take undeflected reactants to fly past each other, through a total distance of 5 Å). The bend vibrational period is shorter than τ_{flyby}, seemingly invalidating this approach to thinking about vibrational effect. Note, however, that the relevant time is not the overall collision time, but rather the much shorter time that the system spends in the critical region of the potential surface, where reactivity is determined. In that case, because a vibrating molecule classically spends most of its time at the turning points of the vibration, fast collisions are likely to "catch" the molecule in a vibrationally distorted geometry when it reaches this critical region. We have used quasi-classical trajectories to explore this issue for a number of ion-molecule reactions in the energy range of interest here, and have found that reactant distortions at such critical points can account for at least part of the observed vibrational effects.[37, 39-41] The $HOD^+ + CO_2$ reaction is direct at all energies, thus the critical times may be short enough to justify considering the effect of colliding in vibrationally distorted geometries.

Figure 8.6 examines the effect of bending distortion on the H_2O^+-CO_2 interaction potential. The figure is a set of 2-dimensional reduced potential surfaces, showing the effects of H_2O^+ bending on key features of the reactant approach and product separation energetics. The reduced surfaces were calculated at the PBE1PBE/6-311++G** level of theory, by the following process. The HOH^+ angle was frozen at one of three values: 133° (outer classical turning point of the bend vibration), 110° (equilibrium angle at this level of theory), and 90° (inner classical turning point). The turning points correspond to H_2O^+ with 1.5 quanta of bending excitation (1.5 · 153 meV) relative to the bottom of the entrance valley at infinite reactant separation. The potential energy was then calculated at a grid of points mapping the reactant approach and product separation. To represent the approach coordinate, we used the distance between the O of HOH and the nearest O of CO_2, as shown in the sketch at the top of the figure. For the exit coordinate, we used the H-OH distance, between the transferred proton and the departing OH product. The only other constraint was that the O-H-O angle was frozen at 180°, corresponding

to the minimum energy path, where there is an attractive hydrogen bonding interaction between approaching reactants (HO-H--OCO) and separating products (HO---H-OCO). All other coordinates were optimized at each point, so that these surfaces, in essence, show the minimum energy paths for reaction under the constraint of fixed HOH bend angles. Along the reactant approach, it turns out that the OCO-HO axis is near linear, as shown in the sketch above the entrance valley, but during the product separation, the transferred proton is most stable at an angle of ~120° with respect to the OCO axis, similar to the equilibrium geometry of the CO_2H^+ product (see sketch above the exit valley).

There are two effects evident from this analysis. Fixing the bend angle at the turning point raises the energy of the entrance valley by the value of the vibrational quantum, but because the bend coordinate correlates to rotation of the products, there is almost no effect of this angle constraint on the product channel. In effect, therefore, the vibrational distortion reduces the effective endoergicity of the reaction. Note however, that the same argument could be made for excitation of the stretch of the broken bond, because this mode correlates to translation in the products. On the other hand, if the spectator bond stretch remains as stretching excitation of the OH product, then the effective endoergicity would actually increase slightly, because the energy of the isolated OH stretch is ~67 meV higher in energy than the OH stretch in H_2O^+.

Given that bend excitation has a larger effect on total reactivity than either stretch, despite being the lowest energy mode, it seems that there must be an additional factor at work. One obvious possibility is a change in the shape of the potential in the vicinity of the repulsive wall, that might tend to increase the probability that the system exits the collision into the product valley. Note that with the bend angle frozen at the outer turning point, the energy rises more slowly (i.e., the forces are weaker) as the system moves into the product channel, compared the situation for the equilibrium bend angle. The same effect occurs, but to a lesser extent, when the bend angle is at the inner turning point. We might anticipate that this change in potential shape might the probability of exiting to products.

This analysis is speculative because reactions, particularly at high E_{col}, do not tend to follow the minimum energy path, and thus it is quite possible that some other feature of the potential surface, not observable along the minimum energy path, is actually responsible for the bend enhancement. This kind of effect is a natural target for analysis by quasi-classical trajectories, which sample the actual reaction paths. Such a study is planned.

Conclusions

We have presented a detailed study of the reaction of mode/bond-selectively excited HOD^+ with CO_2. Excitation in the OH stretch (001) mode substantially enhances H^+ transfer, with greater efficiency than E_{col}, but has little effect on the D^+ transfer reaction. Conversely, OD stretch (100) excitation enhances D^+ transfer, but has little effect on H^+ transfer. Surprisingly, excitation of the HOD^+ bend (010) enhances both channels with high efficiency, such that the bend has the largest overall effect. The stretch effects can be rationalized in terms similar to those introduced by Polanyi for late barrier A + BC reactions. The bend and breaking bond stretch effects may also be at least partly attributable to the fact that these vibrational modes are absent in the product, so that excitation energy in those modes effectively lowers the endoergicity of the reaction. In addition, however, there appear to be effects of bend distortion on the shape of the potential energy surface that may help promote transition from reactants into the product valley.

Acknowledgments

This work was supported by a grant from the Chemistry Division of the National Science Foundation (CHE-0647124)

References

1. G. Herzberg, Ann. Geophys. **36**, 605 (1980).

2. W. T. Huntress, Jr., Astrophys. J., Suppl. Ser. **33** (4), 495 -514 (1977).

3. R. A. Morris, A. A. Viggiano, J. M. V. Doren and J. F. Paulson, J. Phys. Chem. **96**, 3051 (1992).

4. P. Gammelgaard and B. Thomsen, Astron.Astrophys. **197**, 320 (1988).

5. M. E. Brown, A. H. Bouchez, H. Spinrad and C. M. Johns-Krull, Astron.Astrophys. **301**, L1 (1995).

6. H. Balsiger, K. Altwegg, F. Buehler, J. Geiss, A. G. Ghielmetti, B. E. Goldstein, R. Goldstein, W. T. Huntress and W. H. Ip, Nature London **321**, 330 (1986).

7. K. Jockers, T. Credner and T. Bonev, Astronomy and Astrophysics **335**, L56 (1998).

8. M. J. Bronikowski, W. R. Simpson, B. Girard and R. N. Zare, J. Chem. Phys. **95**, 8648 (1991).

9. M. J. Bronikowski, W. R. Simpson and R. N. Zare, J. Phys. Chem. **97**, 2204 (1993).

10. M. J. Bronikowski, W. R. Simpson and R. N. Zare, J. Phys. Chem. **97**, 2194 (1993).

11. A. Sinha, M. C. Hsiao and F. F. Crim, J. Chem. Phys. **92**, 6333 (1990).

12. A. Sinha, M. C. Hsiao and F. F. Crim, J. Chem. Phys. **92**, 6337 (1990).

13. A. Sinha, M. C. Hsiao and F. F. Crim, J. Chem. Phys. **94**, 4928 (1991).

14. D. H. Zhang, M. A. Collins and S.-Y. Lee, Science **290**, 961 (2000).

15. J. D. Thoemke, J. M. Pfeiffer, R. B. Metz and F. F. Crim, J. Phys. Chem. **99**, 13748 (1995).

16. B. W. Uselman, J. M. Boyle and S. L. Anderson, Chem. Phys. Lett. **440**, 171 (2007).

17. Z. Karpas and J. W. T. Huntress, Chem. Phys. Lett. **59**, 87 -89 (1978).

18. R. J. Shul, R. Passarella, L. T. DiFazio, Jr., R. G. Keesee and A. W. Castleman, Jr., J. Phys. Chem. **92**, 4947-4951 (1988).

19. M. Heninger, J. Lemaire, G. Mauclaire, S. Fenistein, S. Jullien and M. R., Journal of Chemical Physics **101** (3), 1923-1929 (1994).

20. Y.-H. Chiu, H. Fu, J.-T. Huang and S. L. Anderson, J. Chem. Phys. **102**, 1199 -1216 (1995).

21. J. Liu, B. W. Uselman, B. Van Devener and S. L. Anderson, Phys. Chem. Chem. Phys. **8**, 4575 (2006).

22. D. Gerlich, Adv. Chem. Phys. **82**, 1 (1992).

23. M. J. Frisch, G. W. Trucks, H. B. Schlegel, G. E. Scuseria, M. A. Robb, J. R. Cheeseman, J. J. A. Montgomery, T. Vreven, K. N. Kudin, J. C. Burant, J. M. Millam, S. S. Iyengar, J. Tomasi, V. Barone, B. Mennucci, M. Cossi, G. Scalmani, N. Rega, G. A. Petersson, H. Nakatsuji, M. Hada, M. Ehara, K. Toyota, R. Fukuda, J. Hasegawa, M. Ishida, T. Nakajima, Y. Honda, O. Kitao, H. Nakai, M. Klene, X. Li, J. E. Knox, H. P. Hratchian, J. B. Cross, C. Adamo, J. Jaramillo, R. Gomperts, R. E. Stratmann, O. Yazyev, A. J. Austin, R. Cammi, C. Pomelli, J. W. Ochterski, P. Y. Ayala, K. Morokuma, G. A. Voth, P. Salvador, J. J. Dannenberg, V. G. Zakrzewski, S. Dapprich, A. D. Daniels, M. C. Strain, O. Farkas, D. K. Malick, A. D. Rabuck, K. Raghavachari, J. B. Foresman, J. V. Ortiz, Q. Cui, A. G. Baboul, S. Clifford, J. Cioslowski, B. B. Stefanov, G. Liu, A. Liashenko, P. Piskorz, I. Komaromi, R. L. Martin, D. J. Fox, T. Keith, M. A. Al-Laham, C. Y. Peng, A. Nanayakkara, M. Challacombe, P. M. W. Gill, B. Johnson, W. Chen, M. W. Wong, C. Gonzalez and J. A. Pople, (Gaussian, Inc., Pittsburgh PA, 2003).

24. S. G. Lias, in *NIST Standard Reference Database Number 69*, edited by P. J. Linstrom and W. G. Mallard (National Institute of Standards and Technology, Gaithersburg, MD, 2003), pp. http://webbook.nist.gov.

25. A. P. Scott and L. Radom, J. Phys. Chem. **100**, 16502 (1996).

26. W. M. Hayne, *Handbook of Chemistry and Physics*, 91 ed. (CRC Press/Taylor and Francis, Boca Raton, FL, 2004).

27. J. L. Elkind and P. B. Armentrout, J. Phys. Chem. **89**, 5626 (1985).

28. L. Zhu and W. L. Hase, in *Quamtum Chemistry Program Exchange* (Chemistry Department, Indiana University Bloomington, 1993).

29. R. D. Levine, *Molecular Reaction Dynamics*. (Cambridge U. Pr., Cambridge, 2005).

30. J. Liu, B. Van Devener and S. L. Anderson, J. Chem. Phys. **116**, 5530 (2002).

31. G. A. Fisk, J. D. McDonald and D. R. Herschbach, Discuss. Faraday Soc. **44**, 228 (1967).

32. R. D. Levine and R. B. Bernstein, *Molecular Reaction Dynamics and Chemical Reactivity*. (Oxford University Press, New York, 1987).

33. W. Forst, *Theory of Unimolecular Reactions*. (Academic Press, New York, 1973).

34. M. H. Mok and J. C. Polanyi, J. Chem. Phys. **51**, 1451 (1969).

35. J. C. Polanyi and W. H. Wong, J. Chem. Phys. **51**, 1439 (1969).

36. J. Liu, B. V. Devener and S. L. Anderson, J. Chem. Phys. **119**, 200 (2003).

37. J. Liu, K. Song, W. L. Hase and S. L. Anderson, J. Am. Chem. Soc. **126**, 8602 (2004).

38. J. Liu and S. L. Anderson, Phys. Chem. Chem. Phys. **11**, 8721 (2009).

39. J. Liu, K. Song, W. L. Hase and S. L. Anderson, J. Chem. Phys. **119**, 3040 (2003).

40. J. Liu, K. Song, W. L. Hase and S. L. Anderson, J. Phys. Chem. A **109**, 11376 (2005).

41. J. Liu, B. W. Uselman, J. M. Boyle and S. L. Anderson, J. Chem. Phys. **125**, 133111 (2006).

Table 8.1: Experimental and calculated $\Delta_r H$ (eV) relative to reactants ($H_2O^+ + CO_2$)

	HF	b3lyp	PBE1PBE	MP2	G3	Experimental
Complex A	-0.728	-0.940	-0.924	-0.815	-0.844	
Products	0.556	0.557	0.599	0.593	0.557	0.545

Table 8.2: Product ion velocity distribution fit results

CO_2H^+	(000)			(001)			(100)			(010)		
E_{col}	E_{ratio}[a]	τ_{ratio}[b]	E_{col}	E_{ratio}	τ_{ratio}	E_{col}	E_{ratio}	τ_{ratio}	E_{col}	E_{ratio}	τ_{ratio}	τ_{flyby}
0.63	60.1	3	0.63	60.1	3	0.63	59.9	3	0.63	59.7	3	164
0.98	63.8	4.5	0.98	63.7	4.5	0.98	63.6	4.5	0.98	64.0	4.5	137
1.48	66.9	7	1.48	67.0	7	1.48	66.2	5	1.48	67.0	5	113
1.87	69.8	9	1.87	67.0	8	1.87	67.0	8	1.87	67.0	8	97
2.87	67.0	12	2.87	67.0	12	2.87	67.0	12	2.87	67.1	12	79

CO_2D^+	(000)			(001)			(100)			(010)	
E_{col}	E_{ratio}	τ_{ratio}	E_{col}	E_{ratio}	τ_{ratio}	E_{col}	E_{ratio}	τ_{ratio}	E_{col}	E_{ratio}	τ_{ratio}
0.63	60.0	3	0.63	60.1	3	0.63	60.0	3	0.63	60.1	3
0.98	64.1	4.5	0.98	64.0	4.5	0.98	63.7	4.5	0.98	63.8	4.5
1.48	67.0	7	1.48	67.0	5	1.48	67.0	7	1.48	67.1	5
1.87	67.0	9	1.87	67.0	8	1.87	67.0	8	1.87	67.0	8
2.87	67.1	12	2.87	67.1	12	2.87	67.1	12	2.87	67.0	12

[a] $E_{ratio} = \langle E_{recoil} \rangle / \langle E_{avail} \rangle$ = average fraction of available energy in recoil

[b] T_{ratio} = measure of forward-backward asymmetry. Increasing values indicate increasing asymmetry

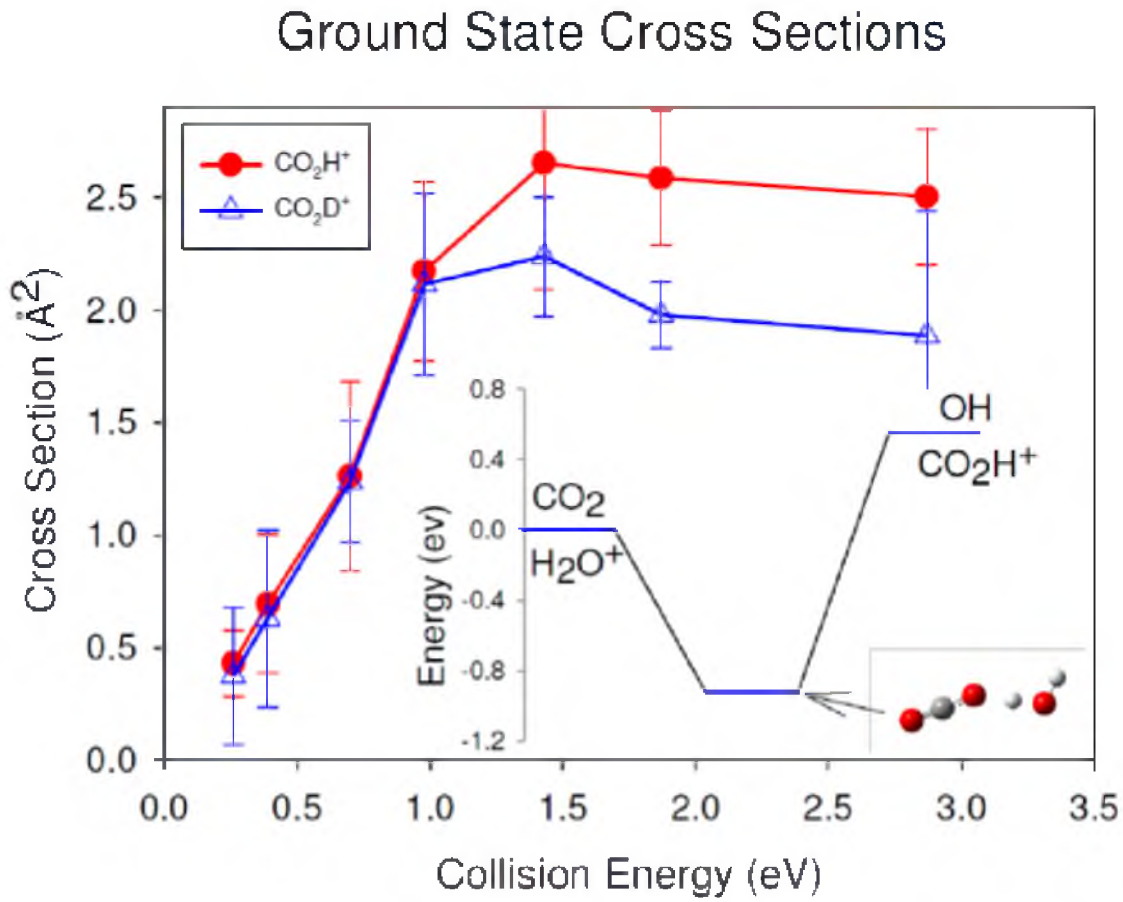

Figure 8.1: Ground state cross sections for production of CO_2H^+ and CO_2D^+ as a function of E_{col}. Inset: The reaction coordinate, using experimental energies for the products and a calculation at the G3 level for the hydrogen-bonded complex.

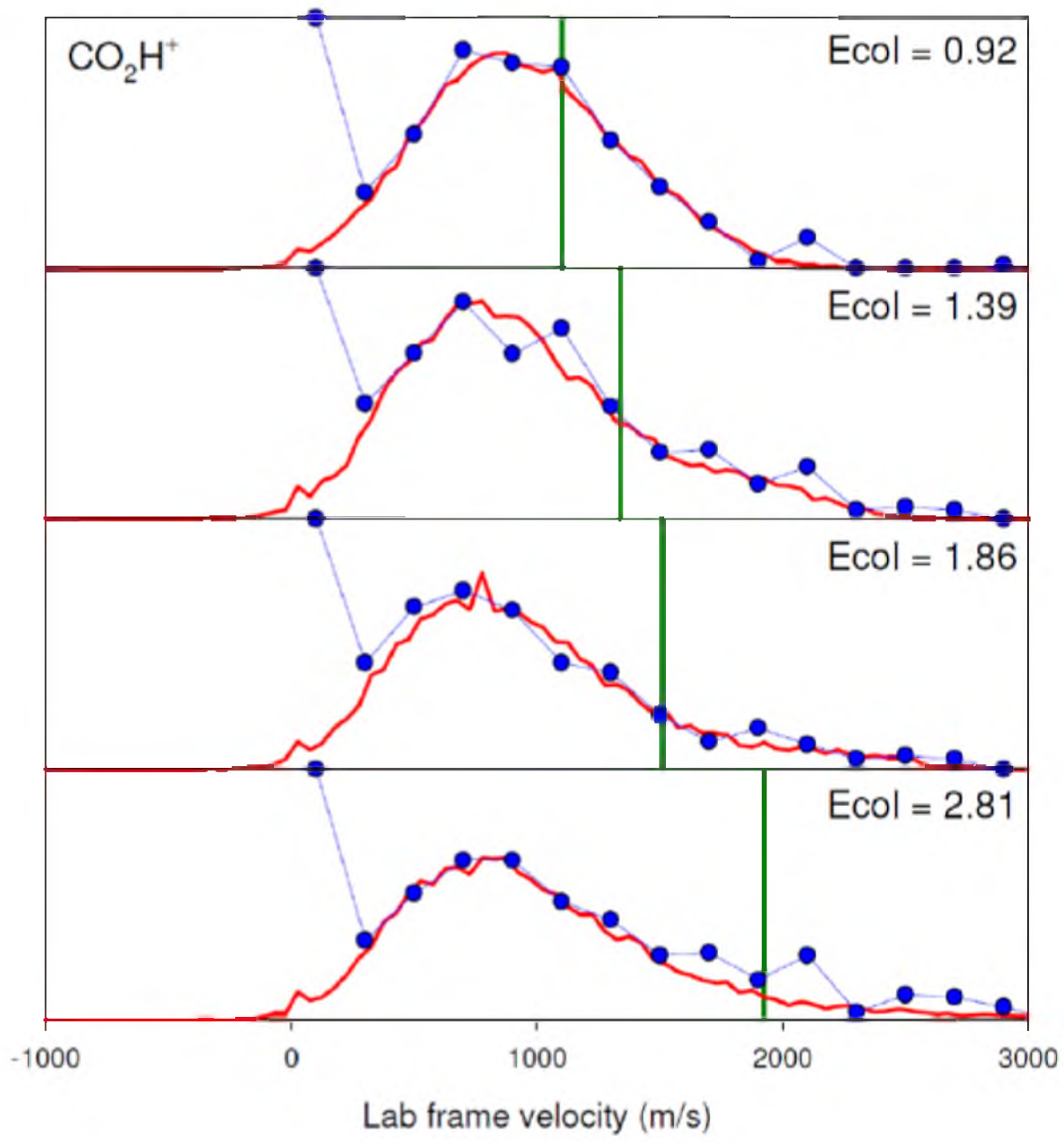

Figure 8.2: Lab frame axial velocity (v_{axial}) distribution for CO_2H^+ produced in reaction of ground state HOD^+. Experimental data denoted by —●— ; Simulations denoted by ——. Heavy vertical lines indicate the lab frame velocity of the center-of-mass frame ($<V_{CM}>$).

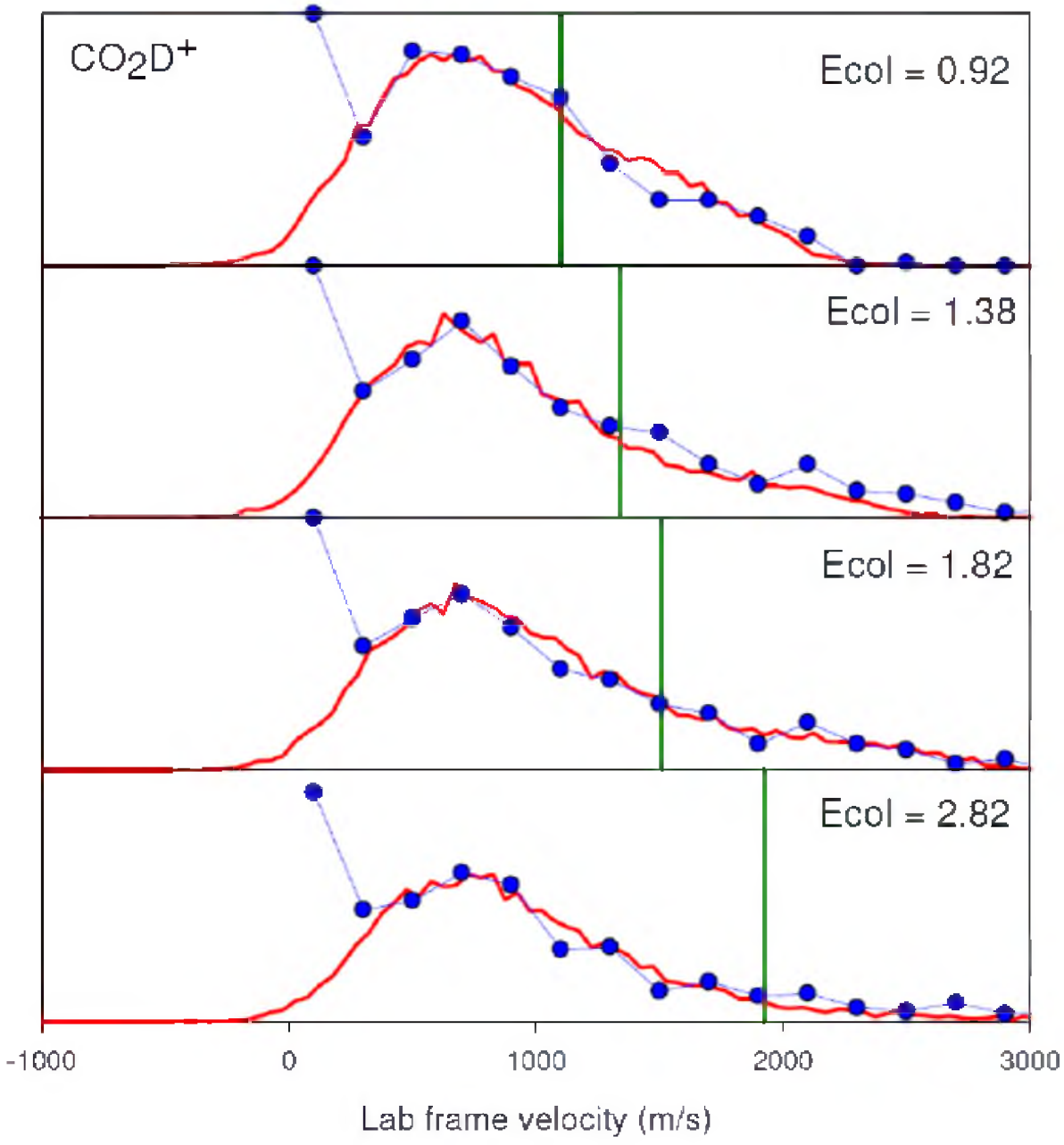

Figure 8.3: Lab frame axial velocity (v_{axial}) distribution for CO_2D^+ produced in reaction of ground state HOD^+. Experimental data denoted by —●— ; Simulations denoted by ——. Heavy vertical lines indicate the lab frame velocity of the center-of-mass frame ($<V_{CM}>$).

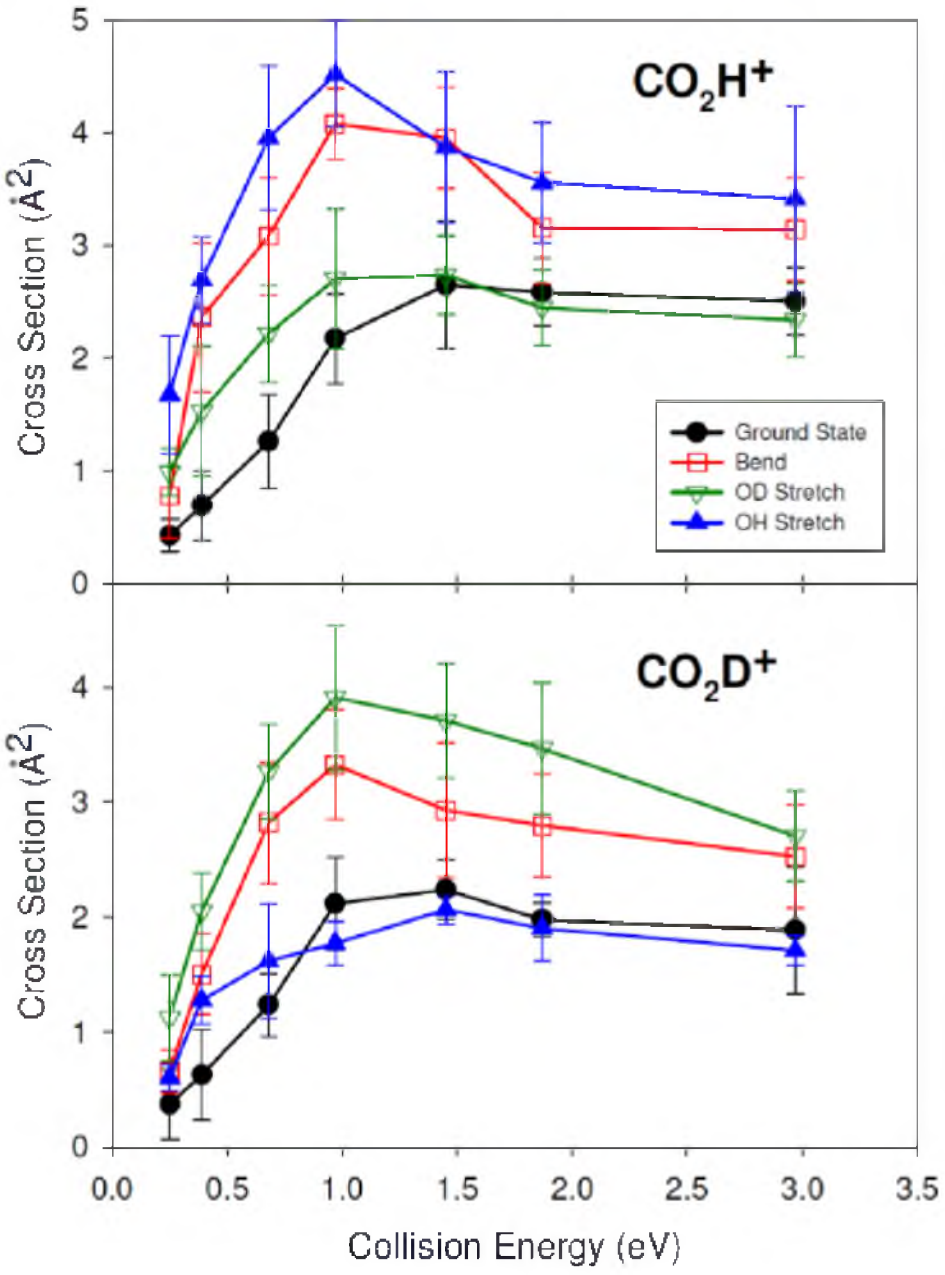

Figure 8.4: The effect reactant vibration has on reactivity for each reaction. Top: Cross sections for production of CO_2H^+ in reaction of HOD^+ in the indicated initial vibrational states, plotted as a function of collision energy (E_{col}). Bottom: Analogous cross sections for the CO_2D^+ channel.

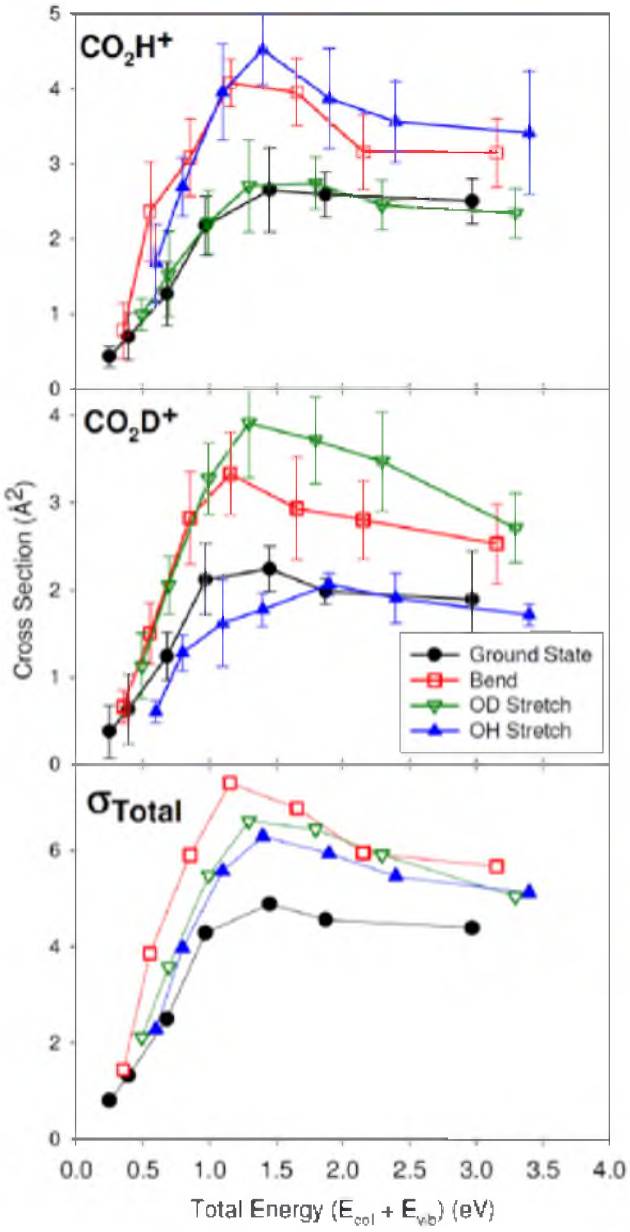

Figure 8.5: Cross sections for production of CO_2H^+ in reaction of HOD^+ in the indicated initial vibrational states, plotted as a function of total energy ($E_{total} = E_{col} + E_{vib}$) Bottom: Analogous cross sections for the CO_2D^+ channel.

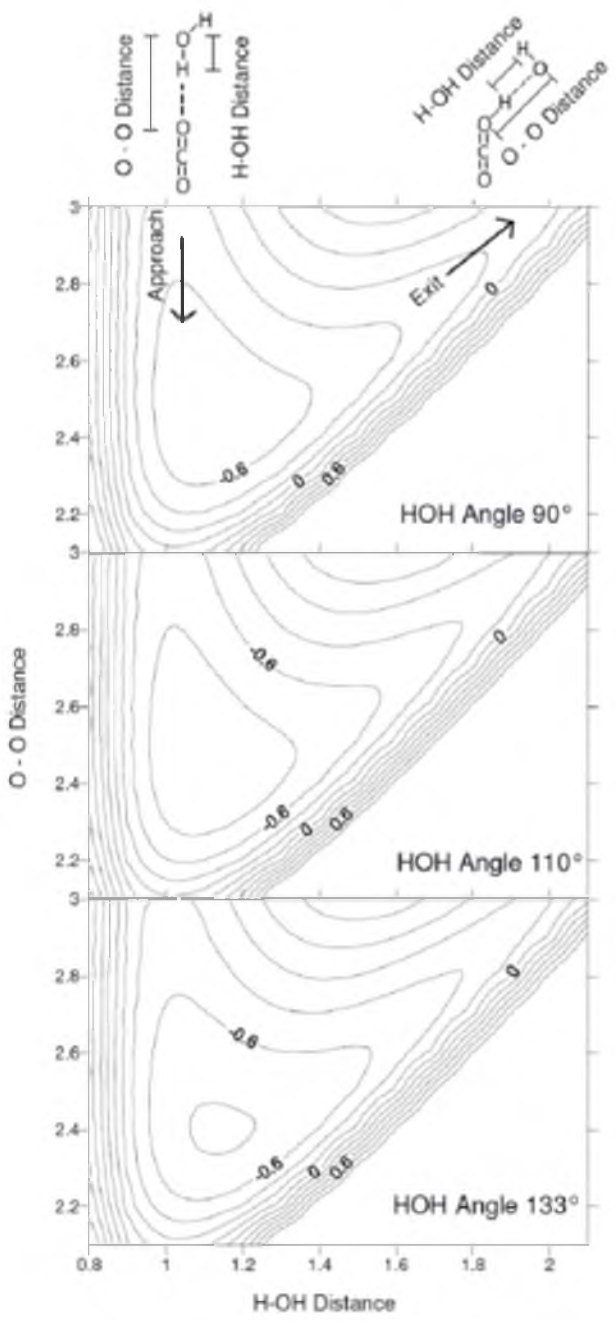

Figure 8.6: Reduced potential energy surfaces showing the minimum energy path for reactant approach and product separation in reaction of H_2O^+ with CO_2. The three frames were calculated with the H_2O^+ bond angle frozen at the indicated values.

CHAPTER 9

H^+ VS. D^+ TRANSFER FROM HOD^+ TO N_2: MODE- AND BOND-SELECTIVE EFFECTS

Reprinted with permission from David M. Bell, Jason M. Boyle, Scott L. Anderson, and Journal of Chemical Physics **135,** 044305. Copyright 2011, American Institute of Physics

Overview

Reactions of HOD^+ with N_2 have been studied for HOD^+ in its ground state, and with one quantum of excitation in each of its vibrational modes: (001) - predominately OH stretch, 0.396 eV, (010) - bend, 0.153 eV, and (100) - predominately OD stretch, 0.293eV. Integral cross sections and product recoil velocities were recorded for collision energies from threshold to 4 eV. The cross sections for both H^+ and D^+ transfer rise slowing from threshold with increasing collision energy; however, all three vibrational modes enhance reaction much more strongly than equivalent amounts of collision energy, and the enhancements remain large even at high collision energy, where the vibration contributes less than 10% of the total energy. Excitation of the OH stretch enhances H^+ transfer by a factor of ~5, but the effect on D^+ transfer is only slightly larger than that from an equivalent increase in collision energy, and smaller than the effect from the much lower energy bend excitation. Similarly, OD stretch excitation strongly enhances D^+ transfer, but has essentially no effect beyond that of the additional energy on H^+ transfer. The effects of the two stretch vibrations are consistent with the expectation that stretching the bond that is broken in the reaction puts momentum in the correct coordinate to drive the system into the exit channel. From this perspective, it is quite surprising that bend excitation also results in large (factor of 2) enhancements of both H^+ and D^+ transfer channels, such that its effect on the total cross section at collision energies below ~2 eV is comparable to those from the two stretch modes, even though the bend excitation energy is much smaller. For collision energies above ~2 eV, the vibrational effects become approximately proportional to the vibrational energy, though still much larger than the effects of equivalent additional of collision energy. Measurements of the product recoil velocity distributions show that reaction is direct at all collision energies, with roughly half the products in a sharp peak corresponding to stripping dynamics, and half with a broad and approximately isotropic recoil velocity distribution. Despite the large effects of vibrational excitation on reactivity, the effects on recoil dynamics are small, indicating that

vibrational excitation does not cause qualitative changes in reaction mechanism or in the distribution of reactive impact parameters.

Introduction

The water cation is important in chemistry of the upper atmosphere[1-3] and in comet tails.[4-7] There is considerable literature on the thermal kinetics of water cation reactions,[8] but relatively little is known about the dynamics of these reactions, outside of two crossed beam experiments on reactions of H_2O^+/D_2O^+ with NH_3 and C_2H_4.[9, 10] We recently reported studies of the reactions of HOD^+ with CO_2[11] and NO_2,[12] examining the effects on reactivity and product branching, of varying collision energy (E_{col}) and of exciting each of the three HOD^+ vibrational modes. In the HOD^+ isotopolog of water cation, the amplitude of the D atom motion in the (100) vibrational mode is ~9.5 times greater than that of the H atom, hence this mode is well described as the "OD stretch" (293 meV). Similarly, the (001) mode has H motion amplitude >30 times that of the D atom motion, and thus is well described as the "OH stretch" (396 meV). Finally, the (010) bend mode (153 meV) excites yet another type of nuclear motion, where both H and D atoms move with comparable amplitudes.

As discussed below, one of the interesting questions is how excitation of the OH and OD stretch modes influences the cross sections for H^+ and D^+ transfer, and how such mode/bond-specific effects vary with the energetics of the process. H^+/D^+ transfer in the $HOD^+ + NO_2$ system is essentially thermoneutral; however, analysis of the dynamics in that system is quite complex because H^+/D^+ transfer can take place on both triplet and singlet surfaces, and is in competition with exoergic charge transfer, dissociative charge transfer ($NO^+ + O\ ^3P + HOD$), and production of $NO^+ + 2$ OH. In that system, all channels except NO^+ production are inhibited by all modes of HOD vibration, and the only clear mode/bond-specific effect was is a propensity for energy in the OH or OD stretch of the bond broken in H^+/D^+ transfer (the "broken-bond stretch") to go into internal energy of the NO_2H^+/NO_2D^+ product, while energy in the stretch of the

"spectator bond" tended to remain as internal energy of the OD or OH product. The reaction with CO_2 is much simpler – the only channels are H^+ and D^+ transfer, which are endoergic by ~0.55 eV. In this system, there are strong mode/bond specific effects. Excitation of the OH stretch roughly doubles the cross section for H^+ transfer, while having almost no effect on D^+ transfer, and OD stretch excitation doubles the cross section for D^+ transfer, but has little effect on H^+ transfer. As discussed below, this behavior is in line with expectations based on "Polanyi rules",[13, 14] and with results for neutral HOD reactions. The surprise was the bend excitation nearly doubles the cross sections for *both* H^+ and D^+ transfer, and thus results in the largest enhancement of the total cross section, σ_{total}, even though the bend mode provides considerably less energy to drive the reaction, compared to the two stretches. The origin of this bend enhancement was not clear, as one would not expect the bending motion to be coupled to the reaction coordinate. One motivation for the current study was to study mode/bond-selective effects in a simpler system, and one with higher endoergicity.

Mode/bond selective chemistry involving the preferential breaking of the stretch-excited OH or OD bonds of water and isotopologs was first shown in studies of neutral water reactions with H and Cl atoms by the Zare and Crim groups.[15-21] These effects are consistent with expectations, first outlined by Polanyi and co-workers,[13, 14] that reactions should be enhanced by energy that puts momentum in the coordinate that corresponds to motion over the rate-limiting barrier. For endoergic reactions, this barrier is late in the collision, and the appropriate coordinate is the stretch of the bond being broken in the reaction. In the neutral experiments, it was not possible to excite the bend mode alone, but stretch-bend combination excitations did provide some insight into bending effects. Zare and co-workers[22] examined bend effects by comparing reaction with H atoms, of D_2O excited to the (011) and (001) levels. They found little effect of the additional bend excitation, suggesting that the bend motion was not coupled to the reaction coordinate, as might be expected from the nature of the motion. Crim and co-workers studied overtone combination effects on the reaction of H_2O with H and Cl.[20, 23] They found that the

(003) (asym. str.) overtone was considerably more reactive than the (022) (bend and asym. str.) overtone, which has similar energy. This comparison suggests that energy in bending vibration is considerably less effective than energy in stretching of the bond being broken, again consistent with expectations. On the other hand, the reactivity of water excited to the (004) and (023) levels (also similar in energy) was found to be similar, which would tend to imply that energy in the bend and asymmetric stretch have similar effects, at least for these very high levels of vibrational excitation.

In this paper, we report a guided ion beam study of the reaction of mode-selectively excited HOD^+ with N_2. The proton transfer (N_2H^+, $\Delta H_{rxn}(0\ K) = 1.03$ eV) and deuteron transfer (N_2D^+, 1.02 eV) reactions are roughly twice as endoergic as analogous reactions for CO_2, and thus comparison provides insight into how energetics relate to vibrational effects. This reaction has been studied previously in a Selected Ion Flow Tube (SIFT) apparatus under thermal conditions by Anicich and co-workers[24] and with an Ion Cyclotron Resonance (ICR) apparatus by Karpas *et al.*[25] No reaction was observed in either case, due to the significant endoergicity of the reaction. We are unaware of any previous beam studies.

Experimental and Computational Methods

The guided ion beam tandem mass spectrometer used in this study has been described previously, along with experimental and analysis protocols.[26, 27] Helium is bubbled through a 50/50 mixture of H_2O and D_2O to generate 96% He with 4% water, half of which is HOD. HOD^+ can be generated in selected vibrational states by REMPI through the **C** ($^1B_1$) state.[28] The HOD^+ was prepared in the following states: (000) ground state, (001) OH stretch 0.396eV, (010) bend 0.153eV, and (100) OD stretch 0.293eV. The state selection purity, measured by photoelectron spectroscopy, is 100% for the ground state, OH stretch, and OD stretch, but only 56% for the bend, with the remaining 44% produced in the ground state. The bend-excited cross sections

reported below have been corrected for this admixture of ground state HOD^+, using the cross sections separately measured for pure ground state HOD^+.

The HOD^+ ions were formed between a pair of planar electrodes, and the resulting ions were injected into a quadrupole ion guide, which focused them into a quadrupole mass filter to remove any unwanted ions produced in the REMPI process (e.g., OH^+, OD^+, H_2O^+, D_2O^+…). If significant amounts of H_3O^+ were produced by ion-molecule reactions in the source, then proton transfer from H_3O^+ to N_2 might contribute spurious signal to the N_2H^+ channel for $E_{col} > 2.07$ eV, where this reaction becomes energetically possible. To avoid this problem, the source was operated under conditions that produced negligible intensities of HD_2O^+ and D_3O^+, i.e., the H_3O^+ isotopologs that can be detected with no mass interferences. A time-of-flight (TOF) gating electrode pair at the end of the primary beam mass filter was used to narrow the ion beam kinetic energy spread to ~0.15 eV, compensating for the space charge broadening that resulted from the need to tightly focus the REMPI laser to pump through the short-lived **C** state. The mass-, state-, and kinetic energy-selected ions were injected into a system of 8-pole ion guides,[29] the first of which guided the ions through a 10cm long scattering cell containing N_2 (from liquid N_2 boil-off) at 1×10^{-4} Torr, measured by a capacitance manometer. Unreacted HOD^+ ions, along with any product ions, were collected by the guide and passed into a second, longer guide section for TOF velocity analysis, before being mass analyzed and detected. Products that were backward-scattered in the laboratory frame were reflected at the entrance of the guide system, and subsequently detected at long times, corresponding to apparent long velocities. Ions were counted using a P7882 FAST ComTec multichannel scalar, controlled by a LabView program that cycled through collision energies and masses of interest, and switched the target gas flow between the scattering cell and chamber background. Integral cross sections were calculated from the ratio of reactant and product ion intensities (integrated from the TOF measurements), corrected for ions formed outside the scattering cell, using the calibrated effective length of the scattering cell and the pressure was measured with a capacitance manometer.

TOF was used both to measure the energy of the reactant ion beam, as well as the axial projection of the recoil velocity distribution of the products (v_{axial}). Several complete sets of cross sections for both product channels were measured for all reactant states of HOD^+ as a function of collision energy, each set taking a day. Because the cross sections are small in this system, separate, longer TOF acquisitions were done for selected collision energies for each HOD^+ vibrational state. To avoid systematic errors due to possible day-to-day variations in instrument conditions, the ground state reaction cross sections were compared for each data set, before averaging. In all cases, the ground state cross sections agreed within the statistical uncertainty, thus all data sets were averaged to generate the data presented below.

The cross section uncertainties are estimated as follows. The standard deviation of the cross sections over the set of runs was < 20 %; however, this run-to-run variation also includes systematic error sources that do not affect the relative uncertainty for comparing cross sections for N_2H^+ vs. N_2D^+, or for reaction of different HOD^+ vibrational states. For example, error in N_2 pressure measurement affects both channels identically, and differences in relative detection efficiency for product vs. primary ions would also tend to have similar effects on both channels because the product masses are similar. For this reason, we estimate that 20% is an upper limit on the relative uncertainty. The exception is the data for collision energies near the reaction threshold, where, from the data scatter, we estimate that the cross section uncertainty is ~0.05 $Å^2$. The main sources of uncertainty in the absolute scale of the cross sections are absolute pressure calibration, and possible differences in detection efficiency for primary and product ions, and our usual methods for calibrating are described elsewhere.[26, 30, 31] In this case, we checked our calibration by measuring the cross sections for $HOD^+ + CO \rightarrow COH^+/COD^+$ under identical conditions. With no adjustments to the calibration, the measured total cross section at low collision energy matches the capture collision cross section within 3%. For that system, unit reaction efficiency is expected from the reported thermal rate constant.[32]

To map out the reaction coordinate, electronic structure calculations were performed at several levels of theory using GAUSSIAN03.[33] For stable points (reactants, complexes, products), energies were calculated at the G3 level of theory. Because the PBE1PBE/6-311++G** method was found to be in reasonable agreement with experimental energetics, and with the G3 calculations of complexes, this method was used in mapping out the reaction coordinate. In addition to optimizing stationary points (transition state, complexes), we also mapped out parts of the potential energy surface, with emphasis on coordinates associated with reactant approach, product recoil, and select vibrational modes.

Results

Computational Results

The reaction coordinate for this system is shown in the inset to Figure 9.1. More detail regarding the potential energy surface is given in the discussion. The energies shown in the figure are experimental for the reactants and products,[34, 35] and the energy of the complex is from a G3 calculation, referenced to the G3 calculations for the reactants. The complex has the H_2O^+ forming a weak hydrogen bond to the end of the N_2 moiety with a N-H bond distance of 1.656 Å and a NNH bond angle of 177.7°. The OH bond length for the H atom bound to N_2 is 1.05 Å, which is only slightly elongated relative to the 1.00 Å OH bond length calculated for free H_2O^+ at the same level of theory. Similarly, the HOH bond angle in the complex (110.8°) is quite close to that calculated for free H_2O^+ (109.9°). In the N_2H^+ product, the N-H distance is 1.04, and the NNH angle is 180°. Because no significant rearrangements are needed to form the complex from reactants, it is unlikely that there should be any activation barrier to inhibit its formation. Similarly, we would not anticipate any barrier in excess of the endoergicity, separating the complex from the product channel.

Ground State Integral Cross Sections

Product ions were observed at masses 29 and 30, corresponding to N_2H^+ and N_2D^+, respectively. The integral cross sections for both channels from reaction with ground state HOD^+ are given in Figure 9.1 over a center-of-mass (CM) collision energy (E_{col}) range of 0.48 eV to 3.85 eV. The reactions are:

$HOD^+ + N_2$	$\rightarrow N_2H^+ + OD$	(H^+ transfer)	$\Delta_rH = 1.03$ eV
	$\rightarrow N_2D^+ + OH$	(D^+ transfer)	$\Delta_rH = 1.02$ eV

where the enthalpy of reaction given is obtained using the experimental 0 K enthalpy for reaction of H_2O^+ with N_2, corrected for the effects of deuteration using zero point energies from the G3 level calculations on the reactants and products. The threshold energy difference between N_2H^+ and N_2D^+ is far too small to have detectable effects on the experimental cross sections, which are broadened by both thermal motion of the N_2 target and the ~0.15 eV energy spread of the HOD^+ ion beam (full width at half maximum of the Gaussian distribution obtained by fitting TOF data). The fact that products are seen below the ~1 eV thermodynamic threshold also reflects these broadening factors. Because the threshold energies are not in question for this system, we did not attempt to extract cross sections corrected for the broadening. We did, however, verify that the experimental cross sections are consistent with the thermodynamic thresholds, i.e., they can be fit within experimental error using a simulation[36] based on the assumption of a modified line-of-centers threshold model[37-40] using 0.15 eV as the primary beam energy spread, and 300 K as the N_2 target temperature.

Vibrational Mode Effects on Integral Cross Sections

The cross sections for the N_2H^+ and N_2D^+ products for the four different HOD^+ reactant states are plotted as a function of total energy (E_{tot}) in Figure 9.2. The three modes examined

(OH stretch = 396meV, OD stretch = 293meV, Bend = 153meV) differ by more than a factor of 2 in energy, and all three significantly change the available energy, especially in the threshold energy range. To allow the effects of the vibrational modes to be compared directly, and to allow easy comparison with the effects of adding equivalent amounts of collision energy, Figure 9.2 plots the cross sections vs. total energy. If vibrational excitation had effects equivalent to collision energy, then the cross section curves would all be superimposable on the ground state cross section. With one exception (OD stretch excitation, N_2H^+ product) the vibrational effects are substantially larger than those from E_{col}, and the effects on both σ_{total} and N_2H^+/N_2D^+ branching are quite mode specific. In the following discussion, we will refer to the stretch of the bond broken in the H^+/D^+ transfer as the "broken-bond stretch", and the stretch of the other bond as the "spectator" bond stretch. For example, in the reaction $HOD^+ + N_2 \rightarrow N_2H^+ + D$, the (001) mode is the broken-bond (i.e., OH) stretch, and the (100) mode is the spectator (OD) stretch.

Product Recoil Velocity Distributions

Additional insight into the reaction mechanism can be obtained by considering the product ion recoil velocity distributions. Because our experiment is axially symmetric, considerable dynamical insight can be extracted by simply measuring the projections of the full 2-D velocity distributions on the axis of the experiment, i.e., v_{axial} distributions. Selected lab frame v_{axial} distributions for the N_2H^+ and N_2D^+ product ions from reaction of HOD^+ in various states are given in Figures 9.3 and 9.4, respectively. In each frame, the distributions are scaled so that their integrals are equal to the magnitude of the corresponding integral cross sections. In our geometry, the average relative velocity of the collisions and the average velocity of the CM frame with respect to the lab, $<V_{CM}>$, lie along the axis of the ion guide. Therefore, products that are forward scattered in the CM frame have lab velocities greater than $<V_{CM}>$, and backward-scattered products have lab velocities below $<V_{CM}>$. In the figure, the values of $<V_{CM}>$ at each E_{col} are indicated by heavy vertical lines. If the reaction proceeds via a complex with a lifetime

($\tau_{collision}$) greater than its rotational period ($\tau_{rotation}$), the resulting v_{axial} distribution must be forward-backward symmetric about $<V_{CM}>$; an asymmetric v_{axial} distribution is proof the mechanism is direct (fast compared to the complex rotational period), and also reveals the dominant scattering mechanism. Finally, the shape of the distributions provides insight into partitioning of the available energy (E_{avail}) into recoil energy (E_{recoil}).

Two experimental factors must be kept in mind when considering the distributions. The velocity distributions of the reactant ions and N_2 target result in a distribution of collision energy and geometry, which broadens the v_{axial} distributions significantly. Analysis of the distributions to correct for this broadening is discussed below. The other issue for the present system is that some product ions are scattered at very low lab velocities where they are highly susceptible to small potential or effective potential distortions in the ion guides.[41] As a result of these distortions, a fraction of the slow ions tends to arrive at the detector at very long times (due to reflections in the ion guide), contributing to artifactual v_{axial} peaks with apparently near-zero lab velocities. While the ion optics are biased to ensure that such reflected ions are collected and counted in the integral cross sections, we ignore ions with apparent v_{axial} below 500 m/sec in fitting of the v_{axial} distributions.

In this system, the distributions are strongly asymmetric, indicating that proton transfer is direct at all E_{col} examined. Direct scattering is not surprising given the reaction coordinate shown in Figure 9.1. The well depth is small compared to the endoergicity, ensuring that even for collisions near threshold, the lifetime of the collision complex should be small. The distributions are strongly backward-peaked, but with a significant tail extending well into the forward hemisphere ($v_{axial} > <V_{CM}>$). Note that because we measure scattering of the ionic products, "backward" corresponds to small angle, stripping-type dynamics, while large angle, rebound scattering would produce forward-scattered product ions. To interpret the distributions more quantitatively, the data were simulated/fit in order to account for broadening from the distributions of ion beam kinetic energy and N_2 thermal motion. The simulation[26, 42] takes a

model recoil angular and energy distribution, and convolutes it with the experimental broadening factors, then projects the results to create a v_{axial} distribution for comparison with experiment. The model distribution is varied until the simulation matches the data. For this system, we used a two component model – one to fit the sharp backward-scattered peak, and one to fit the broad tail extending into the forward hemisphere. Each component was represented by a simple three parameter model, where the osculating complex model[43] was used to represent the angular distribution, and the E_{recoil} distribution was assumed to be a Gaussian, defined by E_{ratio} and f_{width} parameters which give the peak energy and width as a fraction of E_{avail} (= E_{col} + E_{vib} + E_{rot} – $\Delta H_{rxn}(0K)$). The E_{recoil} distribution is truncated at E_{avail}, if necessary, to ensure energy conservation. The osculating complex model assumes that there is a preferred scattering direction (assumed to be 180° here), but that the scattering is broadened by rotation of the collision complex, with the broadening determined by the parameter τ_{ratio} (= $\tau_{rotation}$ / $\tau_{collision}$). For the present system, where reaction is direct at all energies, the angular distribution probably depends as much on impact parameter as on collision time. Therefore, we consider the osculating complex model and its τ_{ratio} parameter as simply means to generate model distributions with controllable shape, and do not attribute any particular significance in terms of collision time.

It turns out that good fits (the solid curves in Figures 9.3 and 9.4) can be generated for the entire data set (i.e., both N_2H^+ and N_2D^+, all collision energys, and for all HOD^+ states) using rather similar sets of simulation parameters. In each case, the backward peak was fit using a narrow backward-peaked component ($10 \leq \tau_{ratio} \leq 18$), with a recoil energy distribution peaking sharply at the maximum available energy ($E_{ratio} = 1$, $f_{width} = 0.25 – 0.5$). Because the distributions are truncated at E_{avail}, the resulting recoil energy distribution is really a half Gaussian peaking at $E_{recoil} = E_{avail}$. The broad tail extending into the forward direction was fit by an isotropic component ($\tau_{ratio} = 0.1$), with a broad E_{recoil} distribution ($E_{ratio} = 0$, $f_{width} = 10$) that has substantial intensity for energies up to where it is truncated at E_{avail}. Furthermore, the coefficients of the sharp backward, and broad isotropic components are also similar across the entire data set,

varying only from 40:60 to 55:45. The similarities in the simulation parameters imply that the scattering dynamics are not strongly influenced by either E_{col} or HOD^+ state, in contrast to the strong effects on σ_{total} and product branching. Table 9.1 summarizes the results. Values are given for $\langle E_{recoil}\rangle/\langle E_{avail}\rangle$, i.e., the average fraction of available energy appearing in recoil, and for $\langle E_{recoil}\rangle$, the average recoil energy. In addition to these simulation results, the table also lists values for R_{asym} ($I_{backward}/I_{forward}$), which is simply the ratio of integrated experimental intensity below and above $\langle V_{CM}\rangle$, provided to give a model-independent measure of the forward-backward asymmetry.

Discussion

Ground State Mechanism

Given the tiny difference in energetics for N_2H^+ vs. N_2D^+ formation, it is not surprising that the ground state cross sections for N_2H^+ and N_2D^+ are identical with experimental error near threshold, where available energy is expected to be the most important factor determining reactivity. At higher energies, dynamical effects have the potential to cause isotope effects. For example, in the analogous reaction of ground state HOD^+ with CO_2 (~0.55 endoergic), the cross section for CO_2H^+ production is ~30% larger than that for CO_2D^+ for $E_{col} > 2$ eV.[11] For N_2, the difference in H^+/D^+ transfer cross sections is insignificant (~5%), indicating that such dynamical isotope effects are small for this reaction in the energy range probed. For the ground state reaction, the total cross section rises quite slowly from threshold, such that it is only ~0.5 $Å^2$ (~3.5% of $\sigma_{collision}$) and still rising at E_{col} = 4 eV. At this energy, $\sigma_{collision} = \sigma_{HardSphere}$ = ~14 $Å^2$ calculated using covalent radii[44] for the atoms. In contrast, the ground state cross section for the proton transfer reaction with CO_2 rises rapidly to ~ 5 $Å^2$ at E_{col} of only 1 eV, and then levels off at higher energies.[11]

There are a number of reasons why a simple proton transfer reaction like this might be quite inefficient (more than an order of magnitude less efficient than the analogous reaction with

CO_2). For example, if reaction were facile only in a narrow range of reactant orientations, a drastic reduction of efficiency would result.[42, 45] One would not expect any steric hindrance in either the N_2 or CO_2 cases, but it might be that the energetics are only favorable in a narrow range of angles. Both N_2 and CO_2 are $^1\Sigma_g^+$ molecules, thus reaction cannot depend on azimuthal angle. We might expect that the structures of the N_2H^+ or CO_2H^+ product ions, or possibly the structures of the intermediate complexes, might provide insight into the geometries that are most favorable for the proton transfer event (i.e., the structure of the rate-limiting transition state). Furthermore, the magnitude of the frequency corresponding to H-NN or H-OC bending in the product ions should provide some idea of how rapidly the reaction coordinate energy might increase upon distortion away from the most favorable geometry. The H_2O^+-N_2 complex has a near-linear HNN bond, as shown in Figure 9.1, and the N_2H^+ product ion is linear, suggesting that the preferred proton transfer geometry also has linear HNN. For $H_2O^+ + CO_2$, there is an analogous complex with similar bond lengths[11]; however, the HOC angle is ~146° in the H_2O^+-CO_2 complex, and ~120° in the $HOCO^+$ product ion, suggesting that the preferred proton transfer geometry has water attacking from the side with HOC angle somewhere in the 120 – 150° range (the CO_2 moiety remains essentially linear in the complex and $HOCO^+$ product). The fact that the HOC bending mode of $HOCO^+$ (997 cm^{-1}) has higher frequency than that of the corresponding HNN^+ bend (823 cm^{-1}) would tend to suggest that reaction with N_2 might be slightly *less* sensitive to orientation than CO_2; however, a requirement for HNN to be linear would result in a severe bottleneck to reaction. Assuming that reaction can occur only when reactants approach with HNN or HCO polar angles within $d\theta$ of the most energetically favorable angle (θ_{Emin}), the reaction probability would scale (in the limit as $d\theta \rightarrow 0$) like $\sin(\theta_{Emin}) \cdot d\theta$. The fact that θ_{Emin} is almost certainly near 0° for N_2, implies that only a small fraction of collisions occur with near-optimal geometries, which would account for the very low reactivity. At low E_{col}, there may be some orientational steering as reactants approach; however, such effects are unlikely to be significant for $E_{col} > 1$ eV, where reaction is possible. The increase in reactivity with increasing E_{col} may

relate to decreasing sensitivity to approach geometry as the available energy increases above threshold. As shown below, it does not appear that increases in the range of reactive impact parameters (i.e., the opacity function) can be responsible for increasing reactivity.

Velocity Distributions

We first consider the velocity distributions for the ground state reaction (Figures 9.3 & 9.4). Several points are obvious. Based on the simulations (Table 9.1), the average amount of energy appearing in recoil increases from ~0.3 eV at E_{col} = 1.4 eV, to ~2 eV at E_{col} = 3.8 eV; however, the average fraction of energy appearing in recoil is constant at ~70% for both N_2H^+ and N_2D^+, independent of E_{col}. The 70% reflects the average of the contributions from the backward peak ($E_{recoil} \approx E_{avail}$) and the broad tail, where E_{recoil} is in a broad distribution ranging from zero to E_{avail}. If we assume, as is almost certainly true at high E_{col}, that the recoil behavior is strongly influenced by impact parameter, then the results indicate that H^+/D^+ stripping in large impact parameter collisions leads to nearly all available energy appearing in recoil, i.e., not much excitation of product internal energy. More central collisions, recoiling to generate the broad forward tail, lead to broad distributions of recoil energy, with correspondingly large variation in partitioning E_{avail} between internal and recoil energy. The R_{asym} values are also similar for N_2H^+ and N_2D^+; however, they do change significantly with E_{col}. At the highest E_{col}, the ratio is ~5.5, increasing to ~10 at E_{col} = 2 eV, where there are hardly any forward-scattered product ions from the ground state reaction. At E_{col} = 1.4 eV, the ratio apparently decreases to ~2.4; however, this decrease is at least partly an artifact of experimental broadening. Consider that for energies just above threshold, the CM frame recoil velocities must be near zero (i.e., lab velocities near $<V_{CM}>$); therefore, experimental broadening will tend to generate apparently forward-backward symmetric distributions (R_{asym} = 1), regardless of how asymmetric the true v_{axial} distributions might be. By E_{col} = 1.4 eV (0.4 eV above threshold), the v_{axial} distributions are clearly

asymmetric, but the recoil velocities are still low enough that the apparent backward/forward ratio is significantly reduced by broadening.

The line-of-centers model is commonly used to simulate the cross sections for endoergic reactions near threshold.[46] In this model, the increase in cross section as E_{col} is increased above threshold results from an increase in the maximum impact parameter leading to reaction. For the $HOD^+ + N_2$ system, the maximum reactive impact parameter predicted by the line-of-centers model, b_{max}, increases from $\sim 0.53 \cdot R_{HardSphere}$ for $E_{col} = 1.4$ eV, to $\sim 0.87 \cdot R_{HardSphere}$ for $E_{col} = 4$ eV, and if scattering were also hard sphere-like, this would set a limit on how large the scattering angle could be: $\theta_{max} = \pi - 2\text{acos}(b_{max}/R_{HardSphere})$, where the factor of π is included because the charge is transferred in the reaction, and we are detecting the product ions. This maximum scattering angle would be only ~64° for 1.4 eV, which would imply only forward-scattered ions; clearly inconsistent with the strongly backward-peaked v_{axial} distributions. Even at 3.8 eV, the maximum angle would be ~120°, and the resulting v_{axial} peak would be considerably closer to V_{CM} than what we observe. Rather than this slow evolution from forward to backward-peaked distributions with increasing energy, we observe strong backward peaking at all energies, indicating that a line-of-centers/hard sphere scattering model is not even approximately reasonable for this reaction in the under 4 eV E_{col} range.

In fact, between $E_{col} = 2$ and 3.8 eV, R_{asym} drops significantly, which is opposite to what would be expected if the maximum reactive impact parameter increased with E_{col}. The sharpness of the backward-peaked (stripping-like) component of the distribution does increase, which would tend to suggest reaction at larger impact parameters; however, the broad tail extending into the forward hemisphere increases as well. In an impulsive scattering mechanism, this tail would correspond to increased reactivity at small impact parameters, and such an increase is not unreasonable, given that the reaction efficiency is so small for the ground state reaction (<3.5% at 4 eV). The conclusion is that reaction occurs over a broad range of impact parameters at all energies, but with low probability that increases slowly with E_{col}.

The factor of 3 to 5 enhancements in N_2H^+ and N_2D^+ production when the broken-bond stretch is excited, and the doubling of the cross sections observed upon bend excitation, suggest that there might be some qualitative change in the reaction mechanism enabled by vibrational excitation. Figures 9.3 and 9.4 show the v_{axial} distributions for the two channels for all four HOD^+ reactant states, at E_{col} from 1.4 to 3.8 eV. These data are at energies well below, near, and well above the $E_{total} \approx 2$ eV breakpoint where the E_{col} and vibrational mode dependence of the integral cross sections (Figure 9.2) undergo qualitative changes, suggesting the possibility of a change in reaction mechanism. The effects of HOD^+ vibrational excitation on the recoil behavior are quite small but do provide some indication of how energy in different initial states is partitioned in the products. For example, when HOD^+ is vibrationally excited, the average energy appearing in recoil increases. The effect is seen most easily for the lower E_{col} data, where the contribution of vibration to E_{avail} is most significant. For example, at 1.4 eV, $E_{avail} \approx 0.4 + E_{vib}$, i.e., OH and OD stretch excitation (396 and 293 meV) nearly double E_{avail}, and even bend excitation (153 meV) increases E_{avail} by 50%. The average energy appearing in recoil (according to the simulations) does increase, but by a smaller factor, such that the ratio, $\langle E_{recoil} \rangle / \langle E_{avail} \rangle$, decreases from ~70% for the ground state, to ~60% for the OH stretch excited reaction. Based on the breaking bond – spectator bond picture, we might also expect that there should be a difference in the fraction of energy going to recoil in the N_2H^+ and N_2D^+ products, for excitation of the OH and OD stretch modes. Such an effect, if present, is within the uncertainty of the E_{recoil} values extracted by fitting the distributions (uncertainty estimated at 10% – 16%).

It is somewhat surprising that HOD^+ vibrational excitation can have such dramatic effects on the integral cross sections, without more obvious effects on the recoil behavior. The fact that reaction efficiency is strongly mode-dependent implies that the rate-limiting step in the reaction is early in the collisions, where the system still "remembers" the initial state. In contrast, product recoil is affected by dynamics through the entire collision, including rotation during the collision time, energy redistribution between E_{col} and internal modes, and interactions between products as

they separate. Nonetheless, one might expect that the large vibrational enhancements might imply significant changes in the distribution of reactive impact parameters, and that would almost certainly result in obvious changes in the v_{axial} distributions. In this system, the results suggest, instead, that vibrational excitation increases the probably of reaction at all impact parameters, such that scattering at all angles is enhanced.

Vibrational Effects

As shown in the top frame of the Figure 9.2, excitation of the broken-bond (i.e., OH) stretch results in a ~5x enhancement of the N_2H^+ channel, excitation of the bend roughly doubles the cross section, but excitation of the spectator bond (i.e., OD) stretch has no effect beyond that from adding available energy. For N_2D^+ production (middle frame), the situation is approximately reversed. Broken-bond (i.e., OD) stretch excitation results in a large (3x – 4x) enhancement, and bend excitation, again, roughly doubles the cross section. Excitation of the spectator (OH) stretch does enhance the D^+-transfer reaction, presumably because it provides such a large increase in E_{avail}; however, the effect is smaller than that of the much lower energy bend mode. In essence, the observation is that stretch excitation of the OH or OD bonds greatly enhances the probability of transferring H^+ or D^+, respectively, while having little or no effect on transfer of the D^+ or H^+ of the spectator bond. As described in the Introduction, and in our previous paper on $HOD^+ + CO_2$,[11] this is just the effect that might be expected from consideration of the reaction coordinates for H^+ or D^+ transfer. On the other hand, the relatively large, 2x enhancement from bend excitation (153 meV) is unexpected, as this mode is not obviously coupled to the H^+/D^+ transfer reaction coordinate, and is considerably lower in energy than two stretch modes.

The bottom frame of Figure 9.2 shows the effects of vibrational excitation on σ_{total}. The energy dependence of the cross sections suggests that there may be two mechanistic regimes. For E_{tot} below ~2 eV, all modes of vibration excitation, as well as collision energy, strongly enhance

reactivity, with effects that depend on mode, not just energy. Note, for example, that bend excitation gives a larger enhancement than OD stretch excitation, even though the OD stretch has nearly twice the energy of the bend. Above ~2 eV, vibrational excitation continues to cause large enhancements; however, the relative effect of the different modes changes considerably. By E_{total} ~ 4 eV, the enhancements become roughly proportional to the energy of the modes.

This pattern is just the opposite of what might be expected. The strongest mode-specific effects are seen near threshold, yet this is where we might expect the energy content of the vibrational modes to be most important. At energies well above threshold, the energy of the vibrations is negligible compared to E_{tot}, yet this is where the enhancements of σ_{total} are proportional to E_{vib}. In fact, we argue that vibrational dynamics, rather than E_{vib}, are the important factor at all energies. Several features of the data show the strong influence of dynamics even at high energies. Obviously, the branching between H^+ and D^+ is still strongly mode specific, which implies control by dynamics, rather than energetics. Furthermore, even for σ_{total}, the vibrational effects at high energies remain much larger than the collision energy effects, which become weak and variable in the high energy range. For HOD^+ in its ground state or with OD stretch excitation, E_{col} still enhances reaction, but weakly. For HOD^+ with bend or OH stretch excitation, E_{col} actually slightly inhibits reaction. Extrapolating the dependence of the vibrational effects on E_{tot}, it seems likely that as energy continues to increase, the effects of OH and OD stretch excitation will remain significant, and the bend enhance appears to be disappearing.

Origin of the Vibrational Effects

In this system, the reaction coordinate (Figure 9.1) is attractive for reactant approach, and the endoergicity is manifest as the products separate. In this sense, the reaction could be described as being controlled by a late barrier, and as discussed by Polanyi and co-workers[13, 14] for A + BC model reactions. The mechanism for the enhancement shown in these classic studies

is that stretching motion of the BC bond gives the system momentum along the correct coordinate to get around the bend on the potential energy surface so that the available energy is effective in driving the system over the late barrier. For a late barrier system, partitioning energy into E_{col} was predicted to be less effective, because the momentum is perpendicular to the product exit channel, and the system is likely to simply reflect off the repulsive wall, exiting back to reactants. This last point, at least, is true for the $HOD^+ + N_2$ system, where E_{col} is much less efficient than vibrational excitation in driving reaction.

There are several factors to keep in mind when considering how vibrational excitation might affect this reaction. The fact that the effects are strongly mode-specific implies that the critical point where vibration affects reactivity must be early enough on the reaction coordinate that the system still "remembers" the initial mode of excitation. For polyatomic reactants, the different vibrational modes correspond to momentum along different coordinates, which may be coupled differently to the reaction coordinate. Finally, note that all of the vibrations in this system have energies well below the threshold energy for reaction, thus reaction is driven by some combination of energy initially in vibration and collision energy. Furthermore, the vibrational enhancements are much larger than the effects of similar amounts of E_{col}, which suggests that vibrational excitation must greatly increase the efficiency with which momentum initially in relative motion is converted to momentum up the slope into one of the product channels.

In hopes of providing additional insight into the origins of the vibrational effects, we calculated a reduced potential energy surface (PES) for the reaction, using the PBE1PBE/6-311++G(d,p) level of theory and referencing the energy to the reactants at the same level of theory. The result is shown in Figures 9.5 and 9.6 for H^+ and D^+ transfer, respectively. The zero of the PES is in reference to the reactants at infinite separation at their equilibrium geometries. The idea is to try to focus on coordinates that represent reactant motions and distortions of interest (reactant approach, product separation, vibrations of interest), either freezing or

optimizing all other degrees of freedom. Because the most favorable reactant approach (see above) has N-H-O angle near linear, the surfaces shown in Figures 9.5 and 9.6 were calculated as follows: The NHO angle was fixed at 179.9°, and the two coordinates scanned for the case of H^+ transfer were the NN-HOD and NNH-OD distances, which correspond to reactant approach and product separation. For the case of D^+ transfer (Figure 9.6), the relevant coordinates are the NN-DOH and NND-OH distances. All other bond lengths were allowed to optimize, as were all other angles, with the exception of the HOD bend angle, which was frozen at one of three angles: 110° (the equilibrium angle in free HOD^+, 90° (the inner turning point of the bend vibration for free HOD^+), and 133° (the outer turning point of the bend vibration for free HOD^+). In essence, therefore, we are modeling the reaction as a near-collinear, pseudo-triaomic reaction, A+ BC → AB + C, where A = N_2, B = H^+/D^+, C = OD/OH).

For a reaction like this, where a light atom (H^+ or D^+) is transferred between two heavy moieties (N_2 and OD/OH), plotting the PES in Cartesian coordinates gives a misleading impression of the expected motion, because the inertia associated with motion in different directions is so different. As described by Levine and Bernstein,[46] the PES can be transformed to mass-weighted coordinates in which the reactant approach and product recoil coordinates are scaled and skewed such that on the transformed surface, the motion is just what intuition would predict. In Figure 9.5 and 9.6, we show the PES scaled and skewed for the cases of H^+ and D^+ transfer in reaction of HOD^+, and the scale factors and skew angles are given in Table 9.2. The "a" and "b" scaling parameters, which stretch the reactant and product valleys, respectively, are similar for all isotope combinations. The skew angle, however, is highly sensitive to the mass of the transferred H^+ or D^+, with D^+ transfer having a skew angle that is significantly less acute. It is somewhat surprising that this difference in skew angle does not result in a significant change in reactivity for H^+ vs. D^+ transfer. In the $HOD^+ + CO_2$ system, where similar mass-weighting parameters apply, H^+ transfer is ~30% more efficient than D^+ transfer for E_{col} for energies greater that about three times the threshold energy (E_0 = ~0.5 eV).

Given the PES results, the enhancement from exciting the broken-bond stretching vibration can be seen as putting momentum into a coordinate that helps the system transfer to the product valley. To illustrate this point, the dashed curves in the figures shows what the broken-bond and spectator stretch modes look like when projected onto the PES, assuming that the NHO angle or NDO angles are linear. These projections are intended only to give a qualitative idea of the nature of the stretch motions in the entrance channel, and were calculated by simply adding the motion in the OH or OD stretches of free HOD^+ to the relative motion, here corresponding to E_{col} of 1.5 eV, i.e., 0.5eV above threshold. In actual trajectories, the motion would be complicated by zero point motion in all modes, the vibrations would evolve as the system moves into the strong-interaction region of the PES, and the molecular orientations and vibrational phases would be random. With these limitations in mind, it is still clear that the broken-bond stretch puts substantial momentum into the coordinate corresponding to crossing from the reactant to product valleys, whereas excitation of the spectator stretch results in hardly any motion in the coordinate transverse to the reactant valley.

It is less obvious why HOD^+ bending vibration should enhance reaction. From the perspective of vibrational momentum, one might think that the bend excitation would carry over into rotation of the products, which is not expected to be accompanied by any enhancement of reactivity. To help assess how bending couples the system to the reaction coordinate, Figures 9.5 and 9.6 shows how the PES varies with bend angle, frozen at its equilibrium bend angle (110°) and at angles corresponding to the classical inner (90°) and outer (133°) turning points of the fundamental of the bend vibration. It can be seen that the shape of the repulsive wall is somewhat dependent on the bend angle, and in particular, when HOD^+ is near its outer turning point, the transition into the product valley is significantly less repulsive. It is not unreasonable to expect that this change might help the system move into the product valley, retaining sufficient momentum up the slope leading to products. For the inner turning point, the situation is reversed, and thus reactivity is presumably strongly inhibited in collisions that occur with HOD^+ strongly

bent. Because overall reaction efficiency is so low, however, it would not take a very large enhancement of reaction for HOD^+ near its outer (more linear) turning point, to offset a total loss of reaction for HOD^+ colliding in strongly bent geometries.

It would be interesting to examine trajectories of the $HOD^+ + N_2$ system to see if the qualitative rationalizations proposed to explain the vibrational effects are borne out by in more detailed calculations. For a reasonable hope of understanding the origins of the vibrational effects, our experience has been that several hundred *reactive* trajectories are needed for each reactant state. In the N_2 system, the v_{axial} results indicate that reaction occurs over a wide range of impact parameters, but with < ~3% efficiency, thus on the order of twenty thousand trajectories would be needed. This size trajectory set is not feasible if the force and Hessian calculations are carried out at a high enough level of theory to reproduce subtle effects like vibrational mode effects. In principle, microscopic reversibility applied to a trajectory study of the reverse reaction (which is presumably more efficient), could shed some light on the vibrational effects; however, it is far from obvious what initial conditions (partitioning of E_{avail} between NNH^+/OD vibrations, rotations, translation) should be used to connect to the reactant states we have studied for the forward reaction. Fortunately, the reactions of HOD^+ with N_2 and CO_2 appear to be dynamically quite similar, but reaction efficiency with CO_2 is an order of magnitude higher. We are currently completing a large set of *ab initio* trajectories of $HOD^+ + CO_2$ collisions, in an attempt to understand the origins of the dynamical effects more clearly.

Conclusion

We have presented a detailed study of the mode and bond selective reaction of $HOD^+ + N_2$. Exciting the OH stretch (001) mode enhances H^+ transfer much more efficiently than adding collision energy, but has little effect on D^+ transfer. The converse is true when the OD stretch (100) mode is excited. These effects are consistent with expectations, and reflect the fact that the OH and OD stretch modes correlate directly the corresponding H^+/D^+ transfer reaction

coordinates. Surprisingly, excitation of the bend results in a factor-of-two enhancement for both channels, and the origin of this effect is unclear, but may relate to effects of water cation distortion on the shape of the repulsive wall and product channels on the potential energy surface.

Acknowledgment

This work was supported by a grant from the Chemistry Division of the National Science Foundation (CHE-0647124).

References

1. G. Herzberg, Ann. Geophys. **36**, 605 (1980).

2. W. T. Huntress, Jr., Astrophys. J., Suppl. Ser. **33**, 495 (1977).

3. R. A. Morris, A. A. Viggiano, J. M. V. Doren and J. F. Paulson, J. Phys. Chem. **97**, 3051 (1992).

4. P. Gammelgaard and B. Thomsen, Astron.Astrophys. **197**, 320 (1988).

5. M. E. Brown, A. H. Bouchez, H. Spinrad and C. M. Johns-Krull, Astron. Astrophys. **301**, L1 (1995).

6. H. Balsiger, K. Altwegg, F. Buehler, J. Geiss, A. G. Ghielmetti, B. E. Goldstein, R. Goldstein, W. T. Huntress and W. H. Ip, Nature **321**, 330 (1986).

7. K. Jockers, T. Credner and T. Bonev, Astronomy and Astrophysics **335**, L56 (1998).

8. V. G. Anicich, *An Index of the Literature for Bimolecular Gas Phase Cation-Molecule Reaction Kinetics*. (National Aeronautics and Space Administration, and Jet Propulsion Laboratory,California Institute of Technology, Pasadena, California, 2003).

9. Y. Li and J. M. Farrar, J. Phys. Chem. A **108**, 9876 (2004).

10. L. Liu, X. Cai, Y. Li, E. R. O'Grady and J. M. Farrar, J. Chem. Phys. **121**, 3495 (2004).

11. D. M. Bell, J. M. Boyle and S. L. Anderson, J. Chem. Phys **134**, 64312 (2011).

12. J. M. Boyle, D. M. Bell, S. L. Anderson and A. A. Viggiano, J. Phys. Chem. A **115**, 1172 (2011).

13. M. H. Mok and J. C. Polanyi, J. Chem. Phys. **51,** 1451 (1969).

14. J. C. Polanyi and W. H. Wong, J. Chem. Phys. **51**, 1439 (1969).

15. M. J. Bronikowski, W. R. Simpson, B. Girard and R. N. Zare, J. Chem. Phys. **95**, 8647 (1991).

16. M. J. Bronikowski, W. R. Simpson and R. N. Zare, J. Phys. Chem. **97**, 2194 (1993).

17. A. Sinha, M. C. Hsiao and F. F. Crim, J. Chem. Phys. **92**, 6333 (1990).

18. F. F. Crim, A. Sinha, M. C. Hsiao and J. D. Thoemke, Jerusalem Symp. Quantum Chem. **24**, 217 (1991).

19. R. B. Metz, J. D. Thoemke, J. M. Pfeiffer and F. F. Crim, J. Chem. Phys. **99**, 1744 (1993).

20. J. D. Thoemke, J. M. Pfeiffer, R. B. Metz and F. F. Crim, J. Phys. Chem. **99**, 13748 (1995).

21. J. M. Pfeiffer, J. D. Thoemke, R. B. Metz, A. Sinha, M. C. Hsiao, E. Woods and F. F. Crim, Springer Ser. Chem. Phys. **61**, 32 (1996).

22. M. J. Bronikowski, W. R. Simpson and R. N. Zare, J. Phys. Chem. **97**, 2204 (1993).

23. A. Sinha, M. C. Hsiao and F. F. Crim, J. Chem. Phys. **94**, 4928 (1991).

24. G. B. I. Scott, D. A. Fairley, C. G. Freeman, M. J. McEwan and V. G. Anicich, J. Chem. Phys. **109**, 9010 (1998).

25. Z. Karpas and J. W. T. Huntress, Chem. Phys. Lett. **59**, 87 (1978).

26. Y.-H. Chiu, H. Fu, J.-T. Huang and S. L. Anderson, J. Chem. Phys. **102**, 1199 (1995).

27. J. Liu, B. Van Devener and S. L. Anderson, J. Chem. Phys. **116**, 5530 (2002).

28. B. W. Uselman, J. M. Boyle and S. L. Anderson, Chem. Phys. Lett. **440**, 171 (2007).

29. D. Gerlich, in *State-selected and state-to-state ion-molecule reaction dynamics, Part I. Experiment*, edited by C. Y. Ng and M. Baer (Wiley, New York, 1992), Vol. LXXXII, pp. 1-176.

30. J. M. Boyle, D. M. Bell and S. L. Anderson, Journal of Chemical Physics **134**, 034311 (2011).

31. J. Liu, B. W. Uselman, B. Van Devener and S. L. Anderson, Phys. Chem. Chem. Phys. **8**, 4575 (2006).

32. J. D. C. Jones, K. Birkinshaw and N. D. Twiddy, Chem. Phys. Lett. **77**, 484 (1981).

33. M. J. Frisch, G. W. Trucks, H. B. Schlegel, G. E. Scuseria, M. A. Robb, J. R. Cheeseman, J. J. A. Montgomery, T. Vreven, K. N. Kudin, J. C. Burant, J. M. Millam, S. S. Iyengar, J. Tomasi, V. Barone, B. Mennucci, M. Cossi, G. Scalmani, N. Rega, G. A. Petersson, H. Nakatsuji, M. Hada, M. Ehara, K. Toyota, R. Fukuda, J. Hasegawa, M. Ishida, T. Nakajima, Y. Honda, O. Kitao, H. Nakai, M. Klene, X. Li, J. E. Knox, H. P. Hratchian, J. B. Cross, C. Adamo, J. Jaramillo, R. Gomperts, R. E. Stratmann, O. Yazyev, A. J. Austin,

R. Cammi, C. Pomelli, J. W. Ochterski, P. Y. Ayala, K. Morokuma, G. A. Voth, P. Salvador, J. J. Dannenberg, V. G. Zakrzewski, S. Dapprich, A. D. Daniels, M. C. Strain, O. Farkas, D. K. Malick, A. D. Rabuck, K. Raghavachari, J. B. Foresman, J. V. Ortiz, Q. Cui, A. G. Baboul, S. Clifford, J. Cioslowski, B. B. Stefanov, G. Liu, A. Liashenko, P. Piskorz, I. Komaromi, R. L. Martin, D. J. Fox, T. Keith, M. A. Al-Laham, C. Y. Peng, A. Nanayakkara, M. Challacombe, P. M. W. Gill, B. Johnson, W. Chen, M. W. Wong, C. Gonzalez and J. A. Pople, (Gaussian, Inc., Pittsburgh PA, 2003).

34. S. G. Lias, in *NIST Standard Reference Database Number 69*, edited by P. J. Linstrom and W. G. Mallard (National Institute of Standards and Technology, Gaithersburg, MD, 2003), pp. http://webbook.nist.gov.

35. M. W. Chase, Jr., *NIST-JANAF thermochemical tables*, 4th ed. (American Chemical Society, and American Institute of Physics for the National Institute of Standards and Technology, 1998).

36. J. Liu, B. W. Uselman, J. M. Boyle and S. L. Anderson, J. Chem. Phys. **125**, 133115 (2006).

37. L. Hanley, S. A. Ruatta and S. L. Anderson, J. Chem. Phys. **87**, 260 (1987).

38. P. B. Armentrout, in *The Encyclopedia of Mass Spectrometry. Volume 1: Theory and Ion Chemistry*, edited by P. B. Armentrout (Elsevier, Amsterdam, 2003), pp. 417-426.

39. P. B. Armentrout, in *The Encyclopedia of Mass Spectrometry. Volume 1: Theory and Ion Chemistry*, edited by P. B. Armentrout (Elsevier, Amsterdam, 2003), pp. 426-434.

40. P. B. Armentrout, Int. J. Mass Spectrometry **200**, 219 (2000).

41. D. Gerlich, Adv. Chem. Phys. **82**, 1 (1992).

42. J. Liu, B. V. Devener and S. L. Anderson, J. Chem. Phys. **119**, 200 (2003).

43. G. A. Fisk, J. D. McDonald and D. R. Herschbach, Discuss. Faraday Soc. **44**, 228 (1967).

44. W. M. Hayne, *Handbook of Chemistry and Physics*, 91 ed. (CRC Press/Taylor and Francis, Boca Raton, FL, 2004).

45. J. Liu, K. Song, W. L. Hase and S. L. Anderson, J. Am. Chem. Soc. **126**, 8602 (2004).

46. R. D. Levine and R. B. Bernstein, *Molecular Reaction Dynamics and Chemical Reactivity*. (Oxford University Press, New York, 1987).

Table 9.1. Product ion velocity distribution fit results

		Ecol = 1.4		Ecol = 2.0		Ecol = 4.0	
		N_2H^+	N_2D^+	N_2H^+	N_2D^+	N_2H^+	N_2D^+
Ground State	$\langle E_{recoil} \rangle / \langle E_{avail} \rangle$	0.70	0.70	0.70	0.75	0.70	0.68
	$\langle E_{recoil} \rangle$ (eV)	0.30	0.29	0.60	0.63	2.00	1.95
	R_{asym} [a]	2.4	2.4	9.1	10.0	5.5	5.6
Bend	$\langle E_{recoil} \rangle / \langle E_{avail} \rangle$	0.68	0.68	0.68	0.76	0.68	0.68
	$\langle E_{recoil} \rangle$ (eV)	0.39	0.36	0.70	0.78	2.1	2.1
	R_{asym}	2.6	4.0	4.6	5.0	4.3	3.2
OD Stretch	$\langle E_{recoil} \rangle / \langle E_{avail} \rangle$	0.61	0.68	0.65	0.67	0.68	0.69
	$\langle E_{recoil} \rangle$ (eV)	0.38	0.42	0.74	0.76	2.1	2.1
	R_{asym}	2.3	1.8	3.9	6.0	6.6	4.4
OH Stretch	$\langle E_{recoil} \rangle / \langle E_{avail} \rangle$	0.58	0.61	0.62	0.64	0.72	0.70
	$\langle E_{recoil} \rangle$ (eV)	0.45	0.48	0.79	0.81	2.2	2.2
	R_{asym}	2.5	3.8	4.9	5.0	6.0	5.0

[a] R_{asym} = experimental value of forward-backward asymmetry. A larger value indicates a larger value of backward-scattered products (slower than the velocity center of mass).

Table 9.2: Mass-weighted coordinate parameters for the pseudo-A+BC system, where A = N_2, H = H/D, and C = OD/OH

Parameter	$N_2 + HOH^+ \rightarrow N_2H^+ + OH$	$N_2 + HOD^+ \rightarrow N_2H^+ + OD$	$N_2 + DOH^+ \rightarrow N_2D^+ + OH$
a[1]	3.31	3.36	3.36
b[2]	3.27	3.33	3.29
β[3]	17.27°	16.98°	23.96°

[1] Scaling factor for R(A-B) = R(N_2 – H)

[2] Scaling factor for R(B-C) = R(H-OH)

[3]Skew angle between reactant and product valleys

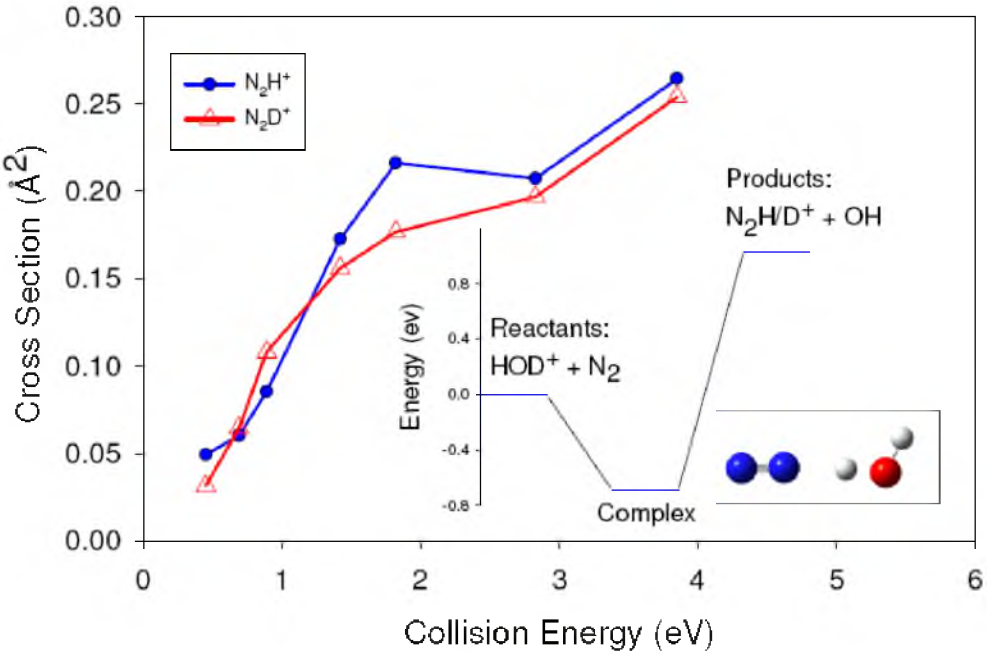

Figure 9.1: Ground state cross sections for production of N_2H^+ and N_2D^+ as a function of E_{col}. Inset: The reaction coordinate, using experimental energies for the products and a calculation at the G3 level for the hydrogen-bonded complex.

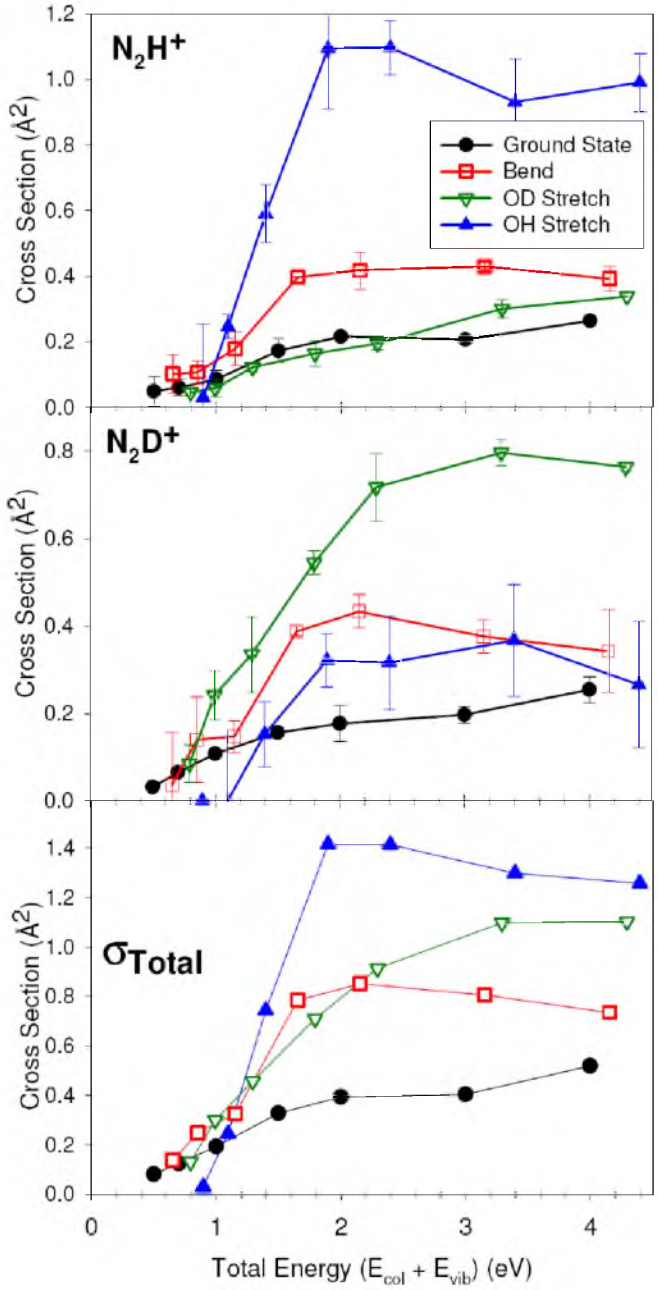

Figure 9.2: The enhancement in reactivity for all reactions occurring. Top: Cross sections for production of N_2H^+ in reaction of HOD+ in the indicated initial vibrational states, plotted as a function of total energy ($E_{total} = E_{col} + E_{vib}$) Middle: Analogous cross sections for the N_2D+ channel. Bottom: Total cross section (σ_{tot}) plotted as a function of E_{total} for the indicated vibrational states.

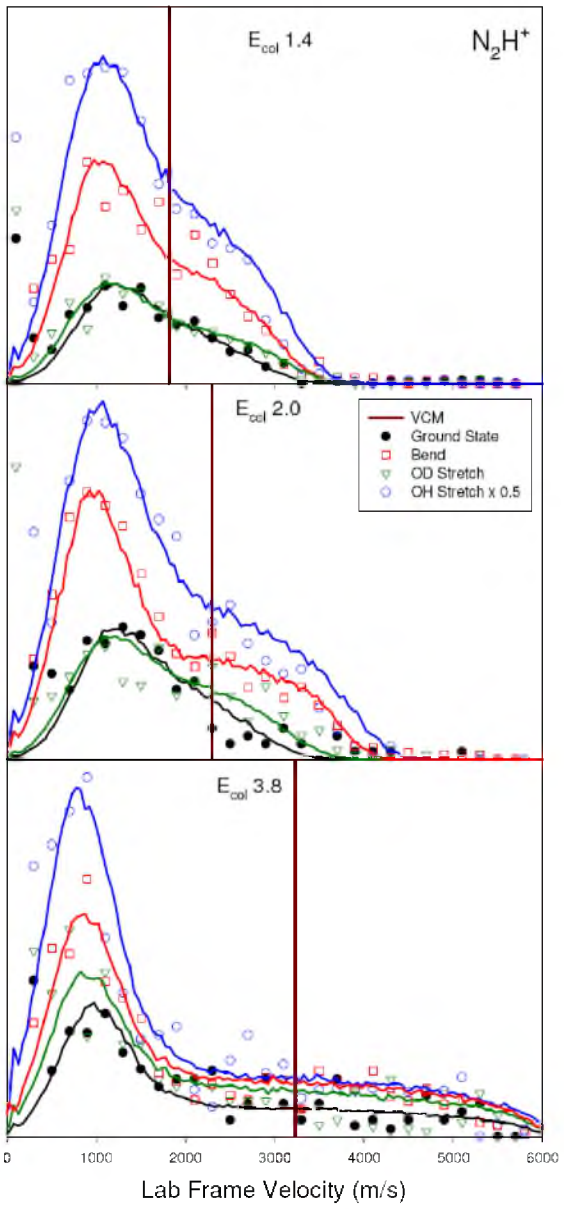

Figure 9.3: Lab frame axial velocity (v_{axial}) distribution for N_2H^+ produced in reaction of HOD^+. Experimental data denoted by ● Ground State, □ Bend, ▽ OD Stretch, and ○ OH Stretch; Simulations denoted by the curves passing through the data. Heavy vertical lines indicate the lab frame velocity of the center-of-mass frame ($<V_{CM}>$).

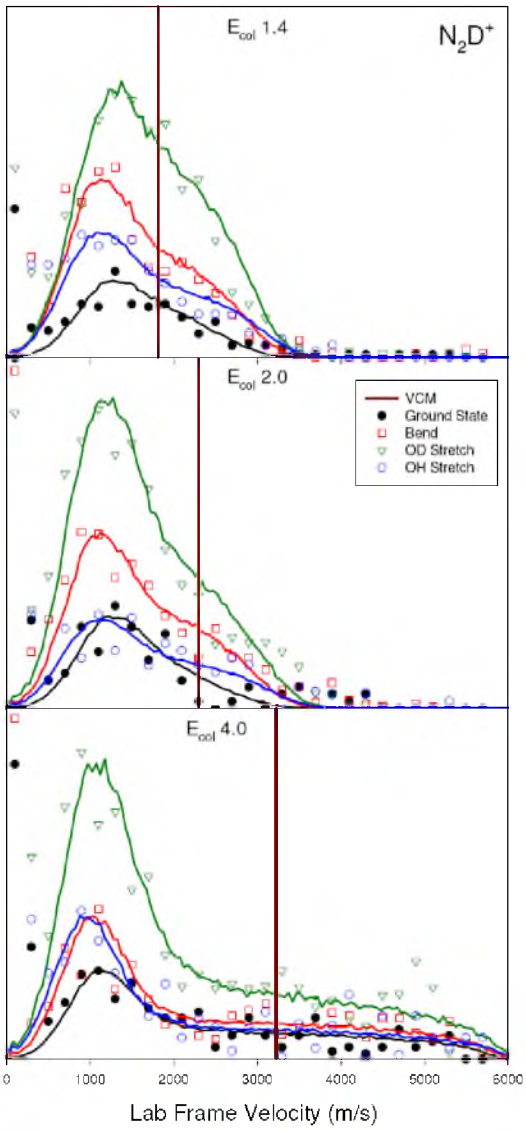

Figure 9.4: Lab frame axial velocity (v_{axial}) distribution for N_2D^+ produced in reaction of HOD^+. Experimental data denoted by ● Ground State, □ Bend, ▽ OD Stretch, and ○ OH Stretch; Simulations denoted by the curves passing through the data. Heavy vertical lines indicate the lab frame velocity of the center-of-mass frame ($<V_{CM}>$).

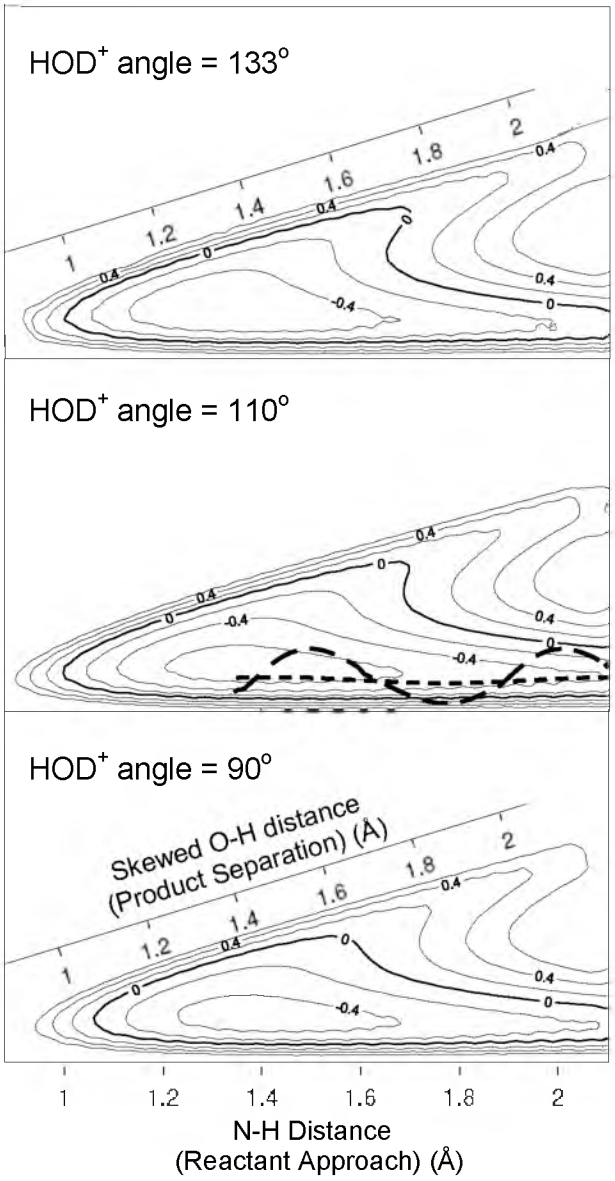

Figure 9.5: Reduced potential energy surface for H^+ transfer between HOD^+ and N_2, calculated as described in the text. The dashed oscillatory curve higher amplitude is a projection of the OH (broken-bond) stretch, while the almost-straight dashed line shows the projection of the OD (spectator bond) stretch mode onto surface.

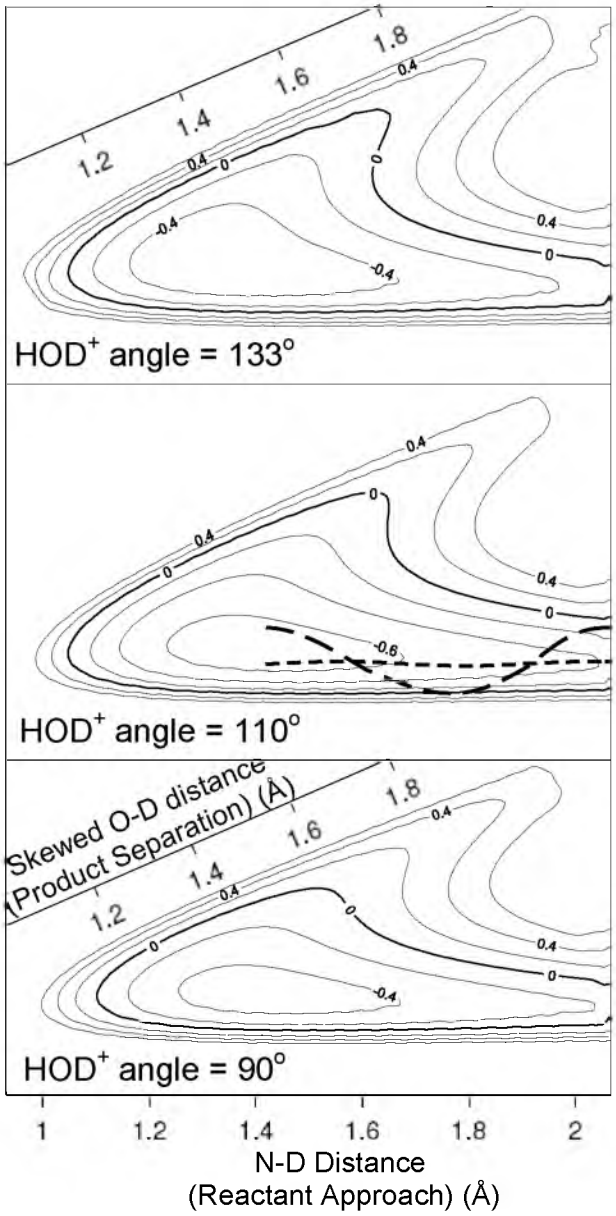

Figure 9.6: Reduced potential energy surface for D^+ transfer between HOD^+ and N_2, calculated as described in the text. The dashed oscillatory curve higher amplitude is a projection of the OD (broken-bond) stretch, while the almost-straight dashed line shows the projection of the OH (spectator bond) stretch mode onto surface.

CHAPTER 10

EFFECTS OF COLLISIONAL AND VIBRATIONAL VELOCITY ON PROTON AND DEUTERON TRANSFER IN THE REACTION OF HOD^+ WITH CO

Reprinted with permission from David M. Bell, Scott L. Anderson, and Journal of Physical Chemistry A **117,** 1083. Copyright 2013, American Chemical Society

Overview

Reaction of HOD^+ with CO was studied over the collision energy (E_{col}) range between 0.18 eV and 2.87 eV, for HOD^+ in its ground state and with one quantum in each of its vibrational modes: (001) - predominately OH stretch; (010) - bend, and (100) - predominately OD stretch. In addition to integral cross sections, product recoil velocity distributions were also measured for each initial condition. The dominant reactions are near-thermoneutral proton and deuteron transfer, generating HCO^+ and DCO^+ product ions by a predominantly direct mechanism. The HCO^+ and DCO^+ channels occur with combined efficiency of 76% for ground state HOD^+ at our lowest E_{col}, increasing to 94% for E_{col} around 0.33 eV, then falling at high E_{col} to ~40%. The HCO^+ and DCO^+ channels have a complicated dependence on HOD^+ vibrational state. Excitation of the OH or OD stretch modes enhances H^+ or D^+ transfer, respectively, and inhibits D^+ or H^+ transfer. Bend excitation preferentially enhances H^+ transfer, with no effect on D^+ transfer. There is no coupling of energy initially in any HOD^+ vibrational mode to recoil velocity of either of the product ions, even at low E_{col} where vibrational excitation doubles or triples the energy available to products. The results suggest that transfer of H or D atoms is enhanced if the atom in question has a high vibrational velocity, and that this effect offsets what is otherwise a general inhibition of reactivity by added energy. $HOCO^+$ + D and $DOCO^+$ + H products are also observed, but as minor channels despite being barrierless and exoergic. These channels appear to be complex-mediated at low E_{col}, essentially vanish at intermediate E_{col}, then reappear with a direct reaction mechanism at high E_{col}.

Introduction

The singly-deuterated water cation (HOD^+) is interesting from a dynamical perspective because the break in symmetry converts what would be the symmetric and asymmetric stretches in H_2O^+ into a pair of modes that have substantial local character. In the (100) mode (293 meV), the OD bond displacement is ~9.5 times greater than that of the OH bond, and conversely the OH

displacement in the (001) mode (396 meV) is ~30 times greater than the OD displacement. We will, therefore, refer to the (100) vibration in HOD^+ as the "OD stretch", and the (001) vibration as the "OH stretch". In addition to the two stretches, there is the (010), bend mode (153 meV), which is also local in the sense that the amplitude, hence velocity, of the H atom is twice that of the D atom.

By preparing HOD^+ with selected excitation in the three modes, we are able to examine how motion localized in specific bonds, as well as bending, may lead to mode- and bond-specific effects on H^+ and D^+ transfer reactions. In the reaction of $HOD^+ + CO_2$ (0.55eV endoergic),[1] exciting the OH stretch doubles the cross section for H^+ transfer, while having little effect on D^+ transfer, while OD stretch excitation preferentially enhances D^+ transfer and has little effect on H^+ transfer. Both the OH and OD stretch effects are substantially larger than the effect of equivalent increases in the collision energy (E_{col}). Such effects are in line with what might be expected from considering vibrational motion driving the system toward the H^+ or D^+ transfer product channels, and similar bond-specific stretching effects have been reported for reactions of neutral HOD.[2-8] For the $HOD^+ + CO_2$ system, bending excitation enhances both H^+ and D^+ transfer, such that bending gives the largest enhancement of the total cross section, despite having no obvious coupling to the reaction coordinate. HOD^+ reaction with N_2 (1.03eV endoergic)[9] has stronger, and qualitatively different, vibrational effects. OH stretch excitation enhances the cross section for H^+ transfer by a factor of five, but also results in a ~70 – 90% enhancement of the D^+ transfer channel. Excitation of the lower energy OD stretch enhances the D^+ transfer channel by a factor of 3.5, and has essentially no effect on H^+ transfer. In this system, bend excitation also enhances both H^+ and D^+ transfer by about a factor of two; because the OH stretch effects are so large, this mode has the largest effect on total reactivity. All three modes produce much larger enhancements than equivalent increases in E_{col}, except near threshold, where all forms of energy are equally effective.

Reactions of the water cation are of interest both for the dynamical reasons discussed above, and because water is common in both terrestrial and interstellar environments.[10, 11] The reaction of H_2O^+ with CO has been investigated under thermal conditions in selected ion flow tubes[12-14] and using ion cyclotron resonance,[15] as part of the process of developing a table of proton affinities. As discussed above, in systems where H^+ and D^+ transfer are substantially endothermic, the vibrational effects are large and strongly bond/mode-specific. Conversely, exothermic proton transfer in ion-molecule reactions is often found to occur with essentially unit efficiency,[16] implying that the reaction is insensitive to initial conditions, and suggesting that bond- or mode-specific effects might vanish. The HOD^+ + CO system is interesting because the proton affinities of CO (594 kJ/mol) and OH (593.2 kJ/mol) are virtually identical,[17] such that proton transfer in this system is thermoneutral, within the uncertainty of the thermochemistry. From our perspective, therefore, this system is ideal for examining how mode- or bond-specific effects evolve as the energetics change from endothermic to exothermic. We previously reported a study of the reaction of HOD^+ with NO_2, where H^+ and D^+ transfer are also near thermoneutral[18]; however, that system is quite different because reaction occurs on both triplet and singlet potential energy surfaces, and because charge transfer is exoergic by over 3 eV, and dominates the chemistry. Here we report a study of the reaction of mode-selectively excited HOD^+ with CO. Integral cross sections and product recoil velocity distributions are reported for all products over the center-of-mass collision energy (E_{col}) range from 0.18eV to 2.87 eV.

Methodology

The experiments were done using a guided ion beam tandem mass spectrometer that has been described previously.[1, 19] To produce the HOD molecular beam, we mixed 50% H_2O and 50% D_2O, creating a mixture that contains 25% H_2O, 50% HOD, and 25% D_2O. Helium was bubbled through the mixture to generate a gas mixture that is 96% He, 1% H_2O, 2% HOD, and 1% D_2O. This gas mixture was pulsed into our experiment as a skimmed supersonic beam, in

order to internally cool HOD. The HOD was subsequently ionized by REMPI through the **C** ($^1B_1$) state, allowing the HOD^+ to be produced in the following states: (000) - ground state, (001) - OH stretch, 0.396eV, (010) – bend, 0.153eV, and (100) - OD stretch, 0.293eV.[20] The purity of these ion states was measured by photoelectron spectroscopy, which found that the (000), (001), and (100) states are 100% pure, while ionizing through the bend level of the **C** state produces a mixture of 56 % ions in the bend state (010), with the balance in the ground state. Because we also measure cross sections for ground state HOD^+, it is straightforward to subtract out the contribution from the ground state contamination, and the data presented below have been so corrected.

The REMPI laser intersected the water molecular beam between a pair of planar electrodes, and the ions generated were first injected into a quadrupole ion guide and then into a quadrupole mass filter. The mass filter was used to produce a beam of pure HOD^+, at 19 amu, and the ion source was operated under conditions to avoid formation of H_3O^+ (also 19 amu), as shown by absence of signal for isotopologs of H_3O^+ such as HD_2O^+ or D_3O^+ which can be detected without interference. The primary beam was then passed through a time-of-flight (TOF) gating electrode set that was used to narrow the kinetic energy spread of the primary beam to ~0.15 eV. The state-, mass-, and energy- selected ions were guided into a series of 8-pole ion guides,[21] powered by a pair of homemade radio-frequency generators[22] operating at 3.1 MHz. The first ion guide passed through a 10 cm long scattering cell containing $1x10^{-4}$ Torr of CO, measured by a capacitance manometer. Product ions, together with remaining reactant ions, were then passed into a longer ion guide for TOF velocity analysis. Finally, the ions were passed through a quadrupole mass filter and then detected by an electron multiplier. The ion signal was counted with a P7882 FAST ComTec multichannel scalar, controlled by a LabView program. Integral cross sections were calculated from the ratio of reactant and product ion intensities (integrated from the TOF measurements), using the calibrated effective length of the scattering cell and the pressure of the scattering cell. To allow subtraction of reactions occurring with CO

in the chamber background outside the scattering cell, the gas inlet system alternately injects CO into the cell, and into the chamber background.

To check reproducibility and determine uncertainty, several complete data sets were taken on different days, each set including reactions of the four HOD^+ vibrational states of interest. The data below consist of average values, with uncertainty determined from the standard deviation of the cross sections. In addition to random errors indicated by error bars in the figures, there are possible systematic effects that are harder to quantify. Error in the absolute scattering cell pressure and length calibration would result in an error in the absolute scale of the cross sections, but would have no effect on the most dynamically important results, including branching ratios, vibrational effects, velocity distributions, and collision energy dependences. We estimate that the absolute cross section scale is within ±20% of the correct value, and this assessment is consistent with thermal rate measurements in the literature,[12, 13] discussed below. If detection efficiency varies with ion mass, there might be errors in both the absolute cross section scale, and the relative intensities of different products. To minimize these effects, we operated at the lowest possible mass spectrometer resolution. Because the corresponding product ion masses are nearly identical, the effects should be insignificant for comparing cross sections for production of products that differ only in whether they contain H vs. D, but there might be some effect on the relative cross sections for heavy ($HOCO^+/DOCO^+$) vs. light (HCO^+/DCO^+) products. Again, such errors would not affect comparison of data for different vibrational states.

To map out the reaction coordinate, electronic structure calculations were performed at the B3LYP/6-311++G** level of theory, using Gaussian03.[23] The vibrational frequencies and zero-point energies were scaled by factors of 0.9613 and 0.9804, respectively.[24] Transition states were verified to be first order saddle points by frequency calculations. When necessary, intrinsic reaction coordinate (IRC) calculations were used to determine which minima are connected by each TS.

To determine the kinetics and product branching that would result from statistical breakup of the various complexes identified on the reaction coordinate, Rice-Ramsperger-Kassel-Marcus (RRKM) rate and density of state calculations were performed using a program developed by Zhu and Hase.[25] Direct state counting was used and the energetics, moments of inertia, and vibrational frequencies (scaled as mentioned above) were obtained from the B3LYP/6-311++G** calculations.

Results

Ground State Results

Products were observed at mass-to-charge ratios (m/z) of 29, 30, 45, and 46, corresponding to HCO^+, DCO^+, $HOCO^+$, and $DOCO^+$, respectively. The integral cross sections for the reaction of ground state HOD^+ with CO are shown in Figure 10.1 over the center-of-mass (CM) collision energy (E_{col}) range from 0.18 eV to 2.87 eV. For reference, Figure 10.1 also shows the total reaction cross section (σ_{total}) and the collision cross section ($\sigma_{collision}$). The hard sphere cross section ($\sigma_{HardSphere}$), calculated from reactant geometries and atomic radii[26] with appropriate angle averaging, provides a reasonable estimate for the collision cross section at high E_{col}. For lower E_{col}, the attractive long range ion-dipole and ion-induced-dipole interactions increase the collision cross section by deflecting (capturing) large impact parameter collisions that would otherwise "miss". Therefore, we use the capture cross section ($\sigma_{capture}$), as formulated by Troe,[27] to estimate $\sigma_{collision}$ for $E_{col} \leq \sim 1.6$ eV, where $\sigma_{capture}$ exceeds $\sigma_{HardSphere}$, switching to $\sigma_{HardSphere}$ higher energies.

The reactions generating these products are as follows:

$HOD^+ + CO$	$\rightarrow HCO^+ + OD$	(PT)	$\Delta_r H = 0.072 \pm 0.042$eV
	$\rightarrow DCO^+ + OH$	(DT)	$\Delta_r H = 0.061 \pm 0.042$eV
	$\rightarrow HOCO^+ + D$	(DL)	$\Delta_r H = -0.422$ eV
	$\rightarrow DOCO^+ + H$	(HL)	$\Delta_r H = -0.485$ eV

where the enthalpies of reaction are calculated for 0 K, determined using 0 K heats of formation, and corrected for deuteration effects by using zero point energies from G3 level calculations on the reactants and products. The heat of formation of HCO^+ was determined from the 0 K proton affinity of CO.[17] The major reaction channels are proton and deuteron transfer (PT and DT), which are both calculated to be slightly endoergic using 0 K energetics; however, at 298 K, the thermochemistry shifts such that PT is 8 meV endothermic and DT 4 meV exothermic, i.e., both are thermoneutral within the uncertainty. In our experiment, the CO is thermal at ~298K, but the ion beam should be rotationally cold and in its vibrational ground state. The observation that the cross section for DT is ~6% greater than that for PT at E_{col} = 0.18 eV, may reflect the 12 meV energy difference between the two channels.

For low collision energies (≤~0.33 eV), σ_{total} is within experimental uncertainty of $\sigma_{collision}$, i.e., reaction efficiency is near unity, overwhelmingly dominated by the combination of PT and DT. At high E_{col}, the total reaction efficiency drops to ~40%. There is also some suggestion, although not outside our error limits, that reaction efficiency drops slightly at our lowest lowest E_{col} ($\sigma_{total}/\sigma_{collision}$ ~76%). Such an apparent drop could simply reflect collection efficiency problems with slow product ions; however, a drop is consistent with the expectation that for thermoneutral, barrierless reactions like PT and DT, the total reaction efficiency should be about 2/3rd in the low energy limit, because the density of states (DOS) is roughly equal in the three arrangements: $HOD^+ + CO$, $HCO^+ + OD$, and $DCO^+ + OH$. In fact, room temperature measurements of the $H_2O^+ + CO \rightarrow HCO^+ + OH$ kinetics indicate that reaction occurs at only ~55% of the collision rate,[12, 13] possibly because the reaction is not exactly thermoneutral, but also

because H_2O^+ is nonlinear, and therefore, the reactant arrangement has an additional rotational degree of freedom (vibrational degrees of freedom are inaccessible at thermal energies).

The other pair of products observed are $HOCO^+$ and $DOCO^+$, which correspond to hydrogen loss (HL) and deuterium loss (DL) from a $[HDOCO]^+$ complex. Despite the fact that both channels are substantially exoergic, their cross sections are quite small. The low reaction efficiency is clearly not due to an energy barrier above the reactant asymptote, because both cross sections rise sharply with decreasing energy in the low E_{col} ranges. The HL and DL cross sections go through minima around 0.75 eV, where the reaction efficiency is below 1%, then increase slowly at higher E_{col}. One interesting question is why $HOCO^+$ was not observed in any of the thermal energy experiments, despite being barrierless (as shown below) and considerably more energetically favorable than the HCO^+ channel.[12-15] This product presumably formed to some extent in the thermal energy experiments, but was probably destroyed by secondary reactions with the CO neutral reactant to form $HCO^+ + CO_2$. Because this secondary reaction occurs with unit efficiency at thermal energies,[15] it is likely that $HOCO^+$ product ions were simply detected as HCO^+ (the major product ion).

Computational Results

The computational results for $HOD^+ + CO$ are summarized in Figure 10.2 and Table 10.1, where energetics are reported as $\Delta_r H^\circ(298K)$ in order to allow direct comparison with both the experimental results (where the neutral reactant is thermal) and literature data compiled by Lias *et al.*[28] For simplicity, Figure 10.2 shows the low energy reaction pathways for the undeuterated $H_2O^+ + CO$ system, with energetics for transition states and complexes calculated at the B3LYP/6-311++G** level of theory, referenced to experimental values for reactants and products. Table 10.1 gives the energetics for the various isotopic and isomeric analogs that are possible in the $HOD^+ + CO$ system. There is a reactant-like complex (RC) bound by 1.41 eV with respect to reactants, which has the oxygen of HOD bound to the carbon end of CO, at a

distance of 1.89 Å, with the three heavy atoms bent at 129.7°. The Mulliken charge is equally shared between the HOD and CO moieties in RC.

There is a product-like complex (PC_{PT}) which can be accessed from RC via the low energy TS1. This PC_{PT} complex can be thought of as a proton-bound complex between the PT products (HCO^+ +OH), with a H^+-CO distance of 1.25 Å and H^+-OH distance of 1.37 Å. There is also a product-like complex (PC_{HL}) that can be thought of as a complex between the HL products ($HOCO^+$ + H). The binding energy of PC_{HL} with respect to the HL product channel is small compared to the available energy in this channel, thus we expect this complex to have negligible lifetime and to be dynamically insignificant. The TS leading to PC_{HL} and HL products (TS2) is only 0.029 eV below the reactants at this level of theory. The fact that the HL/DL cross sections peak at low E_{col} is consistent with TS2 being below the reactant limit, and the small branching observed for HL/DL products suggests that TS2 is just below the reactant energy. Further insight into the energetics of TS2 is obtained from RRKM calculations discussed below.

Finally, the most stable point on the potential energy surface corresponds to the formic acid cation (FA), which is bound by 1.70 eV with respect to reactants. Decomposition of FA was studied using a combination of quantum chemistry and photoion-photoelectron coincidence methods by Baer and co-workers,[29] who showed that FA can decompose to both product channels. This study also concluded that there is a barrier to H elimination from FA due to the large change in geometry and small polarizability of the H atom (i.e., TS4 is above the $HOCO^+$ + H limit). They also found that the branching ratio strongly favored the HCO^+ products when the available energy was sufficient to open that product channel. For reaction of H_2O^+ with CO, we expect reaction pathways mediated by FA to be insignificant, because the TS controlling FA formation (TS3) is quite high in energy, and also tight compared to TS1 and TS2.

Velocity Distributions

To provide insight into the dynamics of the reactions in this system, including possible mediation by complexes, we measured the axial component (v_{axial}) of the product recoil velocity distributions for the entire range of reactant initial conditions (vibrational state and E_{col}). Figures 10.3 - 10.7 show the lab frame v_{axial} distributions for HCO^+, DCO^+, $HOCO^+$, and $DOCO^+$, respectively, formed in reaction of ground state HOD^+ with CO. In each figure, the experimental data are shown by solid circles connected by thin lines, and the heavy solid curves show simulations of the data, discussed below. The heavy vertical lines indicate $\langle V_{CM} \rangle$, i.e., the velocity of the center-of-mass frame with respect to the lab, averaged over the distributions of ion beam and target velocities. Velocity distributions were also measured for the $HOCO^+$ and $DOCO^+$ products, and are presented in Figure 10.5 and 10.6. As expected for a product channel where the neutral product is much lighter than the product ion being measured, the $HOCO^+/DOCO^+$ v_{axial} distributions are centered on V_{CM}, and provide no dynamical insight.

Collisions in our experiment are, on average, co-axial with the ion guide, and therefore, both $\langle V_{CM} \rangle$ and the average relative velocity vector of the collisions, $\langle \mathbf{v}_{rel} \rangle$, are also co-axial with the ion guide. For this reason, considerable dynamical insight can be inferred directly from the lab frame v_{axial} distributions. For example, ions that appear with v_{axial} slower than $\langle V_{CM} \rangle$ correspond to ions that are backward-scattered in the center-of-mass frame, while v_{axial} faster than $\langle V_{CM} \rangle$ corresponds to forward scattering. If reaction is mediated by a complex with lifetime, $\tau_{complex}$, greater than the rotational period of the complex, $\tau_{rotation}$, then the v_{axial} distribution must be forward-backward symmetric about $\langle V_{CM} \rangle$. Therefore, a distribution that is not symmetric about $\langle V_{CM} \rangle$ is a sign that reaction is not mediated by a long-lived complex. Finally, the width and displacement of the measured v_{axial} values from $\langle V_{CM} \rangle$ provide insight into energy partitioning into recoil.

Note that we define "forward" and "backward" in terms of the direction of the product ion velocity relative to the reactant ion beam velocity in the center-of-mass frame. For reactions

like PT and DT, where the charge is transferred, this definition leads to a reversal of the usual meaning of "forward" and "backward". For example, a large impact parameter "stripping" collision of DO-H^+ with CO, where H^+ transfers with little deflection of the heavy DO and CO moieties, will result in HCO^+ product ions that are backward-scattered relative to the reactant ion beam. Conversely, a head-on collision in which the heavy moieties rebound at 180° with respect to their initial direction will give rise to HCO^+ that is forward-scattered with respect $<V_{CM}>$. In both PT and DT channels, there is a clear propensity toward backward scattering at high E_{col}, which suggests stripping-like dynamics.

One issue for this system is that, due to the thermal velocity of the CO reactant, a small fraction of the product ions are scattered with negative lab frame velocities (i.e., moving away from the detector). To insure that these ions are collected, the electrode used to inject ions into the scattering ion guide is always biased slightly positive with respect to the scattering ion guide, reflecting these ions toward the detector. Clearly, the TOF values measured for these ions are distorted by the reflection process, contributing to an artificial peak at positive, but near-zero lab velocity. In addition, slow ions are particularly susceptible to any distortions in the surface potential of the ion guides, which can result in additional perturbation of the low velocity portion of the v_{axial} distributions. For this reason, we ignore the v_{axial} range below 500m/s in fitting of the distributions.

To obtain insight into energy disposal in the reactions, and correct for the broadening from the reactant velocity distributions, the data are fit to a model of the scattering dynamics. The fits are done using a Monte Carlo simulation of the experiment that samples the distributions of HOD^+ energy and angle, and the thermal distribution of CO velocities, and convolutes these with recoil velocity and angle values sampled from the scattering dynamics model.[30] This model has three adjustable parameters. The recoil energy distribution is modeled as a Gaussian, with peak energy and width expressed as fractions (f_{peak}, f_{width}) of the energy available to the products, E_{avail}. For the angular distribution, we use the osculating complex model,[31] where it is assumed

that there is a preferred scattering direction, but that the angular distribution is broadened by rotation of a short-lived collision complex. The degree of broadening is controlled by the parameter T_{ratio}, which is the ratio of the complex rotational period, $\tau_{rotation}$, to its lifetime, $\tau_{complex}$. In energy ranges where collision complexes are expected to have negligible lifetimes, T_{ratio} can be considered as a simple indicator of the asymmetry of the v_{axial} distributions. T_{ratio}, f_{peak}, and f_{width} are varied until the simulated v_{axial} distribution is in good agreement with experiment.

The quality of the fits can be judged in Figures 10.3 and 10.4, and the results are summarized in Table 10.2 for reaction of ground state HOD^+. For each reactant initial condition, the table reports $<E_{avail}>$, which is the average available energy including collisional, vibrational, and rotational energy. E_{ratio} is simply the average fraction of E_{avail} appearing as recoil energy($<E_{recoil}>/<E_{avail}>$), and T_{ratio}, as noted, is essentially a measure of the forward-backward asymmetry of the angular distribution (asymmetry increases with increasing T_{ratio}).

For E_{col} values greater than 0.35 eV, the v_{axial} distributions for both HCO^+ and DCO^+ products are clearly asymmetric, and become increasingly backward-scattered with increasing E_{col}. As noted above, backward-scattered product ions correspond to small angle scattering, indicating that reaction at high E_{col} is dominated by stripping-like collisions at large impact parameters (b). For reference, Figures 10.3 and 10.4 also indicate, with vertical dashed lines, the spectator-stripping limit velocities at each E_{col}. Clearly, the distributions become increasingly stripping-like at high E_{col}; however, there continues to be significant intensity in the forward direction, indicating that H^+ and D^+ transfer also occur in small b, rebounding collisions. As shown in the table, E_{ratio} is roughly constant at ~40 - 50%. For these thermoneutral reactions, E_{col} is the dominant contribution to E_{avail}, thus it appears that approximately half the initial collision energy is retained in product recoil over the entire range of E_{col}. E_{ratio} of 40 – 50 % is much larger than what would be expected from equipartition of E_{avail} into all the energetically accessible degrees of freedom (translation plus four rotations at low E_{col}, adding vibrational modes with increasing Ecol).

For $E_{col} \leq 0.35$ eV, the fits to the experimental distributions appear almost forward-backward symmetric. Note, that for low E_{col}, the energy available to drive recoil is small for these thermoneutral reactions. As a result, the recoil velocity of the HCO^+/DCO^+ products may simply be too small to allow angular asymmetry to be resolved, given the broadening from the reactant velocity distributions. Therefore, while the v_{axial} distributions do not rule out mediation by complexes at low E_{col}, neither do they support complex mediation. The fact just noted, that E_{ratio} is considerably larger than what would be expected from equipartition, could be taken as evidence supporting a direct reaction mechanism at low E_{col}.

The v_{axial} distributions were also measured for reaction of vibrationally excited HOD^+, and the raw results for all vibrational states are plotted for HCO^+ and DCO^+ in Figure 10.7. To allow direct comparison between the data for different states, the distributions were normalized to constant integrated area. As shown in the figures, the distributions are quite similar for all vibrational states. Such similarity is not surprising for high E_{col}, where the vibrational energy is a small fraction of the E_{avail}; however, it is quite surprising that distributions are so similar even for $E_{col} = 0.2$ eV, where excitation of the OH (OD) stretch approximately triples (doubles) E_{avail}. If the v_{axial} distributions are simulated using the parameters used to fit the ground state distributions, i.e., assuming that the same fraction of E_{avail} is partitioned to recoil, then the simulations predict that the distributions should be much broader at low E_{col} than is observed. Instead, good fits are obtained by assuming that little or none of the reactant vibrational energy is partitioned to product recoil energy, which continues to be 40 – 50% of the collision energy. This absence of coupling from reactant vibration to recoil supports the idea that PT and DT are direct reactions even at low E_{col}, rather than mediated by a complex where reactant energy would tend to be randomized among the accessible degrees of freedom.

Vibrational Mode Effects on the Integral Cross Sections

Although vibrational excitation is uncoupled to product recoil, HOD^+ vibration has significant mode- and bond-specific effects on the cross sections for HCO^+ and DCO^+, as shown in Figure 10.8. Note that each channel is enhanced by stretch excitation of the bond broken in the collision (the "broken-bond stretch"), and inhibited by stretch excitation of the other bond (the "spectator bond stretch"). Bend excitation enhances HCO^+ production at low E_{col}, and DCO^+ production appears to be slightly inhibited, but the inhibition is within the experimental uncertainty. In Figure 10.9, the $HOCO^+$ and $DOCO^+$ cross sections are plotted for the same range of E_{col} and HOD^+ vibrational state. For these minor channels, vibration appears to inhibit reaction at low E_{col}, and may enhance reaction at high E_{col}; however, it should be noted that these cross sections are quite small, thus the uncertainties in the comparisons are relatively large at low energies (~20%) and increases with increasing energy (up to ~60%). The vibrational effects on σ_{total} are shown in Figure 10.10. The effects on σ_{total} are relatively small, because the effects of broken-bond and spectator bond stretch excitation largely cancel. In other words, the total cross section is relatively insensitive to reactant initial state, as might be expected from the near-unit total reaction efficiency; however, the PT/DT branching ratio changes by over a factor of three, depending on which stretch is excited.

Discussion

$HOCO^+$ and $DOCO^+$

We will begin by discussing the mechanism for the minor $HOCO^+$ and $DOCO^+$ channels. Their collision energy dependences are quite distinct from those of the major HCO^+ and DCO^+ channels, suggesting that they may be dynamically distinct as well. The E_{col} dependence for both channels is bi-modal, with a component at low E_{col} that is strongly inhibited by both E_{col} and vibrational excitation, and a high E_{col} component that is enhanced by E_{col}, and possibly by HOD^+ vibration as well. This kind of bimodal E_{col} dependence is similar to that observed in reactions of

H_2CO^+ with CD_4,[32] and of NO_2^+ with C_2H_2,[33] and in those systems the sharp increase in cross section at low E_{col} is clearly due to mediation by a weakly bound reactant-like complex, which essentially gives the reactants multiple opportunities to find the correct collision geometry to pass over a strongly orientation-dependent TS.

The existence of a low E_{col} component for the $HOCO^+$ and $DOCO^+$ channels demonstrates that there is a low energy pathway to these exoergic products; however, the small cross sections indicate that some bottleneck strongly disfavors these channels relative to the less energetically favorable HCO^+ and DCO^+ channels. The reaction coordinate in Figure 10.2 suggests that this bottleneck is TS2, which is below the reactant energy, as required, but considerably higher in energy than TS1. In addition, the covalently-bonded TS2 is quite tight.

Regardless of whether the low energy mechanism is statistical, angular momentum is also expected to have a suppressing effect on branching to $HOCO^+ + H$. At low E_{col} the system must pass through geometries similar to that of TS2. As it approaches TS2, the reactant orbital angular momentum ($L_{collision}$) must be converted to rotational angular momentum of TS2, with associated rotational energy equal to $L_{collision}^2/2I$, where I is the moment of inertia of TS2. In this case, for b near the capture limit at $E_{col} = 0.18$eV, $L_{collision}$ is in the ~130 $\hbar$ range, and assuming that the TS2 rotation corresponds to the highest moment tumbling motion ($I_{tumbling} = 57.4$ amu-Å^2), the corresponding rotational energy is ~0.6 eV, i.e., TS2 is inaccessible for large b collisions.

One question is to what extent a complex is important in mediating reaction at low E_{col}. Such a complex might tend to increase the probability of passing through TS2, by allowing the reactants multiple chances to find the minimum energy pathway. Unfortunately, the kinematics of these channels precludes extracting any direct insight into this question from the v_{axial} distributions (Figures 10.5 and 10.6). RRKM calculations, using energetics and vibrational frequencies from the *ab initio* calculations, shed some light on this issue. For simplicity, the RRKM analysis was done for the all-hydrogen $[H_2O\text{-}CO]^+$ system.

First, consider the complexes RC and PC_{PT}, which as Figure 10.2 shows, are the only complexes likely to have both formation probabilities and lifetimes that might be significant at low E_{col}. Because TS1 is low in energy compared to both reactants and PT products, the interconversion rates between RC and PC_{PT} should be fast compared to the decay rates leading back to reactants or on to PT products, and this point was confirmed by RRKM calculations, where the rates for interconversion are ~8 times faster than the decay rate, over the low E_{col} and $L_{collision}$ range where complexes are likely to be significant. The RRKM calculation also indicates that the density of states in RC is significantly higher than in PC_{PT}, thus the interconverting RC↔PC_{PT} complex would spend most of its lifetime in the more stable RC well. The lifetime of the RC↔PC_{PT} complex is the inverse of the sum of the rates for decay via the three exit channels, *viz* back to reactants, on to PT products, and over TS2 to HL products. The lifetime of the RC↔PC_{PT} complex is given in Table 10.3 for various E_{col} and $L_{collision}$ values. In addition, the table also gives the RRKM branching into PT and HL product channels, calculated as the rates for decay into the two product channels, divided by the total decay rate (including decay back to reactants).

The lifetime of the complex is a few picoseconds at low E_{col}, but drops below a picosecond by ~0.3 eV. For reference, note that at E_{col} = 0.18 eV, it takes ~0.3 ps for reactants to travel 5 Å of relative distance, which we give as a rough measure of the timescale for a completely direct collision. The RRKM results, therefore, suggest that the complex has dynamically significant lifetime only for our lowest collision energies, and even there, the lifetime is significant only for low $L_{collision}$, i.e., low impact parameter collisions.

The branching ratios are also strongly dependent on E_{col} and $L_{collision}$. The orbiting TSs leading back to reactants and to PT products have several low energy degrees of freedom that are absent in the RC↔PC_{PT} complex, while the covalently bound TS2 has both frequencies and rotational constants that are somewhat higher than the complex. As a consequence, increasing either E_{col} or $L_{collision}$ leads to rapidly increasing rates for decay to reactants and to PT products.

The PT branching ratio, which is determined primarily by competition with decay back to reactants, is nearly constant except for very large $L_{collision}$ values, where PT is favored by an orbiting TS with slightly larger $I_{tumbling}$ than that for the TS controlling decay to reactants. In contrast, while increasing E_{col} increases the branching to $HOCO^+$, increasing E_{col} also increases $L_{collision}$, which strongly suppresses the $HOCO^+$ branching. In summary, if mediation by the $RC \leftrightarrow PC_{PT}$ complex is important for the $HOCO^+/DOCO^+$ channels, the RRKM results suggest that the cross section should be significant only at our lowest E_{col}, should drop with increasing E_{col}, and should never be very large. The low E_{col} component of the $HOCO^+$ and $DOCO^+$ channels have just this behavior.

The effects of reactant vibration on production of $HOCO^+$ and $DOCO^+$ are shown in Figure 10.9. The cross sections for these channels are small, thus there is considerable uncertainty in making these comparisons. The most consistent trend is that HOD^+ vibrational excitation clearly inhibits both channels at low E_{col}, and furthermore, the inhibition is proportional to the energy of the vibrational state, within experimental error. The inhibition from vibrational energy is somewhat smaller than that from equivalent increases of E_{col}; however, adding collision energy also increases $L_{collision}$, which is expected to suppress these channels, as discussed above. Based on the RRKM results, and the measured effects of vibration and E_{col}, we conclude that it is likely that the $RC \leftrightarrow PC_{PT}$ complex is dynamically significant, and is responsible for the low E_{col} component of the $HOCO^+$ and $DOCO^+$ channels. The small magnitude of this component reflects the strong suppression of the branching and complex lifetime by $L_{collision}$, which restricts this mechanism to the small fraction of low impact parameter collisions.

Note that the branching to HL calculated from complex decay is lower than what we observe (0.07% calculated vs. 2% measured at 0.18 eV). It is likely that this discrepancy simply reflects error in the energy of TS2, which was calculated to be only 0.029 eV below the reactants and PT products at the level of theory used to map out the reaction coordinate. Lowering the

energy of TS2 by 0.35eV is sufficient to increase the branching to the experimentally observed level of ~2%.

The increase in the $HOCO^+$ and $DOCO^+$ cross sections at high E_{col} indicates that there must be a direct mechanism leading to C-O bond formation with loss of H or D, because all accessible intermediate complexes would have dynamically insignificant lifetimes above $E_{col} \approx 1$ eV. The direct reaction is rather inefficient, occurring in < 4 % of hard sphere collisions. Low efficiency presumably reflects the need for collisions in the correct HOD – CO orientation to allow CO bond formation in a fast collision; however, angular momentum conservation continues to limit the range of collision impact parameters that can contribute to this channel, and thus limits the size of the cross section. As discussed above, angular momentum conservation raises the effective energy of TS2, which remains the limiting point on the minimum energy path even for high E_{col}. For high E_{col}, the available energy is higher, but so is $L_{collision}$. For example, a collision at E_{col} = 3 eV with b = $b_{hardsphere}$ has $L_{collision} \approx 300\ \hbar$, which forces TS2 to have rotational energy of ~3.5 eV, i.e., such collisions cannot reach compact geometries like TS2. There is a further angular momentum constraint arising from the fact that the reduced mass is ~10.5 times smaller for $DOCO^+$ + H products than for reactants (~6 times smaller for $HOCO^+$ + D), which means that only a small fraction of $L_{collision}$ can be partitioned to recoil orbital angular momentum of the products ($L_{recoil} = \mu_{products} \cdot v_{recoil} \cdot b_{recoil}$), which forces the system to put most of $L_{collision}$ into rotation of the $HOCO^+$/$DOCO^+$ products. These angular momentum constraints, together with the expected orientation sensitivity of the reaction, presumably account for the low efficiency of these channels. The pattern of vibrational effects in the high E_{col} range is mixed. The $DOCO^+$ channel is vibrationally enhanced, while for $HOCO^+$, the vibrational effects are small. Because the cross sections for these channels are so small and the error at high energies is ~50% we do not feel that speculating about these effects is warranted.

Mechanism for HCO^+ and DCO^+ Production – Ground State Reaction

For the major product channels, useful mechanistic information is available from the v_{axial} distribution measurements. The velocity distributions for these products are clearly asymmetric for E_{col} above 0.35 eV, but they become symmetric at our lowest E_{col}, within the uncertainties arising from detection of slow and backward-scattered product ions. As discussed above, this is the energy range where the $RC \leftrightarrow PC_{PT}$ complex has a dynamically relevant lifetime. Because the cross sections for the HCO^+ and DCO^+ channels, summed, are near the capture collision limit, these reactions must be dominated by large impact parameter collisions, with corresponding high $L_{collision}$. Table 10.3 shows; however, that the lifetime is large enough to give symmetric v_{axial} distributions ($\tau_{complex} > \tau_{rotation} \approx 1$ picosecond) only for relatively small $L_{collision}$ even at our lowest E_{col}. Complex mediation may, therefore, account for a small fraction of the HCO^+ and DCO^+ signal at low E_{col}, but the dominant mechanism must be direct. Other evidence supporting this conclusion is presented below.

For $E_{col} \geq 0.35$ eV, the v_{axial} distributions for HCO^+ and DCO^+ are clearly backward-peaked, with asymmetry that increases with increasing E_{col}. The implication is that the reaction becomes increasingly direct at high energies, with the bulk of the products formed in stripping-like collisions that lead to backward-scattered product ions. Over this E_{col} range, the efficiency for these two channels drops from 40% for PT and 36% for DT (76% for the sum), to 21% for PT and 16% for DT at $E_{col} = 2.87$ eV. This efficiency drop may reflect increasing sensitivity to collision geometry for faster, more impulsive collisions. Above ~2.0 eV, these product masses could include contributions from the higher energy product isomers (HOC^+ or DOC^+); however, if those channels were significant, we might expect an increase in the reaction efficiency as they become accessible. The monotonic decrease in efficiency with E_{col} suggests that the HOC^+ and DOC^+ cross sections are small compared to those for HCO^+ and DCO^+.

Even at our highest energies, there is a forward-scattered component of the v_{axial} distributions, indicating that some products are produced by rebounding, which implies small

impact parameter collisions. Evidently, reaction occurs over a wide range of impact parameters, ranging from head-on to grazing, and the observation that the v_{axial} distributions are backward-peaked simply reflects the fact that the probability of a collision at a given value of b is proportional to b. Competition with the $HOCO^+/DOCO^+$ channels, which require collisions at low b, also tends to deplete the HCO^+/DCO^+ velocity distributions in the forward-scattered hemisphere; however, those channels are too weak to have much effect on the major channels.

Vibrational Effects on the Total Cross Section

The vibrational effects on σ_{total} are shown in Figure 10.10, with an inset that shows just the low E_{col} region, where the total reaction efficiency approaches unity. Note that for reaction of ground state HOD^+, the efficiency is closest to unity (~94%) for E_{col} around 0.33 eV. At lower energies, the efficiency drops to ~76%, and as pointed out above, this drop is consistent with the 55% efficiency observed in thermal energy studies. In the E_{col} range below ~0.33 eV, excitation of both the OD and OH stretch modes of HOD^+ enhances reactivity, such that $\sigma_{total} \approx \sigma_{collision}$. Bend excitation has a somewhat smaller enhancing effect than the two stretches in the low energy regime. As E_{col} increases above 0.33 eV, the total reaction efficiency gradually drops, eventually reaching below 40%, and over the same E_{col} range, the vibrational effects on σ_{total} also become smaller. The highest energy OH stretch mode appears to continue enhancing σ_{total}. The bend appears to inhibit σ_{total} slightly, but these effects are not outside of the error limits. The weak dependence on reactant vibrational state at high E_{col} may be partly a function of the fact that the vibrational energy becomes small compared to E_{avail}; however, we note that for the endothermic reactions of HOD^+ with CO_2,[1] and N_2,[9] the vibrational effects remain large and mode-specific even at high E_{col}. We infer that for this system, high E_{col} reactivity is more a function of factors such as collision geometry.

Vibrational Mode- and Bond-Specific Effects on HCO^+ and DCO^+ Formation

The cross sections for HCO^+ and DCO^+ are presented for each of the four reactant vibrational states of HOD^+ in Figure 10.8. It is apparent that there are mode- and bond-specific effects for these product channels, which continue into the high E_{col} range where vibration has little effect on σ_{total}. Both OH and OD stretch excitations show the same pattern of strongly enhancing the probability of the PT or DT channel that breaks the excited bond, while inhibiting the channel that corresponds to breaking the other bond. In other words, transferring H^+ or D^+ from HOD^+ is enhanced by exciting the broken-bond stretch, while exciting the spectator bond stretch actually inhibits the reaction. This effect can be seen more clearly in Figure 10.11 which shows the vibrational enhancement ($\sigma_{vib\ state} / \sigma_{ground\ state}$) for the three HOD^+ vibrational levels studied. The mode/bond specificity seen for PT and DT are similar to what is seen for PT and DT from HOD^+ to CO_2 and N_2,[1, 9] with one difference. In those systems, excitation of the spectator bond stretch leads to small enhancements, whereas for $HOD^+ + CO$, the spectator stretch excitation actually inhibits both channels. This difference may simply reflect the difference in energetics of these reactions. For N_2 and CO_2, PT and DT are substantially endoergic, and reaction is direct at all energies above threshold. For endoergic reactions, it is not unreasonable that any form of additional energy might enhance reactivity to some extent. PT or DT in the $HOD^+ + CO$ system is essentially thermoneutral, so reactivity presumably is less dependent on available energy. In addition, there is probably some contribution to the PT and DT channels at low E_{col} from a complex-mediated mechanism, and we expect both the formation probability and the lifetime of the complex to be decreased by reactant vibrational excitation.

A somewhat surprising effect is that HOD^+ bend excitation significantly enhances the $HCO^+ + OD$ channel at very low collision energies, but has essentially no effect on the DCO^+ OH channel. In sum, HOD^+ bend excitation favors PT over DT at all E_{col}, and because the reactions are identical aside from the mass of the transferred atom, it seems logical that this effect on PT/DT branching must result from a mass effect associated with the bend vibration. The obvious

candidates are the amplitude and velocity of the vibrational motion, which are twice as large for H as for D in the bending vibration. In previous studies of this type, we have found evidence that vibrational effects in some systems depend on vibration-induced distortion away from the equilibrium reactant geometry; however, for the HOD^+ bend, the distortion effect should be essentially identical for H^+ and D^+ transfer. Therefore, we propose that the propensity of the bend to favor PT over DT is a result of higher H atom vibrational velocity.

A picture that rationalizes all the vibrational effects on reactivity is that, in absence of offsetting dynamical effects, all forms of energy (E_{col} and vibration) tend to inhibit HCO^+ and DCO^+ formation (and $HOCO^+$/$DOCO^+$ at low energies). This general inhibition can be more than offset for the HCO^+ and DCO^+ channels for vibrations that involve substantial motion of the atom being transferred in the reaction. Therefore, OH stretch or bend excitation, both of which result in large amplitude H atom motion in HOD^+, enhance H^+ transfer to produce HCO^+. Similarly, OD stretch excitation enhances DCO^+ formation, and while D^+ transfer is not enhanced by bend excitation (small amplitude D motion), neither is it inhibited.

The one remaining puzzle is why there is essentially no coupling of any of the reactant vibrations into increased recoil velocity, particular at low E_{col} where the vibrational energy increases E_{avail} by up to a factor of three (Figure 10.7). It is, perhaps, not so surprising that there should be no coupling for the spectator bond stretches, as the bonds that are excited in these modes remain intact through the reaction. Furthermore, the OH and OD stretch fundamentals (i.e., the (001) and (100) modes) in HOD^+ are only a 2 – 5% lower in energy than the v=1 levels of the OH and OD products. In that case, we might expect a tendency for energy localized in the spectator stretch to simply remain in vibration of the OH or OD product, and Crim and co-workers have observed a similar propensity in their study of overtone-excited HOD reactions with Cl, H, and O atoms.[34, 35] Energy in the HOD^+ bend and broken-bond stretch modes obviously must be partitioned to some other degree(s) of freedom of the products. The absence of significant effect of bend excitation on recoil may just be the result of the relatively low energy

of this mode; however, the broken-bond stretch, particularly when this is the OH stretch, should result in obvious changes in v_{axial} if there is significant coupling to recoil. Because the transition state controlling PT is bent, it could be that the stretch energy has a propensity to be converted to counter rotation of the two products. For example, the energy of the OH stretch, if converted to rotation of OD and HCO^+ with equal and opposite angular momentum, would correspond to J≈16 for both. It is also possible that the broken-bond stretch energy is partitioned to vibrational energy of the HCO^+ or DCO^+ products. For example, in reaction of HOD with Cl, H, and O atoms,[2, 34, 36] a tendency was found to partition energy into vibration of the bond formed. In HOD + O 87% of the energy available was partitioned into the O-H bond formed in the reaction. In that example, the free OH stretch is 140cm^{-1} lower in energy than the OH stretch in HOD and the free OD stretch is 100cm^{-1} below the OD stretch in HOD. For the HOD^+ + CO system, the nascent CH stretch in HCO^+ is ~110 cm^{-1} lower in energy than the OH stretch in HOD^+,[20, 37] and the CD stretch in DCO^+ is ~220 cm^{-1} higher in energy than the OD stretch in HOD^+.[38] In the reactions of HOD with H and Cl, the vibrational frequency for the stretch of the nascent bond does not match as well to that of the broken-bond, and less of the initial vibrational energy was retained in vibration of the products.[2, 34, 36]

Conclusion

We presented a detailed study of the effects of vibrationally mode-specific excitation, as well as collision energy, on reaction of HOD^+ with CO. The dominant mechanism for H^+ and D^+ transfer is direct at all E_{col} as indicated by product recoil velocities and RRKM calculations. Excitation of the OH or OD stretch modes result in enhancement of H^+ or D^+ transfer, respectively, and inhibition of D^+ or H^+ transfer. Bend excitation preferentially enhances H^+ transfer, having no significant effect on D^+ transfer. The energy associated with these vibrational excitations does not appear in recoil energy, even at low E_{col}, where vibrational excitation doubles or triples the energy available to products. The vibrational effects suggest that vibrational energy,

like collision energy, tends to inhibit H^+ and D^+ transfer, but this general inhibitory effect can be offset if the excited mode causes high velocity motion of the H or D atoms being transferred. A pair of minor product channels ($HOCO^+$ and $DOCO^+$) was observed that has not previously been observed in thermal energy studies, probably because the products were lost to secondary reactions. These channels are complex-mediated at low E_{col} and low $L_{collision}$ and direct at elevated E_{col}. Despite being barrierless and exoergic, these reactions are quite inefficient, presumably due to a combination of a tight transition state, angular momentum constraints, and requirement for collision in a narrow range of orientations.

Acknowledgements

This work was supported by grants from the Chemistry Division of the National Science Foundation (CHE-0647124 and CHE-1111935).

References

1. D. M. Bell, J. M. Boyle and S. L. Anderson, J. Chem. Phys **134**, 64312 (2011).
2. M. C. Hsiao, A. Sinha and F. F. Crim, J. Phys. Chem. **95**, 8263 (1991).
3. A. Sinha, M. C. Hsiao and F. F. Crim, J. Chem. Phys. **92**, 6333 (1990).
4. A. Sinha, M. C. Hsiao and F. F. Crim, J. Chem. Phys. **94**, 4928 (1991).
5. A. Sinha, M. C. Hsiao and F. F. Crim, J. Chem. Phys. **92**, 6337 (1990).
6. M. J. Bronikowski, Z. Rong, D. J. Rakestraw and R. N. Zare, Sci. Tech. Aerosp. Rep. **27**, N89 (1989).
7. M. J. Bronikowski, W. R. Simpson, B. Girard and R. N. Zare, J. Chem. Phys. **95**, 8647 (1991).
8. M. J. Bronikowski, W. R. Simpson and R. N. Zare, J. Phys. Chem. **97**, 2194 (1993).
9. D. M. Bell, J. M. Boyle and S. L. Anderson, J. Chem. Phys **135**, 044305 (2011).
10. H. Gupta, P. Rimmer, J. C. Pearson, S. Yu, E. Herbst, N. Harada, E. A. Bergin, D. A. Neufeld, G. J. Melnick, R. Bachiller Astron. Astrophyss **521**, L47 (2010).

11. V. Ossenkopf, H. S. P. Müller, D. C. Lis, P. Schilke, T. A. Bell, S. Bruderer, E. Bergin, C. Ceccarelli, C. Comito, J. Stutzki and e. al., Astron. Astrophys. **518**, L111 (2010).

12. D. K. Bohme, G. I. Mackay and H. I. Schiff, J. Chem. Phys. **73**, 4976 (1980).

13. J. D. C. Jones, K. Birkinshaw and N. D. Twiddy, Chem. Phys. Lett. **77**, 484 (1981).

14. R. J. Shul, R. Passarella, L. T. DiFazio, Jr., R. G. Keesee and A. W. Castleman, Jr., J. Phys. Chem. **92**, 4947 (1988).

15. W. T. Huntress, Jr., M. J. McEwan, Z. Karpas and V. G. Anicich, Astrophys. J., Suppl. Ser. **44**, 481 (1980).

16. V. G. Anicich, *An Index of the Literature for Bimolecular Gas Phase Cation-Molecule Reaction Kinetics*. (National Aeronautics and Space Administration, and Jet Propulsion Laboratory,California Institute of Technology, Pasadena, California, 2003).

17. G. b. Czakó, E. Mátyus, A. C. Simmonett, A. G. Császár, H. F. Schaefer III and W. D. Allen, J. Chem. Theory Comput **4**, 1220 (2008).

18. J. M. Boyle, D. M. Bell, S. L. Anderson and A. A. Viggiano, J. Phys. Chem. A **115**, 1172 (2011).

19. S. L. Anderson, Acct. Chem. Res. **30**, 28 (1997).

20. B. W. Uselman, J. M. Boyle and S. L. Anderson, Chemical Physics Letters **440** (4-6), 171 (2007).

21. D. Gerlich, Adv. Chem. Phys. **82**, 1 (1992).

22. R. M. Jones, D. Gerlich and S. L. Anderson, Rev. Sci. Instrum. **68**, 3357 (1997).

23. M. J. Frisch, G. W. Trucks, H. B. Schlegel, G. E. Scuseria, M. A. Robb, J. R. Cheeseman, J. J. A. Montgomery, T. Vreven, K. N. Kudin, J. C. Burant, J. M. Millam, S. S. Iyengar, J. Tomasi, V. Barone, B. Mennucci, M. Cossi, G. Scalmani, N. Rega, G. A. Petersson, H. Nakatsuji, M. Hada, M. Ehara, K. Toyota, R. Fukuda, J. Hasegawa, M. Ishida, T. Nakajima, Y. Honda, O. Kitao, H. Nakai, M. Klene, X. Li, J. E. Knox, H. P. Hratchian, J. B. Cross, C. Adamo, J. Jaramillo, R. Gomperts, R. E. Stratmann, O. Yazyev, A. J. Austin, R. Cammi, C. Pomelli, J. W. Ochterski, P. Y. Ayala, K. Morokuma, G. A. Voth, P. Salvador, J. J. Dannenberg, V. G. Zakrzewski, S. Dapprich, A. D. Daniels, M. C. Strain, O. Farkas, D. K. Malick, A. D. Rabuck, K. Raghavachari, J. B. Foresman, J. V. Ortiz, Q. Cui, A. G. Baboul, S. Clifford, J. Cioslowski, B. B. Stefanov, G. Liu, A. Liashenko, P. Piskorz, I. Komaromi, R. L. Martin, D. J. Fox, T. Keith, M. A. Al-Laham, C. Y. Peng, A. Nanayakkara, M. Challacombe, P. M. W. Gill, B. Johnson, W. Chen, M. W. Wong, C. Gonzalez and J. A. Pople, (Gaussian, Inc., Pittsburgh PA, 2003).

24. A. P. Scott and L. Radom, J. Phys. Chem. **100**, 16502 (1996).

25. L. Zhu and W. L. Hase, in *Quamtum Chemistry Program Exchange* (Chemistry Department, Indiana University Bloomington, 1993).

26. W. M. Hayne, *Handbook of Chemistry and Physics*, 91 ed. (CRC Press/Taylor and Francis, Boca Raton, FL, 2004).

27. J. Troe, Chem. Phys. Lett. **122**, 425 (1985).

28. S. G. Lias, J. E. Bartmess, J. F. Liebman, J. L. Holmes, R. D. Levin and W. G. Mallard, J. Phys. Chem. Ref. Data **17**, 1 (1988).

29. N. S. Shuman, , M. Johnson, , W. R. Stevens, , M. E. Harding, , J. F. Stanton, and T. Baer, J. Phys. Chem. A **114**, 10016 (2010).

30. H. Fu, J. Qian, R. J. Green and S. L. Anderson, J. Chem. Phys. **108**, 2395 (1998).

31. G. A. Fisk, J. D. McDonald and D. R. Herschbach, Discuss. Faraday Soc. **44**, 228 (1967).

32. J. Liu, B. V. Devener and S. L. Anderson, J. Chem. Phys. **119**, 200 (2003).

33. J. M. Boyle, B. W. Uselman, J. Liu and S. L. Anderson, J. Chem. Phys **128**, 114304 (2008).

34. J. D. Thoemke, J. M. Pfeiffer, R. B. Metz and F. F. Crim, J. Phys. Chem. **99**, 13748 (1995).

35. A. Sinha, J. D. Thoemke and F. F. Crim, J. Chem. Phys. **96**, 372 (1992).

36. J. M. Pfeiffer, E. Woods, R. B. Metz and F. F. Crim, J. Chem. Phys. **113**, 7892 (2000).

37. J. C. Owrutsky, E. R. Kleim, J. V. Coe and R. J. Saykally, J. Phys. Chem. **93**, 5960 (1989).

38. K. Kawaguchi, A. R. W. McKellar and E. Hirota, J. Chem. Phys **84** (1986).

Table 10.1: Energetics for stationary points on the reaction coordinate in Figure 10.2, calculated at the B3LYP/6-311++G** level of theory, for HOD^+ + CO. The energetics vary, as shown, depending on whether the H or D atom is involved in the bonding. Values are in eV.

	H loss or PT	D loss or DT
Reactant Like Complex (RC)	-1.407	-1.407
TS1	-0.831	-0.819
Proton Transfer Product Like Complex (PC_{PT})	-1.017	-1.003
TS2	-0.029	-0.038
Hydrogen Loss Product like Complex (PC_{HL})	-0.747	-0.693
TS3	0.402	0.44
Formic Acid (FA) (cis)	-1.693	-1.682
Formic Acid (FA) (trans)	-1.709	-1.701
TS4	-0.498	-0.433

Table 10.2: Product ion velocity distribution fit results for reaction of ground state HOD^+ with CO.

HCO^+

E_{col}	E_{recoil}	E_{ratio} [a]	T_{ratio} [b]
0.18	0.081	45.5	0.1
0.35	0.151	44.4	2
0.62	0.246	41.7	4
0.92	0.382	44.4	6
1.85	0.845	49.4	12
2.82	1.348	49.7	20

DCO^+

E_{col}	E_{recoil}	E_{ratio} [a]	T_{ratio} [b]
0.18	0.082	45	0.1
0.35	0.143	42.1	2
0.62	0.247	41.9	4
0.92	0.352	40.9	6
1.85	0.835	48.8	12
2.82	1.248	46.1	20

[a] $E_{ratio} = E_{recoil} / E_{avail}$

[b] T_{ratio} is a measure of asymmetry in the product velocity distributions. $T_{ratio} > 1$ indicates a distribution that is asymmetric about $\langle V_{CM} \rangle$.

Table 10.3: RRKM lifetime of the RC↔PC_{PT} complex and branching to HCO^+ and $HOCO^+$ products.

Lifetime (ps)

E_{col}	L=1	L=26	L=51	L=76	L=101	L=126	L=151
0.18	1.83	1.34	0.75	0.48	0.34	0.27	
0.25	1.20	0.89	0.53	0.36	0.28	0.27	
0.34	0.80	0.61	0.38	0.28	0.26	0.30	
0.62	0.36	0.28	0.18	0.13	0.12	0.13	0.17

Branching to HCO+

E_{col}	L=1	L=26	L=51	L=76	L=101	L=126	L=151
0.18	12.3	12.4	12.6	13.0	13.8	15.6	
0.25	12.8	13.0	13.7	14.9	17.4	23.4	
0.34	13.4	13.8	15.0	17.7	23.3	37.9	
0.62	14.7	15.1	16.3	18.8	23.4	33.2	57.5

Branching to HOCO+

E_{col}	L=1	L=26	L=51	L=76	L=101	L=126	L=151
0.18	0.05	0.02	0.01				
0.25	0.07	0.04	0.01	0.01			
0.34	0.09	0.05	0.02	0.01	0.01		
0.62	0.19	0.13	0.06	0.03	0.02	0.01	

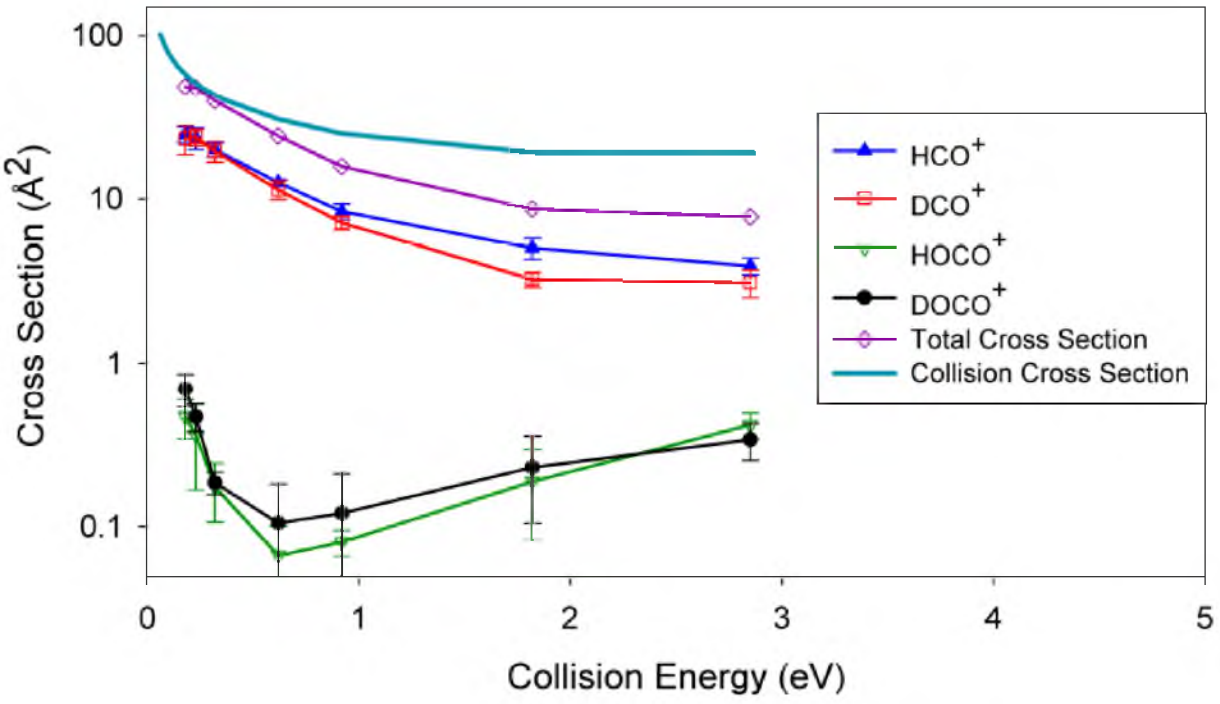

Figure 10.1: Ground state cross sections for production of HCO^+, DCO^+, $HOCO^+$, and $DOCO^+$ are plotted as a function of collision energy (E_{col}). The total cross section (σ_{tot}) is plotted along with the collision cross section, which is the greater of the hard sphere cross section and capture cross section.

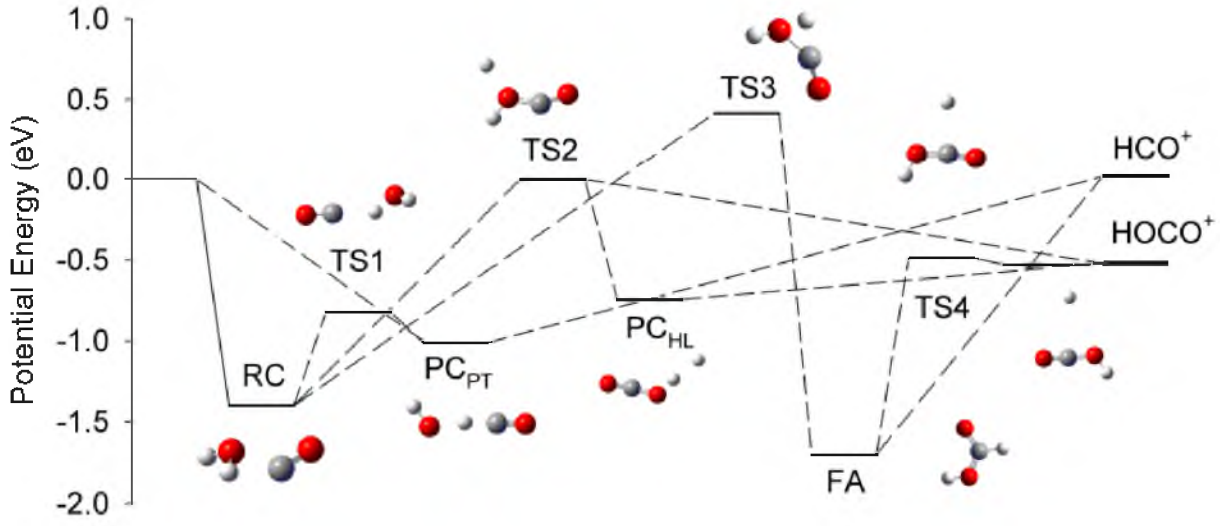

Figure 10.2: The reaction coordinate for H_2O^+ + CO, experimental energies are used for the products and reactants and 0K values using B3LYP/6-311++G** are used for the transition states and complexes separating the products and reactants.

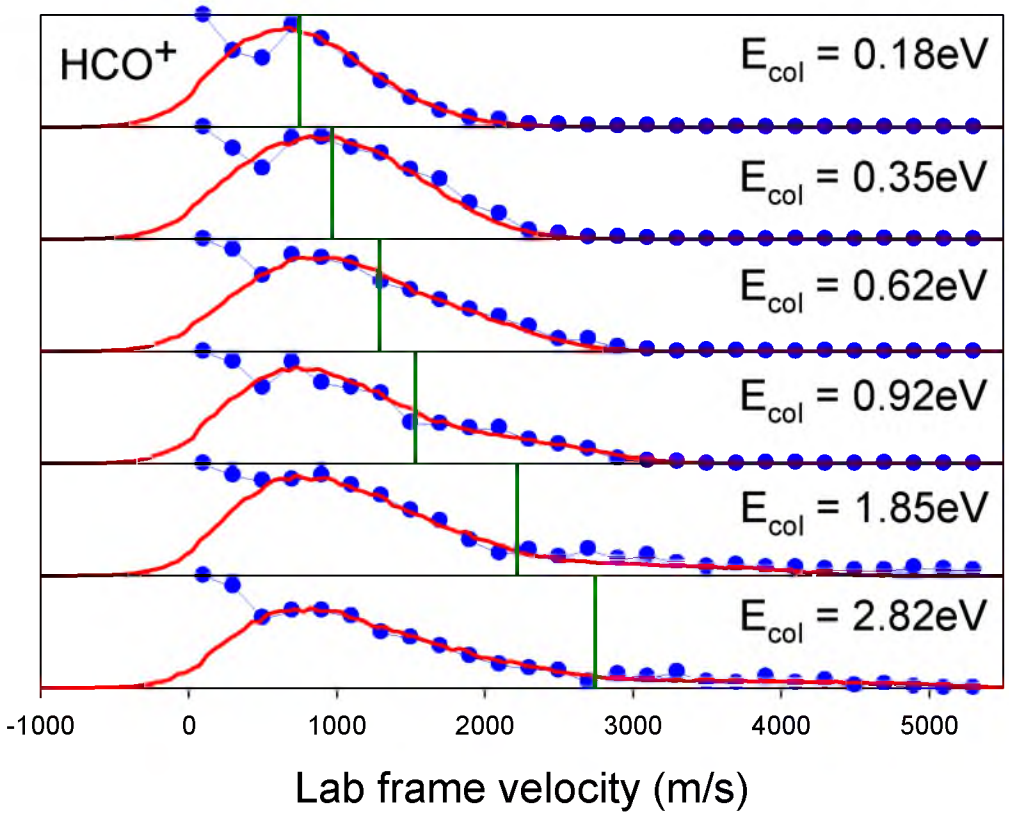

Figure 10.3: Lab frame axial velocity (v_{axial}) distribution for HCO^+ produced in reaction of $HOD^+ + CO$. Experimental data are denoted by points and simulated fit is denoted by the solid line passing through the experimental data. The solid vertical line denotes the velocity center of mass ($<V_{CM}>$)

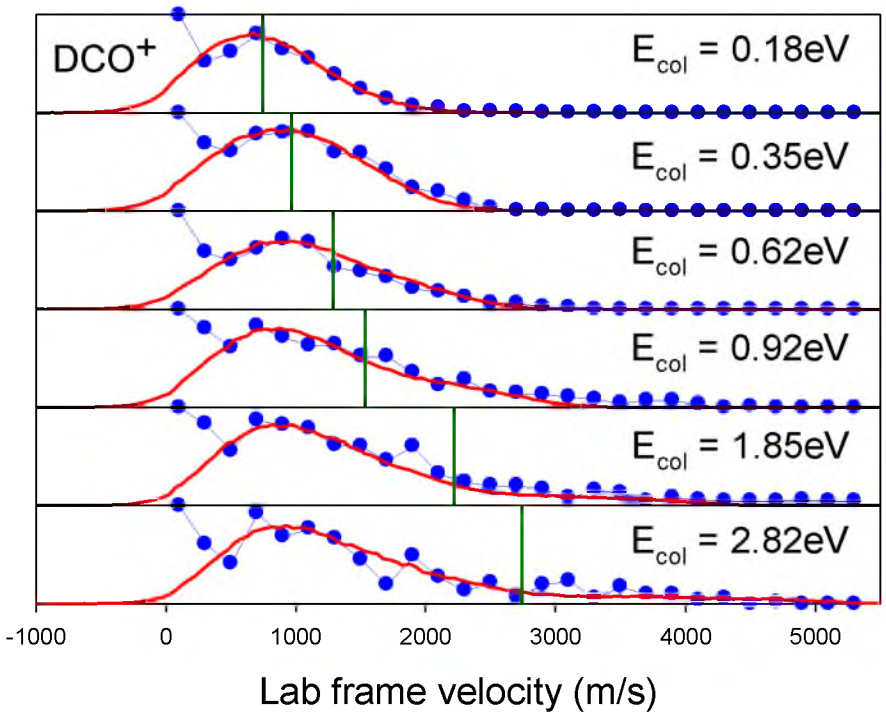

Figure 10.4: Lab frame axial velocity (v_{axial}) distribution for DCO^+ produced in reaction of $HOD^+ + CO$. Experimental data are denoted by points and simulated fit is denoted by the solid line passing through the experimental data. The solid vertical line denotes the velocity center of mass ($<V_{CM}>$)

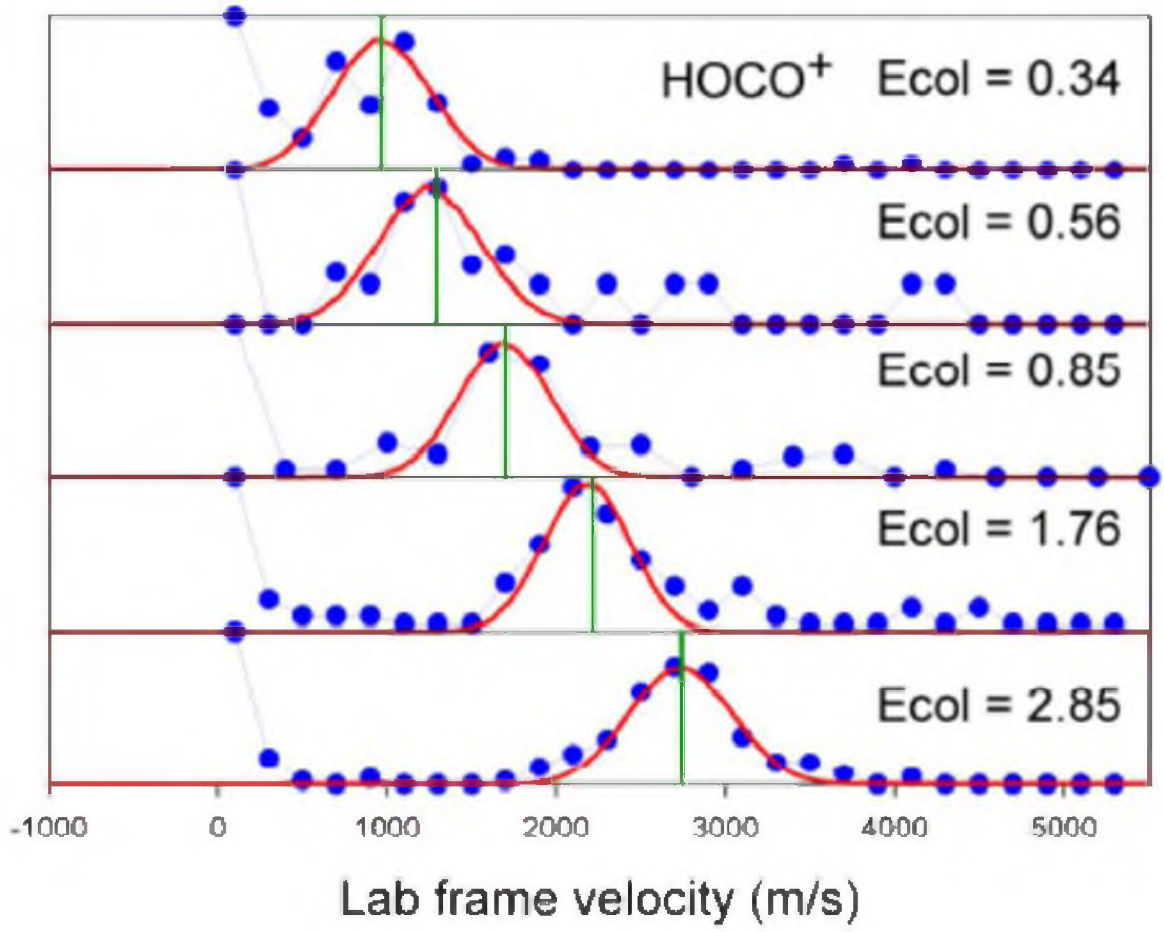

Figure 10.5: Lab frame axial velocity (v_{axial}) distribution for $HOCO^+$ produced in reaction of $HOD^+ + CO$. Experimental data are denoted by points and simulated fit is denoted by the solid line passing through the experimental data. The solid vertical line denotes the velocity center of mass ($<V_{CM}>$).

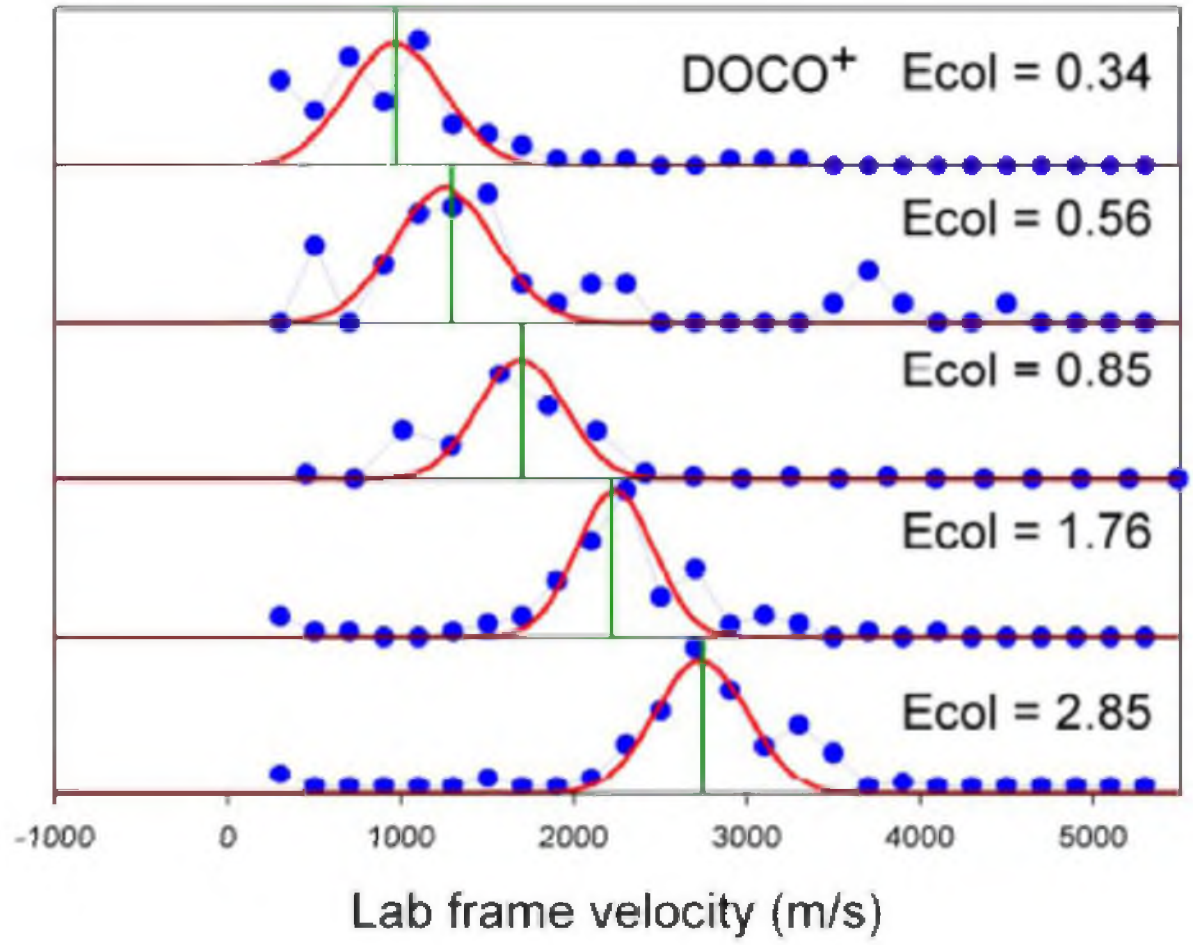

Figure 10.6: Lab frame axial velocity (v_{axial}) distribution for $DOCO^+$ produced in reaction of $HOD^+ + CO$. Experimental data are denoted by points and simulated fit is denoted by the solid line passing through the experimental data. The solid vertical line denotes the velocity center of mass ($<V_{CM}>$)

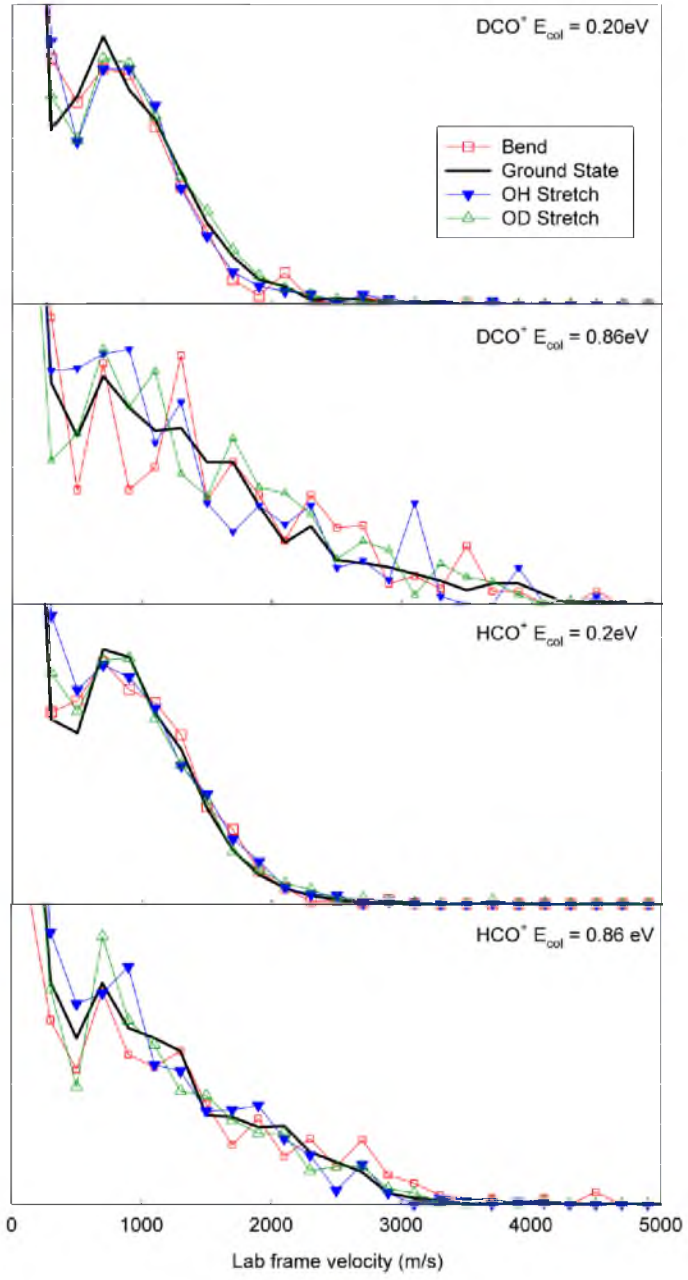

Figure 10.7: Lab frame axial velocity (v_{axial}) distribution for HCO^+ and DCO^+ produced in reaction of HOD^+ + CO at two representative E_{col} for each reactant vibrational state.

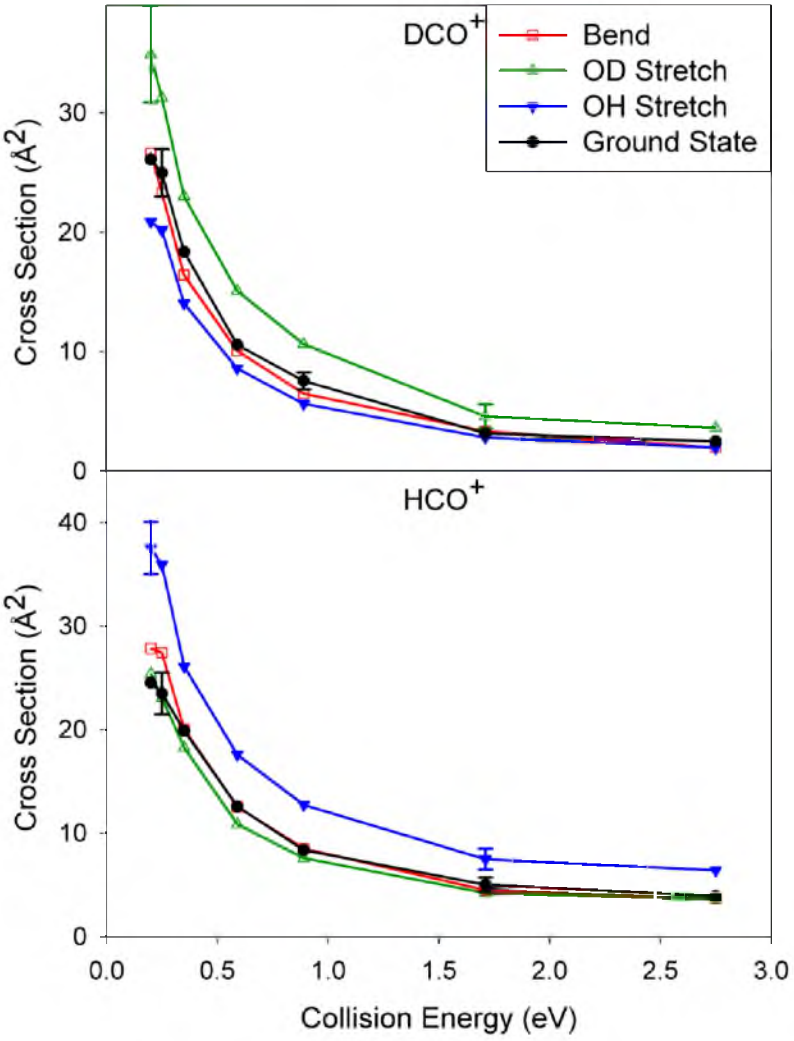

Figure 10.8: Cross sections for DCO^+ and HCO^+ in the reaction of vibrationally excited HOD^+. Top: Cross sections for the product of DCO^+ in the indicated initial vibrational state of HOD^+ as a function of collision energy. Bottom: Cross sections for the product HCO^+ in the indicated initial vibrational state of HOD^+ as a function of collision energy.

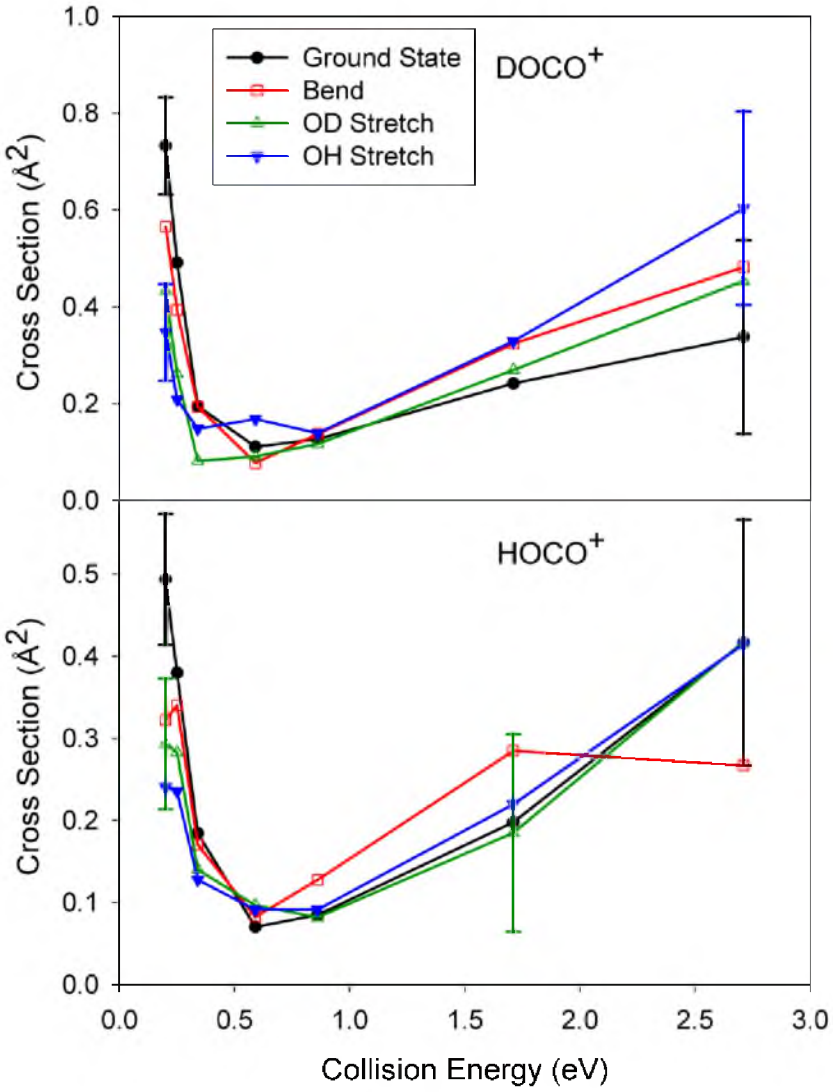

Figure 10.9: Cross sections for $DOCO^+$ and $HOCO^+$ in the reaction of vibrationally excited HOD^+. Top: Cross sections for the product of $DOCO^+$ in the indicated initial vibrational state of HOD^+ as a function of collision energy. Bottom: Cross sections for the product $HOCO^+$ in the indicated initial vibrational state of HOD^+ as a function of collision energy.

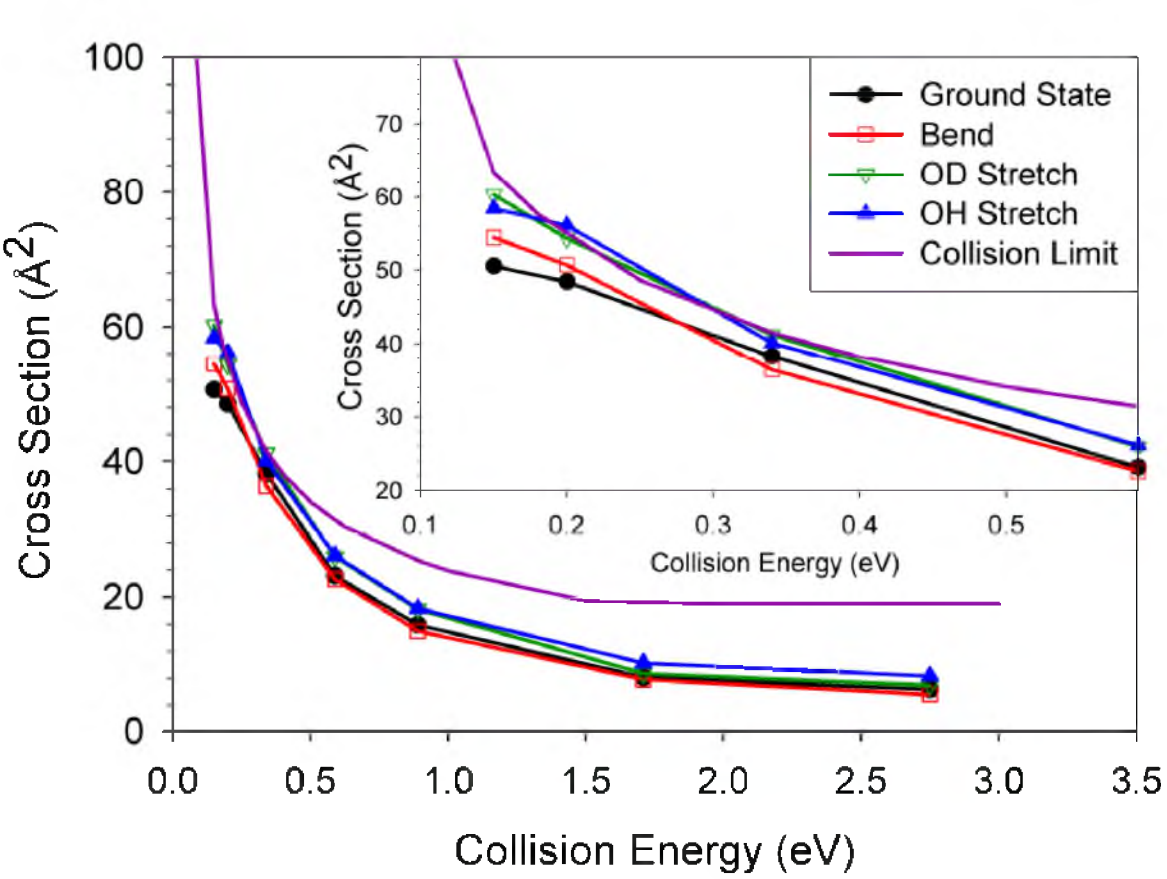

Figure 10.10: The total cross section for each vibrational state of HOD^+ as a function of collision energy. Inset: A zoomed in view on the low energy region (0 – 0.6eV).

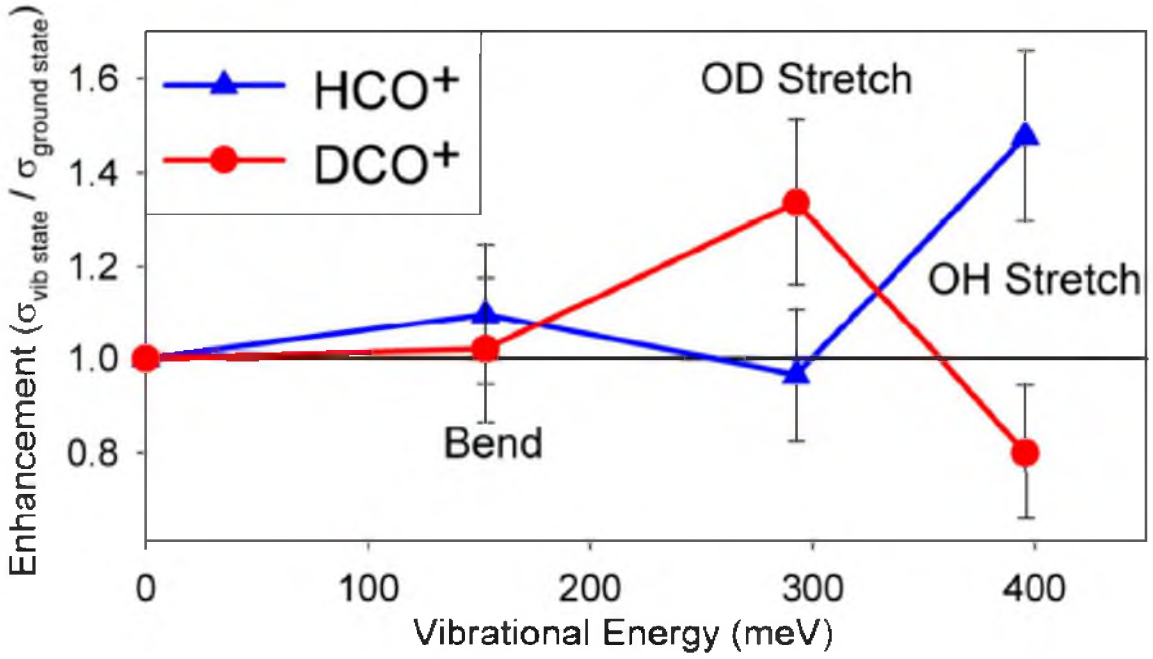

Figure 10.11: Enhancement ($\sigma_{\text{vibrational state}} / \sigma_{\text{ground state}}$) of HCO^+ and DCO^+ are shown as a function of vibrational energy (meV) for $E_{col} = 0.18$eV.

CHAPTER 11

VIBRATIONAL ENHANCED CHARGE TRANSFER AND MODE/BOND-SPECIFIC H^+ AND D^+ TRANSFER IN THE REACTION OF HOD^+ WITH N_2O

Reprinted with permission from David M. Bell, Scott L. Anderson, and The Journal of Chemical Physics **139,** 114305. Copyright 2013, American Institute of Physics

Abstract

The reaction of HOD^+ with N_2O was studied over the collision energy (E_{col}) range from 0.20eV to 2.88eV, for HOD^+ in its ground state and in each of its fundamental vibrational states: bend (010), OD stretch (100), and OH stretch (001). The dominant reaction at low E_{col} is H^+ and D^+ transfer, but charge transfer becomes dominant for $E_{col} > 0.5$ eV. Increasing E_{col} enhances charge transfer only in the threshold region ($E_{col} < 1$ eV), but all modes of HOD^+ v0069brational excitation enhance this channel over the entire energy range, by up to a factor of 3. For reaction of ground state HOD^+, the H^+ and D^+ transfer channels have similar cross sections, enhanced by increasing collision energy for $E_{col} < 0.3$ eV, but suppressed by E_{col} at higher energies. OD stretch excitation enhances D^+ transfer by over a factor of 2, but has little effect on H^+ transfer, except at low E_{col} where a modest enhancement is observed. Excitation of the OH stretch enhances H^+ transfer by up to a factor of 2.5, but actually suppresses D^+ transfer over most of the E_{col} range. Excitation of the bend mode results in ~60% enhancement of both H^+ and D^+ transfer at low E_{col}, but has little effect at higher energies. Recoil velocity distributions at high E_{col} are strongly backward-scattered in the center-of-mass frame, indicating direct reaction dominated by large impact parameter collisions. At low E_{col}, the distributions are compatible with mediation by a short-lived collision complex. Ab initio calculations find several complexes that may be important in this context, and RRKM calculations predict lifetimes and decay branching that are consistent with observations. The recoil velocity distributions show that HOD^+ vibrational excitation enhances reactivity in all collisions at low E_{col}, while for high E_{col} enhancement comes entirely from the subset of collisions that generate strongly backward-scattered product ions.

Introduction

Vibrational effects on chemistry have long been of interest from a fundamental standpoint as they further our understanding of what factors control reactivity. Polanyi and co-workers investigated how vibrational and translational energy affect barrier crossing in the model

A + BC system.[1] It was determined that a barrier early on the reaction coordinate is more efficiently overcome by translational energy, while a late barrier is more efficiently overcome by vibrational energy. For polyatomic reactants, the situation is complicated by presence of multiple vibrational modes which may or may not couple to the reaction coordinate. The singly deuterated water molecule (HOD) and its cation are interesting in this respect because the two stretch modes are largely localized in either the OH or OD bond, making it possible to think in terms of both mode- and bond-selective chemistry. For example, the Crim group utilized overtone-excited HOD with either 4 quanta of the OD stretch or 3 quanta of the OH stretch to overcome the barrier to reaction with H atoms, and observed that when the OD stretch was excited, breaking the OD bond was 200 times more likely than breaking the OH bond.[2-5] Conversely, excitation of the OH stretch made it 220 times more likely that the OH bond would break, compared to the OD bond. The Zare group examined the same reaction with HOD with only 1 quantum of OH or OD stretch excitation, with translationally hot H atoms supplying most of the energy required to drive the reaction.[6, 7] They found similar trends in enhancements for the respective stretches, but the enhancement was smaller, suggesting that vibrational energy was more efficient than translational energy in driving the reaction, as confirmed in a theoretical study.[8]

We have reported studies of reactions of mode-selectively excited HOD^+ with the neutral reactants N_2,[9] CO_2,[10] and CO.[11] In these reactions, the dominant channels are endoergic H^+ and D^+ transfer (with endoergicity decreasing to near zero for CO), and it was found that OH stretch excitation enhances H^+ transfer, while having either a negligible or inhibitory effect on D^+ transfer. The converse is true for the OD stretch; this behavior is in line with the results of the neutral HOD experiments mentioned above. A surprising result was that for reaction with CO_2 and N_2, excitation of the bend vibration (010) of HOD^+ gives the largest overall enhancement, because bend excitation strongly enhances both H^+ and D^+ transfer. The effect of the bend vibration in reaction of neutral HOD was probed by Zare and co-workers via excitation of the (110) combination band, with the result that there was little effect from the additional bend

excitation. We proposed that the large bend enhancements observed in the endoergic H^+ and D^+ transfer reactions with CO_2 and N_2, are due to changes in the shape of the potential surface in the region of closest approach, enhancing the probability of transitioning into the exit channel as the bend angle opens.[10]

The reaction of HOD^+ with N_2O is of interest because the proton affinity of N_2O is such that H^+ and D^+ transfer are endoergic by ~0.2 eV, and there are reactant-like complexes that might mediate the reaction at low collision energy (E_{col}). Also, in addition to the H^+ and D^+ transfer channels, charge transfer is only ~0.27eV endoergic, and thus should be a significant competing channel that may affect the vibrational dependence. Previous work on this system includes studies of the photo-induced dissociation (PID) and collision-induced dissociation (CID) of the $(N_2O \cdot H_2O)^+$ cluster ion as well as its deuterated analog.[12-14] As discussed below, the dissociation experiments observed similar product channels that are observed in this bimolecular collision; however, the product branching is quite different. A detailed study of the potential energy surface for the $(N_2O \cdot H_2O)^+$ system was reported by Stevens *et al.* who examined both ground and low-lying electronically excited surfaces,[15] relevant to both the dissociation and bimolecular reaction experiments.

Methodology

The experiments were done using a guided ion beam tandem mass spectrometer that has been described previously.[16-18] Helium was bubbled through a thermostatted 1:1 mixture of H_2O and D_2O, to generate a mixture of roughly 96% He, 1% H_2O, 2% HOD, and 1% D_2O. This mixture was pulsed into the experiment as a skimmed supersonic molecular beam. HOD was ionized by resonance-enhanced multiphoton ionization (REMPI) through the **C** ($^1B_1$) state,[19] allowing production of HOD^+ in the following states: (000) ground state; (001) OH stretch - 0.396 eV, (010) bend - 0.153 eV, and (100) OD stretch - 0.293 eV. The state purity was checked by photoelectron spectroscopy, and the only state with significant impurity is the bend, where

56% of the ions are produced in the (010) state, with the remaining 44% in the ground vibrational state. Because we also measure cross sections for reaction of ground state ions, the bend results are easily corrected for the ground state impurity, and this has been done in the data presented below.

HOD^+ ions were created between a pair of planar electrodes, collected and focused by a quadrupole ion guide, then passed through a quadrupole mass filter to remove any fragment ions, as well as the small amount of H_2O^+ and D_2O^+ produced. The ionization conditions were optimized so that no D_3O^+ was formed by ion-molecule reactions in the source, and therefore, it should be a good assumption that the HOD^+ beam has negligible contamination from H_3O^+, which would be produced by analogous reactions. If there were H_3O^+ in the beam, the only energetically possible reaction would be $H_3O^+ + N_2O \rightarrow N_2OH^+ + H_2O$, which would contribute to the N_2OH^+ product channel for E_{col} above 1.2 eV. As shown below, the data show no sign of any new contribution to the N_2OH^+ cross section appearing above 1.2 eV.

After mass selection, the beam of HOD^+ was passed through a time-of-flight (TOF) gating electrode to narrow the kinetic energy distribution of the ion beam, and then injected into an 8-pole ion guide system.[20] The first ion guide was surrounded by a 10 cm long scattering cell containing $1x10^{-4}$ Torr of N_2O, measured by a capacitance manometer. All ions (product and unreacted HOD^+) were collected by the first guide and passed into a second, longer guide to allow TOF velocity analysis. The ions were then passed through a final mass filter and detected by an electron multiplier. The ion signal was counted with a P7882 FAST ComTec multichannel scalar, controlled by a LabView program. Integral cross sections were calculated from the reactant and product ion intensities (integrated from the TOF measurements), using the calibrated effective length of the scattering cell and the pressure of the scattering cell. The TOF distributions were also converted to velocity distributions and used both to establish the actual collision energy and energy spread at each nominal energy, and provide insight into the recoil dynamics of the product ions.

Multiple sets of data were taken on different days, and the results presented below are the averages, with error bars calculated from the standard deviations. In addition to random errors indicated by error bars in the figures, there are possible systematic effects that are harder to quantify. Error in the absolute scattering cell pressure and length calibration would result in an error in the absolute scale of the cross sections, but would have no effect on comparisons between different product channels or vibrational states, which are the most important source of dynamical insight. We used reactions of $Ar^+ + D_2$, $HOD^+ + CO$, and $HOD^+ + CO_2$ to calibrate our scattering cell length. We estimate that the absolute cross section scale is within ±20% of the correct value.

To map out the reaction coordinate, electronic structure calculations were performed at the B3LYP/6-311++G(d,p) level of theory, using Gaussian03.[21] The vibrational frequencies and zero-point energies were scaled by factors of 0.9613 and 0.9804, respectively. Transition states were verified to be first order saddle points by frequency calculations. To determine the kinetics and product branching that would result from statistical breakup of the various complexes identified on the reaction coordinate, Rice-Ramsperger-Kassel-Marcus (RRKM) rate and density of state calculations were performed using a program developed by Zhu and Hase.[22] Direct state counting was used and the energetics, moments of inertia, and vibrational frequencies were obtained from the B3LYP/6-311++G(d,p) calculations.

Results

Ground State Cross Sections

Product ions were observed with masses of 44, 45, and 46, corresponding with N_2O^+, N_2OH^+, and N_2OD^+ respectively. Integral cross sections for reaction of HOD^+ in its ground vibrational state are presented in the top frame of Figure 11.1, for center-of-mass (CM) collision energies (E_{col}) ranging from 0.15eV to 2.88eV. Possible reactions and the associated energetics observed are:

$HOD^+ + N_2O \rightarrow N_2OH^+ + OD$ (H^+ transfer = "HT") $\Delta_rH^0 = 0.187 \pm 0.046$ eV

$\rightarrow N_2OD^+ + OH$ (D^+ transfer = "DT") $\Delta_rH^0 = 0.206 \pm 0.046$ eV

$\rightarrow N_2O^+ + HOD$ (charge transfer = "CT) $\Delta_rH^0 = 0.259 \pm 0.002$ eV

where the energetics for charge transfer and H^+ transfer ("HT") are experimental,[23, 24] and the energy for D^+ transfer ("DT") was derived from HT value, using zero point energies calculated at the b3lyp/6-311++G(d,p) level of theory. Figure 11.1 also gives the total reactive cross section ($\sigma_{reactive}$ = sum of HT, DT, CT), and the collision cross section ($\sigma_{collision}$) , which is taken as the capture cross section at low energies, and at high E_{col} is approximated by the hard sphere cross section, calculated from the molecular geometries and atomic radii. The capture cross section was calculated including both ion-induced dipole and orientationally averaged ion-dipole interactions. In addition to the directly observed HT, DT, and CT channels, the cross section for nonreactive scattering (i.e., producing HOD^+) is also indicated. This nonreactive scattering cross section (σ_{NR}) was estimated from the HOD^+ velocity distributions, as discussed below, and includes only collisions in which HOD^+ undergoes a velocity change large enough to be distinguishable from the reactant beam. The nonreactive scattering cross section can also be estimated as the difference between $\sigma_{collision}$ and $\sigma_{reactive}$. This "$\sigma_{NR\text{-}diff}$" cross section is also plotted, and the fact that it is similar to σ_{NR} indicates that most nonreactive collisions do, indeed, result in substantial change in the scattered HOD^+ velocity.

The energetics given above for HT and DT correspond to formation of the most stable product isomer, where the H^+ or D^+ is bound to the O atom of N_2O (i.e., N_2OH^+ or N_2OD^+). There are also HN_2O^+ and DN_2O^+ isomers lying ~0.26 eV higher in energy, where the H^+ or D^+ is bound to the terminal N atom of N_2O. The barrier separating N_2OH^+ and HN_2O^+ isomers was calculated to be 3.8eV relative to N_2OH^+ at the CCSD(T)/cc-pVTZ level of theory,[25] i.e., isomerization between the product isomers is not energetically possible in our experiment. We

observe no increase in HT or DT cross sections at the thresholds for the higher energy isomers, suggesting that they are not major products; however, to the extent that these isomers form, they are included in the HT and DT cross sections.

The E_{col} dependence of the HT, DT, and CT cross sections is consistent with the endoergicities of the product channels, taking the experimental collision energy spread (~0.15eV) into account. The HT and DT cross sections increase with E_{col} up to ~0.34eV, but then decrease at higher E_{col}. Because of its higher endoergicity, CT is a minor channel at low E_{col}, rapidly increasing for E_{col} up to ~0.88eV, then becoming nearly E_{col}-independent at higher energies.

The lower frame of Figure 11.1 gives the branching ratios observed for scattering of ground state HOD^+ from N_2O, including the HT, DT, CT, and nonreactive scattering channels (i.e., σ_{NR}). Because the HT and DT cross sections are very similar for the ground state reaction, they are lumped together for the branching ratio calculation.

Computational Results

Stevens *et al.*[15] reported a detailed reaction coordinate for this system, and we simply re-calculated the part relevant to our bimolecular collision system at the B3LYP/6-311++G(d,p) level of theory. The recalculation was needed to obtain vibrational and rotational frequencies for the monodeuterated system, and these were calculated for all possible isotopologs of each structure. Because deuteration only affects the energetics slightly, for simplicity, the reaction coordinate shown in Figure 11.2 is given for the all-H analog of the system.

The lowest energy product channel for the $[H_2O{\cdot}N_2O]^+$ system corresponds to $H_2O_2^+ + N_2$; however, because $H_2O_2^+$ was not observed in either our results, or in previous studies,[12-14] this channel is omitted from the reaction coordinate in Figure 11.2. There are three reactant-like complexes (designated "RC1", "RC2", and "RC3" in Figure 11.2) bound by 1.42eV, 1.40eV, and 1.16eV, respectively, with respect to reactants. RC1 and RC2 correspond to electrostatic interactions of the O atom in HOD^+ with either terminus of N_2O. RC3 corresponds to HOD^+

hydrogen-bonded to the N terminus of N_2O; however, the O-H and H-N bond lengths are calculated to be 0.998Å, and 1.798 Å, respectively, i.e., RC3 is still quite reactant-like. In all three RC complexes, the charge is roughly equally shared between the two reactant moieties. The RC3 complex was not directly observed in the CID and PID work, but it was hypothesized[12-14] that such a complex might form to some extent as an intermediate to the HN_2O^+ + OH product channels, and that there was a high barrier between RC2 and RC3. In fact, the barrier (TS-23) is small compared to the dissociation limits.

From the perspective of our bimolecular collision experiment, the key point is that all three complexes are similar in energy, with barriers to interconversion that are small compared to the available energy (i.e., well depth + E_{col}). Therefore, even in our lowest E_{col} range, where such complexes might be dynamically significant (see below), the three complexes are better considered as a single complex that samples many geometries, including RC1, RC2, and RC3, via internal rotation of the loosely coupled HOD and N_2O moieties.

In addition to the ground state structures in Figure 11.2, Stevens *et al.*[15] calculated the vertical excitation energies of the RC1 and RC2 complexes to the first two electronically excited doublet states. In C_s symmetry, the ground electronic state has $^2A''$ symmetry, and will be denoted $1^2A''$, following their nomenclature. The vertical excitation energies were calculated to be between 0.8eV and 2.4eV, depending on the structure and level of theory, i.e., well within the range of our available energy. One excited state is optically bright (denoted $2^2A''$) and has 63% of the charge on the water moiety. The other excited state ($1^2A'$) has 90% of the charge residing on N_2O, and in C_s symmetry, this state correlates to the CT products. In randomly oriented collisions; however, all three states have ^2A symmetry, and therefore can be mixed in the collisions, suggesting that there should be adiabatic pathways connecting reactants to the CT product channel.

Recoil Velocity Distributions

Lab frame v_{axial} distributions were obtained for all ions observed in reaction of each HOD^+ vibrational state. Note that the v_{axial} distributions are simply projections of the full velocity distributions on the experimental axis. Before presenting results for product ions, we briefly outline the approach used to extract the nonreactive scattering cross section, σ_{NR}, plotted in Figure 11.1. In essence, we simply compare the HOD^+ v_{axial} distributions measured with and without N_2O in the scattering cell, recorded as part of all cross section measurements. The data for the empty scattering cell consist of a sharp velocity peak, which is analyzed to determine the actual collision energy and collision energy spread. When the cell is filled, nonreactive scattering gives rise to a small amount of HOD^+ in a broad distribution of v_{axial} that is slower than the reactant beam peak, and by integrating this broad distribution, we obtain an estimate of σ_{NR}.[26] Example data and more details of the analysis are presented in the Supporting Information.

The v_{axial} results for the N_2OH^+, N_2OD^+, and N_2O^+ product ions formed in reaction of ground state HOD^+ are presented in Figures 11.3 - 5 for selected collision energies. The solid vertical lines in each frame shows $\langle V_{CM} \rangle$, i.e., the velocity of the CM frame with respect to the lab, averaged over the collision energy distribution. Because the experiment is cylindrically symmetric, the v_{axial} measurements contain easily interpretable dynamical information. For example, lab velocities faster than $\langle V_{CM} \rangle$ correspond to product ions that are forward-scattered in the CM frame, while velocities slower than $\langle V_{CM} \rangle$ correspond to ions that are backward-scattered in the CM frame. Here, and in the discussion below, forward direction is defined by the direction of the reactant beam.

One question is whether the RC complexes (Figure 11.2) play a significant role in mediating any of the reactions. If reaction is mediated by a complex with lifetime long compared to its rotational period ($\tau_{rotation}$), then the v_{axial} distribution must be forward-backward symmetric about $\langle V_{CM} \rangle$. Conversely, if the distribution is not forward-backward symmetric, then the mechanism must be direct, with collision time ($\tau_{collision}$) shorter than $\tau_{rotation}$ for the collision

complex. In that case, the propensity toward forward- or backward-scattering reveals the dominance of rebounding or stripping dynamics, and the position of the velocity peak provides insight into the partitioning of energy in the products.

It can be seen that for all three reactions, the v_{axial} distributions are strongly backward-peaked for high E_{col}, indicating that the dominant mechanism in this energy range is direct, with short collision times. Note that "forward" and "backward" are defined with respect to the initial CM frame direction of the HOD^+ ions. Because all reactions in this system involve transfer of the charge (as e^-, H^+, or D^+), strongly backward-scattered product ions correspond to stripping type dynamics, occurring in large impact parameter collisions. In addition to the backward peak, the v_{axial} distributions at high E_{col} also have a broad component that extends well forward of $\langle V_{CM} \rangle$, indicating that reaction also occurs in collisions at smaller impact parameters that produce ions that are sideways- or forward-scattered. As the collision energy is lowered, the distributions broaden, and $\langle V_{CM} \rangle$ moves to lower v_{axial}. As a result, the distributions become more symmetric looking, although for experimental reasons, we are unable to tell if they actually become symmetric at our lowest E_{col}.

The problem is that product ions with low lab frame velocities are easily perturbed by potential barriers in the ion guide system and also have a higher probability of secondary collisions in the scattering cell,[27] which also perturb the velocity. (In this system, secondary collisions cannot change the product identity.) In exothermic reactions, product ions may recoil with enough energy to appear at negative lab frame velocities (moving away from the detector). Here, where all reactions are endoergic, negative lab velocities are only possible for reactions of vibrationally excited HOD^+. To ensure that all ions are collected, the ion lens just before the scattering ion guide is biased to prevent ions from exiting in that direction; however, the TOFs of ions with very low or negative lab velocities tend to be artificially long, contributing to an artificial peak at near zero v_{axial} (off scale in Figures 11.3 – 11.5, see below). The TOF measurements extend 8 ms after the laser pulse, which appears to be long enough to collect even

the very slow product ions. For this reason, while all ions are counted in the integral cross section calculations, the shape of the v_{axial} distributions below ~500 m/s is not reliable. Because $<V_{CM}>$ decreases with decreasing E_{col}, essentially the entire backward-scattered half of the distribution is below 500 m/s for our lowest collision energies.

The solid curves in Figures 11.3, 11.4, and 11.5 are simulations in which model recoil velocity distributions were convoluted with the velocity distributions of the reactants and projected onto the lab frame axis for direct comparison to the experimental v_{axial} distributions. The angular part of the model recoil velocity distributions was based on the osculating complex model,[28] which assumes that a collision complex is formed with a rotational period $\tau_{rotation}$ and lifetime $\tau_{collision}$. The ratio $\tau_{ratio} = \tau_{rotation} / \tau_{collision}$ controls the angular distribution, i.e., if $\tau_{ratio} << 1$ the distribution is isotropic due to rotational randomization, while $\tau_{ratio} >> 1$ gives a sharp angular distribution peaked at an angle θ_{peak}. For the reactions here, where the charge transfers along with little mass (e^-, H^+, D^+), it is reasonable to assume $\theta_{peak} = 180°$, corresponding to stripping dynamics in large impact parameter collisions. The recoil speed distributions were modeled by assuming Gaussian recoil energy distributions, where the distribution is controlled by f_{width} and f_{peak} parameters that set the width and peak energy values as fractions of the available energy, E_{avail}. This model allows fitting based on just three adjustable parameters (τ_{ratio}, f_{width}, and f_{peak}). For scattering at high E_{col}, the experimental distributions are sharply backward-peaked, but there is also a broad component that extends well forward of V_{CM}. To fit such distributions, it was necessary to include two components in the simulation. The major component is sharply backward-peaked with τ_{ratio}, f_{width}, and f_{peak} parameters well constrained by position and shape of the peak. The minor component was assumed to be symmetric about $\langle V_{CM} \rangle$, with a broad distribution of recoil energy. For energies below 0.88 eV, the distributions are well fit by a single model component.

We are primarily interested in two results from the v_{axial} distribution fits, and these are presented in Table 11.1. One question is how energy initially in E_{col} and in various reactant vibrational modes is partitioned to the products. To address this question, Table 11.1 provides results for the average percent of E_{avail} partitioned into recoil: $\%E_{recoil} = 100 \cdot \langle E_{recoil} \rangle / \langle E_{avail} \rangle$, where the average recoil energy, $\langle E_{recoil} \rangle$, is obtained from the fits, and $\langle E_{avail} \rangle$ is $E_{col} + E_{vib} + E_{rot} - \Delta_r H^0$, with E_{vib} equal to the excitation energy for each state studied, and E_{col} and E_{rot} averaged over the appropriate experimental distributions. We are also interested in the extent to which the products are forward- or backward-scattered, as an indication of the reaction mechanism. Table 11.1 also gives the backward/forward ratio ("B/F"), which is simply the ratio of the intensities for v_{axial} faster and slower, respectively, than $\langle V_{CM} \rangle$. For a complex mediated mechanism, B/F must be ~1; therefore, if B/F is very different than unity, the mechanism must be direct. "Direct", in this context, means that the collision time is short compared to the rotational period, $\tau_{rotation}$, of any complexes that might form during the collision. The rotational periods can be estimated from the complex moment of inertia, and the angular momentum, $L = \mu \cdot v_{rel} \cdot (\sigma_{collision} / \pi))^{1/2}$), where μ is the reduced mass of the reactants, v_{rel} is the relative velocity of the reactants, and $\sigma_{collision}$ is given in Figure 11.1. Table 11.2 gives estimates of $\tau_{rotation}$ assuming that the moment of inertia is equal to those for the reactant-like complexes (RC1, RC2, and RC3). Roughly, $\tau_{rotation}$ drops from ~1 ps for E_{col} = 0.2eV to ~0.5 psec at 2.88 eV. For reference, Table 11.2 also gives $\tau_{fly\text{-}by}$, which is simply the time it would take undeflected reactants to fly past each other over a relative distance of 5Å.

Effects of HOD^+ Vibrational Excitation

Integral cross sections for N_2O^+, N_2OH^+, and N_2OD^+ are shown for all four HOD^+ reactant states in Figures 11.6 and 11.7. In Figure 11.6, the cross sections for CT are plotted as a function of E_{col} in the top frame, and as a function of total energy (E_{tot}) in the bottom frame. The

only significant source of rotational energy is thermal rotation of the N_2O reactant, and because this is small (~75 meV) and independent of the HOD^+ vibrational state, it has been omitted to focus on the comparison of the effects of E_{col} and E_{vib}. For CT, all modes of HOD^+ vibrational excitation lead to substantial enhancements, and these effects persist to high E_{col}, where the collision energy no longer enhances CT.

The effects of HOD^+ vibrational excitation on the HT and DT channels are quite mode/bond selective, as shown in the top and middle frames of Figure 11.7. The bottom frame shows how the branching between HT and DT varies with E_{col} and HOD^+ vibrational state. In the discussion below, the stretch of the bond that is broken in reaction will be referred to as the "broken-bond stretch" and the stretch of the opposite bond will be called the "spectator stretch", i.e., the OH stretch is the broken-bond stretch for HT, but is the spectator stretch for DT. It can be seen that for both HT and DT, the vibrational effects are mode-specific, and vary qualitatively with E_{col}.

To provide additional insight into the origins of the vibrational effects, we also measured and simulated v_{axial} distributions for reaction of HOD^+ in all vibrational states, and the $\%E_{recoil}$ and B/F results are summarized in Table 11.1. In most systems we have studied previously, reactant vibrational excitation has little if any effect on recoil behavior, most likely because the vibrational energy is relatively small, and tends to be randomized in reactive collisions. Figure 11.8 shows that for this system, vibrational excitation leads to significant differences in the shape of the v_{axial} distributions. For two representative E_{col} values, data are shown for reaction for HOD^+ in its ground state, with one quanta of the OD stretch (0.293eV), and with one quantum of OH stretch excitation (0.396 eV). The intensities have been normalized so that the integrated area of the distributions (including the low v_{axial} spike due to slow ions, which was off-scale in Figures 11.3 – 11.5) is proportional to the integral cross section, allowing the absolute intensities in different velocity ranges to be compared directly. For CT (left side of figure), it can be seen that in the threshold energy range ($E_{col} \leq 0.62$ eV), the v_{axial} distributions for all the HOD^+ reactant states

have similar shapes, i.e., the vibrational enhancement is uniform across the N_2O^+ v_{axial} distribution. In contrast, for high E_{col}, vibrational excitation no longer enhances CT for those collisions that produce N_2O^+ in the broad tail of the v_{axial} distribution above ~500 m/sec. The observed enhancement, instead, comes entirely from enhanced probability of CT in collisions that produce strongly backward-scattered N_2O^+. Because vibration selectively enhances products with high CM frame recoil velocity, the implication is that the average fraction of E_{avail} appearing as E_{recoil} must also be increased by OH or OD stretch excitation. Because the enhancements are in the velocity range below 500 m/sec, where the velocities are unreliable, the v_{axial} simulations necessarily require some additional assumptions. The simulations were adjusted to fit the v_{axial} > 500m/s range, as usual, but also to make the integrated intensity over the entire v_{axial} range fit the integrated area of the experimental distributions, including the sharp, near-zero-velocity peak. The resulting $\%E_{recoil}$ values are collected in Table 11.1, and show that $\%E_{recoil}$ generally increases with increasing E_{col} for all reactant vibrational states, and for a given E_{col}, the pattern of $\%E_{recoil}$ is not mode specific and increases with increasing reactant vibrational energy.

For the HT and DT reactions (middle and right-hand columns), the pattern of enhancements are similar. At low E_{col}, vibrational excitation enhances intensity over the entire velocity range, preserving the shape of the v_{axial} distributions. The effects at high E_{col} for HT and DT are mode-specific. HT is enhanced only for excitation of the broken-bond (i.e., OH) stretch, but as in CT, that enhancement appears only in the component of backward-scattered product ions. Excitation of the spectator (i.e., OD) stretch has essentially no effect on one HT, as might have been expected from the absence of a significant effect on the HT integral cross section. The pattern of vibrational effects on the DT reaction at high E_{col} is more complicated. Excitation of the broken-bond (i.e., OD) stretch enhances DT, and the increase comes primarily in the backward-scattered v_{axial} peak, as in the other reactions. Excitation of the spectator (OH) stretch actually inhibits DT at high E_{col} (Figure 11.7), and the right-hand frame of Figure 11.8 shows that

the inhibition takes the form of a reduction in intensity in the broad component, with a relatively smaller inhibitory effect on the strongly backward-scattered peak.

A final point to make about Figure 11.8 is that for high E_{col}, the broad tail of the v_{axial} distribution is most intense for DT, and least intense for CT. This difference is simply a consequence of the mass being transferred in the reaction, i.e., an electron for CT, H^+ for HT, and D^+ for DT. As the transferred mass is increased, so is the minimum momentum transferred in the stripping-type collisions that dominate at high E_{col}. With increasing momentum transfer, there is less intensity in the near-zero v_{axial} peak, and correspondingly higher intensity at higher v_{axial} values.

Discussion

Previous Studies

The bimolecular $H_2O^+ + N_2O$ reaction was previously studied at thermal energies in a selected ion flow tube (SIFT) experiment,[29] which observed production of N_2OH^+ at about 0.4% of the collision rate. The low rate is expected because the endothermicity of the HT reaction allows only the high energy tail of the Boltzmann distribution to react. An association product was also observed, corresponding to buffer gas stabilization of a collision complex;[30] however, CT products were not observed under thermal conditions because this channel is too endothermic.

As mentioned in the introduction, there have also been both collision and photo-induced dissociation (CID[12, 13] and PID[12-14]) studies of $(N_2O \cdot H_2O)^+$ cluster ions, and both cases, dissociation to H_2O^+, N_2O^+, and N_2OH^+ product ions was observed. The clusters in these studies were thought to correspond to "RC1" and "RC2" in Figure 11.2. The branching to $N_2OH^+ + OH$ (i.e., our HT/DT channel) was ~5-10% in both studies, but increased with collision energy in the CID study and decreased with photon energy in the PID study. In CID, the lowest energy $H_2O^+ + N_2O$ channel (i.e., our σ_{NR}) accounted for ~90% of the products, decreasing somewhat with increasing collision energy, and the highest energy $N_2O^+ + H_2O$ (i.e., our CT channel) accounted

for only 5 - 10% of the products. For PID, the highest energy $N_2O^+ + H_2O$ channel was initially reported to dominate[12, 14]; however, after correction of a detection discrimination problem, its branching was reduced to ~30% and the corresponding branching to the lowest energy $H_2O^+ + N_2O$ channel was increased to ~60%, increasing with increasing photon energy.[13]

The branching ratios observed here (lower frame of Figure 11.1) are quite different, particularly at high E_{col}; however, the differences are not unexpected because the three types of experiments activate the system quite differently. For low E_{col}, we observe primarily nonreactive scattering (i.e., $HOD^+ + N_2O$), similar to what is observed in both CID and PID, but the branching simply reflects the fact that the CT, HT, and DT channels are all endoergic and therefore inaccessible for all but the high energy tail of our collision energy distribution. As these channels open with increasing E_{col}, we see roughly equal branching for all three channels (i.e., ~30% each for CT, HT/DT, and no reaction) for E_{col} around 1 eV, then at high energies, the HT/DT branching drops below 20%, and $HOD^+ + N_2O$ (σ_{NR}) and $N_2O^+ + HOD$ (CT) both increase to ~40%. This contrasts with the 60% - 90% branching for $H_2O^+ + N_2O$ observed in PID, and CID, respectively.

One important difference between bimolecular collisions compared to CID or PID is that those experiments start with a complex which is then activated to drive dissociation, while in our experiment, complexes are only dynamically significant at our lowest energies, as shown by the v_{axial} distributions. A related factor is that the angular momentum ($L_{collision}$) associated with bimolecular collisions is high, and all of this angular momentum is available to affect dissociation of the collision complex. $L_{collision} = \mu\, v\, b$, where μ is the reduced mass of the reactants, v is the collision relative velocity, and b is the impact parameter, which ranges from zero to $b_{max} = (\sigma_{collision}/\pi)^{1/2}$, so that the corresponding $L_{collision} \leq 175$ h for $E_{col} = 0.25$eV, rising to 318 h at our highest energy. In PID, the angular momentum comes from the thermal rotation of the initial complex ion, and is much lower. In CID, the complex is activated by collisions with an inert target atom, and these collisions also have high $L_{collision}$, ranging from ≤ 197 h near threshold up to

$L_{collision} \leq 580$ h for conditions corresponding to our highest E_{col}. Note; however, for the large impact parameter collisions that give rise to the highest $L_{collision}$ values, conservation of angular momentum requires that most of $L_{collision}$ go into complex - target recoil, such that relatively little can remain as rotational angular momentum of the activated $(N_2O \cdot H_2O)^+$ complex. In contrast, for bimolecular collisions, all of $L_{collision}$ is available to drive separation of the collision complex to products, and as shown by the v_{axial} results (Figure 11.8), high angular momentum collisions are important in all three channels, giving rise to the strongly backward-scattered product ions.

A final factor is the role of excited electronic states. As discussed above, there are several doublet excited states within the energy range accessible in our experiments,[15] and in the broken symmetry of a collision experiment (including CID), these all are ^2A, and therefore can collisionally mix. In this context, it is important to note that the $H_2O^+ + N_2O$ (our σ_{NR}) and $N_2OH^+ + OH$ products correspond to channels on the ground state surface, while the $N_2O^+ + H_2O$ (i.e., CT) products correspond to an electronically excited state of the separated reactants. In the PID experiment, the complex ion is optically excited to some distribution of electronically excited states, which can dissociate directly to excited state products, or after relaxation to the ground adiabatic surface. In contrast, the CID and bimolecular scattering experiments start on the ground state surface, and must connect to the $N_2O^+ + H_2O$ (CT) excited channel by some pathway enabled by collision-induced mixing of the states of the collision complex.

Ground State Reaction Mechanism

As shown by the v_{axial} distributions for N_2O^+, N_2OH^+, and N_2OD^+ in Figures 11.3, 11.4, 11.5, and 11.8, all three reactions in this system are direct at high E_{col}. The sharp backward peaking indicates that stripping-like dynamics characteristic of large impact parameter collisions dominate, and the broad components extending forward of V_{CM} show that all three reactions also occur in smaller impact parameter collisions, where the products are forward- or sideways-scattered.

At low E_{col}, the distributions broaden in a way that suggests that they might become forward-backward symmetric for E_{col} near threshold. Symmetry could indicate mediation by a complex; however, direct reaction mechanisms can also give symmetric distributions. Therefore, while the RC geometries in Figure 11.2 might plausibly stabilize a complex, we need to examine other features to tell if such complexes are actually dynamically important at low E_{col}. If complex mediation is important, then the RC complexes would need to have significant lifetimes, and the observed product branching should also be consistent with branching in decay of the complexes. To test this proposition, statistical unimolecular decay lifetimes were calculated for the collision complex, using the RRKM program developed by Zhu and Hase.[22] Because the available energy is far in excess of the barriers to interconversion of the RC1, RC2, and RC3 complexes (Figure 11.2), it is more reasonable to treat the problem as a single interconverting complex ("RC") with density of states equal to the sum of the density of states of the three complexes. The decay to products or reactants was assumed to be governed by an orbiting transition state, since there are no barriers to these pathways. Decay rates were calculated over the range of collisional angular momenta appropriate to each E_{col}, and then the rates were appropriately averaged under the assumption that all capture collisions contribute to complex formation. The lifetimes ($\tau_{complex}$) as a function of E_{col} were calculated as the inverse of the sum of the rates for decay into each channel, averaged over $L_{collision}$ with appropriate weighting assuming all capture collisions form complexes. The branching was calculated from the ratios of the rates for each channel, also with appropriate averaging over the $L_{collision}$ distribution. For comparison, the experimental branching at each collision energy is also given. The calculations were done only for E_{col} = 0.20eV, 0.34eV, and 0.62eV, i.e., for the range of E_{col} where complexes might plausibly be significant. The calculated lifetimes vary from ~15 psec for E_{col} = 0.20eV to ~1.5 ps for E_{col} = 0.62 eV. These complex lifetimes are longer than the rotational periods (Table 11.2), which is consistent with the apparently symmetric v_{axial} distributions for $E_{col} \leq 0.34$ eV. As noted; however, symmetry is a necessary, but not sufficient condition to show that the mechanism is complex-mediated.

Another test of the possible contribution of complex mediation to the mechanism is the product branching ratio. If the RC complexes really are mediating reaction, then the measured product branching should match the predicted branching for decay of the RC complexes. For E_{col} = 0.2 eV, the RRKM prediction for decay of the RC complexes gives branching of 13% for HT+DT, and 87% for $HOD^+ + N_2O$ (i.e., no reaction) with no CT possible due to insufficient available energy. This prediction is in reasonable agreement with the experimental branching of 21% HT+DT, 72% No reaction, and 7% for CT, if we take into account the fact that there is a 0.15 eV wide collision energy distribution, and that collisions with higher available energy will tend to have higher branching to the endoergic CT, HT, and DT channels. The RRKM prediction for E_{col} = 0.34 eV (43% for HT+DT, 57% for No Reaction, and less than 0.5% for CT) is in worst agreement with the experimental branching (27% HT/DT, 62% No reaction, and 11% CT), particularly for CT channel, which RRKM predicts to increase more slowly with E_{col} than is observed. Finally, for E_{col} = 0.62 eV, the experimental HT+DT branching is much smaller than predicted by the RRKM calculation, and the CT branching is much larger. The CT branching may not be correctly treated by RRKM calculations because there may be contributions by both adiabatic and nonadiabatic pathways leading to the CT channel, which is an excited electronic state of the reactants.

We conclude that in the near-threshold E_{col} range, the RC complexes are likely to contribute to the reaction mechanism, at least to some extent. With increasing E_{col}, the importance of the RC complexes diminishes, although they may still form in some collisions (e.g., low b collisions where E_{col} to $E_{internal}$ conversion should be most efficient). The vibrational effects discussed below provide additional evidence regarding the important of complex mediation. What is completely clear; however, is that with increasing E_{col}, the lifetime of the available complexes rapidly becomes dynamically insignificant, and for $E_{col} \geq 0.62$ eV, the dominant mechanism is direct, as shown by the asymmetric v_{axial} distributions, and poor agreement of the product branching with predictions for complex decay. At our highest energies,

where the available energy is much larger than the well depths on the potential surface, scattering is probably impulsive, and the shapes of the v_{axial} distributions are probably determined primarily by the distributions of impact parameter (b) contributing to each channel. Since all three channels have similar v_{axial} distributions at high energies, we conclude that all three occurs in large b collisions that give rise to strongly backward-scattered products, as well as in small and medium b collisions which give rise to products in the broad tail that extends into the forward direction.

The reactions observed in this system involve transfer of either a light atom (HT or DT) or an electron (CT), and the very similar v_{axial} distributions suggest that they are in competition for collisions at all impact parameters. The ratio of HT+DT to CT is ~3 at low E_{col}, as might be expected because CT is slightly more endoergic than HT or DT, but the ratio drops to ~0.33 at E_{col} = 2.88 eV, i.e., probability of transferring an electron is 3 times greater than the combined probability of transferring H^+ or D^+. It should be noted that for this system, there are no energetically accessible secondary reactions that might lead to loss of HT or DT products, or that might contribute to the CT product signal. For example, the $N_2O^+ + OH + D$ and $N_2O^+ + OD + H$ channels are >5.3 eV endoergic. Dissociation of the HT (DT) product ion by OH^+ (OD^+) elimination is ~2.85 eV endoergic, and in principle could lead to some loss of HT or DT signal; however, this could occur only at our highest E_{col}, and only if nearly all the available energy were partitioned to internal energy of the N_2OH^+ (N_2OD^+) product ion. In fact, as shown by the v_{axial} distributions, these product ions have substantial recoil energy, and therefore, this dissociation process is negligible in the E_{col} range studied. We can conclude, therefore, that the predominance of CT at high energies reflects the dynamics of the $HOD^+ - N_2O$ collisions.

Another ratio of interest is the HT/DT ratio (bottom frame of Figure 11.7). As noted, for the threshold E_{col} range, where reaction may be mediated by a statistical complex, the ratio is ~1.05, as might be expected because HT is ~20 meV less endoergic than DT. At high energies, where reaction appears to occur in impulsive collisions, the ratio rises to nearly 1.4. There are a number of mechanisms which might tend to favor either H^+ transfer or D^+ transfer in impulsive

collisions. In HOD, the center of mass is offset from the center of charge, thus the long-range attractive force during reactant approach might tend to orient the HOD^+ to impact H on N_2O. Because the offset is small due to the presence of the massive O atom, it seems unlikely that this effect could result in a 40% enhancement of HT, particularly at high E_{col} where the approach time is short.

For an endoergic stripping reaction in the impulsive limit, it may be useful to think about the energy associated with collision of N_2O with either the H or D atom which is being transferred. Because the N_2O-D reduced mass is nearly a factor of two greater than that for N_2O-H, the "local" collision energy is also much greater for D^+ stripping, compared to H^+ stripping, thus if collisional energy transfer is the limiting factor in HT/DT, this effect would favor DT, in contrast to the observed enhanced HT branching. It might be thought that this same factor would tend to result in higher internal energy of the DT product ion, which might therefore be depleted by secondary dissociation; however, as mentioned above, there are no energetically accessible dissociation channels in the E_{col} range studied.

In the impulsive limit, HT (DT) in the $HOD^+ + N_2O$ system can be thought of as an A + BC system, where A = OD (OH), B = H^+/D^+, and C = N_2O, i.e., light atom transfer between two heavy groups (a HLH system). Because the reduced mass associated with the light atom transfer is much lower than for approach and recoil of the system, it is useful to think about the dynamics in terms of motion on a mass weighted, scaled, and skewed potential energy surface.[31] Here, the main effect is that the skew angle between the reactant and product valleys is 15.7° for HT and 22.3° for DT, i.e., HT requires the system to negotiate a tighter bend than DT. One might think that this effect might favor DT; however, it could be that the shape of the repulsive wall favors rebounding around the tighter bend associated with HT. It is possible that HT is enhanced by tunneling through the "ridge" that separates the reactant and product valleys; however, tunneling effects are usually more important at low energies, as was observed in HT vs. DT in the Cl + HCl and Cl + DCl (HLH) systems.[32]

Vibrational Effects and the Relative Efficiency of Different Forms of Energy

All product channels in this system are enhanced by vibrational excitation, at least at low E_{col}; therefore, there is a net enhancement of the total reaction cross section, $\sigma_{reaction}$, over the entire range of energies examined. Even in the low E_{col} range where collision energy also enhances reaction, the effects from E_{vib} are substantially greater than those from equivalent amounts of E_{col}. For example, exciting the OH stretch increases $\sigma_{reaction}$ at our lowest E_{col} by a factor of 220%, while increasing E_{col} by the same amount (0.396 eV), results in only a ~40% increase. For E_{col} above 0.6 eV, the difference is qualitative – adding E_{vib} continues to enhance reactivity, while E_{col} suppresses it.

The Charge Transfer Channel

For CT (Δ_rH^0 = 0.259 eV), the ground state cross section increases slowly with E_{col}, and levels off only above ~1 eV, i.e., ~ four times the threshold energy. This slow growth suggests that energy in relative motion of the reactants is not efficiently converted to forms that can drive CT. Similarly, even though the energies of the OD and OH stretch modes (0.293 eV and 0.396 eV, respectively) are, by themselves, greater than Δ_rH^0, the CT cross sections still increase with increasing E_{col} at low energies (Figure 11.6), indicating that vibrational energy is also not particularly efficient at driving CT.

For an endothermic reaction, where the available energy is the limiting factor in the threshold energy range, all forms of energy are expected to enhance reaction, but there could potentially be differences in the efficiency of energy put in different vibrational modes and in E_{col}. By plotting cross section vs. E_{tot} (Figure 11.6, bottom frame), the efficiencies can be compared. In the E_{tot} range closest to threshold (< ~0.6 eV), the data for ground state, bend, and OD stretch excited HOD^+ are nearly superimposable, although there does seem to be slightly larger effect from vibrational excitation than from putting the same amount of energy in E_{col}. As the total

energy increases (including the lowest energy point for OH-stretch-excited HOD^+), CT is clearly enhanced more efficiently by energy put in any of the vibrational modes, rather than in E_{col}.

The threshold energy range where E_{vib} and E_{col} have similar effects is also the energy range where the RC complexes have dynamically significant lifetimes (Table 11.3), and where the product branching is roughly consistent with expectations for breakdown of a statistical intermediate complex. If mediation by a complex is important at low energies, then rotation of the complex should average out any asymmetries in the v_{axial} distributions, including any tendencies for vibrational excitation to enhance scattering into particular v_{axial} ranges. Just such behavior is seen in the v_{axial} distributions for CT products in the low E_{col} range (Figure 11.8), i.e., the enhancements are uniform across the entire v_{axial} range.

For energies above ~ 1 eV, collision energy begins to slightly inhibit the CT reaction, but all three vibrational modes continue to enhance CT by up to a factor of ~50%. The enhancement is not mode-specific, i.e., is proportional to E_{vib} for the excited modes. In this energy range, the v_{axial} data in Figure 11.8 show that vibrational excitation has no effect on the ~50% of collisions that produce NO_2^+ with v_{axial} in the broad component of the distribution that extends from ~500 m/sec to well forward of $<V_{CM}>$. Instead, the vibrational enhancement appears as a ~2x enhancement of the strongly backward-scattered peaks near zero lab velocity. In this high E_{col} range, reaction is direct, and the product v_{axial} is probably mostly a function of the collision impact parameter. Therefore, the results show that vibrational excitation strongly enhances the probably of CT in large b "grazing" collisions. Such collisions are expected to have inefficient collision-to-internal energy conversion, and therefore, it is reasonable that the presence of vibrational energy in the reactants would enhance CT, by reducing the energy conversion required to overcome the endoergicity. Conversely, in the more central collisions that contribute to the broad v_{axial} component, collision-to-internal energy conversion is expected to be facile, and therefore, it is not surprising that the small amount of energy in reactant vibration has little effect.

H^+/D^+ Transfer

The cross sections for N_2OH^+ and N_2OD^+ production for each HOD^+ vibrational state are shown vs. E_{col} in Figure 11.7, which also gives the HT/DT branching. All modes of HOD^+ excitation and E_{col} enhance the endoergic HT and DT at the lowest E_{col}, which is not surprising for an endoergic reaction. Unlike CT, the enhancements from vibrational excitation are much larger than the effects from increasing E_{col}, even at our lowest energies. Indeed, E_{col} inhibits both HT and DT except at our lowest energy. In addition, the vibrational effects on HT and DT are quite mode-specific, even at low E_{col}, where it appears that mediation by complexes may be important in the reaction mechanism.

In a complex-mediated mechanism, we might expect the initial mode of vibrational excitation to be scrambled, and in that case, reactivity should depend only on the total energy, and possibly the total angular momentum. The fact that strongly mode-specific vibrational enhancements are observed for HT and DT may, therefore, appear to preclude significant participation of the RC complexes in the reaction mechanism, even at low E_{col}. In fact; however, there are many examples of ion-molecule reactions that clearly proceed via intermediate complexes, but which nonetheless show strong mode selective vibrational effects.[17, 33, 34] The complexes in these cases are weakly bound reactant-like structures, which can form from reactants without breaking or forming any covalent bonds. In such complexes, the reactant moieties are loosely coupled and therefore, formation of a complex does not necessarily lead to rapid scrambling of the reactant vibrations. Therefore, the system can still "remember" the initial vibrational excitation when it passes through the rate-limiting step on the reaction coordinate, which comes as the reactant-like complex transitions either to one of the product channels, or to a product-like complex that leads eventually to one of the product channels. In the $HOD^+ + N_2O$ system, the RC complexes are bound by over an electron volt; however, the energy appears to depend weakly on the geometry, and thus it is not unreasonable to expect that vibrational mode scrambling may be slow.

It is interesting that the near-threshold dependence on E_{col} is so different for HT/DT compared to CT, even though the differences in threshold energy (E_0) are small. As discussed above, conversion of E_{col} and all three modes of vibrational excitation to drive CT is relatively inefficient, so that the maximum cross sections occur at total energies nearly four times E_0. In contrast, the HT (Δ_rH^0 = 0.187 eV) and DT (0.207 eV) channels increase rapidly with E_{col}, peaking near E_{col} = 0.34 eV, and in reaction of vibrationally excited HOD^+, the HT/DT cross sections peak at the lowest energy point, even for the bend, where the vibrational energy is well below Δ_rH^0. The implication is that conversion of both E_{col} and vibrational energy to drive HT or DT is substantially more efficient than it is for CT, presumably reflecting the fact that HT and DT involve bond breaking, whereas CT requires an electronic excitation.

As noted, the effects of HOD^+ vibrational excitation on HT and DT are quite mode/bond-specific (Figure 11.7). Excitation of the broken-bond stretch enhances both HT and DT, whereas spectator stretch excitation only enhances reaction at low E_{col}, and actually inhibits DT at higher energies. Bend excitation provides some enhancement at low E_{col}, but has little effect at high energies. The behavior at low E_{col} indicates that all forms of energy are somewhat effective at driving these endoergic reactions, although all modes of vibration are considerably more efficient than E_{col}. At high E_{col}, vibrational excitation still has significant effects, even though E_{vib} is a small fraction of E_{tot}. The bottom frame of Figure 11.7 shows the HT/DT branching ratio as a function of E_{col} and HOD^+ vibrational state. In the threshold E_{col} range, the ratio changes from ~0.8 for OD stretch excitation, to 1.64 for OH stretch excitation. At high E_{col}, where there is a general tendency toward HT over DT, as discussed above, OH stretch excitation favors HT by a factor of 2.5, while OD stretch excitation gives equal HT and DT branching, i.e., favors DT compared to what is seen for ground state or bend-excited HOD^+.

The observation that all HOD^+ modes enhance both HT and DT in the threshold region is consistent with reaction being mediated by a complex, which would facilitate randomization of

vibrational energy allowing all modes to couple to the reaction coordinate, albeit with very different efficiencies. As E_{col} increases and reaction becomes direct, the broken-bond stretch continues to have a substantial effect, consistent with this mode being directly coupled to the reaction coordinate, as might be expected. The spectator stretch enhancement disappears for $E_{col} \geq 0.6$ eV for HT, and switches to a significant inhibition for $E_{col} > 0.3$ eV for DT. It is not clear why energy in the spectator bond should inhibit reaction; however, we note that E_{col} also inhibits HT and DT in this energy range. Bend excitation continues to enhance HT and DT up to $E_{col} \approx 1$ eV, even though we would expect that this mode should not couple to the reaction coordinate. An unexpected enhancement from bend excitation was also observed for HT and DT in reaction of HOD^+ with CO_2[10] and N_2,[9] and in that case, it was attributed to a bend-induced distortion of the potential surface, which facilitated scattering into the product channel.[10]

As shown in Figure 11.8, at low E_{col}, both OH and OD stretch excitations enhance HT for all v_{axial}, with a larger increase from the higher energy OH stretch, which is also the broken-bond stretch. As in CT, the fact that the enhancement appears over the entire v_{axial} distribution is consistent with reaction being mediated by a complex that lives long enough to rotationally average out any angular dependence of the enhancement. In contrast, the DT reaction at $E_{col} = 0.34$ eV is enhanced across the entire distribution by the OD (broken-bond) stretch, but the OH (spectator) stretch has no effect. This lack of effect is coincidental. $E_{col} = 0.34$ eV just happens to be energy where the OH stretch vibrational effect crosses over from enhancement at low E_{col} to inhibition at high E_{col} (Figure 11.7). Indeed, the v_{axial} distributions at $E_{col} = 0.2$ eV show that OH stretch excitation enhances the entire distribution, with an effect roughly half that from the OD stretch.

At high E_{col}, the effects on HT and DT are also quite different. For HT, the OH (broken-bond) stretch enhances the integral cross section by ~30 % (Figure 11.7 top), but the enhancement is only for collisions that lead to strongly backward-scattered product ions, indicating that OH stretching only enhances stripping in large impact parameter collisions

(Figure 11.8 center). The OD (spectator) stretch has no significant effect on either the integral cross section or v_{axial} distribution for HT. In contrast, the integral cross section for DT at 2.88 eV (Figure 11.7) is still enhanced ~40% by OD (broken-bond) stretch excitation, but Figure 11.8 shows that the enhancement occurs in collisions producing N_2OD^+ in a broader, but still backward-scattered, range of v_{axial}. The implication is that reactivity is enhanced for a wider range of impact parameters, though still all leading to backward-scattered product ions. Excitation of the OH (spectator) stretch inhibits DT (Figure 11.7), and Figure 11.8 shows that the inhibition primarily affects the broad component of the v_{axial} distribution, with only a small decrease in the sharply backward-scattered peak. This suggests that OH stretching inhibits reaction for small to medium impact parameters, but has little effect on stripping at the largest reactive impact parameters.

The observation that at high E_{col}, HT and DT are enhanced selectively by the stretch of the bond that is broken in reaction, and either inhibited or unaffected by the spectator stretch, is consistent with the "Polanyi rules" developed for A + BC reactions, that were briefly mentioned in the introduction[1]. The "rules" state that translational energy should be more efficient than vibrational energy at overcoming an early barrier in the reaction coordinate and that vibrational energy (in the BC stretch) should be more efficient than translational energy at overcoming a late barrier in the reaction coordinate. As shown in Figure 11.2, there are no (early) barriers to reactant approach in typical ion-molecule reactions, but since the reaction is endoergic, there is a late barrier to HT and DT. For polyatomic reactants, of course, only vibrations that correspond to the barrier crossing motion are effective, and in this case, it should be clear that the vibration of interest is the broken-bond stretch. The spectator stretch is, to zeroth order, not coupled to the reaction coordinate, but obviously there is some coupling even when reaction is direct, as shown by the inhibition of DT by excitation of the OH stretch at high E_{col}. At low E_{col}, where collision times are long, and complexes may be mediating reaction to some extend, vibrational mode scrambling allows all modes to couple to drive HT and DT.

Conclusion

Reaction of HOD^+ with N_2O appears to be complex-mediated at low E_{col} and is clearly direct at high E_{col}. Vibrationally exciting HOD^+ enhances CT nonspecifically, i.e., with effects that are proportional to the energy of the vibration, but larger than the effects of equivalent amounts of E_{col}. Increasing E_{vib} also increases the partitioning of energy to E_{recoil}. The vibrational results for HT/DT are strongly mode- and bond-selective. The broken-bond stretch enhances HT and DT by a factor of ~2 at low E_{col} with enhancement diminishing with increasing energy. The broken-bond stretch also increases the partitioning of energy to E_{recoil}. Exciting the spectator stretch results in smaller enhancement at low E_{col}, and either no effect or inhibition at higher E_{col}. The recoil v_{axial} distributions shows that for low E_{col}, vibrational excitation enhances reaction in all collision, while at high E_{col}, the enhancement mainly occurs in large impact parameter collisions, with little effect, or even inhibition, in smaller impact parameter collisions.

Acknowledgements

This work was supported by grants CHE-0647124 and CHE-1111935 from the Chemistry division of the National Science Foundation.

References

1. J. C. Polanyi and W. H. Wong, J. Chem. Phys. **51**, 1439 (1969).
2. M. C. Hsiao, A. Sinha and F. F. Crim, J. Phys. Chem. **95**, 8263 (1991).
3. R. B. Metz, J. D. Thoemke, J. M. Pfeiffer and F. F. Crim, J. Chem. Phys. **99**, 1744 (1993).
4. A. Sinha, M. C. Hsiao and F. F. Crim, J. Chem. Phys. **92**, 6333 (1990).
5. A. Sinha, M. C. Hsiao and F. F. Crim, J. Chem. Phys. **94**, 4928 (1991).
6. M. J. Bronikowski, W. R. Simpson, B. Girard and R. N. Zare, J. Chem. Phys. **95**, 8647 (1991).
7. M. J. Bronikowski, W. R. Simpson and R. N. Zare, J. Phys. Chem. **97**, 2204 (1993).

8. D. H. Zhang, M. A. Collins and S.-Y. Lee, Science **290**, 961 (2000).

9. D. M. Bell, J. M. Boyle and S. L. Anderson, J. Chem. Phys **135**, 044305 (2011).

10. D. M. Bell, J. M. Boyle and S. L. Anderson, J. Chem. Phys **134**, 64312 (2011).

11. D. M. Bell and S. L. Anderson, J. Phys. Chem. A **117**, 1083 (2012).

12. M. J. Bastian, R. A. Dressler, D. J. Levandier, E. Murad, F. Muntean and P. B. Armentrout, J. Chem. Phys. **106**, 9570 (1997).

13. S. Williams, Y.-H. Chiu, D. J. Levandier and R. A. Dressler, J. Chem. Phys. **108**, 9383 (1998).

14. S. T. Graul, H.-S. Kim and M. T. Bowers, Int. J. Mass Spectrom. Ion Proc. **117**, 507 (1992).

15. J. E. Stevens, M. C. Holthausen and K. Morokuma, J. Chem. Phys. **111**, 7766 (1999).

16. Y.-H. Chiu, H. Fu, J.-T. Huang and S. L. Anderson, J. Chem. Phys. **102**, 1199 (1995).

17. J. Liu, B. V. Devener and S. L. Anderson, J. Chem. Phys. **119**, 200 (2003).

18. J. M. Boyle, D. M. Bell and S. L. Anderson, Journal of Chemical Physics **134**, 034313 (2011).

19. B. W. Uselman, J. M. Boyle and S. L. Anderson, Chemical Physics Letters **440**, 171 (2007).

20. D. Gerlich, in *State-selected and state-to-state ion-molecule reaction dynamics, Part I. Experiment*, edited by C. Y. Ng and M. Baer (Wiley, New York, 1992), Vol. LXXXII, pp. 1-176.

21. M. J. Frisch, G. W. Trucks, H. B. Schlegel, G. E. Scuseria, M. A. Robb, J. R. Cheeseman, J. J. A. Montgomery, T. Vreven, K. N. Kudin, J. C. Burant, J. M. Millam, S. S. Iyengar, J. Tomasi, V. Barone, B. Mennucci, M. Cossi, G. Scalmani, N. Rega, G. A. Petersson, H. Nakatsuji, M. Hada, M. Ehara, K. Toyota, R. Fukuda, J. Hasegawa, M. Ishida, T. Nakajima, Y. Honda, O. Kitao, H. Nakai, M. Klene, X. Li, J. E. Knox, H. P. Hratchian, J. B. Cross, C. Adamo, J. Jaramillo, R. Gomperts, R. E. Stratmann, O. Yazyev, A. J. Austin, R. Cammi, C. Pomelli, J. W. Ochterski, P. Y. Ayala, K. Morokuma, G. A. Voth, P. Salvador, J. J. Dannenberg, V. G. Zakrzewski, S. Dapprich, A. D. Daniels, M. C. Strain, O. Farkas, D. K. Malick, A. D. Rabuck, K. Raghavachari, J. B. Foresman, J. V. Ortiz, Q. Cui, A. G. Baboul, S. Clifford, J. Cioslowski, B. B. Stefanov, G. Liu, A. Liashenko, P. Piskorz, I. Komaromi, R. L. Martin, D. J. Fox, T. Keith, M. A. Al-Laham, C. Y. Peng, A. Nanayakkara, M. Challacombe, P. M. W. Gill, B. Johnson, W. Chen, M. W. Wong, C. Gonzalez and J. A. Pople, (Gaussian, Inc., Pittsburgh PA, 2003).

22. L. Zhu and W. L. Hase, in *Quamtum Chemistry Program Exchange* (Chemistry Department, Indiana University Bloomington, 1993).

23. S. G. Lias, J. E. Bartmess, J. F. Liebman, J. L. Holmes, R. D. Levin and W. G. Mallard, J. Phys. Chem. Ref. Data **17**, 1 (1988).

24. S. G. Lias, in *NIST Standard Reference Database Number 69*, edited by P. J. Linstrom and W. G. Mallard (National Institute of Standards and Technology, Gaithersburg, MD, 2003), pp. http://webbook.nist.gov.

25. J. M. L. Martin and T. J. Lee, J. Chem. Phys. **98**, 7951 (1993).

26. J. Liu, B. Van Devener and S. L. Anderson, J. Chem. Phys. **123**, 204313 (2005).

27. J. M. Boyle, D. M. Bell, S. L. Anderson and A. A. Viggiano, J. Phys. Chem. A **115**, 1172 (2011).

28. G. A. Fisk, J. D. McDonald and D. R. Herschbach, Discuss. Faraday Soc. **44**, 228 (1967).

29. J. D. C. Jones, K. Birkinshaw and N. D. Twiddy, Chemical Physics Letters **77**, 484 (1981).

30. C. B. Moore and P. F. Zittel, Science **182**, 541 (1973).

31. R. D. Levine, *Molecular Reaction Dynamics*. (Cambridge U. Pr., Cambridge, 2005).

32. B. C. Garrett, D. G. Truhlar, A. F. Wagner and T. H. Dunning, Jr., J. Chem. Phys. **78** , 4400 (1983).

33. J. Liu and S. L. Anderson, Int. J. Mass Spectrom. **241**, 173 (2005).

34. Y.-H. Chiu, H. Fu, J.-T. Huang and S. L. Anderson, J. Chem. Phys. **101**, 5410 (1994).

Table 11.1. Product ion velocity distribution results for each product and each vibrational state of $HOD^+ + N_2O$

N_2O^+	Ground State		Bend		OD Stretch		OH Stretch	
E_{col}(eV)	$\%E_{recoil}$[a]	B/F[b]	$\%E_{recoil}$	B/F	$\%E_{recoil}$	B/F	$\%E_{recoil}$	B/F
0.34	47.9	1.60	49.8	1.62	43.5	1.56	45.3	2.10
0.62	46.0	3.25	52.1	3.63	50.9	3.36	52.1	3.91
0.88	43.0	4.44	47.4	5.06	50.7	4.58	57.5	5.75
1.88	48.8	9.09	53.4	10.73	57.6	10.34	63.7	13.3
2.88	52.7	11.13	61.1	14.37	64.4	14.12	66.4	16.13

N_2OH^+	Ground State		Bend		OD Stretch		OH Stretch	
E_{col}(eV)	$\%E_{recoil}$	B/F	$\%E_{recoil}$	B/F	$\%E_{recoil}$	B/F	$\%E_{recoil}$	B/F
0.2	45.4	1.81	42.2	1.66	49.5	1.53	52.2	1.42
0.34	49.0	1.86	42.1	1.67	40.0	1.71	46.1	1.69
0.62	50.3	3.07	42.3	2.99	50.2	2.95	45.3	3.26
0.88	47.7	3.45	52.5	3.23	50.1	3.45	57.8	4.70
1.88	49.7	7.26	59.5	6.37	54.8	7.78	65.5	10.53
2.88	55.2	15.46	62.5	14.42	53.1	17.77	74.3	19.19

[a] $\%E_{recoil} = 100 \cdot E_{recoil} / E_{avail}$

[b] B/F is a measure of asymmetry in the product velocity distributions. B/F = 1 indicates a symmetric distribution about $<V_{CM}>$ and a B/F > 1 indicates an asymmetric and backward scattered distribution about $<V_{CM}>$.

Table 11.2 Rotational lifetimes of reactant-like complexes

E_{col}(eV)	RC 1/2 $\tau_{rotation}$	RC3 $\tau_{rotation}$	$\tau_{fly\text{-}by}$[a]
0.2	0.85	1.27	0.29
0.34	0.74	1.11	0.22
0.62	0.64	0.96	0.17
0.88	0.59	0.88	0.14
1.88	0.49	0.73	0.1
2.88	0.44	0.66	0.08

All lifetime values are in picoseconds.

[a] Time it takes the reactants to travel 5Å.

Table 11.3 RRKM lifetime and branching ratios

E_{col}(eV)	$\tau_{complex}$(ps)	Branching HT+DT : CT : No Rxn
0.2	15.0	12.7 : 0 : 87.3 RRKM
		21.3 : 6.5 : 72.3 Exp.
0.34	7.0	42.6 : 0.5 : 56.9 RRKM
		27.5 : 11.1 : 61.3 Exp.
0.62	1.45	73.6 : 3.4 : 23.0 RRKM
		33.6 : 24.5 : 41.8 Exp.

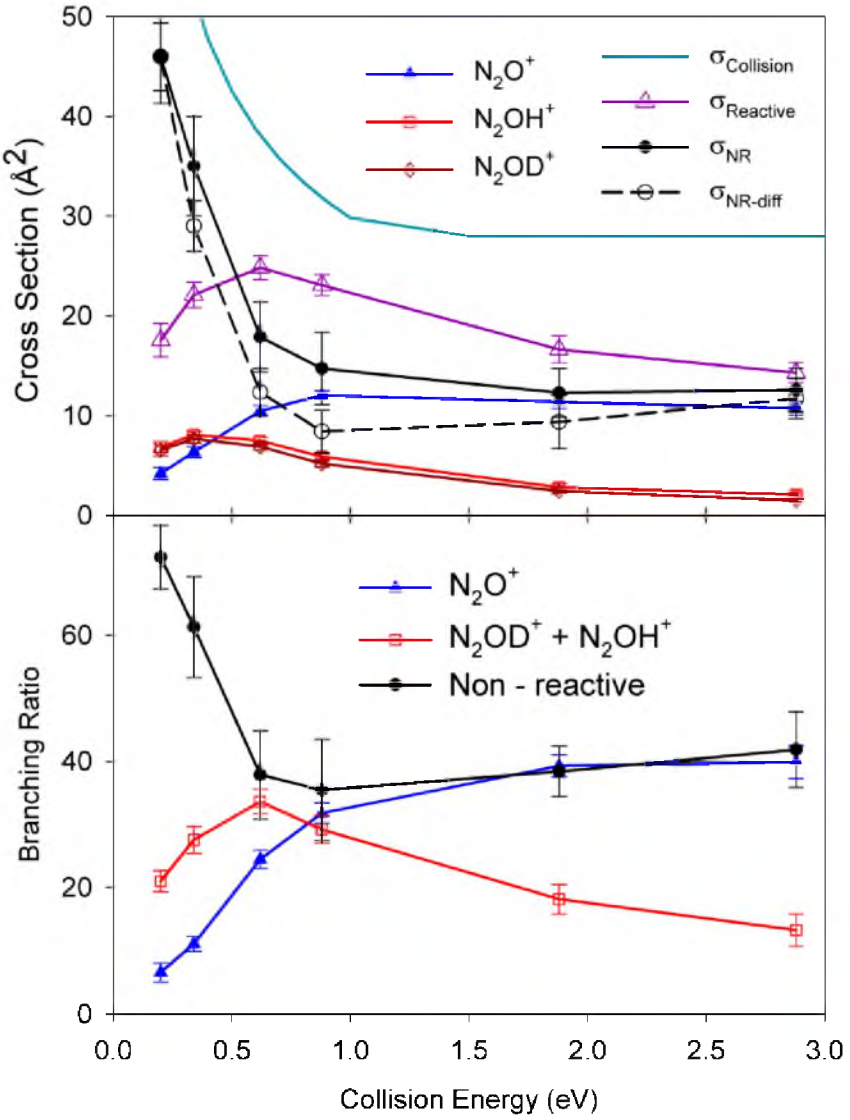

Figure 11.1: Cross sections and branching ratios for $HOD^+ + N_2O$. (Top) Cross sections for reactive and nonreactive scattering of ground state HOD^+ with N_2O, as a function of center-of-mass collision energy. The collision cross section is indicated as a curve with no data points. (Bottom) Branching ratios for CT, HT + DT, and nonreactive scattering vs. E_{col}.

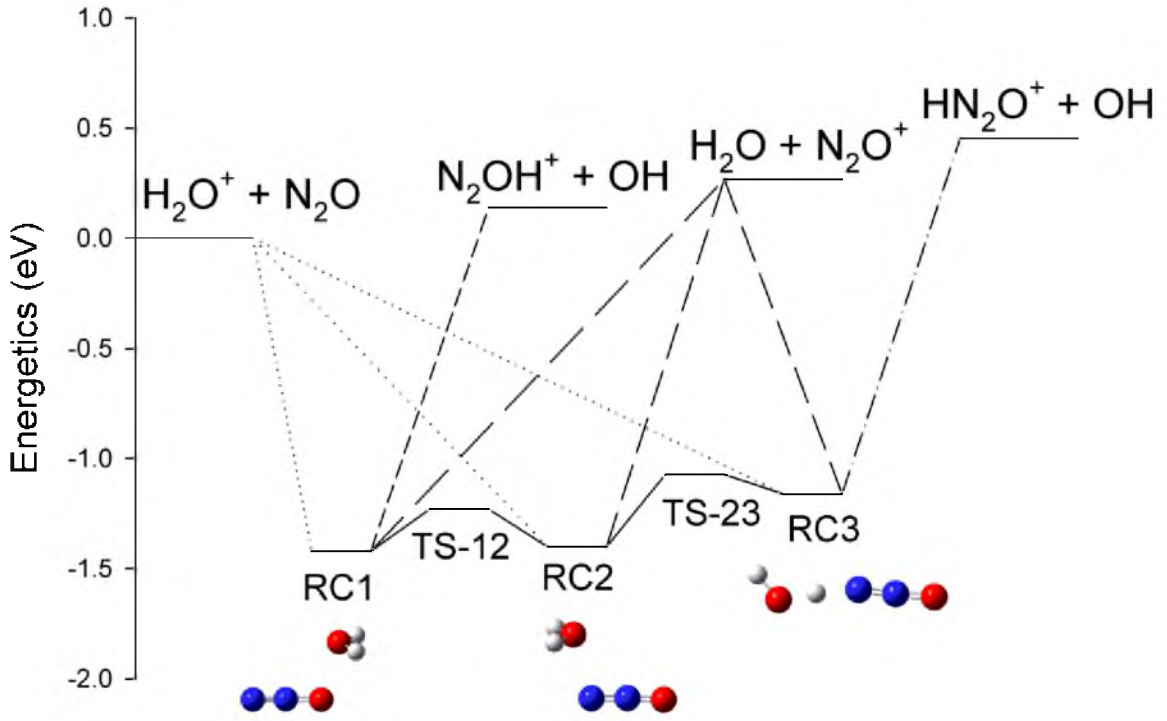

Figure 11.2: Reaction coordinate based on experimental energies for products and reactants and b3lyp/6-311++G(d,p) calculations for complexes and transitions states

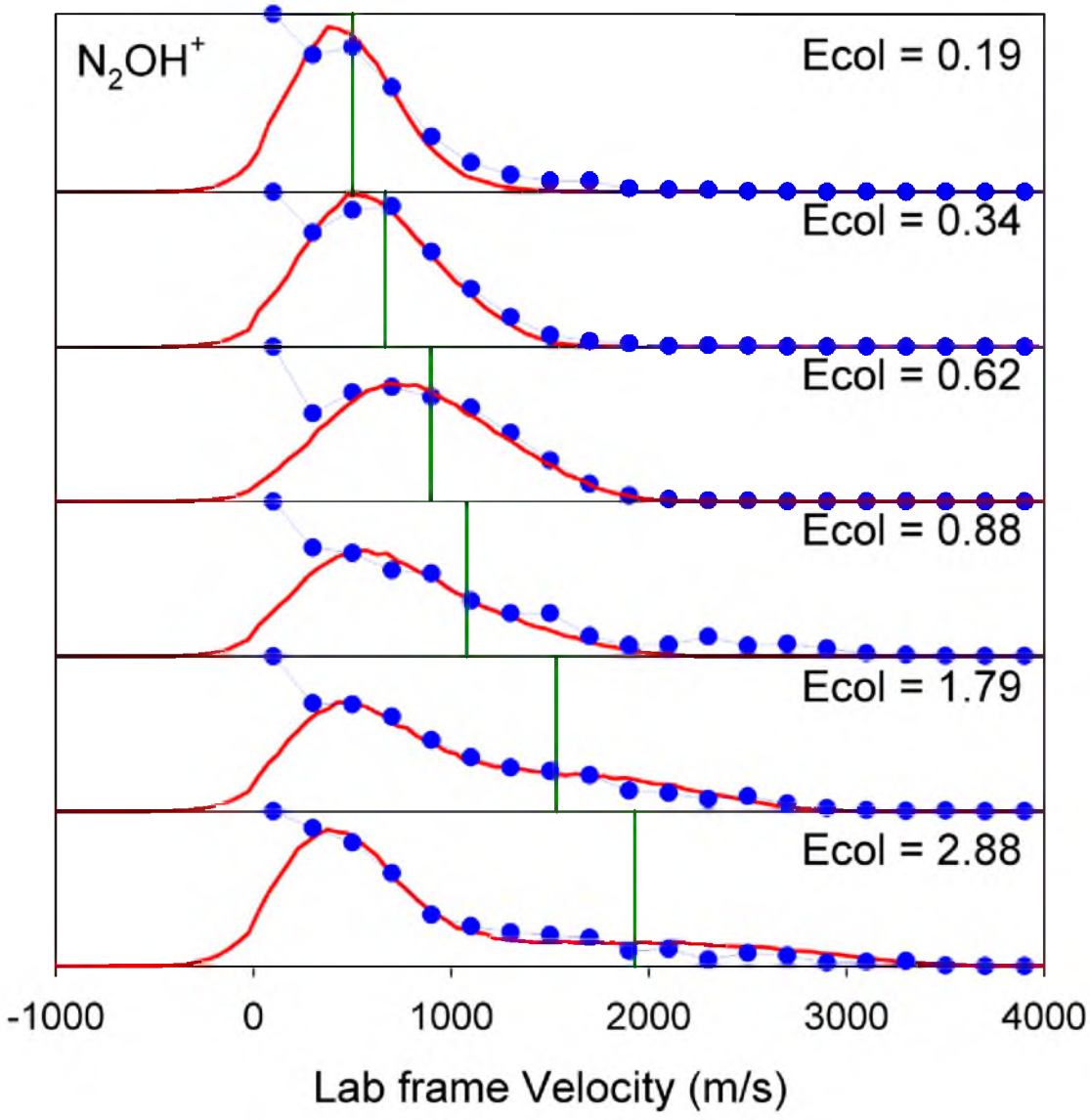

Figure 11.3: Lab frame axial velocity (v_{axial}) distributions for N_2OH^+ produced in the reaction of ground state HOD^+. Points - experimental data. Solid curves - simulations. Solid vertical lines indicate $<V_{CM}>$.

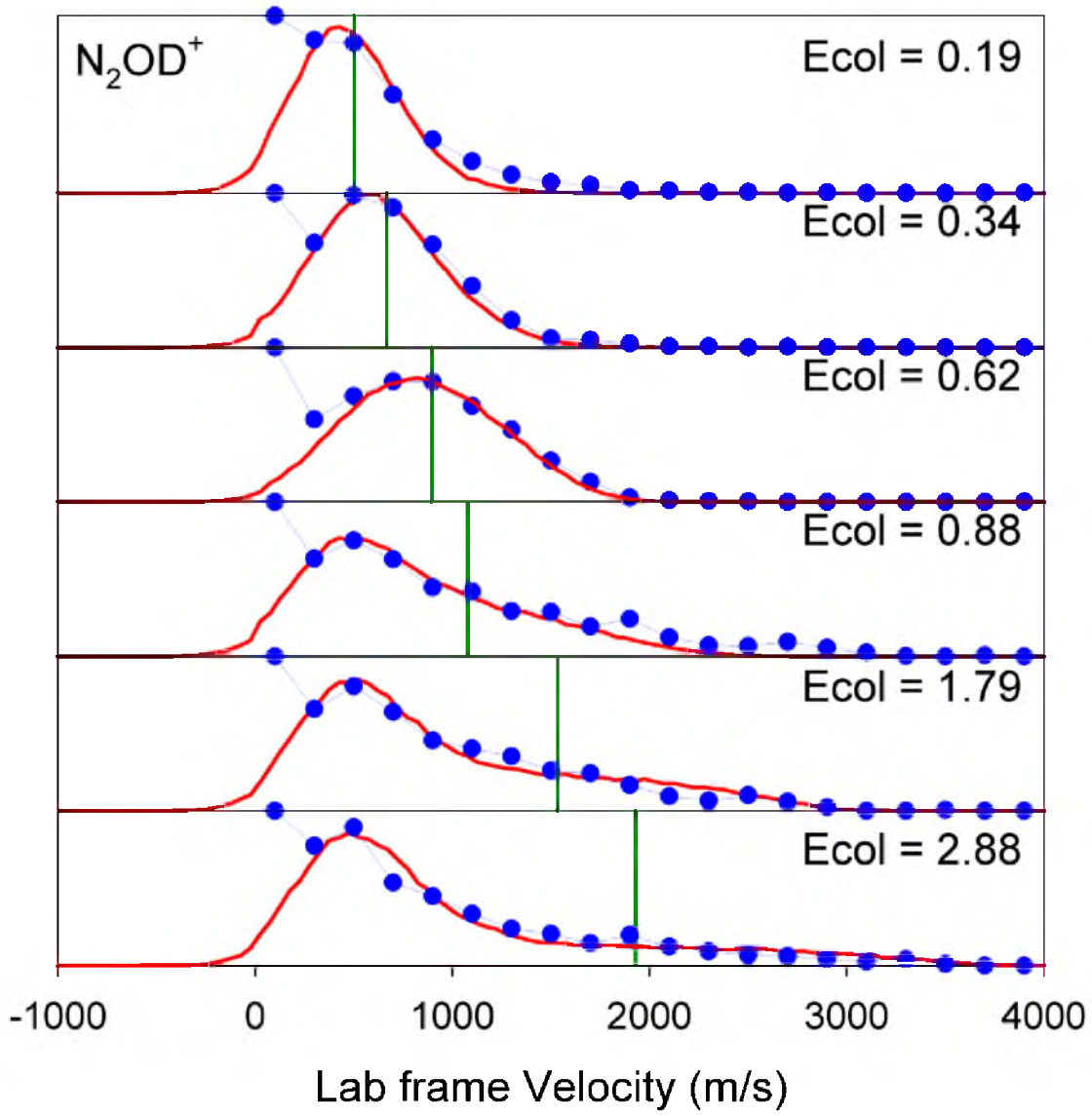

Figure 11.4: Lab frame axial velocity (v_{axial}) distributions for N_2OD^+ produced in the reaction of ground state HOD^+. Points - experimental data. Solid curves - simulations. Solid vertical lines indicate $\langle V_{CM} \rangle$.

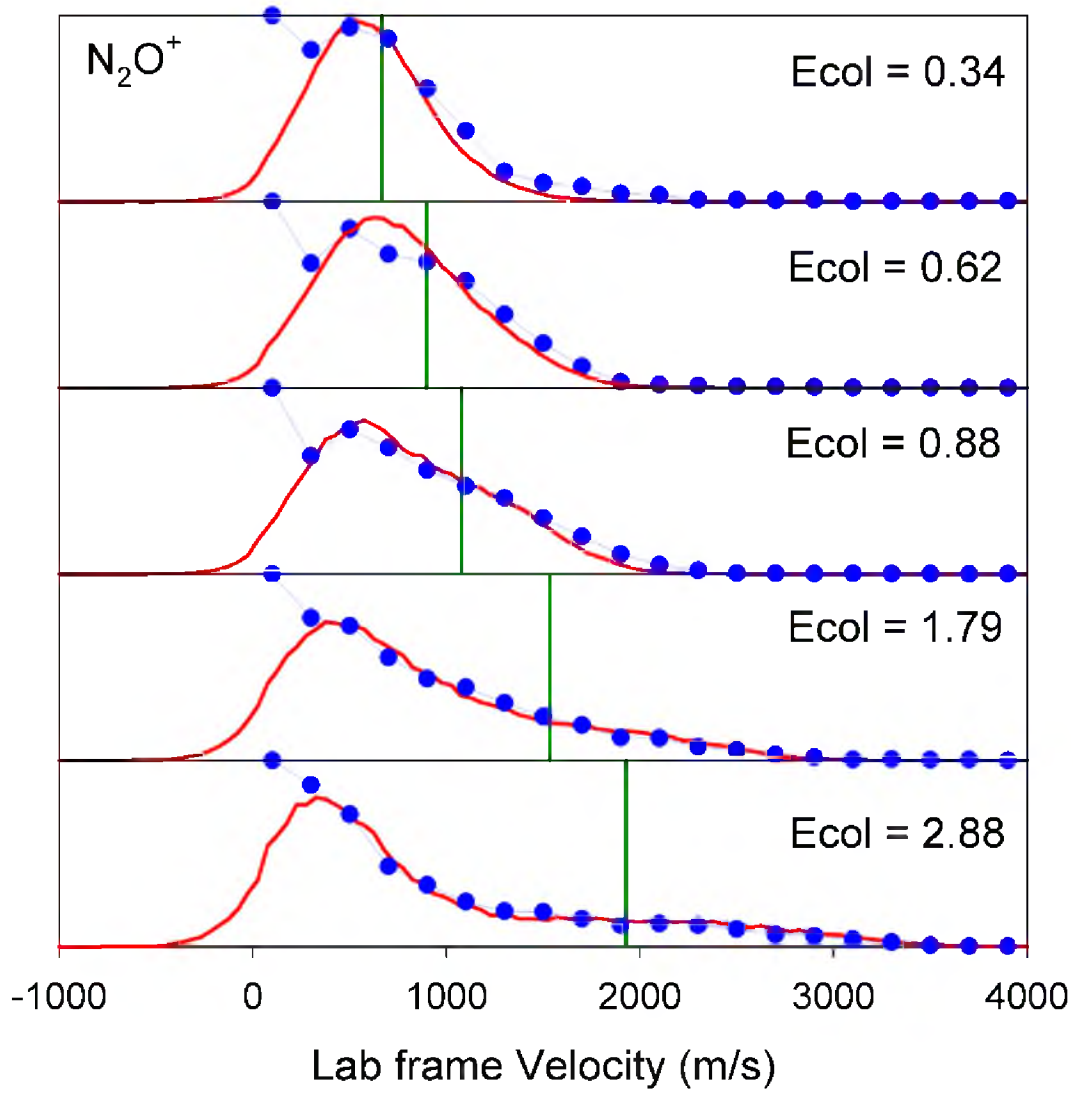

Figure 11.5: Lab frame axial velocity (v_{axial}) distributions for N_2O^+ produced in the reaction of ground state HOD^+. Points - experimental data. Solid curves - simulations. Solid vertical lines indicate $<V_{CM}>$.

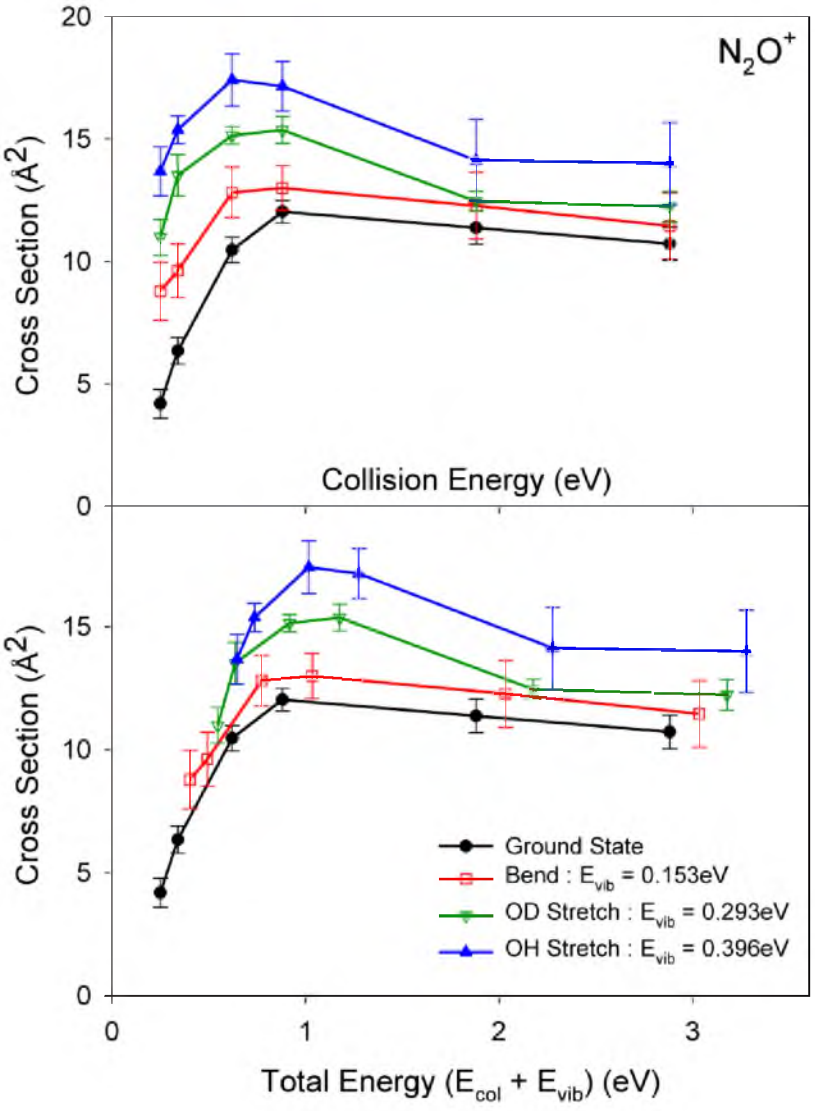

Figure 11.6: Cross sections for CT in the reaction of $HOD^+ + N_2O$. (Top) Cross sections for production of N_2O^+ from reaction of HOD^+ in the indicated vibrational states as a function of collision energy. (Bottom) Analogous cross sections vs. $E_{tot} = E_{col} + E_{vib}$.

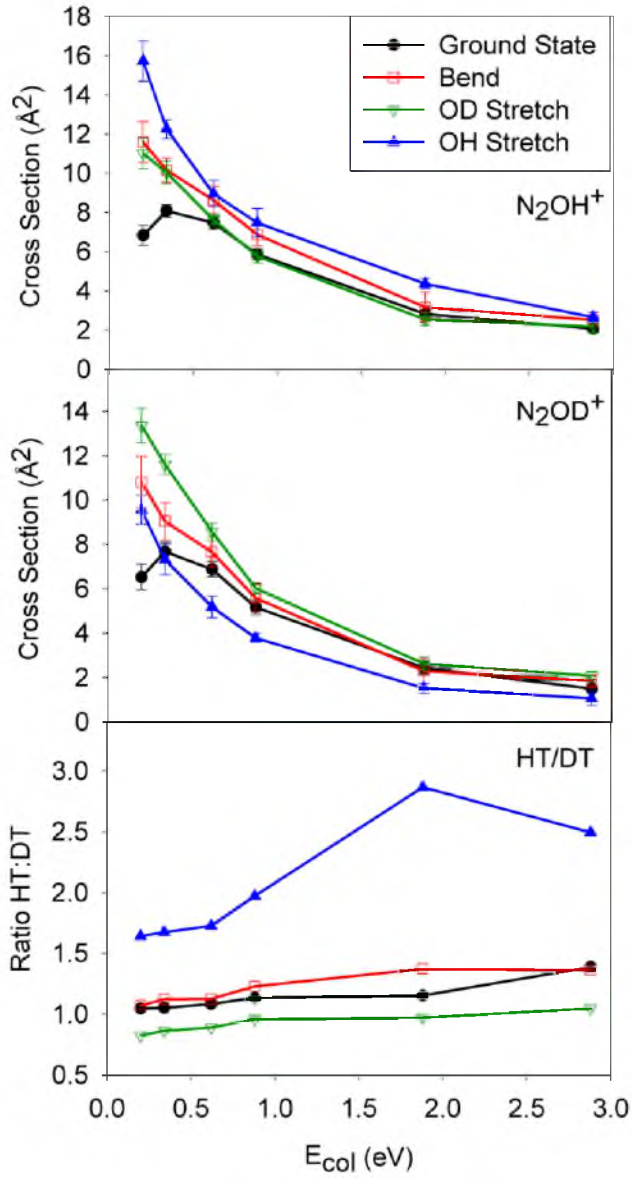

Figure 11.7: Cross sections and HT/DT ratio for N_2OH^+ and N_2OD^+. (Top) Cross sections for production of N_2OH^+ from reaction of HOD^+ in the indicated vibrational states as a function of E_{col}. (Middle) Analogous plots for N_2OD^+. (Bottom) Ratio of HT to DT as a function of E_{col} for reach vibrational state of HOD^+.

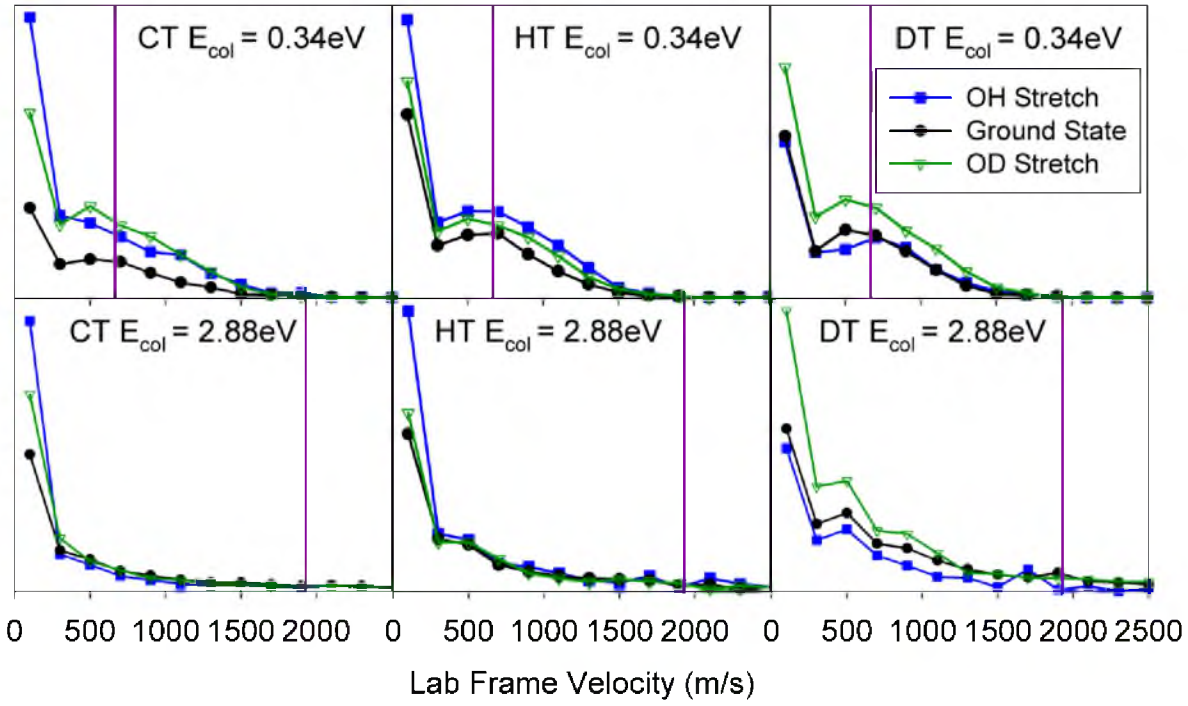

Figure 11.8: Axial velocity (v_{axial}) distributions for N_2O^+ (right), N_2OH^+ (middle), and N_2OD^+ (left) produced from reaction of HOD^+ in its ground state, and with one quantum of either the OD stretch of the OH stretch. The vertical line in each frame indicates $<V_{CM}>$.